The Development of Ionic Zinc(II) Phthalocyanines for Sono-Photodynamic Combination Therapy of Cervical and Breast Cancer

A thesis submitted in fulfilment of the degree of

DOCTOR OF PHILOSOPHY

By

LINDOKUHLE CINDY NENE

2022

RHODES UNIVERSITY
Where leaders learn

DEDICATION I

This work is dedicated to individuals that are battling with cancer and those affected by cancer of a loved one.

DEDICATION II

This work is specially dedicated to my guardian angels, my late parents, Mandlenkosi Blessing Nene and Mildred Tilly Nene.

ACKNOWLEDGEMENTS

A special appreciation to my supervisor, Distinguished Professor Tebello Nyokong. You are a great inspiration to me, as a Woman in Science who continues to make an immense impact in the scientific research and innovation space in a progressive manner.
Thank you for all the knowledge imparted, encouragement and support through the course of my research journey.

I would also like to acknowledge the following:

Ms. Gail Cobus for all the administrative work and support.

Dr Jonathan Britton and Professor John Mack for your general assistance through the course of this research.

Professor Earl Prinsloo and the Biotechnology Innovation Centre, for your assistance with the cell culture work.

The National Research Foundation (NRF) for support and funding of this research project.

The International Conference on Porphyrins and Phthalocyanines-12 for the opportunity to communicate my research to a community of international research scientists.

And the Institute for Nanotechnology Innovation (lab S22) and Rhodes University.

Thank you.

Most importantly, I would like to extend a warm appreciation to my family: Nozipho, Nosisa, Mlondolozi, Erika and Kiara Nene, and Khabonina Mathibela; friends: Nqobile Mtshweni and Reitumetse Nkhahle.
For always being on my side every step of the way.

Thank you.

Table of content

ABSTRACT

This study focuses on the development of the sono-photodynamic combination therapy (SPDT) activity of phthalocyanines (Pcs) on the cervical and breast cancer cell lines *in vitro*. The SPDT technique utilizes ultrasound in combination with light to elicit cytotoxic effects for cancer eradication.

In this work, a selection of *tetra*-peripherally substituted Zn(II) cationic and zwitterionic Pcs were prepared. The photophysical parameters of the Pcs were determined including their fluorescence behaviours and efficiency of the triplet excited state population. The effects of the ultrasonic parameters (frequencies (MHz) and power ($W.cm^{-2}$)) on the stability of the Pcs were evaluated. Four parameters were evaluated: *Par I* (1 MHz: 1 $W.cm^{-2}$), *Par II* (1 MHz: 2 $W.cm^{-2}$), *Par III* (3 MHz: 1 $W.cm^{-2}$) and *Par IV* (3 MHz: 2 $W.cm^{-2}$). The stability of the Pcs reduced with the increase in the ultrasonic power (for *Par II* and *Par IV*). The *Par I* showed the least degradation compared to the other parameters and was therefore used for the SPDT treatments. The sonodynamic (SDT), photodynamic (PDT) therapy activities of the Pcs were studied and compared to their SPDT efficacies. The Pcs showed reactive oxygen species generation during the SDT, PDT and SPDT treatments. For the SDT and SPDT, singlet oxygen ($^1O_2$) and hydroxyl radicals (•OH) were detected. For PDT, only the $^1O_2$ were detected. The cell cytotoxicity studies for the Pcs showed relatively higher therapeutic efficacies for the SDT treatments compared to the PDT treatments, where the SPDT showed higher therapeutic efficacies compared to both the SDT and PDT monotreatments on both the cell lines *in vitro*. Overall, the combination treatments were better compared to the monotreatments.

The activities of the Pcs were compared by their differences in structures, including the type of R-group, type of quaternizing agent and type of nanoparticle conjugates.

List of Abbreviations

ADMA	Anthracene-9,10-diyl-*bis*-methylmalonate
BSA	Bovine serum albumin
CANSA	Cancer Association of South Africa
DBU	1,8-Diazabicyclo(5.4.0)undec-7-ene
DCC	*N*,*N*'-Dicyclohexylcarbodiimide
DLS	Dynamic light scattering
DMEM	Dulbecco medium
DMF	Dimethylformamide
DMPO	5,5-Dimethyl-1-pyrroline-*N*-oxide
DMSO	Dimethyl sulfoxide
DMSO-D_6	Deuterated dimethyl sulfoxide
DPBF	1,3-Diphenylisobenzofuran
DPBS	Dulbecco phosphate buffer saline
EDX	Energy dispersive X-ray
EPR	Electron paramagnetic resonance
FBS	Fetal bovine serum
FT-IR	Fourier transform infrared
GQDs	Graphene quantum dots
GSH	Glutathione
HeLa	Henrietta Lack cervical cancer cell line
HOMO	Highest occupied molecular orbital
LUMO	Lowest unoccupied molecular orbital
MALDI TOF	Matrix-assisted laser desorption/ionization-time of flight
MCF-7	Michigan Cancer Foundation-7 breast cancer cell lines

MNPs	Metallic nanoparticles
MPcs	Metallated phthalocyanines
MX	Metal salt
NGQDs	Nitrogen-doped graphene quantum dots
NHS	*N*-Hydroxysuccinimide
NIR	Near infrared
NMR	Nuclear magnetic resonance
NPs	Nanoparticles
NSGQDs	Nitrogen-sulfur co-doped graphene quantum dots
PBN	Phenyl-*N*-*tert*-butylnitrone
Pc/ s	Phthalocyanine/s
PDT	Photodynamic therapy
Ph_3P	Triphenylphosphine
PSA	Penicillin-streptomycin-amphotericin
QS	Quinine sulphate
R_n (α)	Non-peripheral substituent
ROS	Reactive oxygen species
R_p (β)	Peripheral substituent
S_0	Ground state
S_1	First singlet state
SDT	Sonodynamic therapy
SPDT	Sono-photodynamic combinatorial therapy
T_1	First Triplet state
TEM	Transmission electron microscopy
TEMP	2,2,6,6-*tetra*-methylpiperidone

US	Ultrasound
UV-vis	Ultraviolet-visible
WST-1	Cell proliferation reagent
XPS	X-ray photoelectron spectroscopy
ZnPc	Zinc phthalocyanine

List of Symbols

α	Alpha (non-peripheral)
β	Beta (peripheral)
Φ_F	Fluorescence quantum yield
Φ_T	Triplet quantum yield
Φ_Δ	Singlet oxygen quantum yield
τ_F	Fluorescence lifetime
τ_T	Triplet lifetime
$A(\lambda)$	Absorbance at irradiation area
I	Light intensity
N_A	Avogadro's constant
A	Absorbance at the excitation wavelengths
ΔA_T	Change on the triplet state absorption
ε_T	Molar extinction coefficient at the triplet excited state
F	Area under the fluorescence emission curve
n	Solvent refractive index (photophysical parameters)
n	Number of binding sites on protein (protein binding)
λ_{max}	Maximum absorption wavelength (Q-band)

Preface

This work explores the sono-photodynamic combinatorial activity of a selection of differently substituted phthalocyanines on breast and cervical cancer cell lines *in vitro*. The effects of several factors, including the structural compositions of the Pcs, the presence of nanoparticles, and the ultrasonic parameters on the activities of the phthalocyanines were studied, **Fig. 1.1**. These studies were conducted on a quest to determine factors that may maximise the harnessing of ultrasonic energy for the development of non-invasive and efficacious cancer treatment techniques.

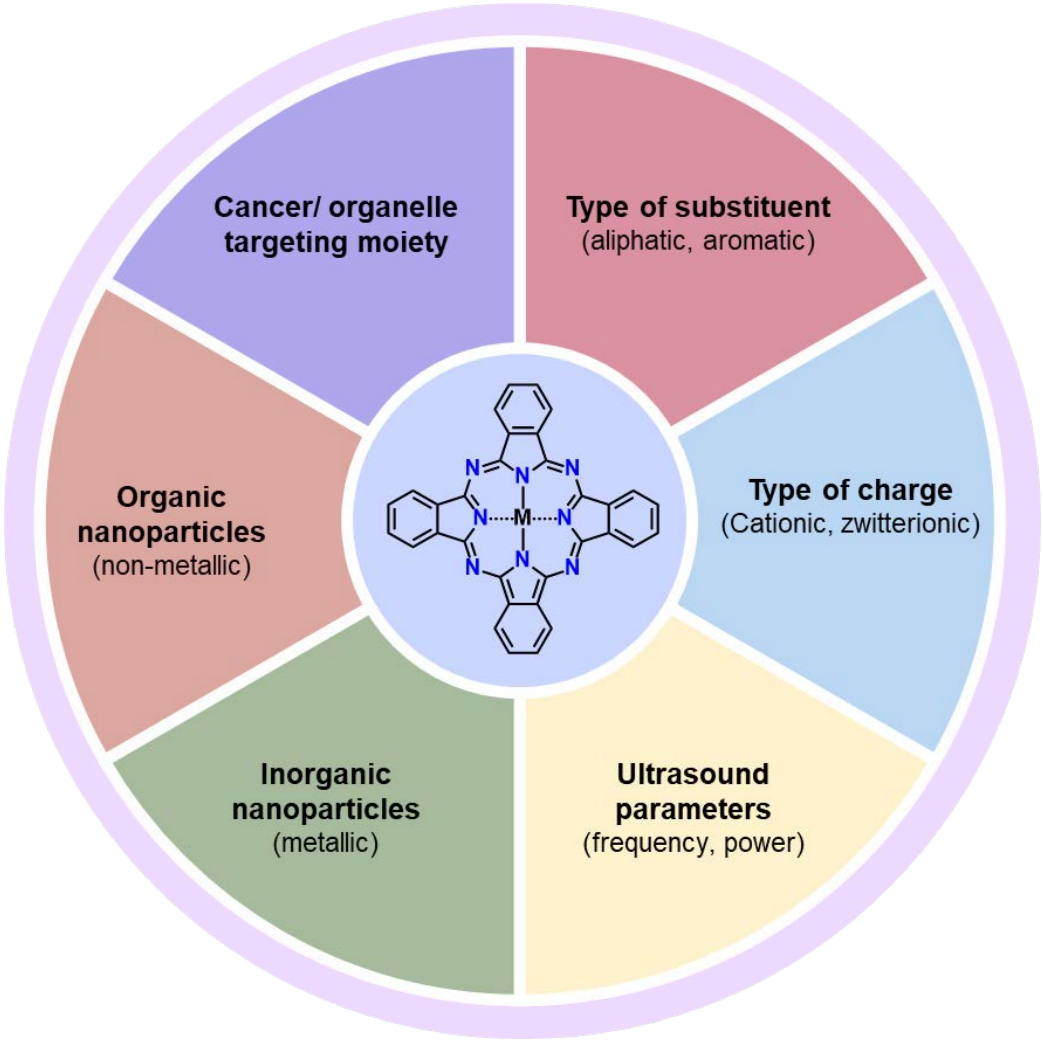

Figure 1.1. Factors affecting the activity of phthalocyanines as sensitizers in the sonodynamic and photodynamic therapy for eradication of cancer *in vitro*.

CHAPTER ONE

1. Introduction

1.1. Problem statement.

Breast and cervical cancer are two of the most prevalent cancer types affecting women in South Africa, as reported by the Cancer Association of South Africa (CANSA), 2021 [**1**]. Both breast and cervical cancers can metastasize through the body, affecting deep seated organs and tissue [**2**,**3**]. These cancer types have been identified as a national priority due to the increasing occurrence of incidences, nationally and even globally. The search for more efficacious cancer treatment techniques continues as most of the known conventional treatments have limitations including invasiveness, toxic side-effects, and the development of resistance, to mention a few. These include surgery, radiation and the most common, chemotherapy [**4**-**6**].

Photodynamic therapy (PDT) is a minimally invasive and controllable technique developed as an alternative to conventional techniques. PDT involves the use of a non-toxic sensitizer which may be activated by light to elicit cytotoxic effects [**7**]. Although PDT has shown impressive results for cancer treatment, the light used in the activation of the sensitizers has limited penetrability and may traverse tissue up to 10 mm past the epidermis [**8**,**9**]. Therefore, PDT is only effectively used for the eradication of superficial cancers and not deep-seated soft tissue cancers. Efforts including the use of multimode-fibers for direct light delivery to tissue have been reported [**10**]. This technique is, however, invasive, as the fibres physically pierce through tissue. Ultrasound (US) mediated therapy, known as sonodynamic therapy (SDT), is currently studied as an alternative to PDT. SDT involves the synergistic activity of and the sensitizer to elicit anticancer effects [**11**,**12**]. This technique addresses the limitation of light penetrability in PDT since US can penetrate deeper into tissue and may reach deep-tissue seated tumours [**13**]. Several sensitizers have been studied and reported for SDT including porphyrins, chlorins and phthalocyanines, [**14**-**31**] **Table 1.1**.

Table 1.1. A summary of a selection of sensitizers reported for sonodynamic therapy.

Porphyrins	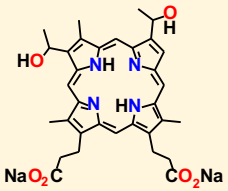 Photofrin II [**14**]	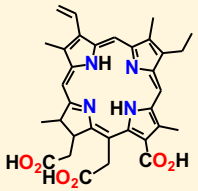 Chlorin e6 [**15**]	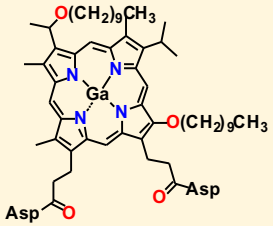 ATX-70 [**16**]	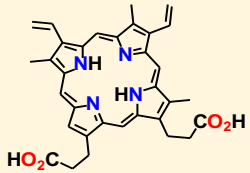 Protoporphyrin IX [**17**]	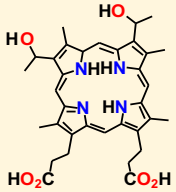 Hematoporphyrin [**17**]
Phthalocyanines	 ZnPc [**18**]	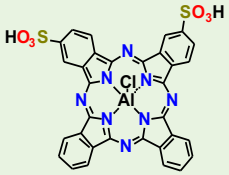 AlCl-*di*-sulfonate [**19**]	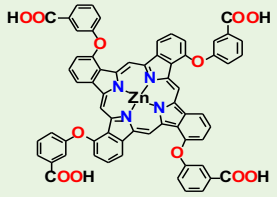 *Tetra*-3-carboxyphenoxy [**20**]	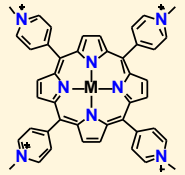 **M**= Fe, Zn, Pd Pyridyl-porphyrin [**21**]	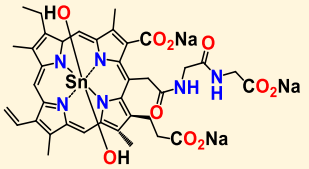 Sonoflora 1 [**22**]
Corroles	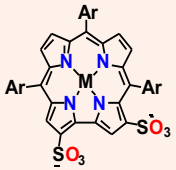 **M**= Fe, Mn, Al, Ga Corrole [**23**]	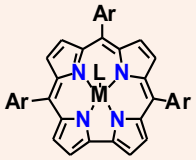 **M**= Fe, Mn, Al, Ga Corrole [**23**]	 AlCl-*tetra*-sulfonate [**24**]	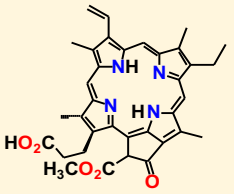 Pheophorbide [**25**]	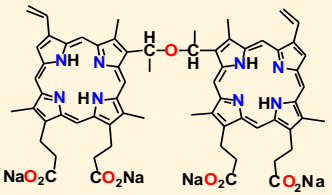 Sinoporphyrin [**26**]
Other	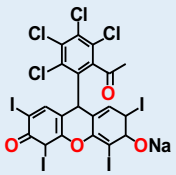 Rose Bengal [**27**]	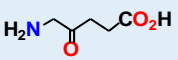 Aminolevulinic acid [**28**]	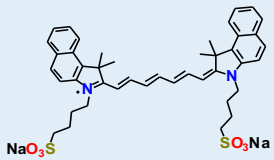 Indocyanine green [**29**]	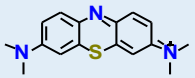 Methylene blue [**30**]	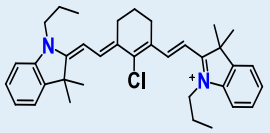 IR-780 dye [**31**]

This work focuses on the study of cationic Zn(II) phthalocyanines as potential sensitizers for SDT and SDT-supplemented PDT, for the development of an efficacious treatment technique for the eradication of deep-tissue cancers.

1.2. Phthalocyanines

1.2.1. General structures and synthesis.

Phthalocyanines (Pcs) are macrocyclic compounds that appear blue or green and sometimes brown in colour. The general structures of Pcs are shown in **Fig. 1.2**.

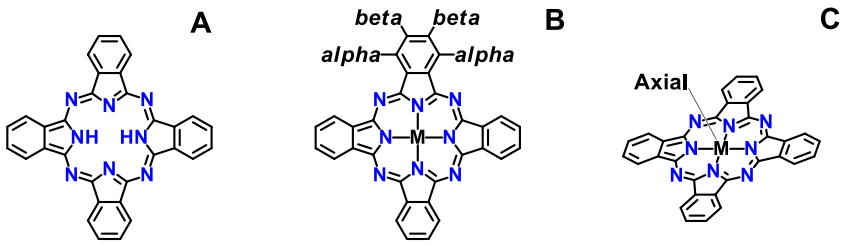

Figure 1.2. General structure of A) metal-free (H_2Pc), B) metallated (MPcs) Pc showing the non-peripheral (*alpha*) and peripheral (*beta*) positions, and C) metallated Pc with axial substituent linked to the central metal. M: metal.

The precursors used in the synthesis of Pcs are shown in **Scheme 1.1**.

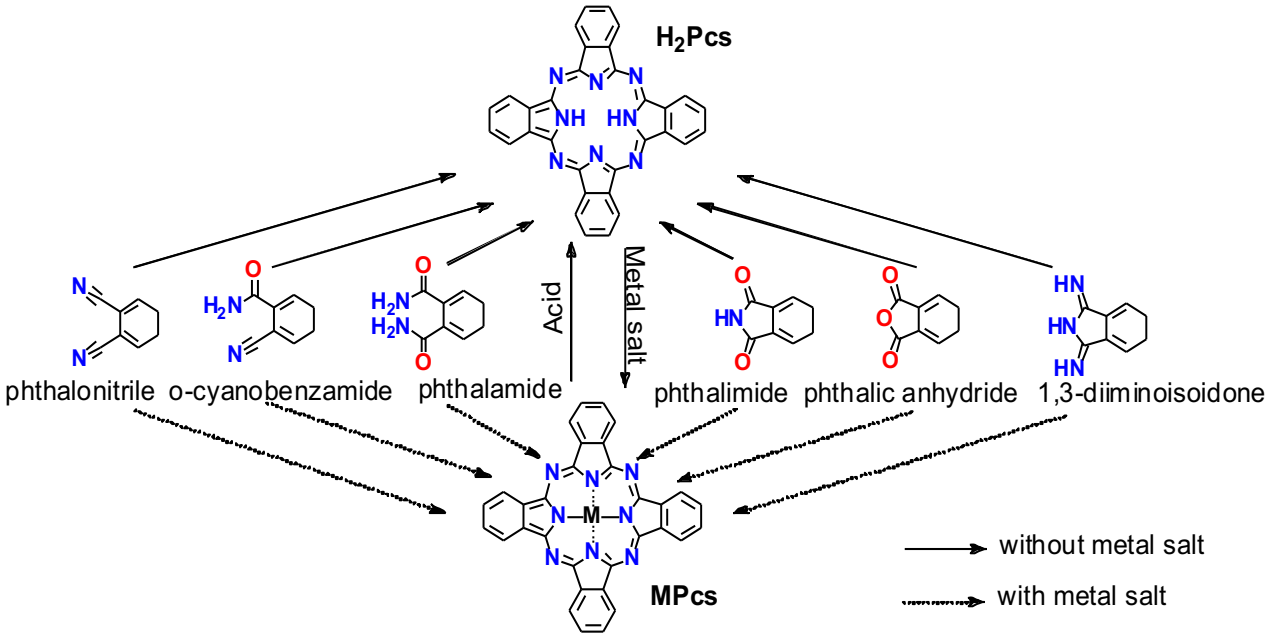

Scheme 1.1. Summary of the phthalocyanine-precursors and the synthetic routes for the preparation of metal-free (H_2Pc) and metallated (MPcs) phthalocyanines.

The Pcs are tetrapyrrolic macrocycles with a central cavity to which a metal atom may be chelated. The Pcs with no central metal are referred to as H_2Pcs, owing to the non-chelating -NH groups at the centre of the core, **Fig. 1.2 A**. The central metals or metalloids for Pcs may include alkali, alkali earth, transition, post-transition groups and sometimes lanthanides. The structures of Pcs may also be expanded by means of attaching R-groups. The R-groups on the Pcs may be attached at the non-peripheral (*alpha*, *α*) positions and/ or the peripheral (*beta*, *β*) positions, **Fig. 1.2 B**. Further modification may be done by adding an axial ligand which is linked to the central metal directly, **Fig. 1.2 C**, when using metals with oxidation states ≥3 such as Al(III), In(III), Sn(IV), *etc*. Various reaction processes may be applied for the preparation of Pcs with varying structural compositions. The Pcs are synthesized through the cyclization of any of the precursors shown in **Scheme 1.1**.

For H_2Pcs, the precursors may be reacted alone to form the macrocycle with a central cavity. An alternative method may include the reaction of the precursors in the presence of a metal salt (MX) to facilitate the cyclization of the precursors to form metallated Pcs (MPcs) [**32**]. The removal of the metal centre would be achieved by using an acid to yield the H_2Pcs [**33**]. For the preparation of MPcs, H_2Pcs may be metallated using a MX to form a MPcs. In this work, the phthalonitrile precursors were used for the preparation of the Pcs. For Pcs with R-group extensions, the Pcs' precursors which are already bearing the desired R-groups are commonly used. For example, *n*-nitro-phthalonitriles, which are commercially available, may be modified by substituting the nitro- group using an electron withdrawing group such as alcohols (R-OH) or thiol (R-SH) in the presence of a base catalyst such as potassium carbonate or sodium carbonate to introduce an R-group extension.

The routes for preparation of substituted Pcs are shown in **Scheme 1.2**.

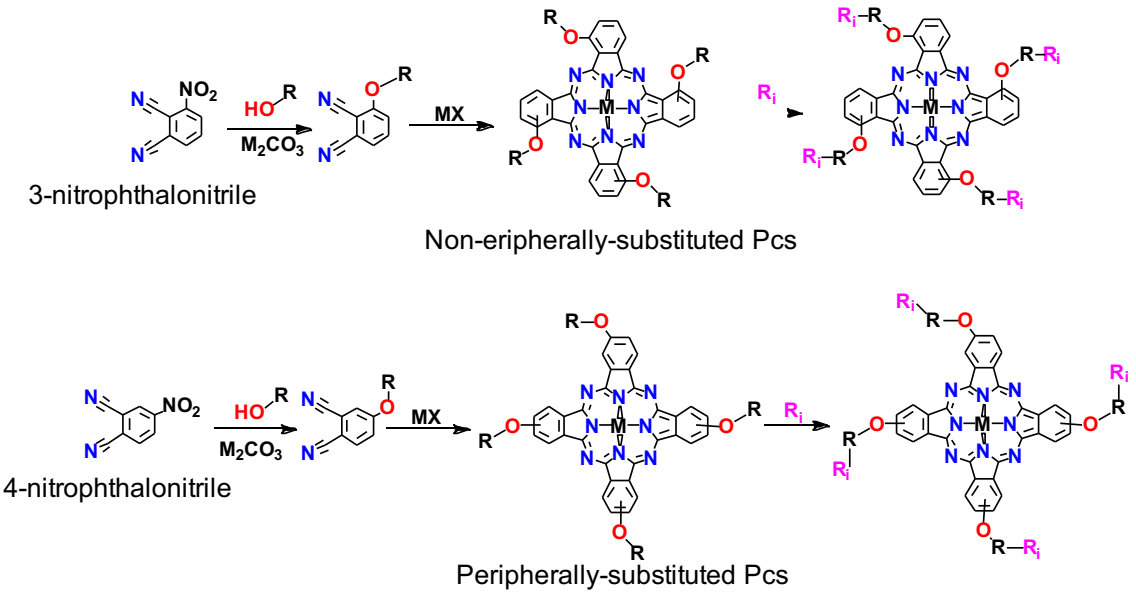

Scheme 1.2. Preparation of substituted phthalocyanines with R-groups.

The additions of R-groups on Pcs are not only limited to introducing extensions on the precursor prior cyclization. The Pcs' R-groups can still be modified with additional groups (R_i) even after the precursors have cyclized to form Pcs, **Scheme 1.2**. This makes Pcs attractive in organic chemistry and drug development as they allow for facile structural modifications. Different Pc structures influence their spectroscopic properties. Thus, Pcs may be modified and tailored for use in different applications. Pcs are versatile compounds reported in a wide range of applications such as, in textiles; catalysis; as antimicrobial agents; and as therapeutics to mention a few [**34**,**35**].

1.2.2. Electronic absorption spectral properties.

The Pcs' tetrapyrrolic-core has an 18 π-electron system [**36**]. This affords Pcs impressive optical properties. The ultraviolet-visible (UV-vis) absorption profiles of Pcs are generally characterized by a strong distinctive absorption peak in the near-infrared

region (NIR) denoted as the Q-band and a second blue shifted absorption peak denoted as the B-band [**37**], **Fig 1.3 A**. This observation is explained by the Gauterman's four-orbital model using the highest occupied molecular orbital (HOMO) and Lowest unoccupied molecular orbital (LUMO) transitions, [**37**,**38**], **Fig. 1.3 B**.

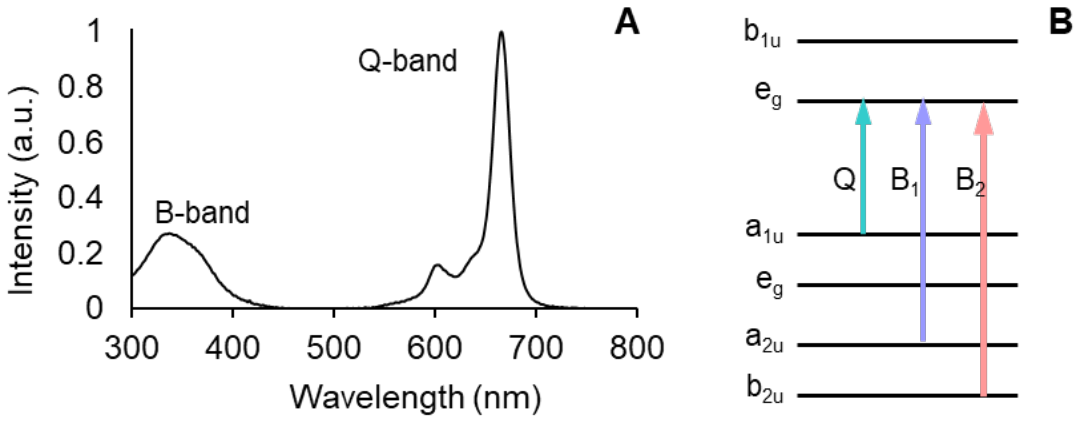

Figure 1.3. A) A typical ground state UV-vis absorption of MPCs and B) the electronic transitions showing the origins of the Q- and B-Bands.

The Q-band appears as a result of the transition occurring between the ground state a_{1u} of the of the HOMO to the e_g of the LUMO, **Fig. 1.3 B**. The B-band appears relatively broader than the Q-band. The B-band broadness is due to the superimposition of two bands, the B_1 band (a_{2u} of the HOMO and e_g LUMO transition) and the B_2 band (b_{2u} of the HOMO and e_g LUMO transition) [**38**].

1.3. Phthalocyanines in cancer therapy development.

The interest in Pcs as sensitizers for PDT is due to their impressive therapeutic efficacies upon exposure to light and their low toxicity in the absence of light [**39**] among other reasons. Pcs are recognized as the second and promising generation of sensitizers for PDT [**40**].

1.3.1. Phthalocyanines in photodynamic therapy.

There are various factors to be considered when preparing Pcs for PDT. The Pcs should be able to efficiently absorb light upon irradiation and generate the cytotoxic reactive oxygen species (ROS). Ideally, Pcs should absorb light of wavelength in the NIR within the phototherapeutic window (between 650 nm to 850 nm) [**41**]. For biological applications such as cancer treatment, this is important since the competition for the photon-energy will be minimized as most absorbing biological matter and tissue are generally transparent at this range [**42**,**43**]. Furthermore, the Pcs should maintain stability under physiological conditions and under light irradiations to maintain high efficacies. Solubility also plays an important role in the general therapeutic efficacies of Pcs as it influences biodistribution and delivery of the therapeutics within a biological system [**44**,**45**]. Thus, soluble Pcs are ideal as sensitizers for PDT. The Pcs tend to form aggregates due to the lipophilic, planar, and conjugated core. The formation of aggregates has been reported to reduce the Pcs therapeutic performance during PDT by quenching photoactivities [**46**].

The mechanism of action for Pcs in PDT has been well defined in the literature using the well-known Jablonski diagram, **Fig. 1.4**.

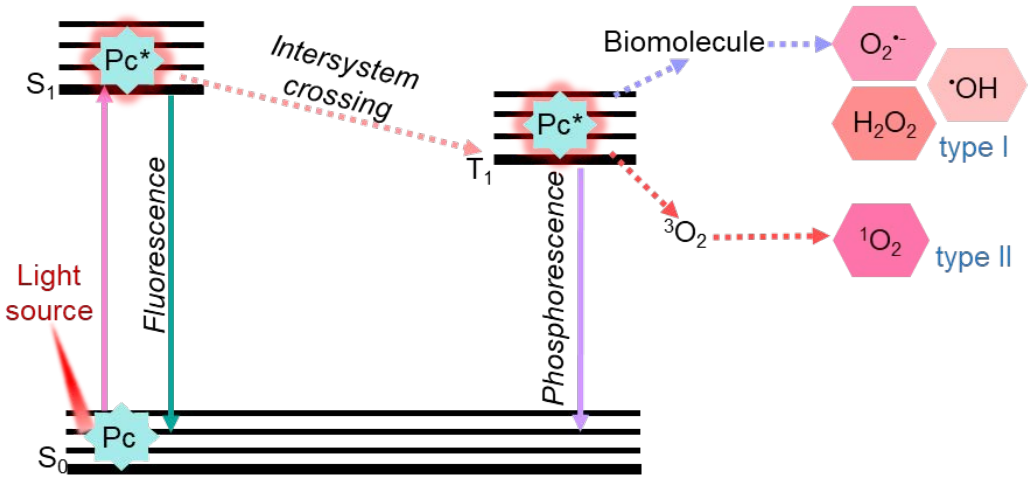

Figure 1.4. The Jablonski diagram showing photoactivation of phthalocyanines and energy pathways to yield reactive oxygen species.

The Jablonski diagram summarizes the energy pathways involved from the light-mediated activation of sensitisers to the generation of the ROS [**47**,**48**]. Briefly, the Pc sensitizer in the ground state (S_0) absorb photons from light to occupy higher energy singlet excited state (S_1) and become activated (Pc*), **Fig. 1.4**. The Pc* may thereafter relax back to S_0 by emitting light through fluorescence [**49**,**50**]. Alternatively, the Pc* may undergo intersystem crossing to occupy the triplet state (T_1). The Pc* in the T_1 may generate ROS through the type I or type II routes [**51**,**52**], **Fig. 1.4**. The type I involves the interaction of the activated sensitizer with biomolecules through electron transfer to form ROS such as the superoxide- ($O_2^{\bullet-}$) and hydroxyl radicals (•OH), and hydrogen peroxide (H_2O_2). For the type II route, the sensitizers form $^1O_2$ through energy transfer from the Pc* to nearby molecular oxygen ($^3O_2$) in the T_1. These processes promote cellular oxidative stress which leads to cell death [**53**].

For Pcs, the formation of ROS during PDT is reported to be predominantly *via* the type II route. A series of cytotoxic biochemical processes such as lipid peroxidation, protein, and DNA oxidation *etc.* which ultimately lead to cytocidal effects are induced during treatment [**53**,**54**]. Although PDT involves various other cytotoxic biochemical processes in addition to oxidative stress, the ROS efficiency of Pcs is important in predicting its efficiency and potential as a sensitizer for PDT.

1.3.2. Phthalocyanines in sonodynamic therapy.

The Pcs have recently been rapidly gaining interest as potential sensitizers in SDT and SDT-supplemented PDT, known as sono-photodynamic combinatorial therapy (SPDT) [**19**,**55**,**56**]. Fewer Pcs have been studied and reported for SDT and SPDT compared to PDT, [**18**-**20**, **24**, **30**, **57**-**64**], **Table 1.2**. The Pcs have shown activity against various cancer cell types in SDT and SPDT, **Table 1.2**.

Table 1.2. A summary of phthalocyanines reported for sonodynamic- and sono-photodynamic combination therapy for cancer.

	Pcs	US parameters	Cancer cell lines	Model	Ref
Sonodynamic therapy	AlS_2Pcs	3.0 MHz; 3.0 $W.cm^{-2}$	Colon tumour carcinoma (CT26) cells	*In vitro, in vivo*	[**19**]
	Zn-α-3-COOH- Pcs	1.0 MHz; 2.0 $W.cm^{-2}$	Hepatocellular carcinoma (HepG2) cells	*In vivo*	[**20**]
	AlS_4Pcs	1,92 MHz; 3.0 $W.cm^{-2}$	Colon tumour carcinoma (CT26) cells	*In vivo*	[**24**]
	AlS_4Pcs	1.93 MHz; 6.0 $W.cm^{-2}$	Human leukocyte (HL60) cells	*In vitro*	[**57**]
	ZnPcs	20 kHz, 10 $W.cm^{-2}$	Murine melanoma (B16F10) cells	*In vitro*	[**58**]
	FePcs	30 kHz	HUVECs and breast carcinoma (4T1) cells	*In vitro, in vivo*	[**59**]
	H_2, M (cinnamyloxy)4 Pc	1 MHz,0.5 $mW.cm^{-2}$	Gastric (MKN-28) cells	*In vitro*	[**60**]
Sono-photodynamic therapy	ZnPcs	1.1 MHz; 1.0 $W.cm^{-2}$	Colon tumour carcinoma (CT26) cells	*In vivo*	[**18**]
	AlS_4Pcs	-	Prostate (PC3, LNCaP) cells	*In vitro*	[**30**]
	AlS_2Pcs	1.0 MHz; 2.0 $W.cm^{-2}$	Human Melanoma (G361) cells	*In vitro*	[**55**]
	AlS_2Pcs	1.0 MHz; 2.0 $W.cm^{-2}$	Mouse melanoma (B16FO) and fibroblast (NIH3T3) cells	*In vivo*	[**61**]
	AlS_2Pcs	1.0 MHz; 2.0 $W.cm^{-2}$	Human breast adenocarcinoma (MCF-7) cells	*In vitro*	[**62**]
	SiPcs	0.5 W	Prostate (PC3) cells	*In vitro*	[**63**]
	Pc-Artesunate	1 MHz,1.5 $W.cm^{-2}$	Hepatocellular carcinoma (HepG2) cells	*In vivo*	[**64**]

US: ultrasound, AlS_4: aluminium(III) chloride *tetra*-sulfonate; AlS_2Pc: aluminium(III) chloride *di*-sulfonate; Zn-α-3-COOH-phenoxy: zinc (II) *tetra*-α-(3-carboxyphenoxy). M (cinnamyloxy) Pc: (M = indium (III) and gallium (III)).

The Pcs reported for SDT and SPDT as shown in **Table 1.2**, are generally neutral or anionic. Atmaca, *et al.* reported on the SiPcs bearing cationic axial groups [**63**] for SPDT. Cationic Pcs are of interests due to their affinity to the anionic cellular membrane of cancer cells [**65**]. Thus, this work expands on cationic Pcs as sensitizers for SDT and SPDT. Furthermore, structural modifications have been reported to a lesser extent for Pcs in SDT including conjugation to nanoparticles. Only liposomes have so far been reported in combination with Pcs for SPDT [**18**]. Nanoparticles have been widely used in combination with Pcs for PDT therapeutics due to their ability to target cancer sites [**66**]. The guide on the Pcs' structural requirements for PDT is relatively clearer compared to SDT as it is not yet known what functional groups would constitute sono-active Pcs. It is therefore important to explore further the factors that may affect the Pcs' applicability for SDT and SPDT. It is, however, necessary that the Pcs should be able to absorb energy from the US to induce cytotoxicity.

1.3.2.1. Mechanism of action in Sonodynamic therapy.

The mechanism of action of Pcs in SDT is not yet well understood and has been defined so far using a phenomenon known as acoustic cavitation [**67, 68**], **Fig. 1.5**.

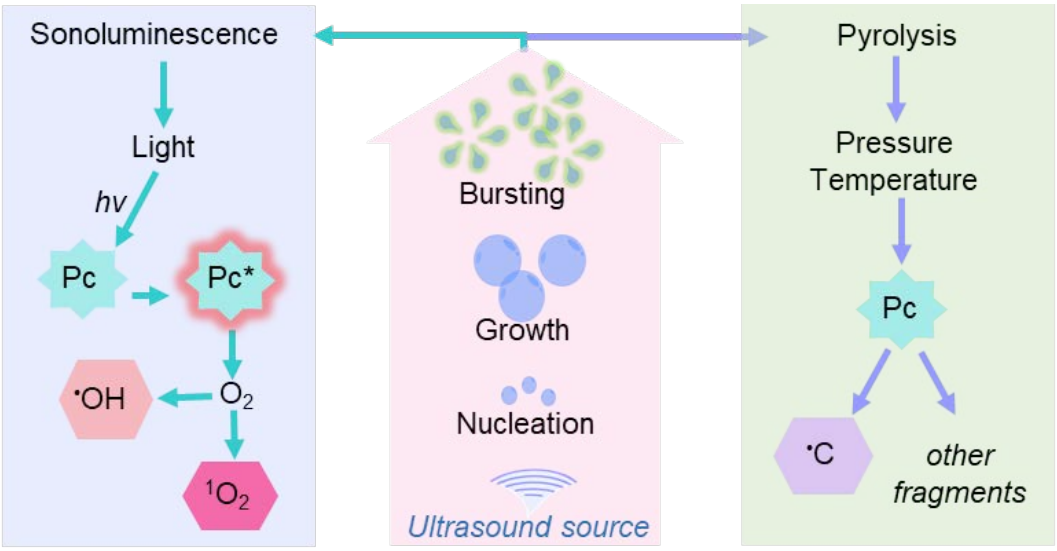

Figure 1.5. Acoustic cavitation in sonodynamic therapy.

The phenomenon of acoustic cavitation involves the nucleation, growth, and implosion of gas-filled bubbles when the ultrasonic mechanical waves are exerted in an aqueous medium [**69**,**70**]. Two main processes may occur during acoustic cavitation, namely: sonoluminescence and pyrolysis, **Fig. 1.5**.

Sonoluminescence is the light emitted from the imploding bubbles [**68**,**71**], **Fig. 1.5**. Several studies have been conducted to characterize the sonoluminescence. In a study looking at the SDT-activity of porphyrins, Giuntini *et al*. measured the emission profile of the sonoluminescence which showed a broad emission within the wavelength ranges between ~300 nm - 700 nm. The maximum emission intensity for this light was observed at 500 nm recorded in an aqueous medium using US-irradiation settings of 1.86 MHz and 1.5 W cm^{-2} [**21**]. In another study, sonoluminescence signals were observed at wavelengths 350 nm - 450 nm, 450 nm - 550 nm and 550 nm - 650 nm in gel phantoms, used as tissue simulators, where the US-irradiation settings were 1.1 MHz and 2 W cm^{-2} [**72**]. Hence, it is believed that the mechanism of sensitizer activation through sonoluminescence is like the light-mediated activation in PDT as described previously.

For pyrolysis, the bursting bubbles may also release high pressures (>81 MPa) and energy of (~10000 K) causing high raise in temperature of the surrounding environment [**73**,**74**]. This localised increase in temperature causes the sensitizer in that vicinity to fracture, forming free sensitizer-derived radicals such as carbon radicals (•C) in the case of organic sensitizers, including Pcs; or may lead to the formation of non-radical sensitizer fragments [**75**], **Fig. 1.5**. The •C may thereafter interact directly with endogenous substrate or the O_2, forming cytotoxic ROS such as peroxyls or alkoxyls derived from the sensitizer monomers [**75**,**76**]. There has been no study that confirms the lysing of Pcs induced by sono-irradiation reported yet.

1.3.2.2. The role of ultrasonic frequency and power.

The rate and efficiency of bubble-formation during acoustic cavitation play a vital role in the efficacy of SDT as they affect the amount of available energy for Pcs activation and ROS yields. Various factors may be considered to manipulate the efficiency of acoustic cavitation. These may include varying the US frequency (MHz) and power ($W.cm^{-2}$). An increase in the ultrasonic frequency results in an increase in the rate of bubble formation per unit time [**77**,**78**]. An increase in the ultrasonic power may enhance the sizes of bubbles formed [**77**,**78**]. Increasing both the frequency and power may result in the formation of larger bubbles rapidly and therefore yielding more energy for ROS generation through acoustic cavitation.

For Pcs, the specific combinations of US frequency and power may be optimized to improve ROS yields and the general therapeutic efficacy of SDT. For SDT in cancer therapy, US of frequencies between 1 MHz – 3 MHz and power between 1 $W.cm^{-2}$ – 6 $W.cm^{-2}$ have been reported **Table 1.2**. Lower US frequencies at kHz ranges have also been reported for SDT using Pcs [**59**,**60**]. These parameters have demonstrated non-destructive effects on cells in the absence of a sensitizer molecule [**79**]. Furthermore, low US frequency has an inverse relationship to wave attenuation and therefore its penetrability into tissue is higher compared to light in PDT [**73**]. Therefore, combining this therapeutic ability of Pcs in SDT with their ability to absorb light of wavelengths in the NIR makes Pcs potentially good candidates for SPDT for treatment of less accessible deep-tissue tumours.

1.3.3. Design of phthalocyanines for photo- and sonodynamic therapy.

While designing sono-active Pcs for SDT, it is important to consider the requirements for efficient sensitizer in PDT, since SPDT is a combination of both PDT and SDT

monotherapies. Various methods may be used to improve the Pcs' photo- and possibly sono-chemical properties and their specificity to cancer. Careful consideration of the functional groups constituting the Pcs is important in designing efficacious compounds for therapy.

1.3.3.1. Effect of central metal.

It is reported that metallated Pcs perform better compared to their non-metallated counterparts in PDT [**80**]. The central metals are known to enhance the T_1 population of the Pc* and consequently, the $^1O_2$ yields. This effect is known as the heavy-atom effect and is reported to increase with an increase in central metal size [**81**]. Additionally, the use of heavy metal Pcs is desirable for PDT since it improves the red-shifting of the Pcs' Q-bands. For SDT, metals including Al, Zn, Fe, Ga, In and Si have been studied [**19,20,59,60,63**]. Güzel *et al*. reported on H_2, Ga and In tetra-cinnamyloxy-substituted Pcs, where the sono-photophysical properties of the Pcs increased with the increase in the central metal molecular weight [**60**]. In another study, the metallated Pcs have shown improved activity compared to the H_2Pc counterparts in SDT [**82**]. Therefore, central metals may have played an important role in the overall SDT-activity of the sensitizers. Although this may be the case, it is still not yet clear what the role of the type and size of the central metal is in the SDT-activity of Pcs. Additionally, corrole-based sensitizers have demonstrated improved sono-activity upon metallation [**23**]. Thus, metalated Pcs may be ideal when designing sensitizers for PDT, SDT and SPDT.

1.3.3.2. Effect of R-groups.

Other methods of improving the therapeutic performance of Pcs may include varying the R-group type and position on the Pcs structures. The planar and generally lipophilic Pcs' core with a rich conjugated system as mentioned earlier, causes the Pcs to stack on top of each other leading to aggregation in aqueous media [**83**]. The aggregation of Pcs in solution have been reported to enhance the rate of non-radiative relaxation, known as internal conversion, which results in the reduction of the T_1 population upon irradiation [**84**]. This effect causes the ROS yield of aggregated Pcs to be reduced. The use of bulky R-groups to reduce aggregation is one of the common methods for addressing the issue of aggregation [**85**].

The position of the R-groups (the α and β positions) have been demonstrated to affect the solubility and overall photo-activity of Pcs [**86**]. Although both the α- and β-substituted Pcs have been studied in SDT, **Table 1.2**, the effect of R-group position has not yet been defined for this type of treatment. Axially substituted Pcs are also known to have reduced aggregation, and have also been reported for SPDT [**63**]. Other methods of improving the solubility of Pcs in aqueous media include the introduction of ionic groups such as the $-COO^-$, $-SO_3^-$ anions on the R-groups. The R-groups bearing 1°, 2°, or 3° amines can be quaternized to yield water-soluble cationic Pcs [**87**]. Ionic Pcs improve the solubility in aqueous media.

1.3.3.3. Improving specificity to cancer and organelle targeting.

The R-groups of Pcs may be designed or modified to target cancer cells from healthy somatic cells. Cancer cells are different from healthy cells in that they have an overall anionic membrane potential due to the expression of anionic membrane lipids and glycoproteins, and the high concentrations of intracellular lactic acids [**88-90**]. The

cationic Pcs may therefore target and accumulate at the tumour sites through electrostatic interactions. It has been reported that cationic Pcs demonstrate improved performance in PDT compared to their neutral counterparts [**91**]. Other methods for targeting include the labelling of the Pcs using bioligands such as folic acids, glucose, biotin to mention a few [**92**-**94**].

Some of the commonly used methods for cellular uptake in cancer therapy are summarized in **Fig 1.6**.

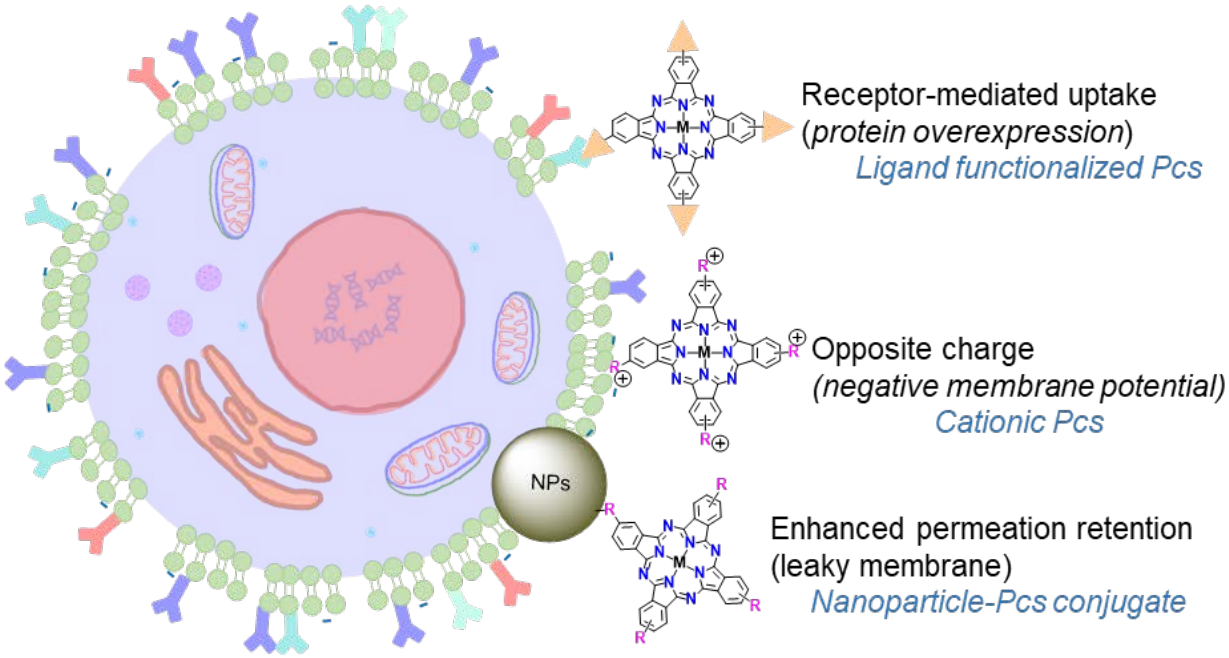

Figure 1.6. Summary of the cancer cell targeting methods for phthalocyanines.

Cancer cells, unlike healthy cells, tend to overexpress membrane receptor proteins for the ligands discussed above, therefore, Pcs labelled in this way may be easily facilitated into the cells through receptor mediated transport [**95**,**96**]. The cationic therapeutics have also been reported to enhance intracellular targeting [**96**], where the therapeutics accumulate at the anionic mitochondria membrane and therefore

internalising within the organelle [**97**,**98**]. Organelle-targeting allows for more precise therapy and has been shown to improve the therapeutic efficacy of anticancer drugs [**99**]. The mitochondria are known as the powerhouse-organelles of the cell and may account for over 80% of the total cellular O_2. For techniques such as SPDT, which depend on the availability of O_2 for therapy, mitochondrial-targeting for sensitizers may be beneficial. Furthermore, the distraction of these organelles may implicate a series of crucial biochemical processes which may lead to cell distraction. In this work, the triphenylphosphine (TPP) moiety was employed to modify Pcs for mitochondria targeting. The TPP-labelled Pcs are reported for the first time for SDT and SPDT in this work. Additionally, the membranes of cancerous cells are known to be leaky and will generally allow the permeation of larger molecules compared to the more stringent membrane of healthy cells. The use of nanoparticles (NPs) of diameter between 1 nm – 100 nm for drug delivery in cancer therapy utilizes this method of passive delivery. This phenomenon is known as enhanced permeation retention [**100**,**101**]. Pcs have been conjugated to various NPs types including organic and inorganic NPs for improving delivery to cancers for therapy, including PDT [**66**,**102**,**103**]. For SDT, Pcs conjugated to NPs have been reported to a lesser extent [**18**,**59**,**64**].

1.4. A summary of the phthalocyanines used in this work.

In this work, a series of ionic Pcs were prepared and studied for PDT, SDT and SPDT activity against breast and cervical cancer cell lines *in vitro*. The effects of the structural variations on the Pcs were studied for the first time for SDT and SPDT in this work. A summary of all the ionic Pc studied in this work is given in **Table 1.3**.

The Pc **1** – Pc **5** are reported in the literature [**104** – **108**], and the Pc **6** – Pc **11** are new.

All the Pcs bear 4° amine groups on their substituents in the peripheral positions. The following structural variations were studied and compared for the Pcs:

- Methylated N-group on meta *vs* para position on pyridine R-group: Pc **2** versus Pc **3**.
- Methylated N-group in aliphatic and aromatic: Pc **1**, Pc **4**, Pc **5** versus Pcv **2**, Pc **3**, Pc **8**.
- R-group extension on morpholine Pcs: Pc **4**, Pc **5** versus Pc **6**, Pc **7**, respectively.
- Methyl- and ethyl- quaternizing agent: Pc **8** versus Pc **9**.
- Methyl- and propanesultone- (cationic vs zwitterionic): Pc **4**, Pc **5** versus Pc **6**, Pc **7**, respectively.
- Methyl- and TPP (number of cations): Pc **3**, Pc **4** versus Pc **10**, Pc **11**, respectively.

The Pc **8** and Pc **9** were also conjugated to NPs and would be compared to the non-conjugates Pcs.

Table 1.3. Summary of the phthalocyanines used in this work.

Structure and name	No.	Ref	NPs conjugated
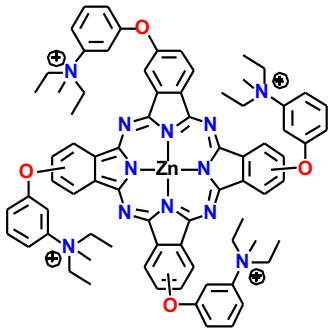 2,9,16,23-*tetrakis*-(*N*-methyl-diethylamino) Zn(II) Pc	**1**	[**104**]	None
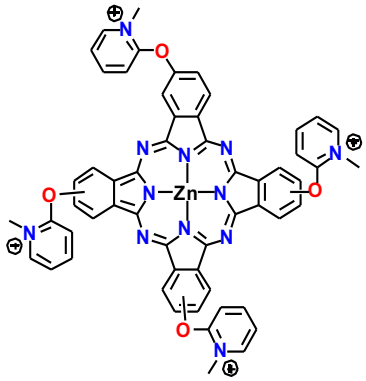 2,9,16,23-*tetrakis*-(4-methyl-2-pyridyloxy) Zn(II) Pc	**2**	[**105**]	None
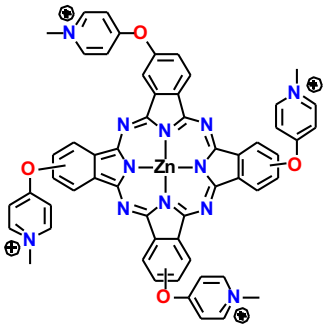 2,9,16,23-*tetrakis*-(*N*-methylpyridyloxy-) Zn(II) Pc	**3**	[**106**]	None
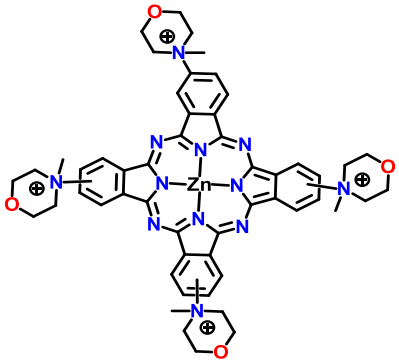 2,9,16,23-*tetrakis*-(*N*-methylmorpholino) Zn(II) Pc	**4**	[**107**]	None

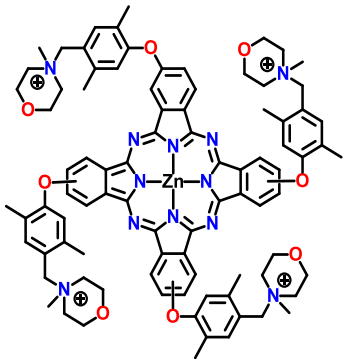 2,9,16,23-*tetrakis*-(2,5-dimethyl-4-(*N*-methylmorpholine)-phenoxy) Zn(II) Pc	**5**	[**108**]	None
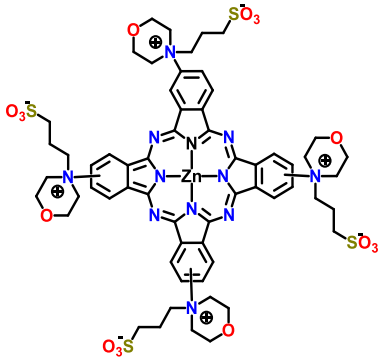 2,9,16,23-*tetrakis*-(*N*-propanesultone-morpholino) Zn(II) Pc	**6**	New	None
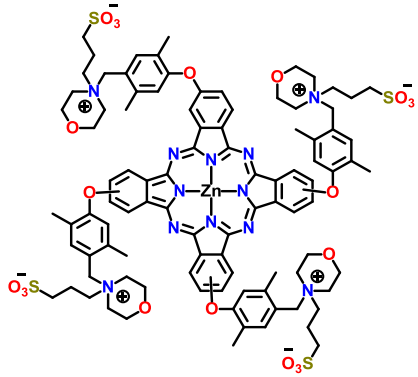 2,9,16,23-*tetrakis*-(2,5-dimethyl-4-(*N*-propanesultone-morpholino)) -phenoxy Zn(II) Pc	**7**	New	None
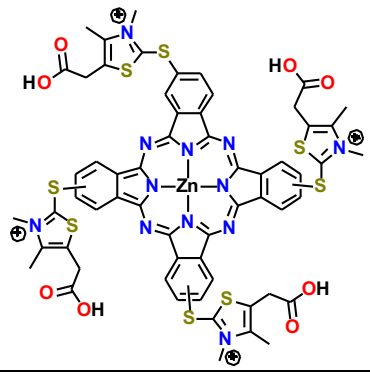	**8**	New	NGQDs, NSQDs AuGSH, AgGSH

2,9,16,23-*tetrakis*-(methyl-2-mercapto-4-methyl-5-thiazoleaceticacid) Zn(II) Pc			
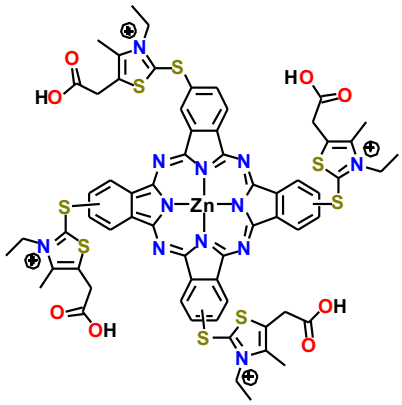 2,9,16,23-*tetrakis*-(ethyl-2-mercapto-4-methyl-5-thiazoleaceticacid) Zn(II) Pc	**9**	New	NGQDs, NSQDs AuGSH, AgGSH
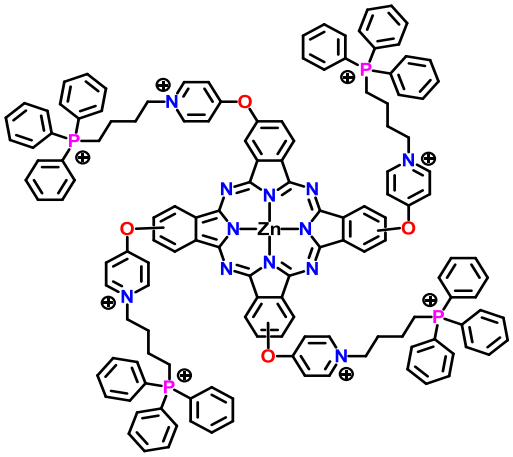 2,9,16,23-*tetrakis*(*N*-(*N*-butyl-4-triphenyl-phosphonium)- pyridine-4-yloxy) Zn(II) Pc	**10**	New	None
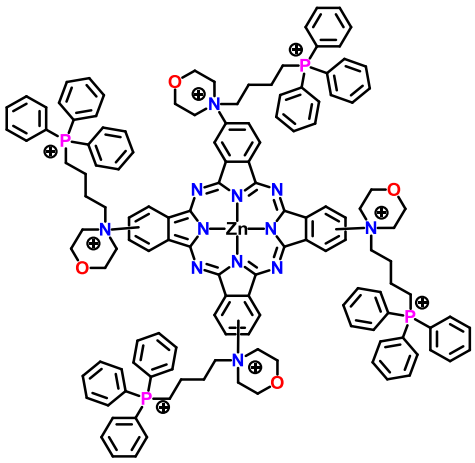 2,9,16,23-*tetrakis*-(*N*-(*N*-butyl-4-triphenyl-phosphonium)-morpholino) Zn(II) Pc	**11**	New	None

1.5. Nanoparticles in photo- and sonodynamic therapy.

There is a plethora of NPs reported for the development of cancer therapeutics. The NPs differ by sizes, shapes, and overall chemical compositions. The NPs used can be grouped into two major groups, *viz.* organic NPs including liposomes and the graphitic fullerenes, nanotubes and sheets; and the inorganic NPs including metallic NPs. Some of the NPs reported for PDT and SDT are shown in **Fig. 1.7**.

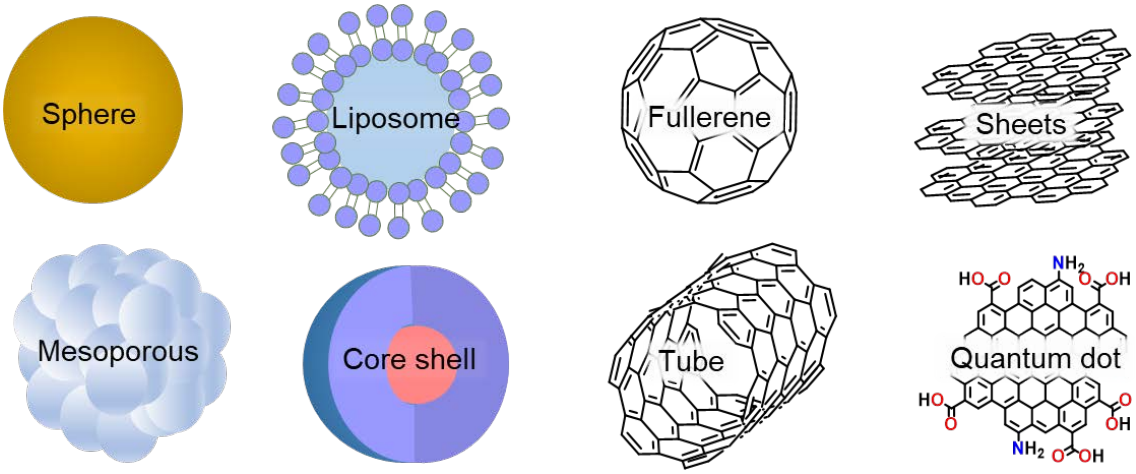

Figure 1.7. Structures of some of the nanoparticles reported in photo- and sonodynamic therapy.

For PDT, the use of NPs has been reported extensively where both organic and inorganic NPs, as shown in the **Fig. 1.7**, have been applied. In SDT however, fewer NPs have been studied and include liposomes [**18**,**109**], micelles [**110**], mesoporous silica [**111**], and gold NPs [**112**]. Some NPs reported in SDT studies in the literature include TiO_2 NPs, which have demonstrated impressive therapeutic efficacies upon sono-irradiation [**113,114**]. In some cases, the NPs were conjugated to the sonosensitizers as delivery vectors and for enhancing efficiency in SDT [**115-119**]. The ability of NPs to demonstrate tumoricidal effects when irradiated with US is not yet clear. However, it is reported that solid particles improve the efficiency of acoustic

cavitation by increasing the surface area for bubble-nucleation sites [**118**]. This results in an increase in the rate of bubble formation, and therefore increasing the yield of ROS during SDT [**119**-**122**]. Fewer Pc-NPs conjugates have been studied for SDT on cancer cells. Bakhshizadeh *et al.* reported on the improvement of Zn Pcs' SPDT performance on colon melanoma CT26 cell line upon encapsulation within liposomes [**18**]. In another study, using protoporphyrin, Sarzgarnia *et al*. reported on the protoporphyrin-gold NPs conjugates with improved SDT efficacies on the CT26 cell line *in vivo* [**123**].

The use of Pcs conjugated to metallic and graphitic NPs for SDT and SPDT treatments are reported for the first time in this work. A summary of the NPs used in this work is given in the **Table 1.4**, [**124-127**].

Table 1.4. A summary of the nanoparticles used in this work.

Organic NPs	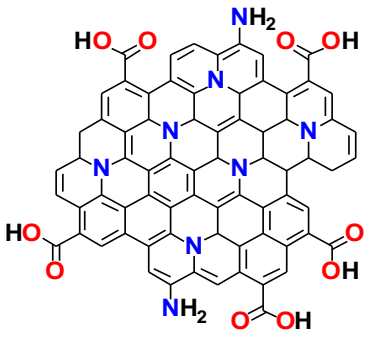 NGQDs [**124**]	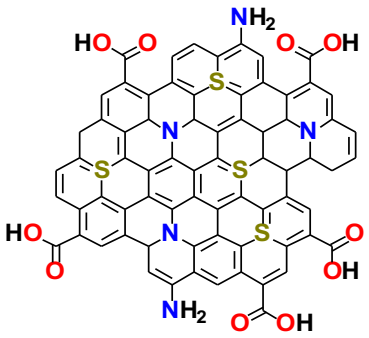 NSGQDs [**125**]
Inorganic NPs	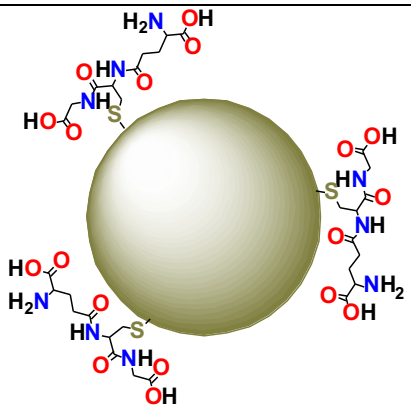 AuGSH [**126**]	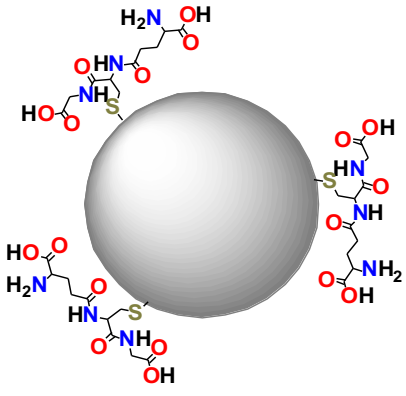 AgGSH [**127**]

In this work two classes of NPs were conjugated to Pcs, including inorganic (metallic) and organic (graphitic) NPs, and employed for the PDT, SDT, and SPDT treatments of cancer cells *in vivo*. The design and synthesis of NPs for cancer treatment requires careful consideration to yield specific structural properties including size, shape, stability, surface properties as well as their toxicity profiles [**128**].

The metallic NPs can be prepared in different sizes and shapes such as spheres, prisms, and rods to mention a few. In this work, glutathione (GSH) functionalized spherical gold (AuGSH) and silver (AgGSH) NPs were employed. The GSH has been widely used as a capping agent for metallic NPs to regulate their sizes and minimize their oxidation to metallic ions. The Ag NPs, for example, are known to oxidise at ambient temperature to yield cytotoxic Ag^{2+} ions [**129**]. The GSH was also used as a linker for Pc conjugation to the AuGSH and AgGSH NPs through covalent linkages. Metallic NPs such as Au and Ag NPs have been extensively studied for PDT and have shown enhancement of the photo-physicochemical properties for Pcs. For SDT, the Au NPs have shown anticancer activity when directly used as a sensitizer [**130**,**131**]. The graphitic NPs may be prepared as fullerenes, tubes or sheets as shown in **Fig. 1.7**. In this work, the graphene quantum dots (GQDs) were used. The GQDs are highly fluorescent graphene sheets with a π-conjugates system. The GQDs are biocompatible NPs that have been widely studied in the development of therapeutics [**132**,**133**]. The GQDs have also been studied in combination with Pcs for PDT where they have demonstrated the ability to enhance the ROS yields and therapeutic efficacies of Pcs [**134**]. Graphitic NPs have not yet been reported in SDT or SPDT in the literature. In this work, the nitrogen doped (NGQDs) and the nitrogen-sulfur co-doped (NSGQDs) GQDs were conjugated to Pcs for the PDT, SDT and SPDT studies.

1.6. Aims and objectives.

The aim of this work was to prepare a series of ionic Zn(II) Pcs varying the type of substituents, type of quaternizing agents, type of charge and number of charges, as well as conjugation to NPs. And thereafter, determine the photo-sonodynamic therapy activities of the different Pcs on breast and cervical cancer cell lines *in vitro*.

	Objectives:
1	**Synthesis and structural characterization of differently substituted**
3	**Photophysical and photochemical characterization** *Determine the photophysical and photochemical parameters of the Pcs*
4	**Sono-stability studies** *Determine stability of Pcs under different US parameters to determine best parameters for treatments.*
5	**ROS generation studies** *Determine the ROS generation under light and US irradiations (Optimize US parameters).*
6	***In vitro* toxicity studies** *Perform the PDT, SDT and SPDT treatments in vitro.*
7	**Effect of nanoparticles** *Determine the effects of different types of NPs on the ROS generations and SPDT activities of the Pcs in vitro.*

1.7. Summary of novelty.

This thesis reports on the SDT and SPDT activity of peripherally ionic Zn(II) Pcs.

- Herein the effects of the ultrasonic parameters on the stability, ROS yields and *in vitro* cytotoxicity of cationic and zwitterionic Pcs on MCF-7 and HeLa cell lines are reported for the first time.

  (The effects of ultrasonic frequencies (MHz) and power ($W.cm^{-2}$) are discussed).
- The SDT and SPDT activity of Zn(II) Pcs bearing cationic and zwitterionic R-groups at the peripheral positions are reported for the first time including their ROS yields and *in vitro* cytotoxicity studies on MCF-7 and HeLa cell lines.

  (The effects of the type of substituents, the type of quaternizing agents and type of charges on the Pcs are discussed).
- Triphenyl phosphine (TPP) is a well-known extensively studied mitochondria targeting moiety used in the development of anticancer therapeutics. The synthesis of TPP-labelled Pcs derivatives is reported. The SDT and SPDT activities of including the ROS yields and *in vitro* cytotoxicity studies on MCF-7 and HeLa cell lines are also reported for the TPP-labelled Pcs for the first time in this work.
- The effects of metallic and graphitic NPs on the SDT and SPDT activity cationic Pcs are reported. Herein, the AuGSH, AgGSH, NGQDs, and NSGQDs in conjugation with Pcs are reported for the first time including the ROS yields and *in vitro* cytotoxicity studies on MCF-7 and HeLa cell lines.

  (The effects of the metallic and graphitic NPs on the anticancer activities are discussed and compared).

CHAPTER TWO

2. Experimental

2.1. Instruments

- The Fourier Transform Infrared (FTIR) spectra were recorded on the Bruker Alpha IR spectrophotometer.

- The ^{1}H nuclear magnetic resonance (NMR) spectra were recorded using the Bruker Advance II+ 400 MHz NMR spectrometer.

- The mass spectra were recorded on the Bruker Auto FLEX III Smart-beam MALDI-TOF mass spectrometer using α-cyano-4-hydrocinnamic acid as the matrix.

- The elemental analyses (CHN) were performed using the Vario-Elementar Microcube ELIII.

- The energy dispersive X-ray spectroscopy (EDS) analyses were performed using the INCA PENTA FET coupled to the VAGA TESCAM operated at 20 kV accelerating voltage.

- The X-ray photoelectron spectroscopy (XPS) analyses were performed using the AXIS Ultra DLD (supplied by Kratos Analytical) using Al (monochromatic) anode equipped with a charge neutralizer.

- The Raman spectra were collected using the Bruker Vertex 70-Ram II Raman spectrometer (equipped with a 1064 nm Nd: YAG laser and liquid nitrogen cooled germanium detector) was used to collect Raman spectral data.

- The nanoparticle size estimations were recorded using the dynamic light scattering (DLS) experiments were performed using a Malvern Zetasizer nanoseries Nano-ZS90.

- The transmission electron microscope (TEM) images were captured using the ZEISS LIBRA® model 120 operated at 90 kV.

- The UV-vis spectra were collected using the Thermo Scientific EVOLUTION 350 UV-vis spectrophotometer connected to the INSIGHT 2 software program for data collection in the range of 300-800 nm.

- The fluorescence emission and excitation spectra were recorded using the Varian Eclipse spectrofluorometer using a 360 nm – 1100 nm filter.

- The fluorescence lifetimes (τ_F) were recorded using the time correlated single photon counting (TCSPC), (FluoTime 300, Picoquant GmbH). A diode laser (LDH-P-670 driven by PDL 800-B, 670 nm 20 MHz repetition rate, Picoquant GmbH) was employed where Pc absorbs, and LDH-P-387 with 10 MHz repetition rate, 88 ps pulse width where GQDs absorb.

  A diagram of the TCSPC set-up is shown in **Fig. 2.1**.

- A laser flash photolysis system, consisting of a LP980 spectrometer with a PMT-LP detector and an ICCD camera (Andor DH320T-25F03) detector was used to determine triplet quantum yields (Φ_T). The signal from the PMT detector was recorded on a Tektronix TDS3012C digital storage oscilloscope. The excitation pulses were produced using a tunable laser system consisting of an Nd:YAG laser (355 nm, 135 mJ/ 4–6 ns) pumping an optical parametric oscillator (OPO, 30 mJ/3–5 ns) with a wavelength range of 420 nm –2300 nm (NT-342B, Ekspla).

  A diagram of the laser flash photolysis set-up is shown in **Fig. 2.2**.

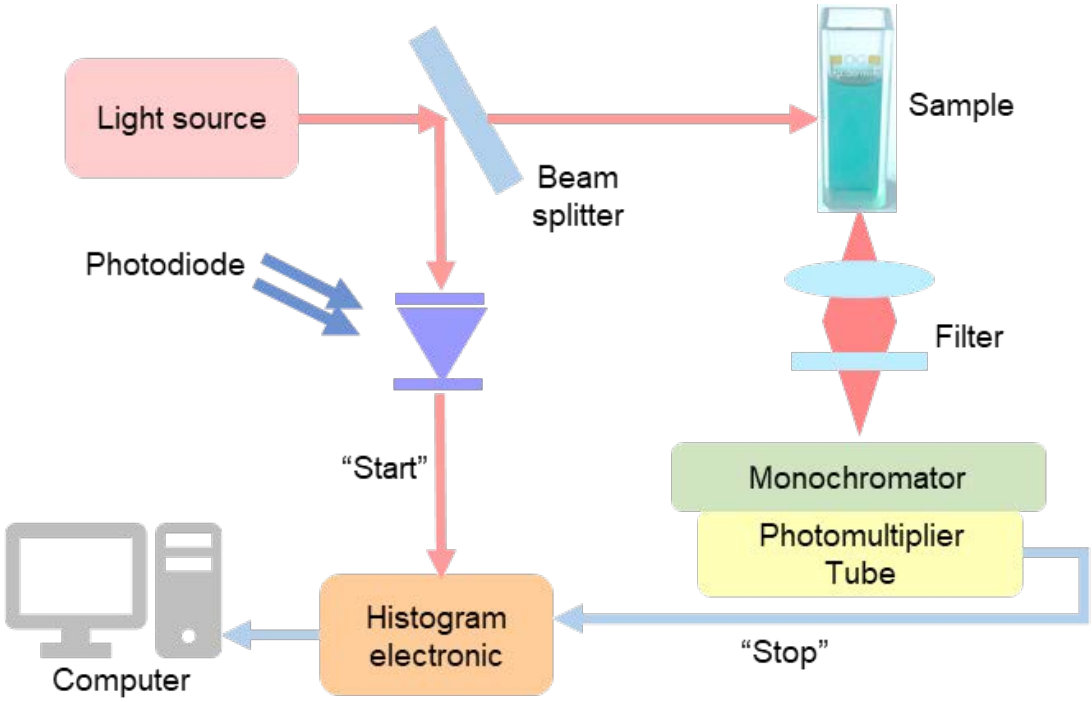

Figure 2.1. A diagram of the time correlated single photon counting set-up.

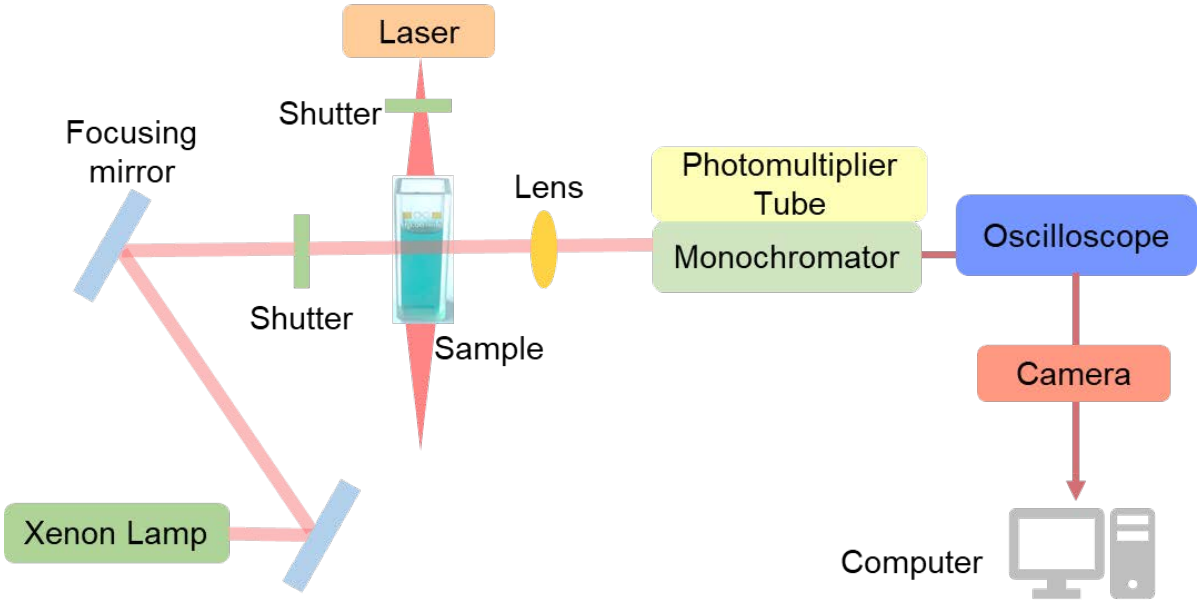

Figure 2.2. A diagram of the laser flash photolysis set-up.

- The photo-treatments were performed using a generic electric quartz line projector lamp (300 W). A 600 nm glass cut off filter (Schott) and a water filter

were used to filter off ultraviolet and infrared radiations, respectively. An interference filter (Intor, 670 nm with a bandwidth of 40 nm) was additionally placed in the light path before the sample. Light intensities were measured with a POWER MAX5100 (Molelectron detector incorporated) power meter to 2.97 × 10^{16} photons^{-1} cm^{-2}.

The quartz line projector set-up used in this work is shown in **Fig. 2.3**.

- The Modulight® Medical Laser System with a 680 nm laser source and irradiation doses of 170 J.cm^{-2} was used for photo-treatments during the PDT treatments of cell cultures *in vitro*. Specifications: 7710–680 channel Turnkey laser system coupled with a 2.3 W channel. The system was connected to cylindrical out-put channels, an integrated calibration module, a foot/hand switch pedal, sub-miniature version-A connectors, and safety interlocks. The illumination kit for in vitro PDT studies can hold 127.76 x 85.48 mm 96 well tissue culture plates.

  The Modulight® set up used in this work is shown in **Fig. 2.4**. An image of the Modulight® is shown in the *Supplementary Information*, **Fig. S1**.

- The ENRAF NONIUS Sonopuls 490B ultrasound medical was used for the sono-treatments. Specifications: (ref no.: 1630.905, $FREQ_{US}$ – 1/3 MHz, INT_{US} – 0-2 W cm^{-2} continuous, $ERA_{US\text{-}Applicator}$ – 5 cm^2, POWER – 15W, IPX7). A bath of water purged with nitrogen as connected to the ultrasound applicator (transducer) fixed at the bottom and connected to a water pump for a continuous flow of water to maintain temperature. For the treatments, the sample holder was secured on the waterbed at 20 mm above the transducer in an opaque water-bath chamber as shown in **Fig. 2.5**.

The ultrasound set-up used in this work is shown in **Fig. 2.5**. An image of the ultrasound system is shown in the *Supplementary Information,* **Fig. S2**.

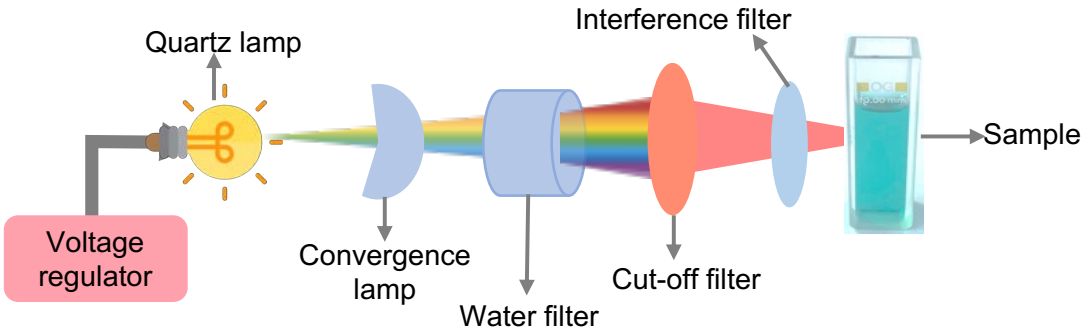

Figure 2.3. The quartz line projector set-up.

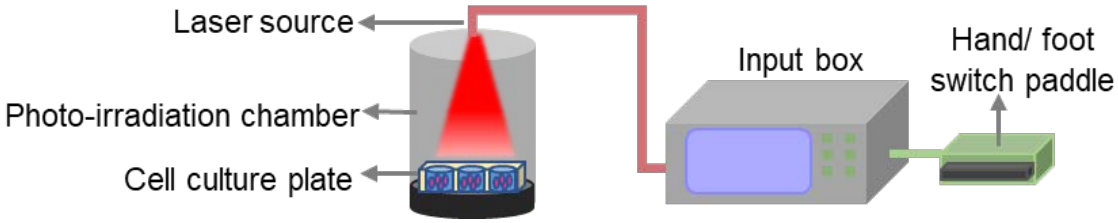

Figure 2.4. The Modulight® Medical laser system set-up.

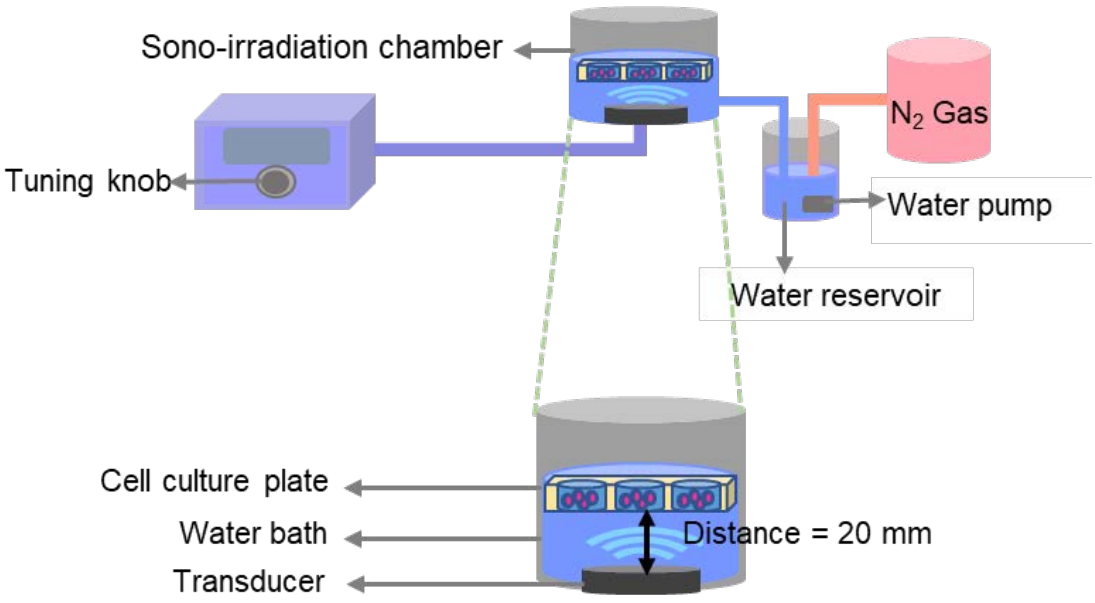

Figure 2.5. The ENRAF NONIUS Sonopuls 490B ultrasound set-up.

- The electron paramagnetic resonance (EPR) spectroscopy measurements were carried out using the Bruker EMX Plus EPR spectrometer, specifications: model number: EMP-9.5/12B/P, fitted with a liquid sample resonator (ST1010); set at 0.632 mW for the microwave power, frequency 9.714 GHz, resolution 2048 points, at a centre field of 3500 G with 200 G for the sweep width and time constant of 5.12. The EPR spectra were recorded using the WinEPR Acquisition Program, version 4.40 Rev11.

  The **Fig. 2.6** shows the EPR spectroscopy used in this work. An image of the EPR spectrometer is shown in the *Supplementary Information*, **Fig. S3**

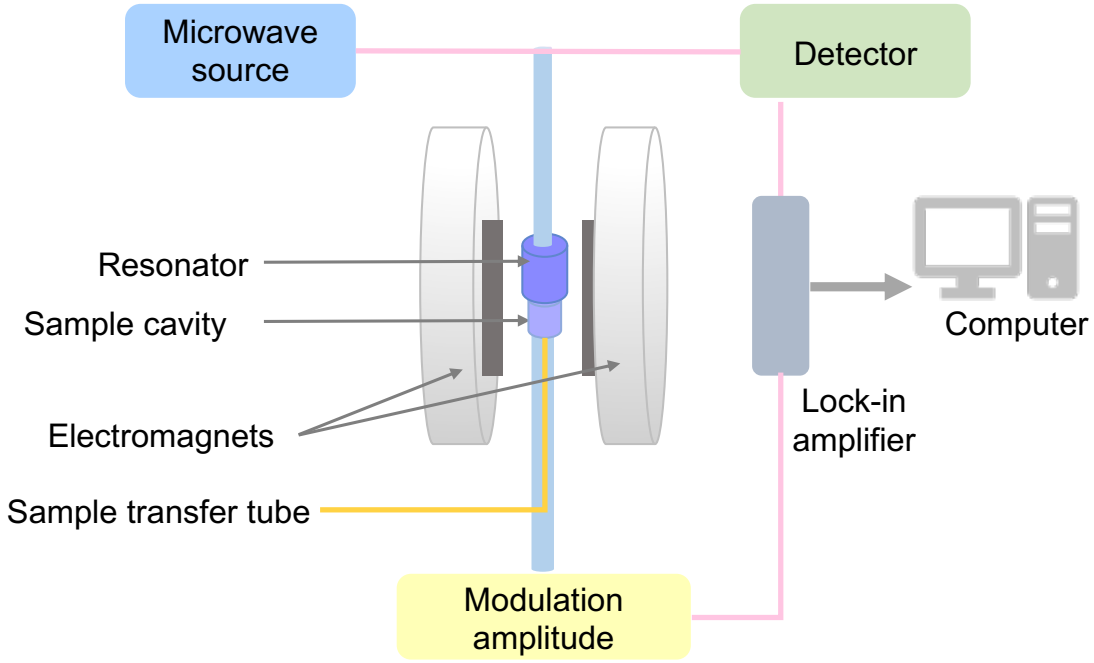

Figure 2.6. The electron paramagnetic resonance spectrometer set-up.

- All the materials and instruments used for cell culture studies were sterilized using the JEIO TECH Lab Companion autoclave containing ultrapure water at 121 °C for 20 min (specifications: Code No. AAHL1015K, Model ST-50G).

- The Heat-Force® incubator set at 37 ºC, and an ~5% CO_2 humidified atmosphere was used for cell culture.
- The cellular images were obtained using the Zeiss® microscope using the Zeiss® A-Plan 10× magnifying lenses and captured using the Zeiss® camera.
- The number of live cells were measured on the SpectraMax® M3, molecular Devices multi-well-plate reader from Separations and recorded using the SoftMax® Pro6.4 software.

2.2. Materials

All the reagents and solvents used were of reagent grade and were purchased from commercial suppliers. The materials were used without further purification.

2.2.1. Solvents

The anhydrous dimethylformamide (DMF), dimethylsulfoxide (DMSO), toluene, ethanol (EtOH), acetonitrile, diethyl ether, chloroform, acetone, hydrochloric acid, ethyl acetate (EtOAc) and tetrahydrofuran (THF) were purchased from Sigma Aldrich®, United States of America. The Ultra-pure water was obtained from ELGA, Veolia water PURELAB, flex system, Marlow, United Kingdom. The deuterated dimethylsulfoxide (DMSO-D_6) was purchased from Magni-Solv®, United States of America.

2.2.2. Reagents for synthesis

The iodomethane, iodoethane, 1,3-propanesultone, triphenylphosphine (Ph_3P), *N,N*'-dicyclohexylcarbodiimide (DCC) and *N*-hydroxysuccinimide (NHS) were all purchased from Sigma Aldrich®, United States of America. The 4-brombutyl-triphenyl-phosphonium bromide was synthesized as reported in the literature [**135**].

2.2.3. Standards, quenchers, and proteins.

The 1,3-diphenylisobenzofuran (DPBF), anthracene-9,10-diyl-*bis*-methylmalonate (ADMA), 2,2,6,6-*tetra*-methylpiperidone (TEMP), 5,5-dimethyl-1-pyrroline-*N*-oxide (DMPO) and phenyl-*N*-*tert*-butylnitrone (PBN), quinine sulphate (QS), unsubstituted zinc Pc (ZnPc) standard and bovine serum albumin protein (BSA) were all purchased from Sigma Aldrich®, United States of America. The aluminium Smix Pc (AlSmix Pcs; composed of a mixture of dissimilarly sulfonated Pcs) were synthesized as previously reported in the literature [**136**].

2.2.4. Materials for cell studies

The cervical cancer Henrietta Lacks (HeLa) cell lines were purchased from from ATCC®, United States of America. The human breast adenocarcinoma Michigan Cancer Foundation-7 (MCF-7) cell line were purchased from Cellonex®, South Africa. The Dulbecco's Phosphate Buffered Saline (DPBS), Dulbecco's modified eagle's medium (DMEM, with 4500 mg/ mL glucose, L-glutamine, sodium pyruvate and sodium bicarbonate), Dulbecco's modified eagle's medium (clear DMEM, with 4500 mg/ mL glucose, without L-glutamine, sodium pyruvate and no phenol red), the Dulbecco's Phosphate Buffered Saline (DPBS, modified, without calcium chloride and magnesium chloride), the trypsin-EDTA solution 1×, and the Greiner CELLSTAR® 96-well cell culture plates (sterile, flat bottom, with lid), were all purchased from Sigma®, United States of America. The heat-inactivated fetal bovine serum (FBS), the antibiotic antimycotic solution with 100 µg/ mL-penicillin:100 unit/ mL-streptomycin-amphotericin-B-mixture (PSA), and neutral red cell proliferation reagent (4-[3-(4-iodophenyl)-2-(4-nitrophenyl)-2H-5-tetrazolio]-1,3-benzene disulfonate, WST-1) were all purchased from Biowest®, France. The cell counting trypan blue dye (0.4% solution in 0.85% sodium chloride) was purchased from Lonza®, Switzerland. The

tissue culture flask 75 (T75, sterile, with vented screw caps) were purchased from Corning®, United States of America.

2.2.5. Previously synthesized Nanoparticles

The NGQDs [**124**] and NSGQDs [**125**] , AuGSH NPs [**126**] and AgGSH NPs[**127**] nanoparticles were synthesizes as described in the literature.

2.3. Synthesis.

The synthesis of the cationic Pc **1** – Pc **5** have been reported in the literature [**104-108**]. The synthesis of the zwitterionic Pc **6** and Pc **7**, and the cationic Pc **8** – Pc **11** are reported in this work.

2.3.1. Synthesis of new ionic phthalocyanines.

The reported neutral Pc used in this work include the 2,9,16,23-*tetrakis*-(*N*-morpholino) Zn(II) Pc **I** [**107**] for the synthesis of the new Pc **6** and Pc **11**; the 2,9,16,23-*tetrakis*-(2,5-dimethyl-4-morpholino) Zn(II) Pc **II** [**108**] for the synthesis of the new Pc **7**; the ,9,16,23-*tetrakis*-(2-mercapto-4-methyl-5-thiazoleaceticacid) Zn(II) Pc **III** [**137**] for the synthesis of the new Pc **8** and Pc **9**; and the 2,9,16,23-*tetrakis*-(4-pyridyloxy) Zn(II) Pc **IV** [**106**] for the synthesis of the new Pc **10**. The neutral Pcs were thereafter quaternized to yield the new ionic Pcs reported in this work, Pc **5** – Pc **11**. A summary of the structures of all the new ionic Pcs reported in this work is shown in the **Fig. 3.1**. The different quaternizing reagents used to yield the ionic Pcs **5** – Pc **11** include: iodomethane, iodoethane, 1,3-propanesultone and 4-brombutyl-triphenyl-phosphonium bromide.

2.3.1.1. Synthesis of 2,9,16,23-*tetrakis*-(*N*-propanesultone-morpholino) Zn(II) Pc **6**, **Scheme 3.1**.

A solution of the neutral Pc **I** (50 mg, 0.05 mmol) in 4 mL of anhydrous DMF was prepared and stirred at 70 °C for 10 min. The 1,3-propanesultone (48 mg, 0.4 mmol) was added and the mixture was left to reflux for 48 h. The product was precipitated using acetonitrile, collected under filtration, and washed with THF, acetone, EtOAc, chloroform and diethyl ether and dried *in vacuo* in an enclosed fume hood. Pc **6**: Yield: 55.3 mg (78%); ^{1}H NMR (400 MHz, DMSO-D_6), (δ: ppm): 8.32 (s, 2H, Ar-H), 7.85 (s, 5H, Ar-H), 7.75 (s, 1H, Ar-H), 7.56 (s, 2H, Ar-H), 7.27 (s, 2H, Ar-H), 3.40 (s, 20H, CH_2-H), 3.02 (t, *J*= 5.9 Hz, 5H, CH_2-H), 2.16 (t, *J*= 5.3 Hz, 14H, CH_2-H), 2.11 (s, 12H, CH_2-H), 1.41-1.25 (m, 5H, CH_2-H); FTIR (KBr): v_{max}/cm^{-1}: 2947 (Ar C-H), 2829 (CH_2), 1162 (S=O), 1029 (C-O-C), 1005 (Ar C=N). Calc. (%) for $C_{60}H_{68}N_{12}O_{16}S_4Zn$: C, 51.22; H, 4.87; N, 11.95. Found C, 51.61; H, 5.05; N, 11.88%. MALDI-TOF, *m/z*: Calc.: 1404.31; Found: 1422.72 $[M+H_2O]^+$. UV/vis Abs_{max} nm DMSO (log ε): 687 (4.79), 608 (4.20), 358 (4.61).

2.3.1.2. Synthesis of 2,9,16,23-*tetrakis*-(2,5-dimethyl-4-(*N*-propanesultone-morpholino)) -phenoxy Zn(II) Pc **7**, **Scheme 3.1**.

A solution of the neutral Pc **II** (50 mg,0.03 mmol) in 4 mL of anhydrous DMF was prepared and stirred at 70 °C for 10 min. The 1,3-propanesultone (48 mg, 0.4 mmol) was added and the mixture was left to reflux for 36 h. The product was purified as described for the Pc **6**. Pc **7**: Yield: 45.6 mg (78%); ^{1}H NMR (400 MHz, DMSO-D_6), (δ: ppm): 8.95-8.77 (m, 2H, Ar-H), 8.70 (d, *J* = 1.4 Hz, 2H, Ar-H), 8.58 (d, *J* = 5.1 Hz, 2H, Ar-H), 8.37 (s, 2H, Ar-H), 8.21 (s, 3H, Ar-H), 8.11 (s, 1H, Ar-H), 7.97 (s, 1H, Ar-H), 7.76 (s, 1H, Ar-H), 7.71 (s, 2H, Ar-H), 7.58 (s, 2H, Ar-H), 7.45 (s, 2H, Ar-H), 3.99 (s, 37H, CH_2-H), 3.77 (s, 10H, CH_2-H), 3.42 (s, 3H, CH_2-H), 3.15 (s, 5H, CH_2-H), 2.98 (t,

J = 5.4 Hz, 6H, CH_2-H), 2.93 (s, 13H, CH_3-H), 2.88 (s, 3H, CH_2-H), 2.38 (s, 3H, CH_3-H), 2.16 (s, 8H, CH_3-H). FTIR (KBr): v_{max}/cm^{-1}: 2959 (Ar C-H), 2873 (CH_2), 1164 (S=O), 1025 (C-O-C), 1007 (Ar C=N). Calc. for $C_{96}H_{107}N_{12}O_{20}S_4Zn$: C, 59.36; H, 5.55; N, 8.65%; Found: C, 59.76; H, 5.62; N, 8.02%. MALDI-TOF, *m/z*: Calc.: 1940.59; Found: 1941.72 $[M+H]^+$. UV/vis Abs_{max} nm DMSO (log ε): 677 (4.76), 610 (4.05), 355 (4.41).

2.3.1.3. Synthesis of 2,9,16,23-*tetrakis*-(methyl-2-mercapto-4-methyl-5-thiazoleaceticacid) Zn(II) Pc **8**, **Scheme 3.2**.

A solution of the neutral Pc **III** (250 mg, 0.188 mmol) was prepared in 4 mL of anhydrous DMF and stirred under inert atmosphere for 48 h at 50 °C in the presence of CH_3I in excess to yield Pc **8**. The product was precipitated using diethyl ether, collected under filtration, washed with acetonitrile, THF, EtOAc and acetone, and dried *in vacuo* in an enclosed fume hood. Pc **8**: Yield: 180 mg (67%); NMR: ^{1}H NMR (400 MHz, DMSO-D_6), (δ: ppm), 8.64 (s, 4H, Ar-H), 8.11 (s, 2H, Ar-H), 7.88 (s, 6H, Ar-H), 2.83 (s, 8H, CH_2-H), 2.67 (s, 6H, CH_3-H), 2.44 (dt, *J* = 3.4, 1.7 Hz, 18H, CH_3-H). FTIR (KBr): v_{max}/cm^{-1}; 3410 (-OH), 3008 (-C-H), 1654 (-C=C), 1482 (-C=O), 1598 (-C=N), 750 (-C-S); Found: C, 51.59; H, 3.28; N, 12.08%; molecular formula $C_{60}H_{48}N_{12}O_8S_8Zn$ requires C, 51.96; H, 3.49; N, 12.12%, MALDI-MS *m/z*: Calc. 347.020; Found: 348.309 $[M+H]^{4+}$. UV/vis Abs_{max} nm DMSO (log ε): 685 (4.59), 617 (4.30), 355 (4.21).

2.3.1.4. Synthesis of 2,9,16,23-*tetrakis*-(ethyl-2-mercapto-4-methyl-5-thiazoleaceticacid) Zn(II) Pc **9**, **Scheme 3.2**.

The Pc **9** was synthesized following a similar method described for the synthesis of the Pc **8**, however, CH_3CH_2I in excess was used instead of CH_3I to yield Pc **9**. Pc **9**: Yield: 150 mg (55%); NMR: ^{1}H NMR (400 MHz, DMSO-D_6), (δ: ppm): 7.92 (s, 7H, Ar-H), 7.66 (s, 5H, Ar-H), 2.60 (s, 12H, CH_3-H), 2.44 (s, 12H, CH_3-H), 2.27 (s, 11H, CH_2-

H), 1.80 (s, 5H, CH_2-H). FTIR (KBr): v_{max}/cm^{-1}; 3410 (-OH), 2997 (-C-H), 1654 (-C=C), 1482 (-C=O), 1598 (-C=N), 750 (-C-S); Found: C, 53.18; H, 3.56%, N,11.19%; molecular formula $C_{64}H_{56}N_{12}O_8S_8Zn$ requires C, 53.27; H, 3.91; N, 11.65%. MALDI-MS *m/z*: Calc. 357.530; Found: 357.447 $[M]^{4+}$. UV/vis Abs max nm DMSO (log ε): 684 (4.71), 614 (4.21), 354 (4.57).

2.3.1.5. Synthesis of 2,9,16,23-*tetrakis*-(*N*-(*N*-butyl-4-triphenyl-phosphonium)-pyridine-4-yloxy) Zn(II) Pc **10**, **Scheme 3.3**.

A solution of the neutral Pc **IV** (100 mg, 0.12 mmol) in toluene was prepared. To this solution, 4-brombutyl-triphenyl-phosphonium bromide (310 mg, 0.8 mmol) was added. The solution was left to reflux for 24 h. The product precipitates out of solution once it was quaternized and was collected under filtration. The product was thereafter washed with toluene, THF, chloroform, acetonitrile, and EtOAc. The solid was dried *in vacuo* in an enclosed fume hood. Pc 3: Yield: 230 mg (87%); NMR: ^{1}H NMR (400 MHz, DMSO-D_6), (δ: ppm): 8.50 (s, 12H, Ar-H), 7.91 (m, 16H, Ar-H), 7.77-7.84 (m, 60H, Ar-H), 3.60-3.63 (m, 8H, CH_2-H), 3.37 (m, 8H, CH_2-H), 1.07-1.10 (m, 16H, CH_2-H); Calc. for $[C_{140}H_{118}N_{12}]^{4+}$: C, 66.11; H, 4.76; N, 6.61%; Found: C, 65.87; H, 4.47; N, 6.33%. FT-IR: v_{max}/cm^{-1}; 2886 (C-H), 1635 (C=C), 1191 (C-O-C), 1430, 1107, 689 (C-P); MALDI-TOF, *m/z*: Calc.: 507.37; Found: 506.799. $[M+H]^{4+}$. UV/vis Abs_{max} nm DMSO (log ε): 680 (4.99), 614 (4.51), 367 (4.24).

2.3.1.6. Synthesis of 2,9,16,23-*tetrakis*-(*N*-(*N*-butyl-4-triphenyl-phosphonium)-morpholino) Zn(II) Pc **11**, **Scheme 3.3**.

A solution of the neutral Pc **I** (100 mg, 0.13 mmol) was prepared in a 1:2 (v/v) DMF: toluene solvent mixture. To the solution, the 4-brombutyl-triphenyl-phosphonium bromide (310 mg, 0.8 mmol) was added and the reaction mixture was left to reflux for

36 h. The product was washed following previously mentioned steps in the preparation of the Pc **10**, and thereafter dried *in vacuo*. Pc **11** Yield: 190 mg (67%); NMR: ^{1}H NMR (400 MHz, DMSO-D_6), (δ:ppm): 8.93-8.92 (d, 5H, Ar-H), 8.40-8.36 (t, 3H, Ar-H), 7.95-7.91 (t, 6H, Ar-H), 7.68-7.66 (d, 10H, Ar-H), 7.62-7.55 (d, 48H, Ar-H), 4.50-4.47 (t, 5H, CH_2-H), 3.71 (s, 2H, CH_2-H), 3.53-3.49 (d, 10H, CH_2-H), 3.16 (s, 30H, CH_2-H), 2.28 (s, 7H, CH_2-H), 1.93 (s, 5H, CH_2-H), 1.32 (s, 5H, CH_2-H); Calc. for $[C_{136}H_{135}N_{12}]^{4+}$: C, 64.93; H, 5.61; N, 6.68%; Found: C, 64.34; H, 5.55; N, 6.59%. FT-IR: v_{max}/cm^{-1}; 2940 (C-H), 1607 (C=C), 1231 (C-O-C), 1437, 1109, 687 (C-P); MALDI-TOF, *m/z*: Calc.: 502.14; Found: 503.126. $[M+H]^{4+}$. UV/vis Abs_{max} nm DMSO (log ε): 710 (4.84), 639 (4.56), 357 (4.23).

2.3.2. Conjugation of Pc **8** and Pc **9** to graphene quantum dots.

The Pcs were π-π stacked on the NGQDs and NSGQDs non-covalently using methods described in the literature [**138**,**139**] with minor modifications.

2.3.2.1. Preparation of **8**-NGQDs and **9**-NGQDs conjugates, **Scheme 3.4**.

To prepare the **8**-NGQDs and **9**-NGQDs conjugates, two solutions containing the NGQDs (5 mg) in 2 mL of 1:5 v/v water: DMF were prepared. The GQDs solutions were sonicated for 30 min. Separate solutions of Pc **8** (10 mg, 0.0075 mmol) and Pc **9** (10 mg, 0.0072 mmol) in 2 mL anhydrous DMF were prepared and mixed well. The NGQDs solutions were thereafter added to each of the Pc solutions. The mixtures were sonicated for a further 2 h and left to stir for 48 h at room temperature. The **8**-NGQDs and **9**-NGQDs were thereafter precipitated using EtOH. The conjugates were collected by centrifugation at 3500 rpm for 5 min and dried *in vacuo*.

2.3.2.2. Preparation of **8**-NSGQDs and **9**-NSGQDs conjugates, **Scheme 3.4**.

The **8**-NSGQDs and **9**-NSGQDs conjugates were prepared similarly to the preparation of the NGQDs conjugates as previously defined, with minor modifications. Two solutions of the NSGQDs (5 mg) in 1 mL of anhydrous DMF were prepared and sonicated for 2 h. Separate solutions of Pc **8** (10 mg, 0.0075 mmol) and Pc **9** (10 mg, 0.0072 mmol) in 2 mL anhydrous DMF were prepared. The NSGQDs solutions were thereafter added to each of the Pc solution. The mixtures were sonicated for a further 2 h and left to stir for 48 h at room temperature. The conjugates were precipitated and washed using a mixture of 3:1 EtOH and acetonitrile. The **8**-NSGQDs and **9**-NSGQDs conjugates were thereafter collected by centrifugation at 3500 rpm for 5 min dried *in vacuo*.

2.3.3. Conjugation of Pc **8** and Pc **9** to gold and silver NPs, **Scheme 3.5**.

The Pc **8** and Pc **9** were conjugated to AuGSH and AgGSH NPs through covalent amide bonds using methods reported in the literature [**140**] with modifications. The Pcs also bear S-groups which may also bond to the NPs through S-metal affinity bonds. This type off conjugation has been reported in the literature [**141**].

To prepare Pc **8** and Pc **9** conjugates with the AuGSH and AgGSH NPs, separate solutions containing 10 mg of the Pc **8** (0.0075 mmol) and **9** (0.0072 mmol) in 2 mL DMF were prepared. To each of the solutions, DCC (5.9 mg, 0.029 mmol) was added and left to stir for 12 h. Thereafter, NHS (3.3 mg, 0.029 mmol) was added, and the mixtures were left to stir for a further 12 h. Separate solutions of the AuNPs and AgGSH (0.01 g) in 2 mL anhydrous DMF were prepared and sonicated for 5 min. The AuGSH/ AgGSH solutions were added to the Pc reaction mixtures and left to stir for 24 h. The Pc-AuNPs and Pc-AgGSH were precipitated using EtOH and collected by

centrifugation at 3500 rpm for 5 min. The solids were washed with EtOH, acetone, diethyl ether and then dried *in vacuo*.

2.4. Sono-Photophysicochemical studies.

The calculations for the determination of the photophysical properties for the Pcs and NPs-conjugates were performed using a comparative method as defined in the literature [**142,143**]. The photophysical parameters determine the efficiency of photon-energy harvesting by a sensitizer during the photo-treatments. The reported photophysical parameters in this work include the fluorescence and triplet quantum yields and lifetimes.

2.4.1. Fluorescence quantum yield (Φ_F) and lifetime (τ_F).

The fluorescence quantum yields (Φ_F) measure the proportion of photons emitted from the total absorbed. The fluorescence lifetime (τ_F) quantifies the average time a molecule in the excited S_1 transitions back to the S_0.

The Φ_F calculations for the Pcs were done using the unsubstituted ZnPc as a standard (with Φ_F of 0.20 in DMSO [**143**]). The Pc solutions were prepared such that the absorption intensities of the Pcs' vibronic bands were ~0.05 a.u. in DMSO. The excitation wavelength for the Pcs used were at the crossover wavelengths between the Q-bands of the test Pc samples and the ZnPc standard's Q-band absorption. The Φ_F calculations for GQDs were done using quinine sulphate (QS) as the standard (with Φ_F of 0.60 in 0.05 M H_2SO_4 solution [**144**]). The solutions were prepared such that the absorption intensities of the GQDs and the quinine sulphate were ~0.5 a.u. The excitation wavelengths were obtained from the crossover of the GQDs test samples and QS absorption peaks. The Φ_F values were calculated using equation 2.1.

$$\Phi_{\mathrm{F}} = \Phi_{\mathrm{F}(std)} \cdot \frac{F.A_{std}.n^2}{F_{std}.A.n^2_{(std)}} \ldots\ldots\ldots\ldots\ldots\ldots\ldots\ldots \text{ equation 2.1}$$

From equation 2.1, the $\Phi_{F(std)}$ is the fluorescence quantum yield of the standard. The areas under the fluorescence emission curves for the sample and the standard are denoted as the *F* and $F_{(std)}$, respectively. The absorbance of the sample and standard at the excitation wavelengths are denoted as the *A* and $A_{(std)}$, respectively. The *n and* $n_{(std)}$ are for the solvent refractive indices for the sample and standard, respectively. For the τ_F calculations, samples solutions were prepared similarly to those for Φ_F. The τ_F were recorded on the TCSPC using a 670 nm laser light source for irradiations at wavelengths where the Pcs absorb. For the GQDs, the 380 nm laser source was used.

2.4.2. Triplet quantum yield (Φ_T) and lifetime (τ_T).

The triplet quantum yields (Φ_T) measures the proportion of Pc in the excited states that undergo intersystem crossing to populate the T_1 from the S_1. The triplet lifetime (τ_T) measures the average time an excited Pc molecule remains in the T_1.

The Φ_T calculations for the Pcs were done using the unsubstituted ZnPc as a standard (with Φ_T of 0.65 in DMSO [**145**]). The Pc solutions were prepared such that the absorbance intensity of the Q-band was ~1 a.u. in DMSO. The excitation wavelengths were obtained from the crossover of the Pc test samples and ZnPc standard's Q-band absorption. The Φ_T calculations were done using equation 2.2.

$$\Phi_{\mathrm{T}} = \Phi_{\mathrm{T}(std)} \cdot \frac{\Delta \mathrm{A_T}.\varepsilon_{\mathrm{T}(std)}}{\Delta \mathrm{A_{T(std)}}.\varepsilon_{\mathrm{T}}} \ldots\ldots\ldots\ldots\ldots\ldots\ldots\ldots\ldots \text{ equation 2.2.}$$

From equation 2.2, the $\Phi_{T(sdt)}$ is the triplet quantum yield of the standard. The changes in the T_1 state absorption is denoted as ΔA_T and the $\Delta A_{T(std)}$ for the sample and the standard, respectively. The molar extinction coefficients in the T_1 are denoted as ε_T

and $\varepsilon_{T(sdt)}$ for the sample and the standard, respectively. The ε_T and $\varepsilon_{T(sdt)}$ are calculated using the equations 2.2.1 and 2.2.2 below, respectively.

$$\varepsilon_T = \varepsilon_s . \frac{\Delta A_T}{\Delta A_s} \quad \text{..... equation 2.2.1}$$

$$\varepsilon_{T(std)} = \varepsilon_{s(std)} . \frac{A_{T(std)}}{A_{s(std)}} \quad \text{..... equation 2.2.2}$$

From the equations 2.2.1 and 2.2.2, the ε_s and $\varepsilon_{s(std)}$ are molar extinction coefficients in the ground states for the sample and standard, respectively. Where the ΔA_s and the $\Delta A_{s(std)}$ are the changes in the absorbance in the ground states for the sample and standard, respectively. The τ_T calculations for the Pcs were determined by the exponential fitting of the kinetic curves using the ORIGIN® 8 Professional software.

2.4.3. Reactive oxygen species generation.

The singlet oxygen quantum yields (Φ_Δ) quantify the amount of $^1O_2$ that are generated per quantum of light photons absorbed. The Φ_Δ values for the Pcs were calculated using comparative photochemical method as described in the literature involving a colorimetric assay monitored by UV-vis spectroscopy [**143**].

Additionally, the ROS generation under the photo-, sono-, or the combination treatments were determined using electron paramagnetic spectroscopy (EPR) in water only.

2.4.3.1. UV-vis spectroscopic method.

The $^1O_2$ generation under the photo-treatments were determined by monitoring the UV-vis absorption spectra of the $^1O_2$ quenchers; DPBF (in DMSO) and of ADMA (in water).

Solutions of the Pcs samples were prepared such that the Q-band absorption intensities were ~1.5 a.u. in DMSO and ~1.0 a.u. in water. The quencher solutions were also prepared, with their maximum absorbances also adjusted to 1.5 a.u. The test samples (Pcs and conjugates) were mixed with the quencher solutions at 1:1 v/v ratios to a maximum of 3 mL.

The solutions were photo-irradiated at increasing time intervals to a total time of 60 s for samples in DMSO, and 30 min for samples in water. The photo-irradiations were performed using the projector lamp at 670 nm ± 40 nm, 300 W, generating 2.97×10^{16} photons^{-1} cm^{-2}. The unsubstituted ZnPc was used as the standard for Φ_Δ calculation in DMSO (with Φ_Δ of 0.67 in DMSO [**146**]) and the AlSmix Pc was used as a standard for Φ_Δ calculation in water (with Φ_Δ of 0.34 in water [**147**]). The Φ_Δ for the Pcs were calculated using the equation 2.3.1.

$$\Phi_\Delta = \Phi_{\Delta(std)} \cdot \frac{R.I_{(std)}}{R_{(std)}.I} \quad \text{..... equation 2.3.1}$$

From the equation 2.3.1, the $\Phi_{\Delta(std)}$ is the Φ_Δ of the standard. Where the R and $R_{(std)}$ are the $^1O_2$ quenchers photodegradation rates by the sample and the standard, respectively. The the rate of the light absorption by the sample and the standard are denoted as the I and $I_{(std)}$, respectively.

The I can be determined using equation 2.3.2:

$$I_{Abs} = \frac{\alpha.A.I}{N_A} \quad \text{..... equation 2.3.2}$$

Where α is $1\text{-}10^{-A(\lambda)}$, and $A(\lambda)$ is the absorbance of the Pcs at the irradiation wavelength, A is the irradiated area (2.5 cm^2). The I is the intensity of the light used (photons/ cm^2) and N_A is the Avogadro's constant.

2.4.3.2. EPR spectroscopy method.

The EPR spectroscopy was used to determine the generation of $^1O_2$ and •OH. Two spin trapping reagents were used, *viz.* TEMP (for $^1O_2$ trapping) and DMPO (for •OH trapping). The spin trapping reagents alone do not show an EPR signal. In the presence of the respective ROS, the spin traps form adducts (TEMPO and DMPO-OH).

The adducts are characterized by EPR signals as shown in the **Fig. 2.7**.

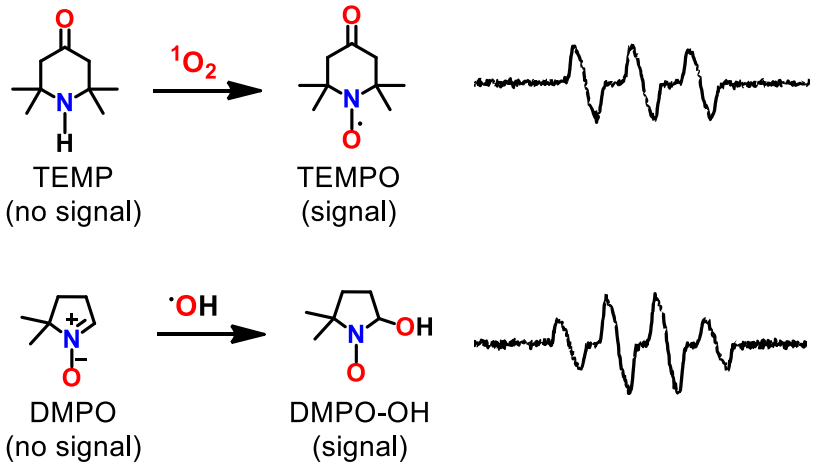

Figure 2.7. Determination of $^1O_2$ and •OH radicals using EPR spectroscopy.

The EPR signals are unique for the different ROS studied as shown in the **Fig. 2.7**. In the presence of the $^1O_2$, TEMP shows three peaks while in the presence of the •OH DMPO show four peaks on the EPR spectra.

Sample preparation:

Solutions containing the Pcs in water were prepared, and their Q-band absorption intensities were adjusted to 1.5 a.u. Separately, solutions of the EPR spin trapping reagents, TEMP and DMPO, were prepared in water to final concentrations of 100 mM. To prepare the test samples, mixtures containing solutions of Pcs or conjugates

and each of the quenchers were prepared separately a 1:1 v/v to a final volume of 3 mL, (reducing the quencher concentration to final 50 mM) for study.

Photo-irradiations:

For the photo-irradiations, the samples were exposed to light using a generic quartz lamp (670 nm ± 40 nm, 300 W, generating 2.97×10^{16} photons^{-1} cm^{-2}) for 10 min.

Sono-irradiations:

For the sono-irradiations, the ENRAF NONIUS Sonopuls 490B ultrasound medical was used. The four ultrasonic parameters were studied first to determine the best sono- conditions to use for SPDT. The sono frequency (MHz) and power (W. cm^{-2}) combinations that were studied included: *Par I* (1 MHz: 1 W. cm^{-2}); *Par II* (1 MHz: 2 W. cm^{-2}); *Par III* (3 MHz: 1 W. cm^{-2}) and *Par IV* (3 MHz: 2 W. cm^{-2}). The test solutions were irradiated at 100% duty cycles for 10 min.

Sono- and photo- irradiations:

For the combination treatment studies, the samples were exposed to the photo-irradiation first, as defined previously. And thereafter exposed to the sono-irradiation using the *Par I* for 10 min.

The control samples for the ROS generation under the photo- and/ sono-irradiations using EPR spectroscopy were also prepared. These included the separate solutions of the Pcs, Pc-NPs conjugates test samples, the spin trapping reagents and water with and without the photo- and/ or sono-irradiations. And the Pcs and spin trapping reagents mixtures in water before treatments (without the photo and/ or sono-irradiations). All the ROS studies were performed in the dark.

The EPR spectra of the TEMP and DMPO for ROS generation determination were recorded at magnetic fields between 3400 G- and 3600 G for the treatments.

2.4.4. Phthalocyanine stability under the sono-irradiations.

The stability of the Pcs upon sono-irradiations at the different parameters (*Par I – Par IV*) were also studied to determine the best parameters for SPDT treatments using UV-vis absorption spectroscopy and EPR spectroscopy.

2.4.4.1. UV-vis absorption spectroscopy.

The Pcs solutions in water were exposed to the sono-irradiation at the different parameters (*Par I – Par IV*) for 30 min at 10 min intervals. The UV-vis spectra of the Pcs prior and post the sono-irradiations were obtained. The UV-vis absorption spectral intensities at the Q-bands of the Pcs were monitored and recorded. The plots of the Q-band intensities against time were obtained and the slope of the trendline were calculated.

2.4.4.2. EPR spectroscopy.

Since the degradation of the Pcs under the sono-irradiations may lead to the formation of Pc-derived $^{\bullet}$C, the determination of the generation of the •C generation was of interest and was performed using EPR spectroscopy. The spin trapping reagent PBN (50 mM) was used for detection of $^{\bullet}$C. The samples were prepared similarly to those for ROS generation. The solutions were exposed to the sono-irradiations at the four studied parameters (*Par I – Par IV*) for 10 min. The EPR spectra were recorded at magnetic fields between of 3400 G- and 3600 G.

The spin trapping reagents PBN alone does not show an EPR signal. In the presence of the respective ROS, the spin traps form adducts (PBN-C). The adducts are characterized by EPR signals as shown in the **Fig. 2.8**.

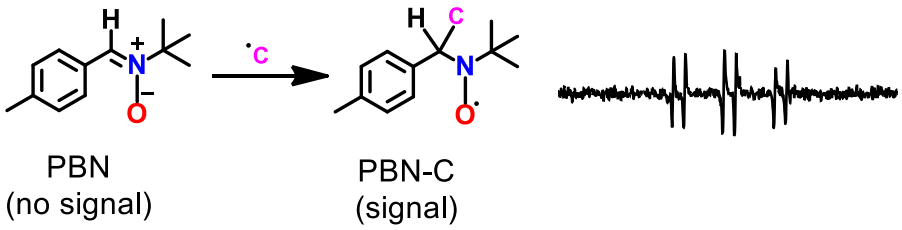

Figure 2.8: Determination of the •C using EPR spectroscopy.

The PBN in the presence of the •C show three-pair peaks on the EPR spectra, **Fig. 2.8**. The control samples for the •C generation by the sono-irradiations using EPR spectroscopy were also prepared. These included the separate solutions of the Pcs, the PBN and water with and without photo- and/ or sono-irradiations. And the Pcs and PBN mixtures in water before irradiations (without the sono-irradiations).

2.5. The *in vitro* cell studies.

All proceedings for cell culture and cell studies were handled under antiseptic conditions to minimize contamination. Material and instruments were disinfected using 70 % alcohol and autoclaved. Sample preparation and cell handling was performed under a fume hood with reduced pressure.

2.5.1. HeLa and MCF-7 cell culture.

For cell studies, two cell lines were used, the Henrietta Lacks (HeLa) cervical cancer and human adenocarcinoma Michigan Cancer Foundation-7 (MCF-7) breast cancer cell lines. The cancer cell lines (HeLa and MCF-7) were cultured in T75 culture flasks

in cell culture media (DMEM with 4.5 g/ L glucose with L-glutamine and phenol red, supplemented with 10% FBS and 1% PSA) in an incubator (at 37 ºC, with ~5% CO_2 humidified atmosphere) for 48 h to ~80% confluency. The cells were washed with PBS and lifted using trypsin-EDTA solution 1× in DPBS for ~15 min. The cells were neutralized using culture media and collected using centrifugation at 1500 rpm for 5 min. The cell cultures pellets were resuspended in culture media. The viable cells were quantified using the trypan blue dye and hemocytometer method as defined in the literature [**148**]. The resuspended cells were seeded into 96-well plates to ~10,000 cells/ well and incubated for 24 h (at 37 ºC, with ~5% CO_2 humidified atmosphere) prior exposure to Pcs for treatments. Separate sets of plates were prepared for PDT, SDT and SPDT treatments for the Pcs. Separate cell culture plates for the control tests included plates for photo-, sono-, sono-photo combination irradiations only without the Pcs, plates for cells exposed to Pcs only (for chemotoxicity studies), and plates for untreated control cells (no Pc and no photo- and/ sono irradiations).

2.5.2. Sono-/ photodynamic therapy cytotoxicity studies

The cell handling for drug inoculation was done in the dark, to prevent Pc activation prior treatments. The cells in the multi-well plates were exposed to the Pcs complexes at increasing concentrations ranging from 0 µM – 100 µM in cell culture media. For the Pc-NPs conjugates, mass concentrations were used ranging from 0 µg/ mL – 50 µg/ mL in cell culture media. The cells were thereafter incubated for 24 h at 37 ºC, with ~5% CO_2 humidified atmosphere. The cells were then washed with DPBS to remove unabsorbed residual Pcs/ conjugates. A volume of 100 µL of the clear DMEM (without phenyl red) was added to each well to prepare for PDT, SDT and SPDT treatments.

The cells were exposed to photo- and/ or sono-irradiations for 10 min. The photo-irradiations in the PDT treatments were performed using the Modulight® Medical Laser system, and the sono-irradiations for the SDT treatments were performed using the ENRAF NONIUS Sonopuls 490B ultrasound medical as described in the section 2.1.

After PDT, SDT and SPDT treatments, the clear DMEM in all the wells was gently removed. A volume of 100 µL of the cell culture media was added to each well and the cells were re-incubated at 37 ºC, with ~5% CO_2 humidified atmosphere for 24 h.

The cytotoxicity efficacies of the treatments were determined by calculating the cell survival percentages. The WST-1 cell proliferation assay was used to quantify the cell survival 24 h post treatments following a protocol defined in the literature [**149**], with minor modifications. In each well, 5 µL of the WST-1 reagent was added. The cells were left in the incubator for ~5 h to allow for the metabolism of the WST-1 reagent to form the orange formazan. Live cells can perform the reduction of WST-1 reagent to formazan. Therefore, the intensity of the formazan at 450 nm will be increased for viable cells compared to dead non-viable cells. Thus, the intensities of the formazan product in each of the treatment samples were determined and compared to the untreated control cell samples. The percentage cellular survival post treatments were thereafter calculated using equation 2.4.

$$\text{Percentage cell survival} = \frac{\text{Abs}_{450\text{nm}}}{\text{Abs}_{450\text{nm(control)}}} * 100\ \% \quad \text{.....equation 2.4}$$

Where $\text{Abs}_{450\text{nm}}$ and $\text{Abs}_{450\text{nm(sample)}}$ are the absorbance intensities of the treatment cell samples and the untreated control cell samples at 450 nm, respectively. The plots of the cell survival percentages against the concentrations were obtained for the Pcs and the Pc-NPs at the different treatments.

The IC_{50} values for the Pcs complexes for each treatment type were determined by extrapolation from the plots of cell survival percentage against concentrations to determine the concentrations of each of the Pcs or Pc-NPs conjugates required to eradicate ~50% of the cells under the different treatments.

2.5.3. Cell morphology studies.

The effects of the PDT, SDT and SPDT treatments on the morphology of the cells were also studied. The cells were cultured, inoculated with Pcs/ Pc-NPs conjugates. The cells were thereafter exposed to the photo and sono-irradiations described earlier. The cells were incubated for 24 h at 37 ºC, with ~5% CO_2 humidified atmosphere after the treatments. The cells were then washed with DPBS and 100 µL of clear DMEM solution was added to each well. The treated and control cells were visualised using the Zeiss® microscope and magnified using the Zeiss® A-Plan 10× magnifying lenses. The cellular images were then captured using the Zeiss® camera.

2.5.4. Cell sensitizer uptake *in vitro*.

The uptake of the Pcs and Pc-NPs conjugates were determined for the cells *in vitro*. The cells were cultured, inoculated with Pcs/ Pc-NPs conjugates at the different test concentrations and incubated 24 h at 37 ºC, with ~5% CO_2 humidified atmosphere, as described earlier. The cells were then washed with DPBS to remove the unabsorbed Pcs or Pc-NPs conjugates. A volume of 100 µL of DMSO was added to each well and left to sit for ~30 min to dissolve the Pcs in the cell cultures. The intensities of the Pcs (at wavelengths where the Pcs absorb) were thereafter recorded for each sample.

2.6. Bovine serum albumin protein binding studies.

The BSA-binding properties of the Pcs were determined as described in the literature [**150,151**]. A stock solution of the BSA (60 μM) in water was prepared. Separately, stock solutions of the Pcs (100 μM) in water were prepared. For the studies, a mixture of the BSA (to a total of 30 μM) solution and Pcs solution (at the different test concentrations) were prepared. The excitation wavelength for the BSA used was 280 nm and the fluorescence emission spectra were recorded from 300 nm – 500 nm. The fluorescence spectrum of the BSA in the absence of the Pcs was recorded. The fluorescence spectra of the BSA in the presence of the Pcs were thereafter collected at increasing Pcs concentrations and compared to the spectra in the absence of Pcs. The maximum emission intensities for the samples were collected and used to determine the binding behaviour of the Pcs to the BSA protein using methods defined in the literature [**151,152**].

The binding constants and number of binding sites for the Pcs-complexes on the BSA proteins were calculated using equations 2.5 and 2.6.1-2.6.3.

$$\mathrm{Log}\left[\frac{(F_0-F)}{(F-F_\infty)}\right] = K_b + n\log[Pcs] \quad \text{..... equation 2.5}$$

Where F_0 is the fluorescence intensity of the BSA prior to exposure to the Pcs and the F are the fluorescence intensities of BSA when exposed to the Pcs at the varied test concentrations ([Pcs]). The F_∞ is the fluorescence intensity of BSA saturated with the Pcs. The K_b is the binding constant and n is the number of binding sites on the BSA molecules. The n is the slope, and the K_b is the intercept of the plots of $Log\ \frac{(F_0-F)}{(F-F_\infty)}$ against Log [*Pcs*].

The changes in BSA fluorescence intensity were related to the Pcs at the varied concentrations by the Stern-Volmer relationship (equation 2.6.1 and 2.6.2).

$$\frac{F_0}{F} = (1 + Ksv[Pcs]) \quad \text{..... equation 2.6.1}$$

The two mechanisms of drug interactions with the BSA proteins, shown by the quenching of the BSA protein fluorescence yields, include dynamic and static quenching. To account for the coexistence of the dynamic and static quenching, a modified Stern-Volmer equation was used equation 2.5.2.

$$\frac{F_0}{F} = (1 + K_{sv}[Pcs])\,(1 + K_a[Pcs]) \quad \text{..... equation 2.6.2}$$

The K_{SV} values are obtained from the plots of F_0/F versus [Pcs], which accounts for the dynamic quenching. The second term on the modified Stern-Volmer equation accounts for the static quenching, K_a values. The K_a values are obtained from the plots of $F_0/F(1+K_{SV}[Pcs])$ versus the [Pcs].

The the bimolecular quenching constant (k_q) values are calculated from the K_{SV} using equation 2.6.3.

$$K_{sv} = k_q\, \tau_{Fo} \quad \text{.....equation 2.6.3}$$

Where the K_{SV} is the Stern-Volmer quenching constant; the k_q is the bimolecular quenching constant; and the τ_{F0} is the fluorescence lifetime of BSA which is reported to be 10 ns [**151**].

RESULTS AND DISCUSSION

The following chapters report on results that have been published/ submitted to peer reviewed journals and are not referenced in this thesis.

The list of publications is provided.

List of Publications

1. **L.C. Nene**, A. Sindelo, J. Britton, T. Nyokong, “Effect of ultrasonic frequency and power on the sonodynamic therapy activity of cationic Zn(II) phthalocyanines”, *J. Inorg. Biochem.* 217, 111397, 2021.

2. **L.C. Nene**, and T. Nyokong, “Photo-Sonodynamic Combination Activity of Cationic Morpholino-Phthalocyanines Conjugated to Nitrogen and Nitrogen-Sulfur Doped Graphene Quantum Dots against MCF-7 Breast Cancer Cell Line In Vitro”, *Photodiagn. Photodyn.* 36, 102573, 2021.

3. **L.C. Nene**, K. Buthelezi, E. Prinsloo, T. Nyokong, “The In Vitro Photo-Sonodynamic Combinatorial Therapy Activity of Cationic and Zwitterionic Phthalocyanines on MCF-7 and HeLa Cancer Cell Lines,” *J. Photochem. Photobiol. A: Chem.* 432, 114116, 2022.

4. **L.C. Nene**, A. Magadla, T. Nyokong, “Enhanced Mitochondria Destruction on MCF-7 and HeLa Cell Lines In Vitro Using Triphenyl-phosphonium-Labelled Phthalocyanines in Ultrasound-Assisted Photodynamic Therapy Activity,” *J. Photochem. Photobiol. B. Biology*, 235, 112553, 2022.

5. **L.C. Nene**, T. Nyokong, “Enhancement of the In Vitro Anticancer Photo-Sonodynamic Combination Therapy Activity of Cationic Thiazole-Phthalocyanines Using Gold and Silver Nanoparticles,” *J. Photochem. and Photobiol. A: Chem.* 435, 114339, 2022.

6. **L.C. Nene**, and T. Nyokong, “Phthalocyanines and Graphene Quantum Dots Nano-Systems as Dual Anti-Cancer Sensitizers for Photo-Sonodynamic Combinatorial Therapy”. *Diam. Relat. Mater*. 131, 109549, 2023.

7. **L.C. Nene** and T. Nyokong, “The In-vitro Proliferation-Suppression of MCF-7 and He-La Cell Lines Mediated by Differently Substituted Ionic Phthalocyanines in Sonodynamic Therapy Supplemented-Photodynamic Therapy”, *J. Inorg. Biochem.* 239, 112084, 2023.

CHAPTER THREE

3. Structural Characterization

This chapter reports on the synthesis of the new peripherally substituted ionic Zn(II) Pc **6** – Pc **11**. The Pcs were structurally characterized using various techniques, including FT-IR, ^{1}H NMR spectroscopy, elemental analysis, and mass spectrometry. The structures of the Pcs used in this work are shown in **Fig. 3.1**.
The preparation of the conjugates of the Pc **8** and Pc **9** with the AuGSH, AgGSH, NGQDs and NSGQDs NPs, and the structural characterizations are also reported in this chapter. The structural characterization studies of the nanostructures were performed using the FT-IR spectroscopy, EDS, DLS and TEM imaging. The XPS studies were performed for the conjugates with AuGSH and AgGSH NPs. While the Raman spectroscopy studies were performed for the conjugates with the NGQDs and NSGQDs.

Furthermore, the studies of the electronic absorption properties of the Pcs and Pc-NPs conjugates in the organic and aqueous solvents using UV-vs spectroscopy are reported herein.

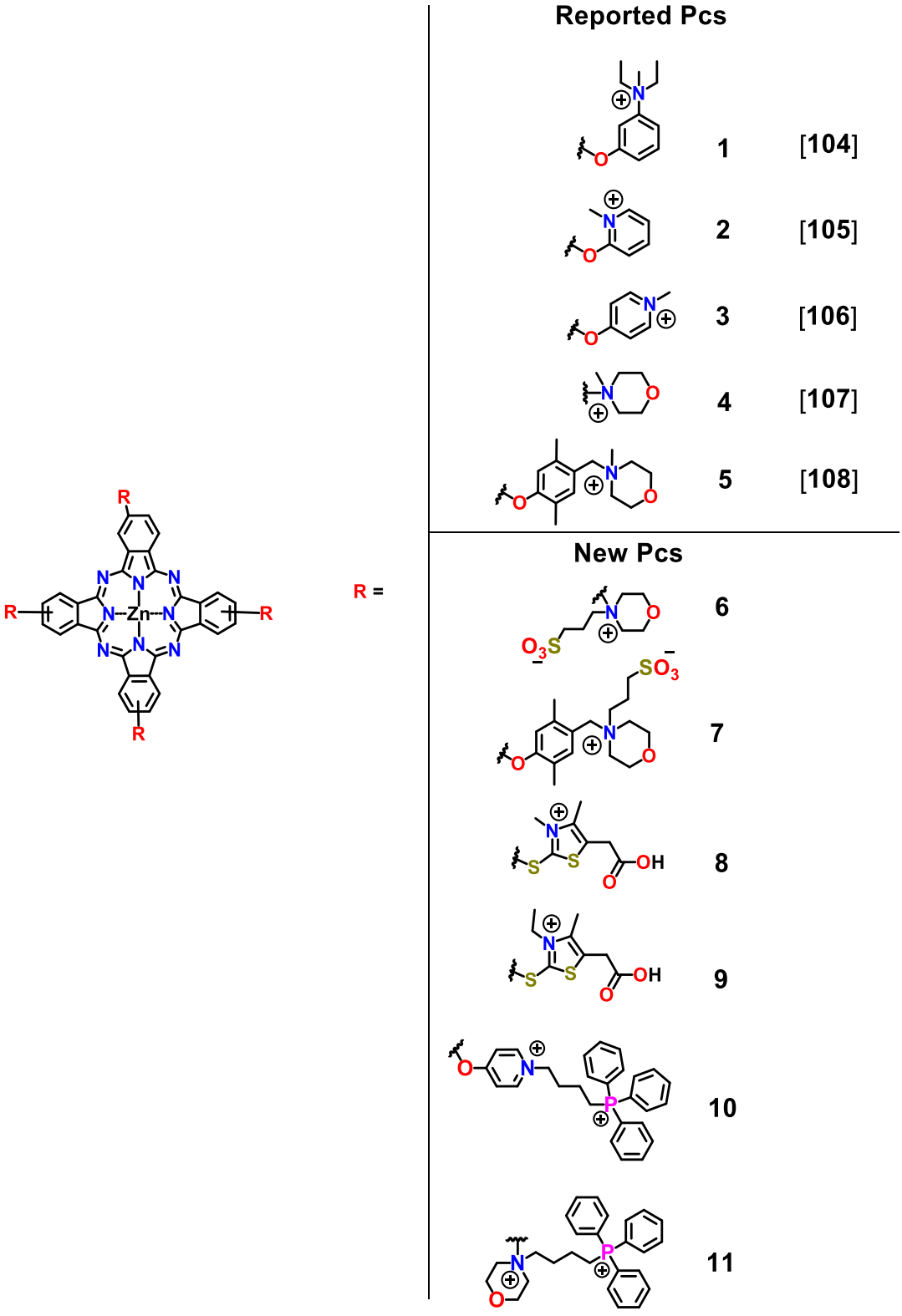

Figure 3.1. Structures of the ionic Pcs used in this work.

This chapter reports on the structural characterization of the new ionic Pc **6** – Pc **11**. The synthesis and characterization of Pc **1** – Pc **5** are reported [**104-108**].

3.1. Structural characterization of phthalocyanines.

3.1.1. 2,9,16,23-*tetrakis*-(*N*-propanesultone-morpholino) Zn(II) Pc **6** and 2,9,16,23-*tetrakis*-(2,5-dimethyl-4-(*N*-propanesultone-morpholinomethyl))-phenoxy Zn(II) Pc **7**.

The synthetic route for the preparation of the zwitterionic Pc **6** and Pc **7** is shown on the **Scheme 3.1**.

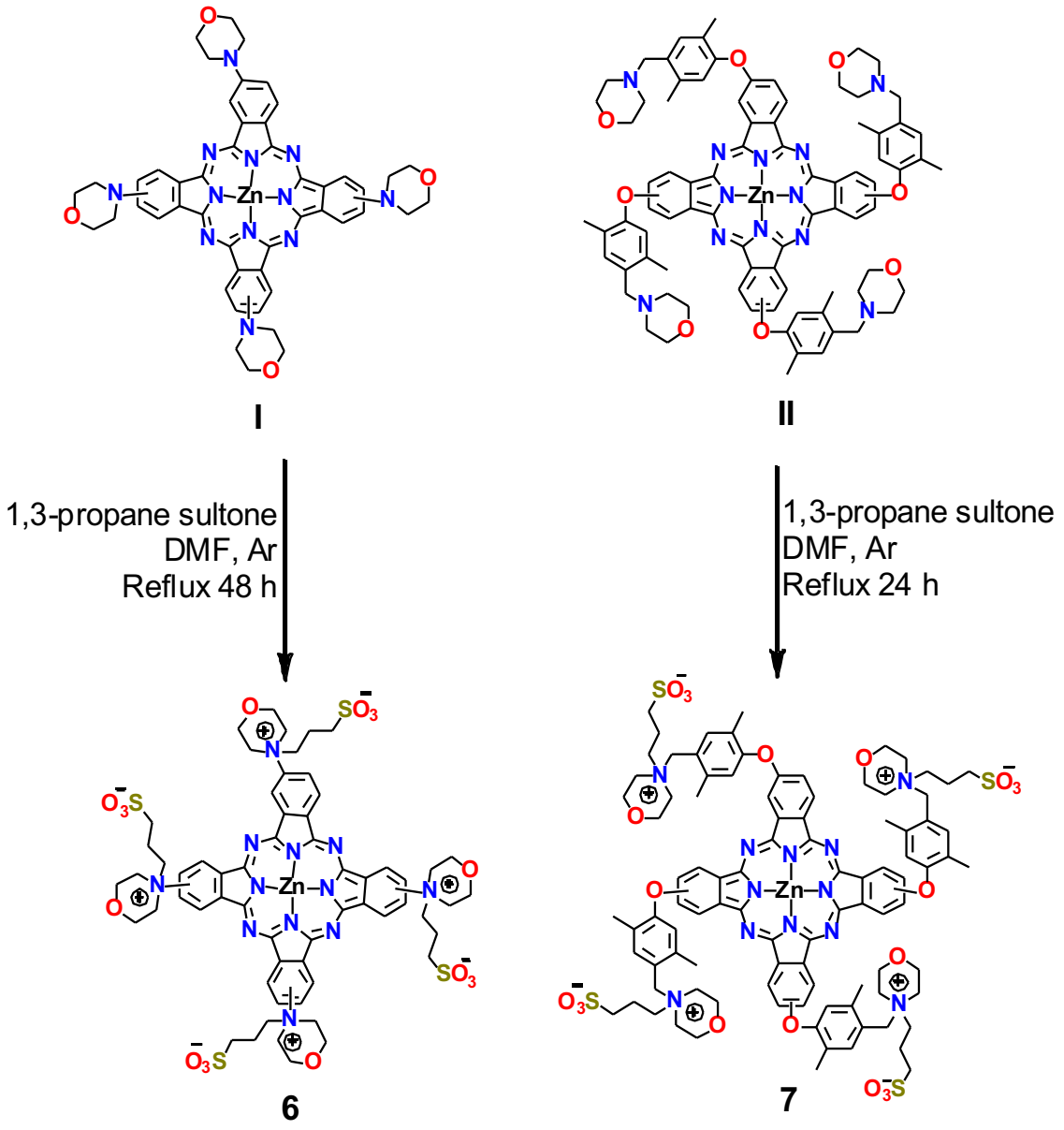

Scheme 3.1. Synthesis of the zwitterionic Pc **6** and Pc **7**.

The tertiary N-groups of the morpholine-moieties on the Pc **I** [**107**] and Pc **II** [**108**] were quaternized using propanesultone to form quaternary N-groups bearing cations, **Scheme 3.1**. The terminal sulphonium group bears anions, thus, yielding the zwitterionic Pc **6** and Pc **7**.

The FT-IR spectra for the Pc **6** and Pc **7** are shown in the **Fig. 3.2**.

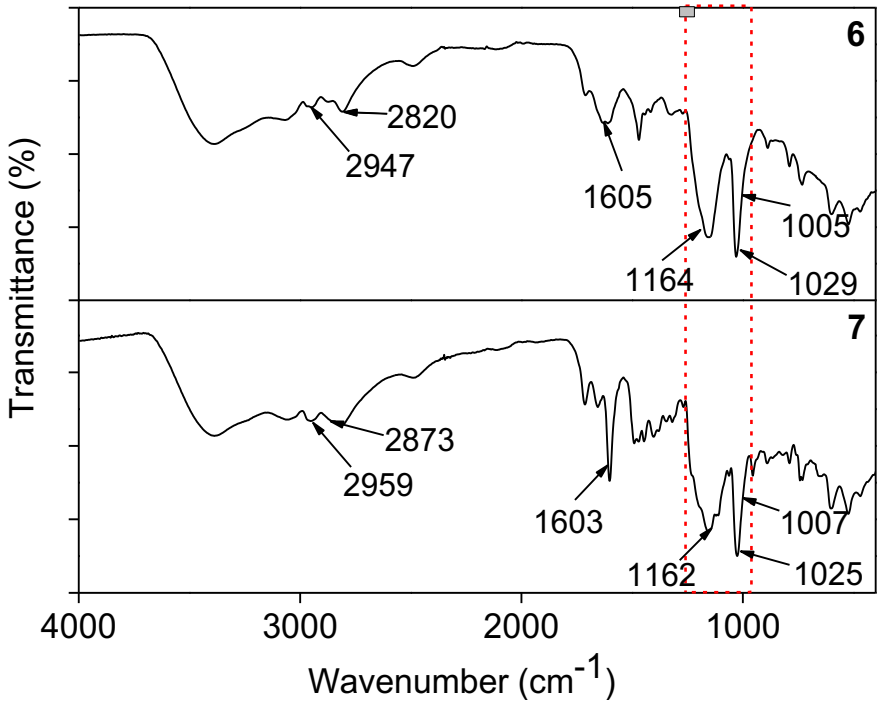

Figure 3.2. The FT-IR spectra of the Pc **6** and Pc **7**.

From the FT-IR spectra, **Fig 3.2**, peaks confirming the presence of the propanesultone (S=O) extension on the Pcs are seen at the wavenumbers 1164 cm^{-1} and 1162 cm^{-1}, for the Pc **6** and Pc **7,** respectively. The peaks for the CH_2 bonds were seen at 2820 cm^{-1} and 2873 cm^{-1}, for the Pc **6** and Pc **7,** respectively. The C-O-C peaks are seen at wavenumbers 1029 cm^{-1} and 1025 cm^{-1} and the Ar C-H peaks at wavenumbers 2947 cm^{-1} and 2959 cm^{-1}, where the Ar C=N peaks at 1005 cm^{-1} and 1007 cm^{-1}, for the Pc **6** and Pc **7**, respectively.

The ^{1}H NMR spectra for the Pc **6** and Pc **7** were obtained to confirm the structures of the synthesized Pcs. For the Pc **6**, 12 aromatic ^{1}H were confirmed for the Pc core; 56 aliphatic ^{1}H were confirmed for the CH_2-groups on the R-groups of the Pcs. For the Pc **7**, there were 20 aromatic ^{1}H confirmed. From which, 12 ^{1}H were from the Pc aromatic ring, and the remaining 8 ^{1}H are from the phenyl-ring extensions on the Pcs R-groups. An additional 88 aliphatic^{1}H were confirmed for the Pc **7** from the CH_3- and CH_2- chains on the R-groups. The total number of protons confirmed for the Pcs confirmed the quaternization of the morpholine moieties on the Pc structures with the 1,3-propanesultone. The ^{1}H NMR in DMSO-D_6 for the Pc **6** and Pc **7** are shown in the **Fig. S4**, in the *Supplementary Information*. The elemental analyses for the Pc **6** and Pc **7** gave the expected values.

The mass spectra for the Pcs were also obtained to determine the mass (*m/z*) of the zwitterionic Pcs. The expected mass for the Pc **6** was 1404.31 *m/z* and the experimental mass obtained was 1422.72 *m/z*. The obtained value is higher than the expected, the difference in the masses obtained from the expected may be accounted for by a water molecule. For the Pc **7**, the expected mass was 1940.59 *m/z*, and the experimental mass obtained was 1941.72 *m/z*. The higher value obtained for the mass of the Pc **7** is attributed to an H atom.

3.1.2. 2,9,16,23-*tetrakis*-(methyl-2-mercapto-4-methyl-5-thiazoleaceticacid) Zn(II) Pc **8** and 2,9,16,23-*tetrakis*-(ethyl-2-mercapto-4-methyl-5-thiazoleaceticacid) Zn(II) Pc **9.**

The synthetic route for the preparation of the cationic Pc **8** and Pc **9** is shown in the **Scheme 3.2**.

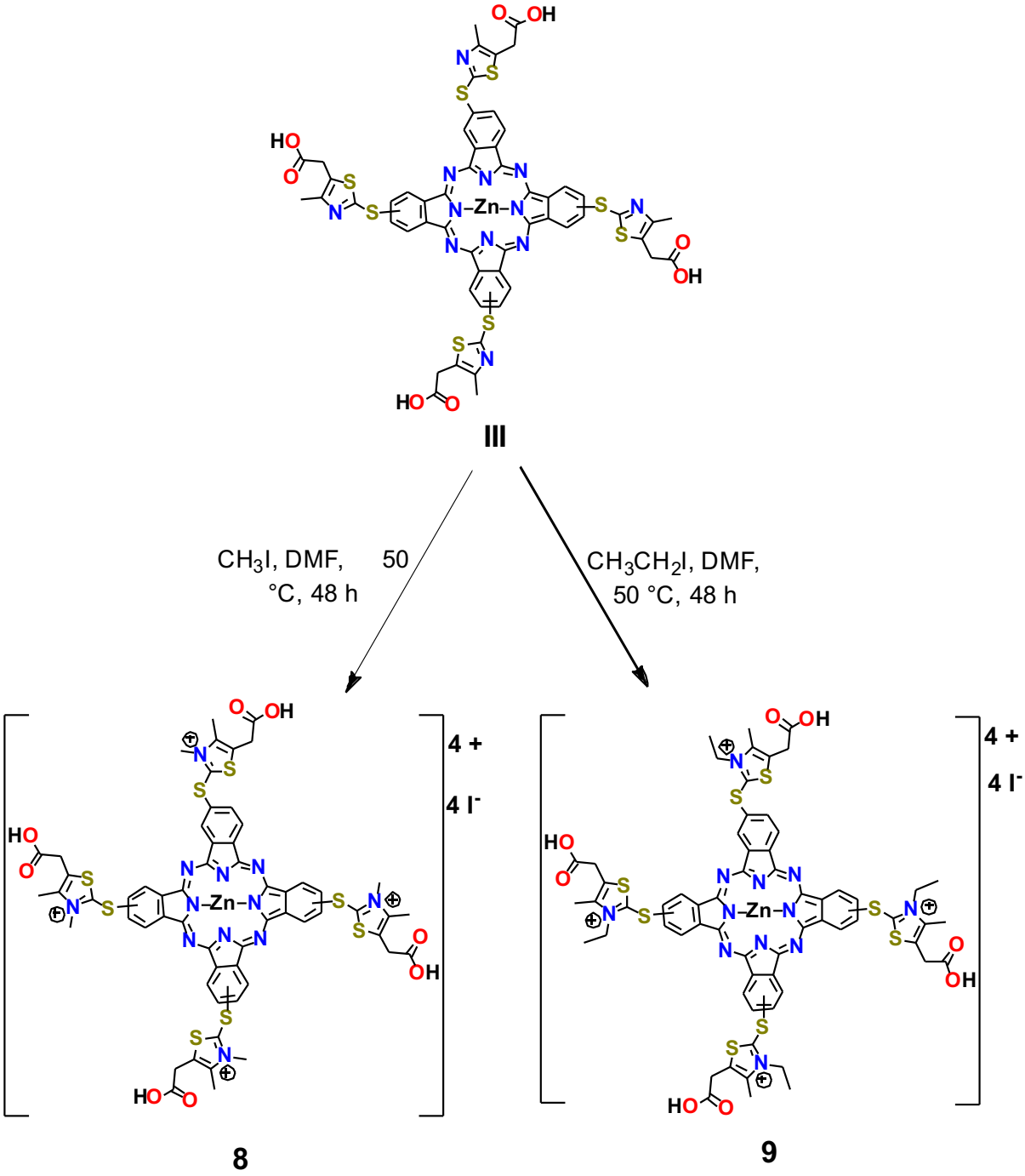

Scheme 3.2. Synthesis of the Pc **8** and Pc **9**.

The tertiary N-groups on the thiazole moiety of the Pc **III** [**137**] quaternized using methyl- and ethyl groups to yield the cationic **8** and **9**, **Scheme 3.2**.

The FT-IR spectra of Pc **8** and Pc **9** are shown in **Fig. 3.3.**

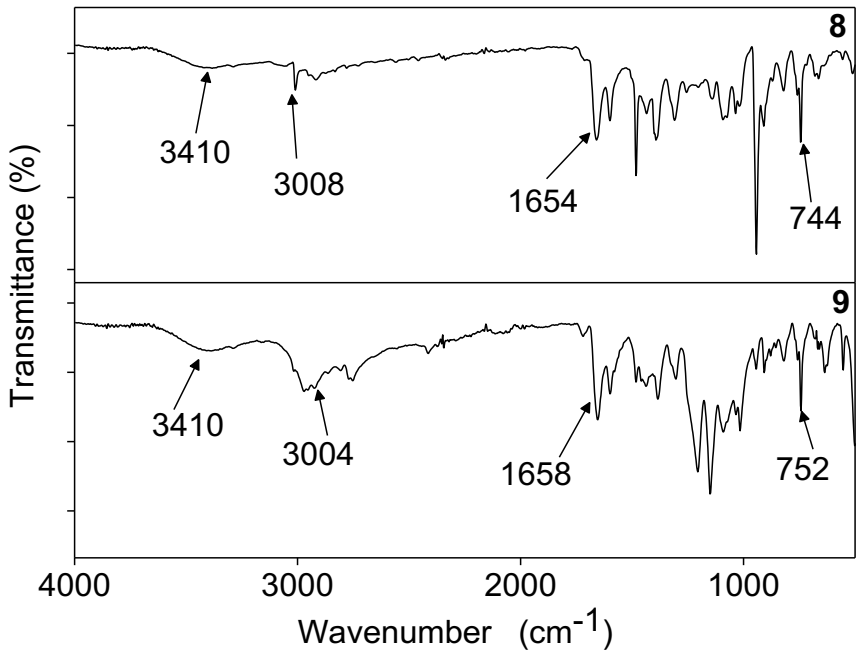

Figure 3.3. The FT-IR spectra of the Pc **8** and Pc **9**.

From the FT-IR spectra, **Fig 3.3**, shows peaks confirming the functional groups constituting the Pc **8** and Pc **9**. For the Pc **8**, the substituents' carbonyl groups O-H and C=O stretches were seen at 3410 cm^{-1} and 1654 cm^{-1} respectively. The C-H and C-S at 3008 cm^{-1} and 744 cm^{-1} respectively, the core C=C stretch is seen at 1654 cm^{-1}. For the Pc **9**, the FT-IR spectra was slightly different. Peaks were seen at 3410 cm^{-1} and 1658 cm^{-1} for the O-H and the C=O of the carbonyl groups. For the C-H and C-S groups, stretches were seen at 3004 cm^{-1} and 746 cm^{-1}, respectively. And the C=C stretches were seen at 1685 cm^{-1}.

The ^{1}H NMR spectra for the Pc **8** and Pc **9** were obtained to confirm the structures of the Pcs. The NMR spectrum of the Pc **8** confirms the presence of 12 aromatic ^{1}H from

the Pc core and 32 aliphatic ^{1}H from the CH_2 and CH_3 groups in the R-groups of the Pc. The NMR spectrum of the Pc **9** also showed the presence of 12 aromatic ^{1}H from the structure core and additional 40 aliphatic protons of the CH_2 and CH_3 groups in the R-groups. The total protons from the ^{1}H NMR spectra of the Pcs are as calculated theoretically and therefore confirm the structures of the Pcs. The protons of the OH-groups of the carboxylic acids on the R-groups could not be visualized. The ^{1}H NMR in DMSO-D_6 for the Pc **8** and Pc **9** are shown in the **Fig. S5**, in the *Supplementary Information*. The elemental analyses for the Pc **8** and Pc **9** gave the expected values.

The mass spectra for the for the Pc **8** and Pc **9** were obtained to determine the masses (*m/z*). For the Pc **8**, the expected mass was 347.020 $[M]^{4+}$ *m/z* and the experimentally obtained mass was 348.309 $[M+H]^{4+}$ *m/z*. For the Pc **9**, the expected mass was 357.530 $[M]^{4+}$ *m/z* and the experimentally obtained mass was 357.447 $[M]^{4+}$ *m/z*.

The Pc **8** and Pc **9** were selected for the study of NPs on the SPDT activities of Pcs. The -COOH groups on the R-groups of the Pcs were used for the formation of the covalent amide bonds for the synthesis of the Pcs to the NPs, bearing -NH_2 groups.

3.1.3. 2,9,16,23-*tetrakis*-(*N*-(*N*-butyl-4-triphenyl-phosphonium)-pyridine-4-yloxy) Zn(II) Pc **10** and 2,9,16,23-*tetrakis*-(*N*-(*N*-butyl-4-triphenyl-phosphonium)-morpholino) Zn(II) Pc **11.**

The synthetic route for the preparation of the cationic TPP-labelled Pc **10** and Pc **11** is shown in **Scheme 3.3**.

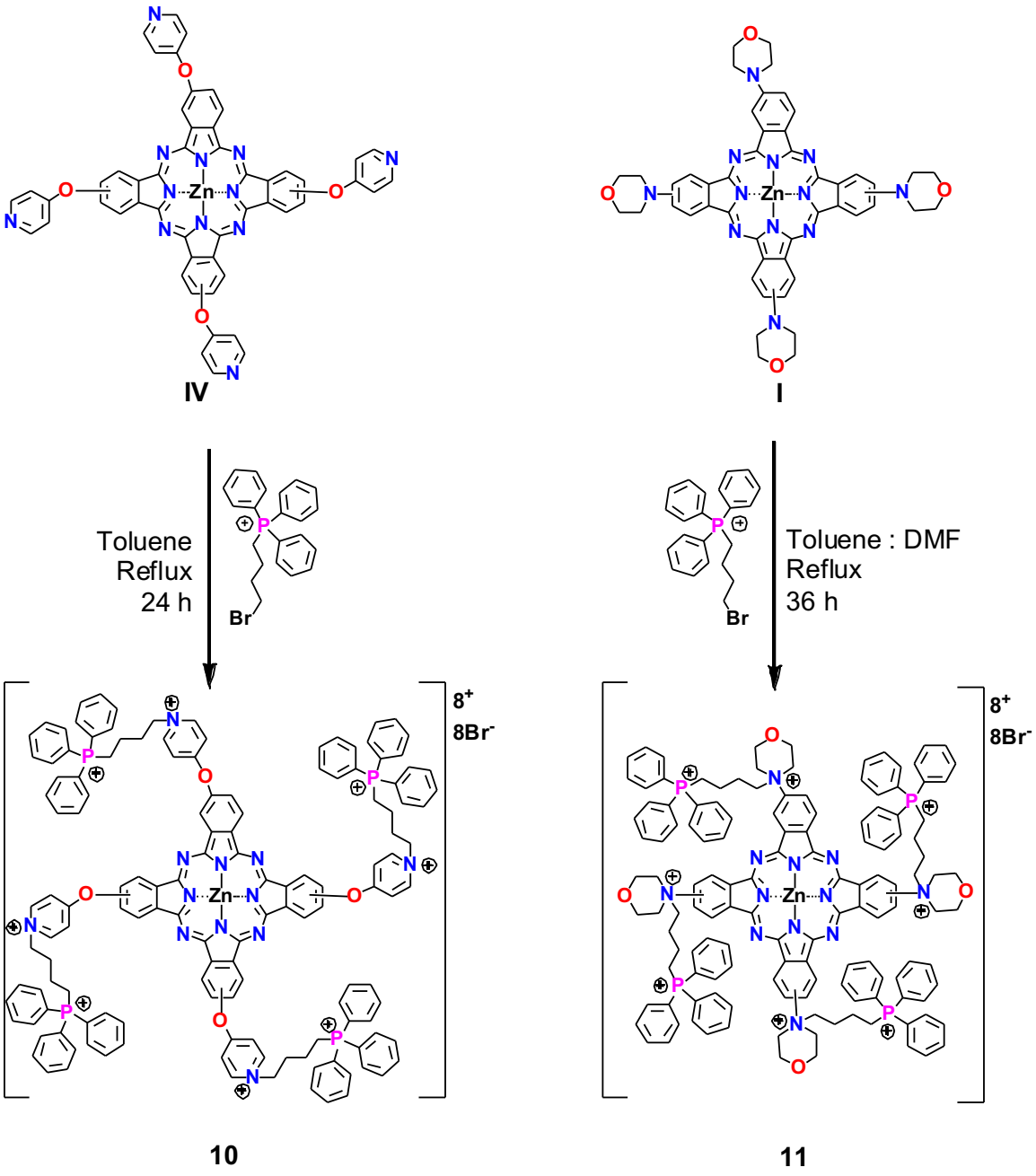

Scheme 3.3. Synthesis of the Pc **10** and Pc **11**.

The tertiary N on the pyridine (Pc **IV** [**106**]) and morpholine (Pc **I** [**107**]) moieties were quaternized using the butyl-TPP groups to yield the cationic Pc **10** and Pc **11**, **Scheme 3.3**.

The FT-IR spectra of Pc **10** and Pc **11** are shown in **Fig. 3.4.**

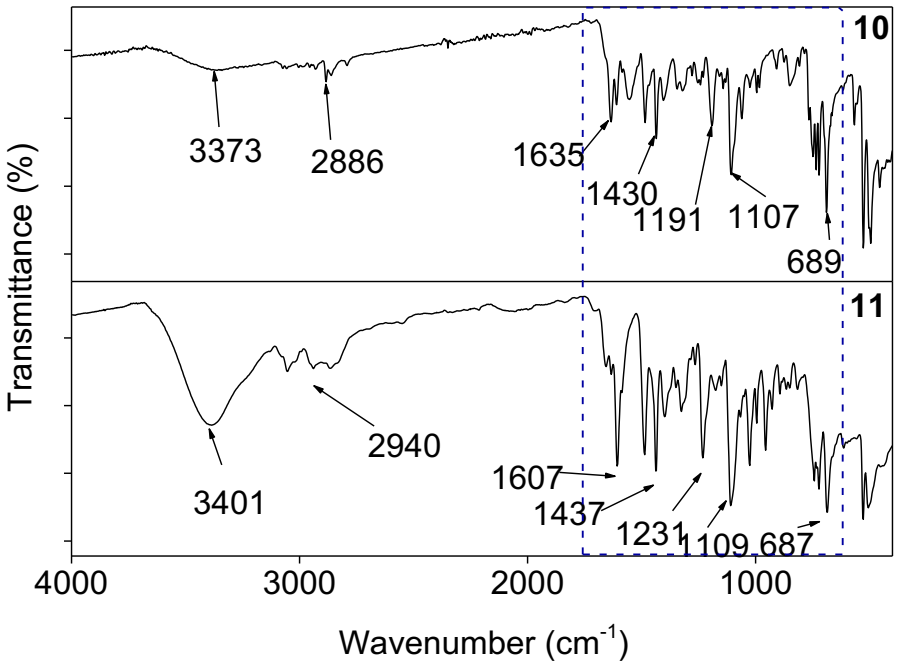

Figure 3.4. The FT-IR spectra of the Pc **10** and Pc **11**.

From the FT-IR spectra, **Fig. 3.4**, peaks confirming the incorporation of the TPP moiety on the Pcs to yield the Pc **10** and Pc **11** were obtained. The FT-IR spectrum for Pc **10** shows peaks at wavenumbers 3373 cm^{-1} for the aromatic C-H stretch, at 2886 cm^{-1} for the aliphatic C-H bonds, at 1635 cm^{-1} for the C=C stretch, at 1191 cm^{-1} for the C-O-C bonds, and the C-P stretches are seen at wavenumbers 1430 cm^{-1}, 1107 cm^{-1} and 689 cm^{-1}. The FT-IR spectrum for the Pc **11** shows peaks at wavenumbers 3401 cm^{-1} for the aromatic C-H stretch, at 2940 cm^{-1} for the aliphatic C-H bonds, at 1607 cm^{-1} for the C=C stretch and at 1231 cm^{-1} for the C-O-C bonds, and the C-P stretches

are seen at 1437 cm^{-1}, 1109 cm^{-1} and 687 cm^{-1}. The FT-IR spectra peaks for the Pc **10** and Pc **11** represented bonds for the functional groups in the Pcs.

The NMR spectra for the for the Pc **10** and Pc **11** were also obtained to further confirm the structures. For the Pc **10**, there were 88 aromatic ^1H were obtained, where 12 are ^1H of the aromatic Pc core and 76 are from the TPP groups. The 32 aliphatic ^1H were also confirmed for the aliphatic CH_2-groups butyl-chain in the R-group for the Pc **10**. From the NMR spectrum of the Pc **11**, there were 72 aromatic ^1H confirmed, where 12 are atttributed to the Pc core ring and the 60 are from the TPP groups. Additional 64 were for the aliphatic CH_2-groups on the morpholine ring and butyl-chain of the R-groups in the Pc **11**. The total number of ^1H obtained from the NMR spectra confirmed the TPP-labelling of the Pcs to yield the Pc **10** and Pc **11**. The ^1H NMR in DMSO-D_6 for the Pc **10** and Pc **11** are shown in the **Fig. S6**, in the *Supplementary Information*.

The elemental analyses of the Pc **10** and Pc **11** gave the expected values.

The mass spectra for the for the Pc **10** and **11** were obtained to determine the masses (*m/z*). For the Pc **10**, the expected mass was 507.37 $[M]^{4+}$ *m/z* and the experimentally obtained mass was 506.799 $[M]^{4+}$ *m/z*. For the Pc **11**, the expected mass was 502.14 $[M]^{4+}$ *m/z* and the experimentally obtained mass was 503.126 $[M+H]^{4+}$ *m/z*.

3.2. Structural characterization of nanoparticles and conjugates.

3.2.1. Characterization of the Pc **8** and Pc **9** conjugates with NGQDs and NSGQDs.

The synthetic route for the preparation of the Pcs conjugates with the NGQDs and NSGQDs is shown in the **Scheme 3.4**.

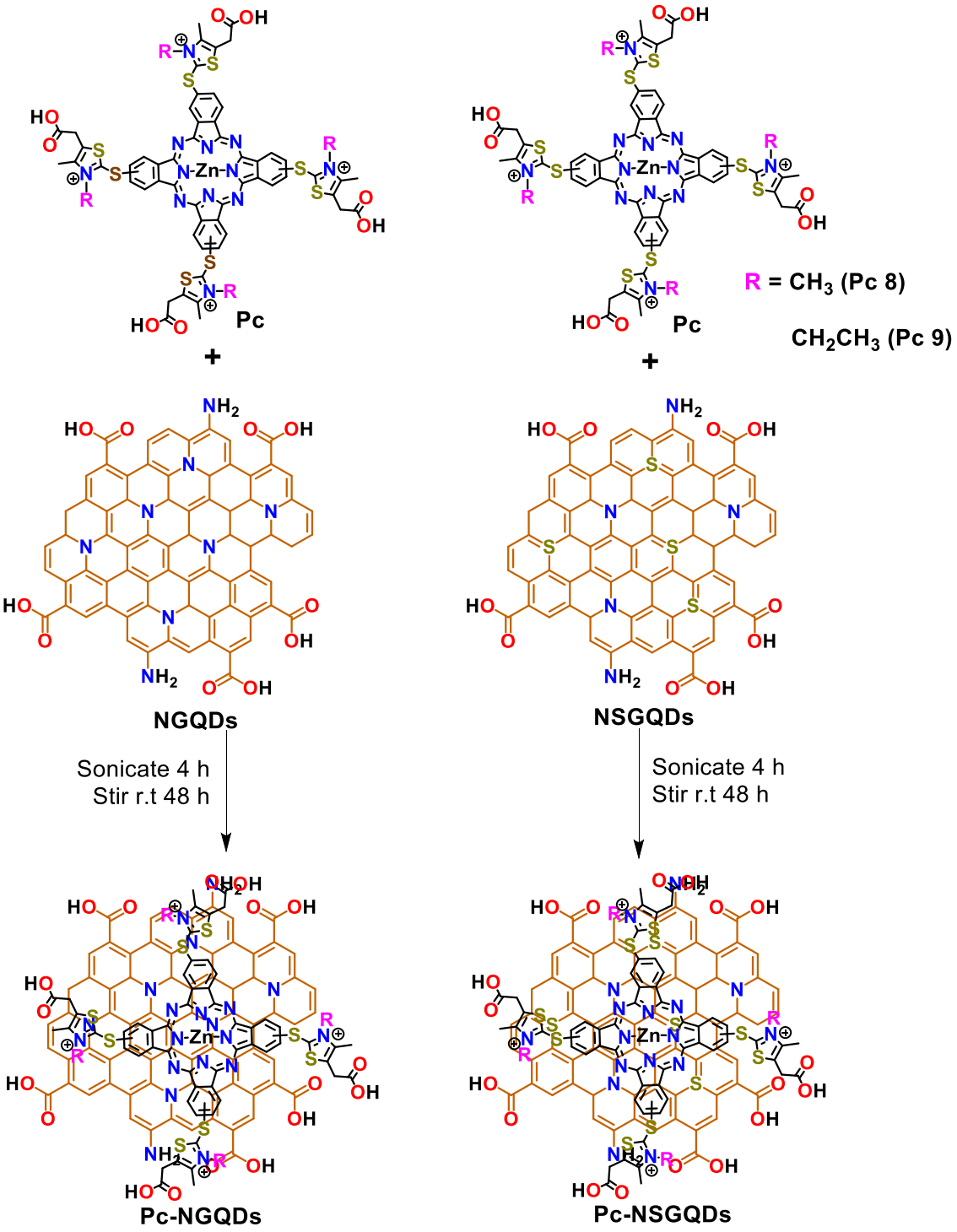

Scheme 3.4. Preparation of Pc **8** and Pc **9** conjugates with the NGQDs and NSGQDs.

The Pc-GQDs conjugates were prepared through the formation of π-π bonds between the Pcs and the GQDs, **Scheme 3.4**.

3.2.1.1. Fourier transform infrared and Raman spectroscopy.

The FT-IR spectra of the Pc **9**, the NGQDs, NSGQDs and the Pc **9** conjugates are shown in the **Fig. 3.5** as an example.

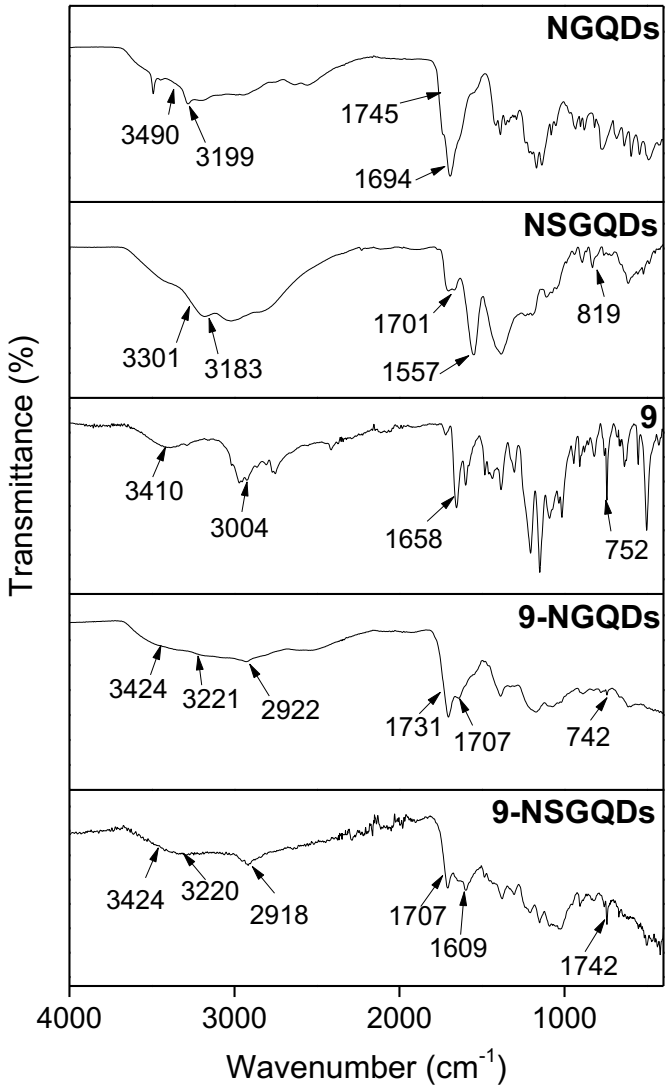

Figure 3.5. The FT-IR spectra of the Pc **8** and Pc **9**, and the NGQDs conjugates.

The FT-IR spectra show -OH stretches at 3490 cm^{-1} and 3301 cm^{-1}, the C=O stretches at 1745 cm^{-1} and 1701 cm^{-1}, and the N-H at 1694 cm^{-1} and 1557 cm^{-1} for the NGQDs and NSGQDs, respectively, **Fig. 3.5**. For the NGQDs, the C-N groups stretches are seen at 3199 cm^{-1} as a result of doping. For the NSGQDs, the stretches for the C-N and C-S groups are seen at 3183 cm^{-1} and 752 cm^{-1}, respectively as a result of co-

doping. Shifts in the FT-IR peaks for the conjugates were seen compared to those obtained for the Pc **9** and GQDs alone. A combination of the stretches for the functional groups in the Pc and the GQDs are observed in the spectra of the conjugates, **Fig. 3.5**.

The Raman spectra for the GQDs and the Pc-GQDs conjugates were also determined and are shown in the **Fig. 3.6**.

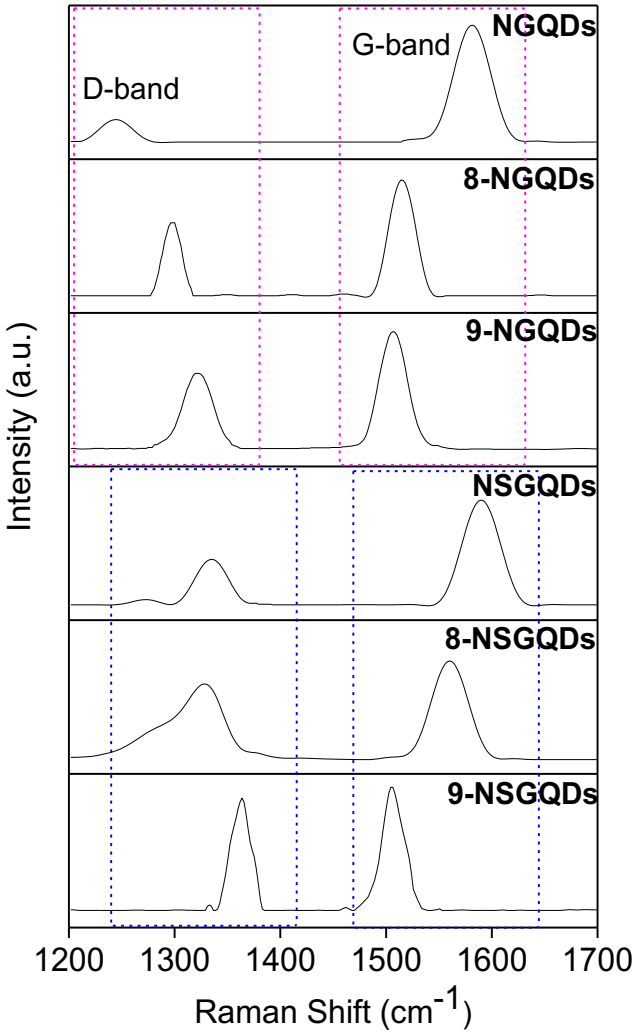

Figure 3.6. The Raman spectra of the GQDs and Pc-GQDs conjugates.

The GQDs surfaces comprise predominantly of sp^2-hybridized C-C bonds making the surfaces of the GQDs relatively flat. The characteristic Raman spectra for the GQDs

show an intense G-band, and a relatively smaller D-band for both the GQDs, **Fig. 3.6**. The G-bands represent the sp^2-hybridized carbons, where the D-bands represent the sp^3-hybridized carbons on the surfaces of the complexes. The ratio of the D to G bands (I_D:I_G) were calculated and are shown in **Table 3.1**. The I_D:I_G values are used to assess the quality of the GQDs surfaces, where lower I_D:I_G values indicate less defects on the surface, and an increase in the I_D:I_G values represent surface roughness due to the presence of out-of-plane sp^3-hybridized groups. The I_D:I_G values for the NGQDs and the NSGQDs were smaller compared to the conjugates. The conjugation of the Pcs to the GQDs enhances the intensities of the D-band, **Fig. 3.6**. This observation is due to the introduction of the sp^3-hybridized groups from the Pcs such as the bulkier carboxylic and thiazole groups on to the sp^2 carbon sheets [**153**]. The changes in the D- and G-bands for Pc-GQDs conjugates have been reported in the literature before [**154**]. The Pc **9** conjugates showed higher I_D:I_G values. This observation may be attributed to the bulkier ethyl-extension compared to the methylated Pc **8**. Overall the NSGQDs showed higher D-band intensities and therefore higher I_D:I_G values for the GQDs alone and in the conjugates compared to the NGQDs, **Table 3.1**. The combination of N- and S- groups in the NSGQDs may cause the reduction of smoothness on the sp^2 carbon sheets. Furthermore, the Raman shifting of the D- and G-bands in the Pc-GQDs conjugates represent multi-layered nanostructures [**155**].

3.2.1.2. Energy dispersive X-ray spectroscopy.

The elemental analysis for the Pcs and GQDs were performed using the EDX spectroscopy. The EDX spectra for the Pc **8**, the NGQDs, NSGQDs and the respective conjugates are shown in the **Fig. 3.7** as examples.

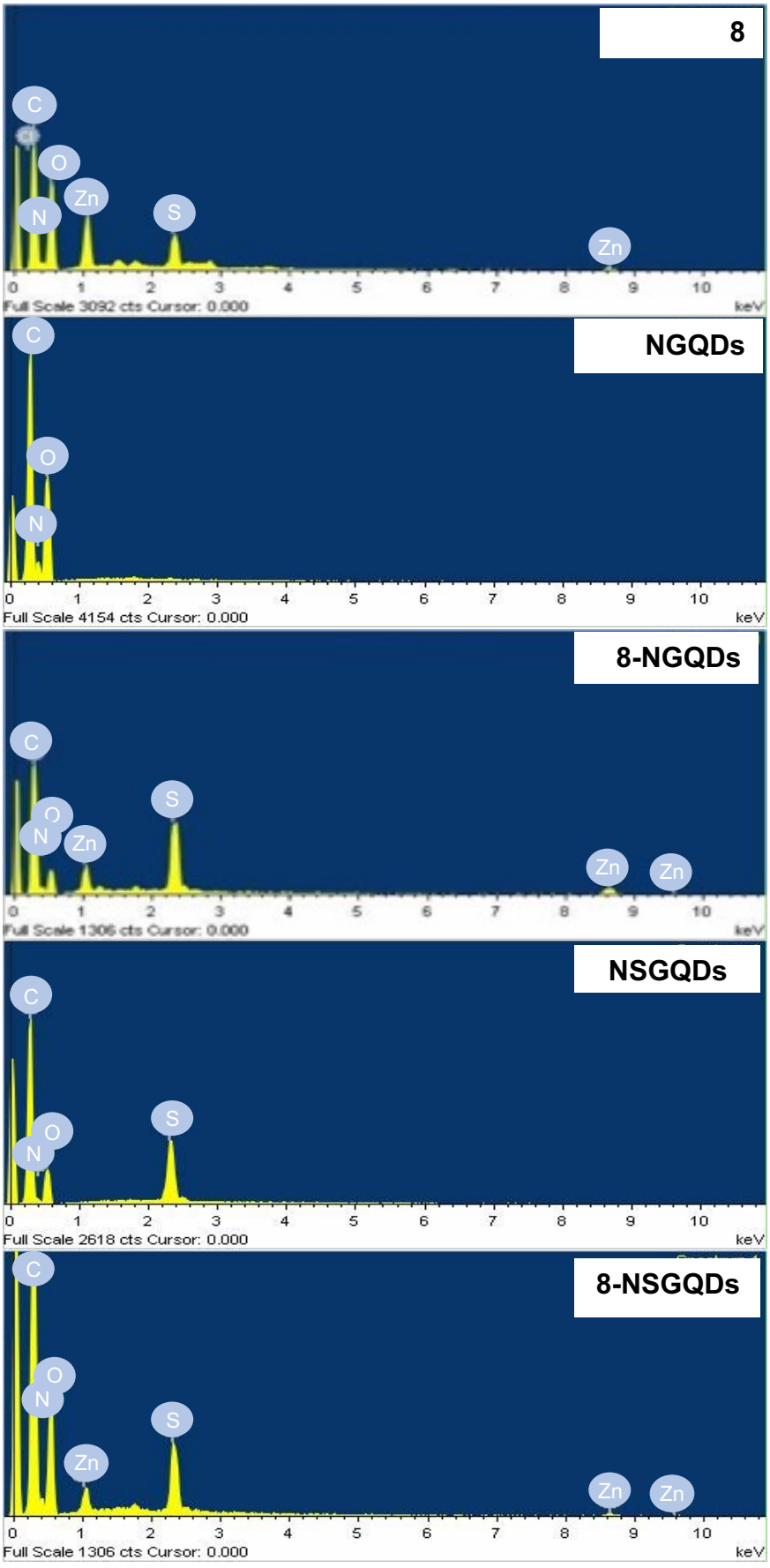

Figure 3.7. The EDX spectra of **8**, NGQDs, **8**-NGQDs, NSGQDs and **8**-NSGQDs.

The elements on the Pc are seen at 0.3 keV, 0.4 keV, 0.5 keV and 2.2 keV for the C, N, O, and S atoms, respectively for the Pc **8**, **Fig. 3.7**. The peaks for the Zn atoms on the Pc **8** are seen at 1.0 keV, 8.6 keV. For the NGQDs, the C, N, O are also seen at 0.3 keV, 0.4 keV, 0.5 keV. The conjugates showed peaks of the atoms observed for the Pc **8**, NGQDs and NSGQDs, including the C, N, O, S and Zn atoms.

3.2.1.3. Transmission electron microscopy.

The morphology of the NPs and conjugates were determined using TEM. The TEM images of the NGQDs, **8**-NGQDs and **9**-NGQDs are shown in **Fig. 3.8**, as examples.

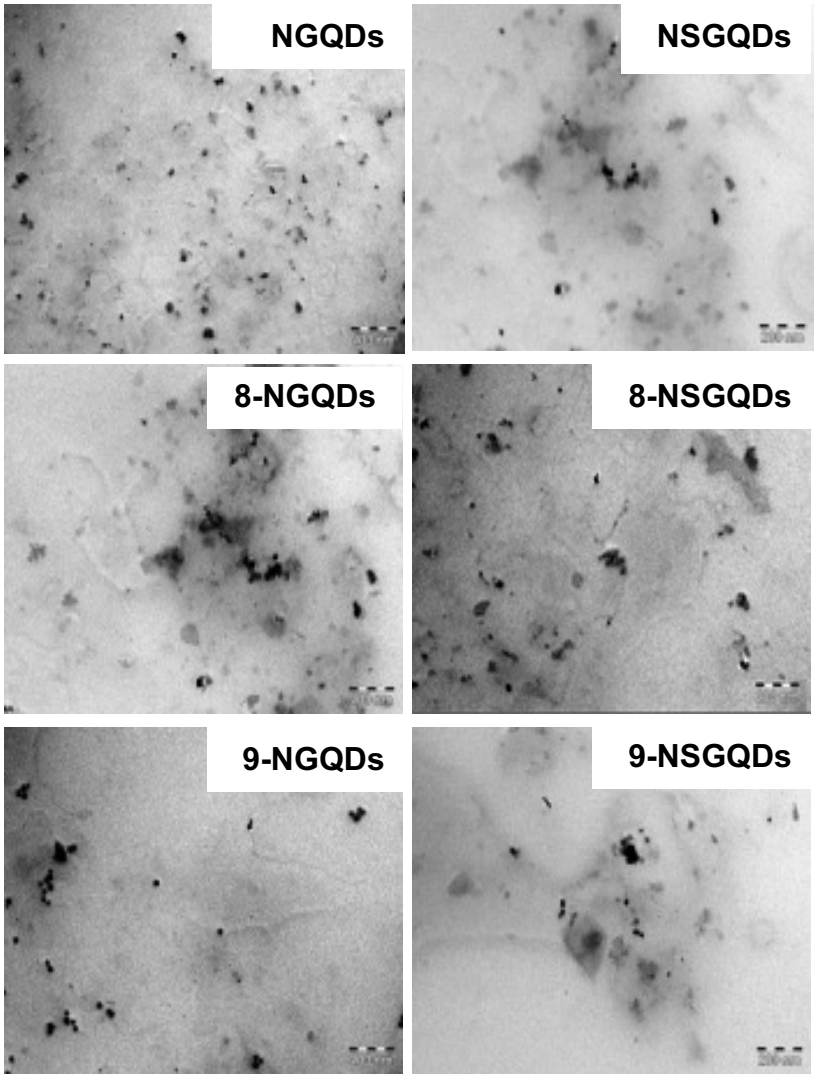

Figure 3.8. The TEM images of the NGQDs, NSGQDs and conjugates.

The GQDs appear as dots and are relatively more dispersed compared to the conjugates, **Fig. 3.8**. Upon conjugation, the dot-morphology is maintained. The size estimations for the NGQDs, NSGQDs and their conjugates with the Pc **8** and Pc **9** were determined and are summarizes in **Table 3.1**. The TEM sizes for the GQDs alone were ~8.0 nm and ~6.5 nm for NGQDs and NSGQs, respectively. Upon conjugation, the sizes increased compared to the non-conjugated GQDs. For the Pc **8** conjugates, the sizes were found to be 15.8 nm and 15.0 nm for **8**-NGQDs and **8**-NSGQDs, respectively. For the Pc **9** conjugates the sizes were 15.2 nm and 13.9 nm for the **9**-NGQDs and **9**-NSGQDs respectively, **Table 3.1**. Increase in the sizes is due to the agglomeration of the Pc-NPs systems.

3.2.1.4. Dynamic light scattering.

The size estimations for the GQDs and conjugates were also determined using DLS spectroscopy as shown in the **Fig. 3.9**.

From the DLS plots, the size estimations of the conjugates were generally larger than those of the NPs alone, **Fig. 3.9**. The size estimations for the NPs and conjugates are summarized in **Table 3.1.** The DLS size estimations for the **8**-NGQDs and **8**-NSGQDs were ~19.0 nm and ~18.6 nm, respectively, and for **9**-NGQDs and **9**-NSGQDs sizes were estimated at ~18.1 nm and ~17.3 nm, respectively. The DLS size estimations for the NGQDs and NSGQDs are 8.5 nm and 7.5 nm, respectively. The values obtained from DLS were relatively larger compared to those obtained from TEM, **Table 3.1**.

The DLS technique generally leans towards larger particles and dispersant interference in DLS results in differences in particle sizes when compared to TEM [**156**].

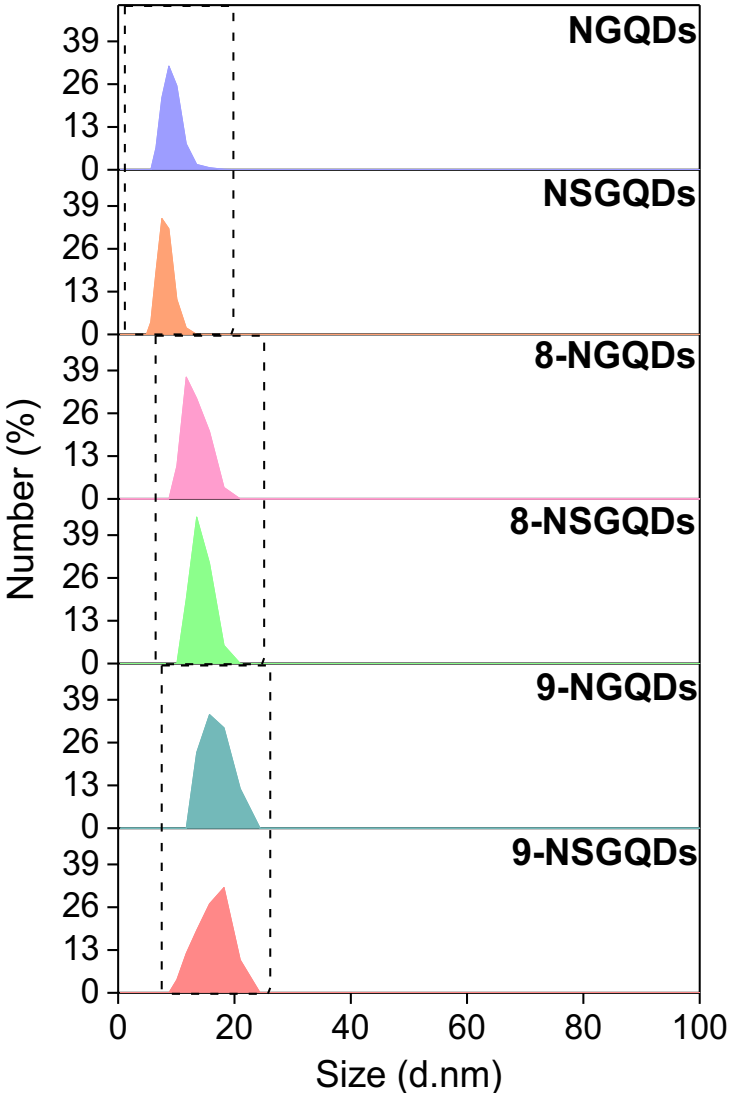

Figure 3.9. the DLS plots for the GQDs and Pc-GQDs conjugates in water.

The loading concentrations of the Pcs on the NPs were determined using the UV-vis spectra method as reported in the literature before [**157**]. The loading values for the Pcs on the GQDs are summarized in the **Table 3.1**.

The loading on the NGQDs were found to be 1.11 $mmol_{Pc}$/ mg_{conj} and 1.06 $mmol_{Pc}$/ mg_{conj} for the Pc **8** and Pc **9**, respectively. And the loading on the NSGQDs was 1.04 $mmol_{Pc}$/ mg_{conj} and 0.97 $mmol_{Pc}$/ mg_{conj} for the Pc **8** and Pc **9**, respectively. Overall, the loading values obtained for thr Pcs were higher for the NGQDs compared to the

NSGQDs, **Table 3.1**. This observation corresponds with the high size estimated from the TEM and DLS results.

Table 3.1. Summary of average sizes of NPs and conjugates.

	TEM (nm)	DLS (nm)	Loading ($mmol_{Pc}$/ mg_{conj})	Raman (I_D/I_G)
NGQDs	8.0	8.5	-	0.19
NSGQDs	6.5	7.5	-	0.43
8-NGQDs	15.8	19.0	1.11	0.63
8-NSGQDs	15.0	18.6	1.04	0.76
9-NGQDs	15.2	18.1	1.06	0.65
9-NSGQDs	13.9	17.3	0.97	0.91
AuGSH	7.5	9.0	-	-
AgGSH	6.9	7.7	-	-
8-AuGSH	13.5	18.2	1.45	-
8-AgGSH	11.0	15.7	1.25	-
9-AuGSH	10.0	14.2	1.26	-
9-AgGSH	10.0	12.4	1.01	-

3.2.2. Characterization of the Pc **8** and Pc **9** conjugates with AuGSH and AgGSH.

The synthetic route for the preparation of the AuGSH and AgGSH Pc-conjugates is shown in **Scheme 3.5**.

The covalent amide linkages were formed between the carboxyl terminals of the Pcs and the amine terminals of the GSH groups on the AuGSH and AgGSH, **Scheme 3.5**.

Furthermore, since the Pcs bear S-groups on the peripheral R-groups, the S-metal bonds with NPs may also form, **Scheme 3.5**.

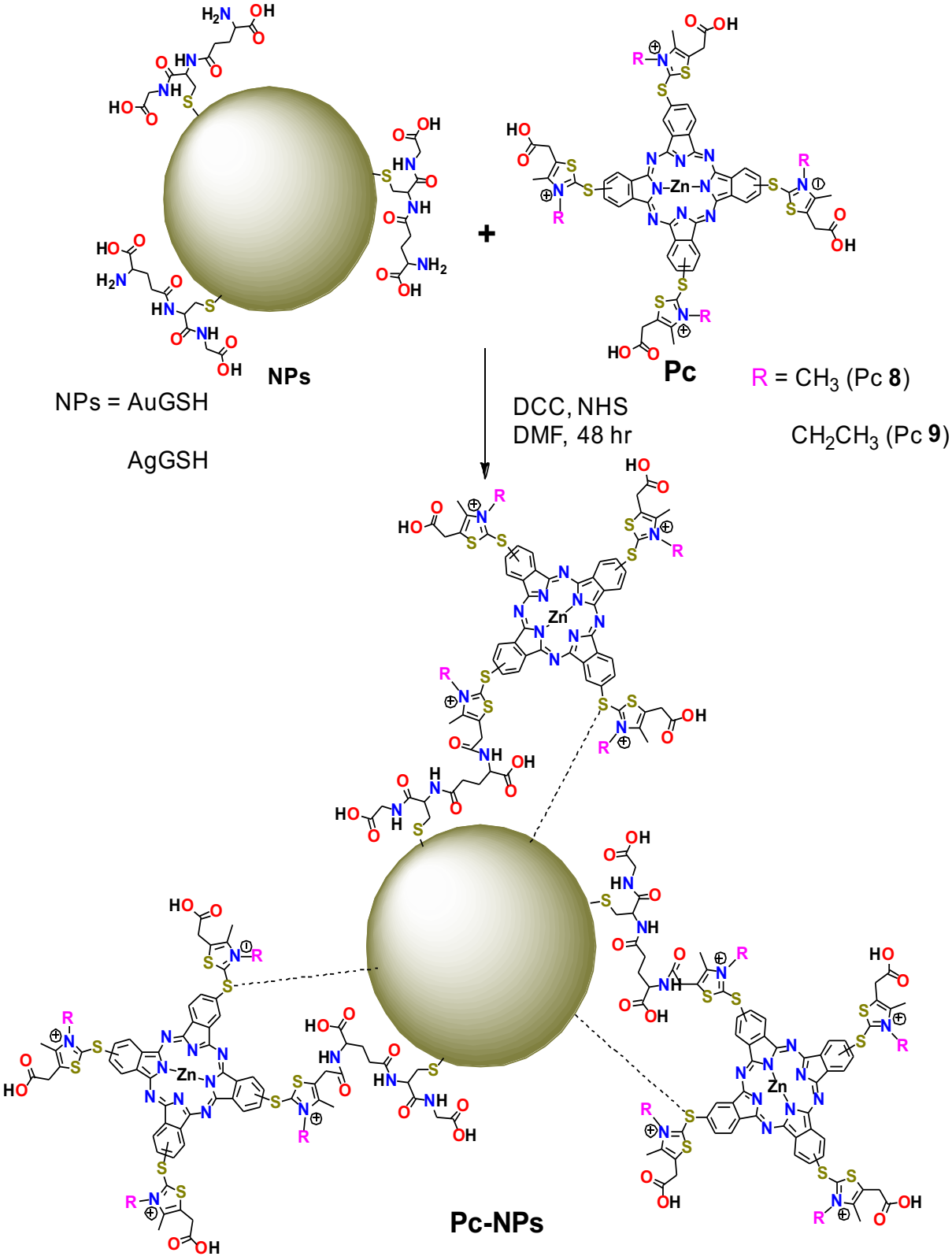

Scheme 3.5. Preparation of the Pc **8** and Pc **9** AuGSH and AgGSH conjugates.

The conjugation of the Pc **8** and Pc **9** to the AuGSH and the AgGSH NPs and the structural characterization were confirmed using various analytical techniques.

3.2.2.1. Fourier transform infrared spectroscopy.

The FT-IR spectra of the Pc **8**, AuGSH, AgGSH and conjugates were obtained and are shown in the **Fig. 3.10** as examples.

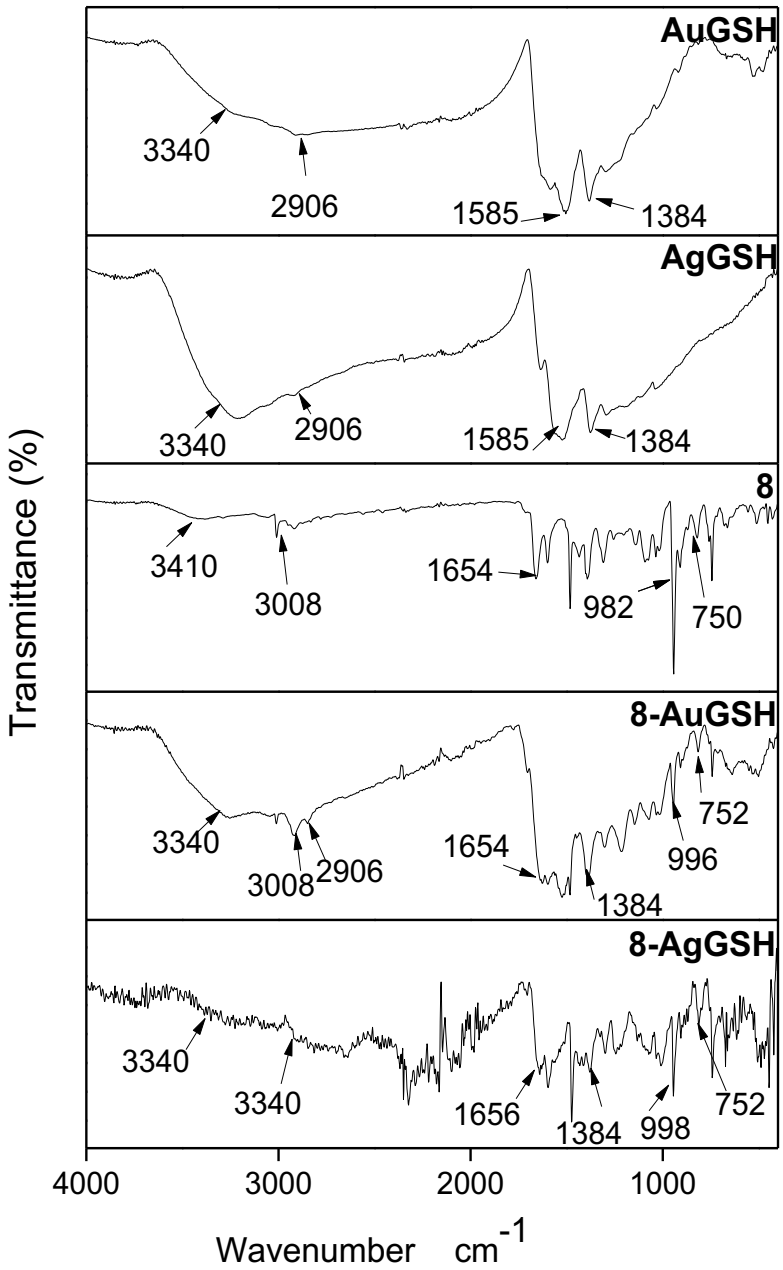

Figure 3.10. The FT-IR spectra of the Pc **8**, and the AuGSH and AgGSH conjugates.

The Pcs were linked to the NPs *via* covalent bonds through the formation of amide bonds. For the AuGSH and AgGSH NPs, the functional groups of the GSH showed peaks for the amide N-H, C-H and C=O at 3340 cm^{-1}, 2906 cm^{-1}, 1585 cm^{-1}, respectively, and the -NH_2 stretches at 1384 cm^{-1}, **Fig. 3.10**. For the conjugates, a combination of the stretches for the functional groups seen for the Pcs and NPs was observed.

3.2.2.2. Energy dispersive X-ray spectroscopy.

The EDX spectra were obtained to confirm the elemental composition of the Pcs, NPs and the Pc-NPs conjugates. The EDX spectra for the Pc **9** and the respective NPs conjugates are shown in the **Fig. 3.11**, as examples.

From the EDX spectrum of the Pc **9**, the C, N, and O atoms show peaks between 0.2 keV – 0.5 keV; where S shows peaks at 2.4 and Zn at 1, 8.8 keV and 9.8 keV, **Fig. 3.11**. The C, N, O, S atoms are also seen in the NPs and conjugates at similar energies. For the AuNPs, the Au atoms are seen at 2.2 keV and 8.6 keV – 13.8 keV on the EDX spectrum of the AuGSH; and the peaks for the Ag atoms are seen at 3.2 keV on the EDX spectrum of the AgGSH. On the spectra of the Pc-NPs conjugates, the peaks of the C, N, O, S atoms are also present, occurring at similar keV values as in the non-conjugated Pcs and NPs. The Au and Ag peaks also occur at similar keV values as in conjugates as in the pristine NPSs. Since the NPs and the Pcs both have the C, N, O, S atoms, the presence of both the Zn atoms and Au and Ag in the conjugates were used to further confirm the presence of Pcs and NPs.

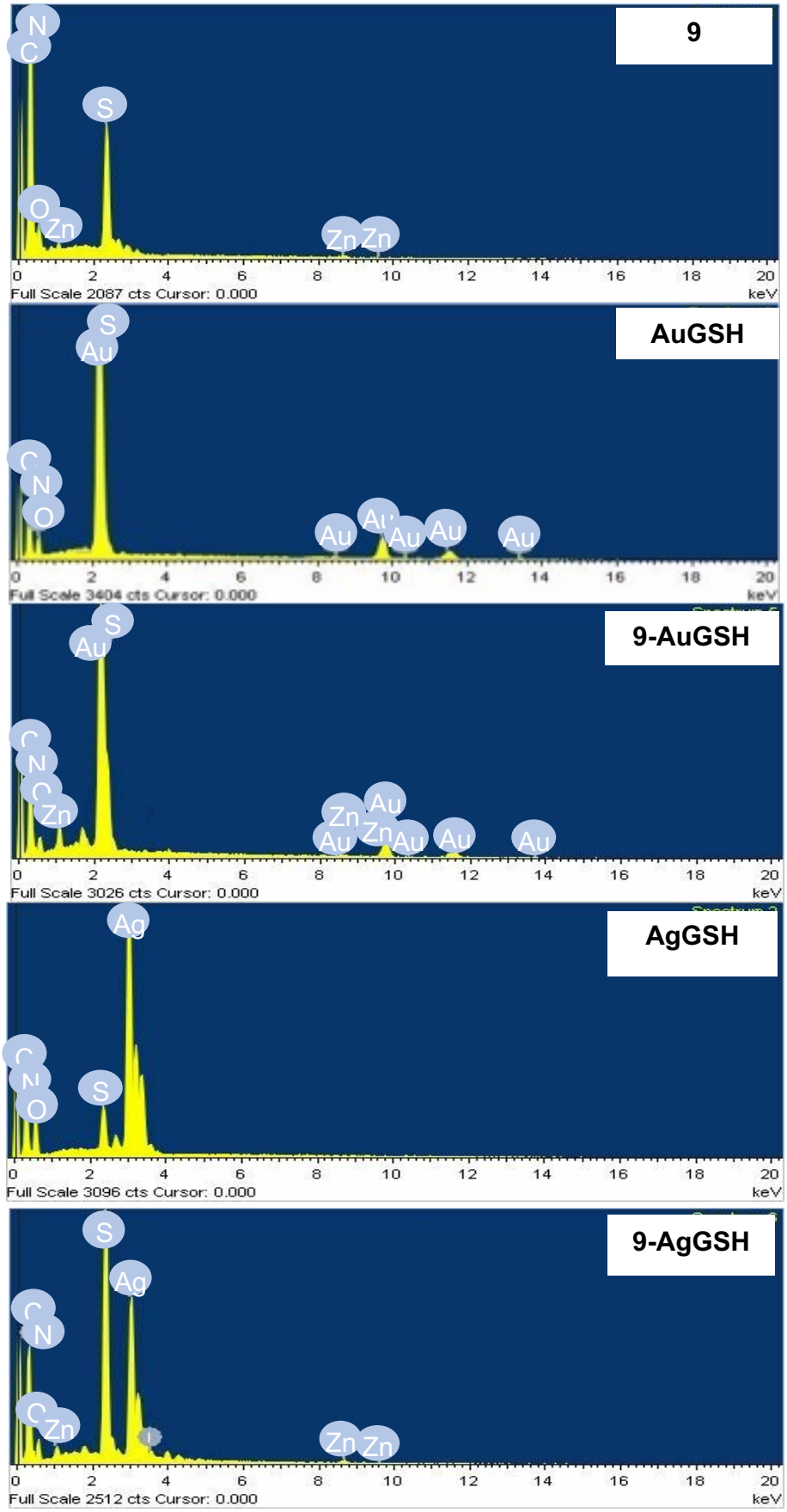

Figure 3.11. The EDX spectra of the Pc **9**, and the AuGSH and AgGSH conjugates.

3.2.2.3. X-ray photoelectron spectroscopy.

The XPS wide scan and N_{1S} spectra of the Pc **8**, the AgGSH and **8**-AgGSH conjugates are shown in **Fig. 3.12** as examples.

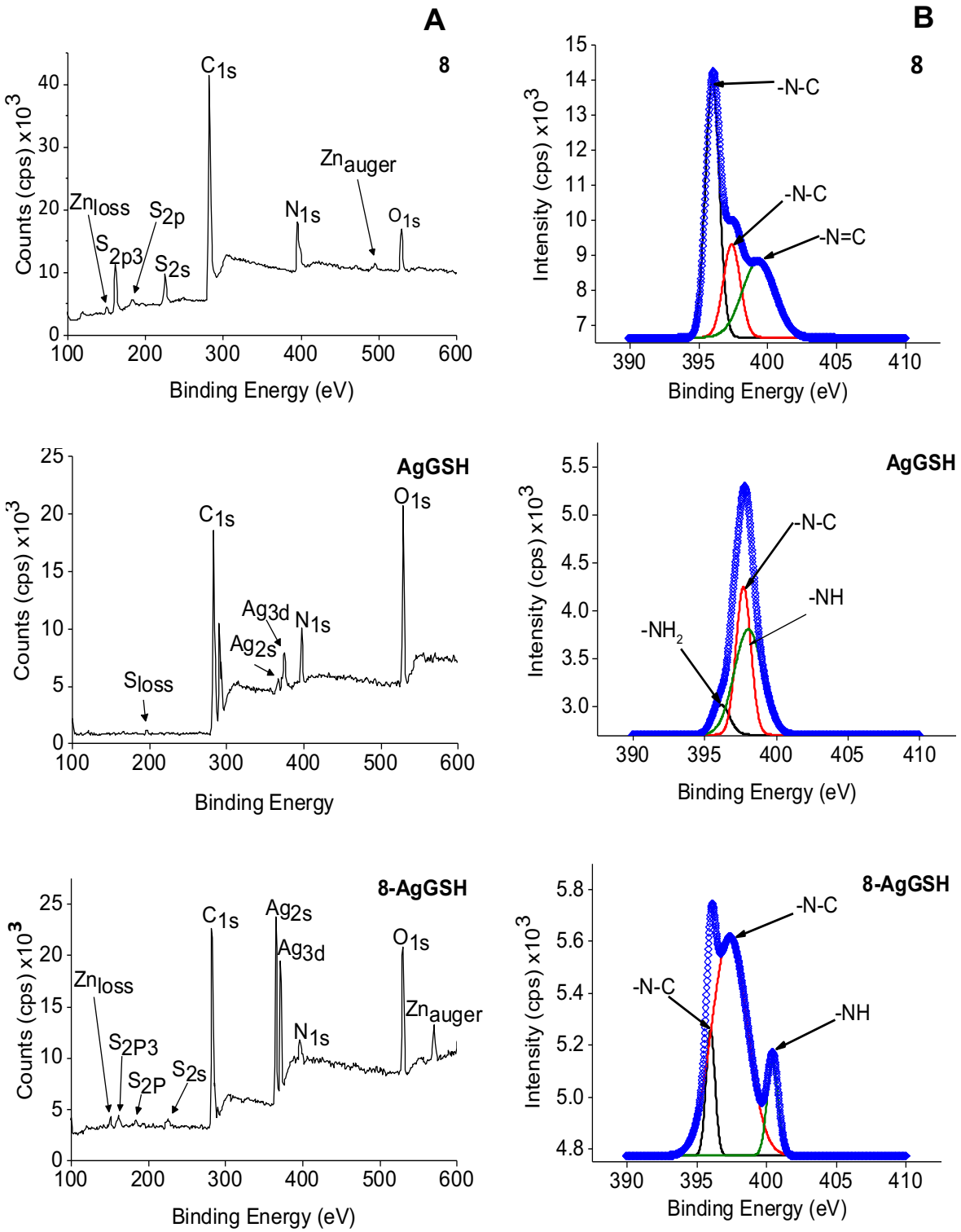

Figure 3.12. The XPS spectra showing A) the wide scans and B) the N_{1S} scans for the Pc **8**, AgGSH and **8**-AgGSH conjugate.

The S_{2p} XPS scans for the Pc **8** , AgGSH and 8-AgGSH is shown in **Fig. 3.13** as examples.

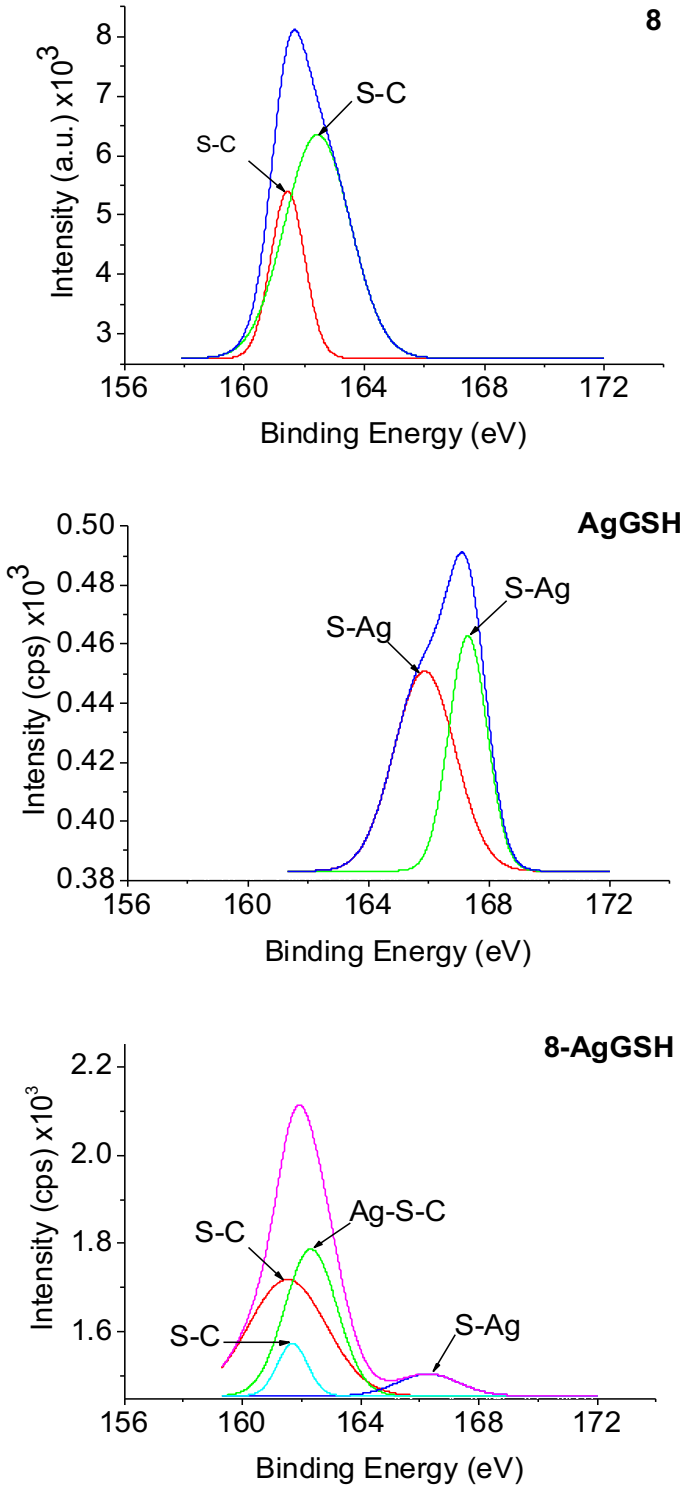

Figure 3.13. The S_{2p} XPS scans for the Pc **8**, AgGSH and **8**-AgGSH conjugate.

From the wide scan spectra, the presence of the C_{1s}, N_{1s}, and O_{1s} peaks at binding energies of 299 eV, 400 eV and 545 eV, respectively, are evident for Pc **8**, **Fig. 3.12 A**. The Zn_{auger} and Zn_{loss} peaks are observed at binding energies 150 eV and 495 eV, and the S_{2p3}, S_{2p} and S_{2s} at binding energies of 161 eV, 185 eV and at 226 eV, respectively, for Pc **8** alone. From the wide scan plots of the AgGSH NPs, peaks of the Ag_{2s} and Ag_{3d} were also seen at 312.5 eV and 325 eV respectively. Upon conjugation of the Pc and NPs to form the **8**-AgGSH, evidence of the Zn and S_{2S} peaks, in addition to the C_{1s}, N_{1s} and O_{1s} on the **8**-AgGSH wide scan spectrum is observed. The N_{1S} high resolution XPS scan of Pc **8** shows the -N-C bonds from the Pc's aromatic core with peaks occurring at binding energies of 396.25 eV and 397.0 eV, as shown in **Fig. 3.12 B**. Another peak at a binding energy of 399.38 eV is also seen for N groups from the -N=C on the Pc **8** substituents. For the AgGSH NPs, the free NH_2 stretch occurs at binding energy of 396.25 eV. Upon conjugation, the amide N (NH) peak occurring at a binding energy of 397.5 eV is enhanced, as seen with peak intensity increase from 3.75 $\times 10^3$ cps in the pristine AgGSH to an intensity of 5.0 $\times 10^3$ cps for the conjugate.

The NPs have been capped with GSH through S-metal affinity linkage. The Au and Ag metals are known to have strong affinity to S groups with lone electron pairs available [**158**]. The Pcs also comprise S-groups on the thiazole-moiety on the R-groups. Therefore, the Pcs may have also bonded to the NPs through these affinity bonds. The S_{2P} high resolution XPS spectra for the Pc **8**, AgGSH alone and the **8**-AgGSH are shown in the **Fig. 3.13**. From the S_{2P} XPS spectra of the AgGSH alone, the S-Ag peaks occur at intensities of ~0.45 and 0.46 $\times 10^3$ cps, upon conjugation to the Pcs, the S-Ag peak intensities are increased to ~1.5 and 1.8 $\times 10^3$ cps. The enhancement in the peak

intensities suggest the formation of additional S-Ag bonds on the surfaces of the NPs from the Pcs.

3.2.2.4. Transmission electron microscopy.

The TEM images for the AuGSH, AgGS and conjugates are shown in **Fig. 3.14**.

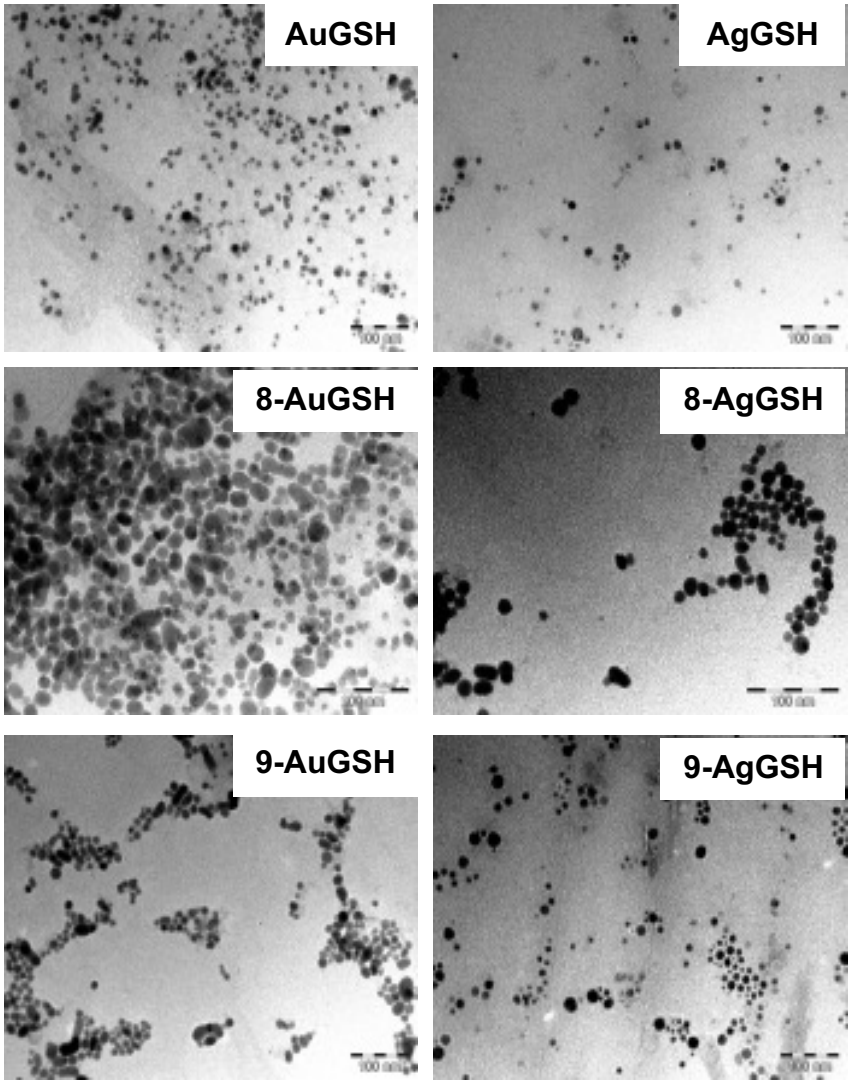

Figure 3.14. TEM images of the AuGSH, AgGSH and Pc conjugates.

The pristine AuGSH and AgGSH NPs appear spherical in shape and are monodispersed prior conjugation, **Fig. 3.14**. Upon conjugation to Pc **8** and Pc **9**, the NPs appear partially dispersed. The NPs in the conjugates maintain the spherical shape, however appear slightly larger than the pristine NPs. This is due to partial

stacking and increase in size is an expected observation for the Pcs-NPs conjugates compared to the pristine NPs. The Pcs are known to tend to stack on each other and may cause the conjugates to cluster as seen with the TEM images [**141**]. The approximated diameter sizes for these complexes were obtained from TEM and are summarised in **Table 3.1**. The diameter sizes of the AuGSH and AgGSH from the TEM estimations were found to be 7.5 nm and 6.9 nm, respectively. Upon conjugation to the Pcs, the sizes increased. The sizes for the **8**-AuGSH and **8**-AgGSH conjugates were found to be ~13.5 nm and ~11 nm, respectively. For the **9**-AuGSH and **9**-AgGSH, the TEM diameter size estimations obtained were 10 nm.

3.2.2.5. Dynamic light scattering spectroscopy.

The sizes of the NPs and conjugates were further analysed using DLS spctroscopy. The DLS spectra for the AuGSH, AgGSH and their respective conjugate to the Pc **8** and Pc **9** are shown in **Fig. 3.15**.

The DLS size estimations for the AuGSH and AgGSH in the conjugates are increased compared to the NPs alone, **Fig. 3.15**. This observation correlated with the size estimations obtained with the TEM results. The DLS size estimations for the AuGSH and AgGSH NPs and conjugates are summarised in **Table 3.1**. Generally, the sizes obtained from the DLS spectra are larger compared to those from TEM, as observed for the GQDs. The sizes of the AuGSH and AgGSH were found to be 9.0 nm and 7.7 nm, respctively. Upon conjugation, the AuGSH sizes increase to 18.2 nm and 14.2 for the Pc **8** and **9** conjugates, respectively. For the AgGSH, the sizes increase to 15.7 nm and 12 nm for conjugates with the Pc **8** and **9**, respectively. The larger sizes for the AuGSH and AgGSH conjugates compared to those of the GQDs may be due to the increase surface area for conjugation and arrangements of the Pcs on the 3D sperical NPs compared to the 2D graphene sheets.

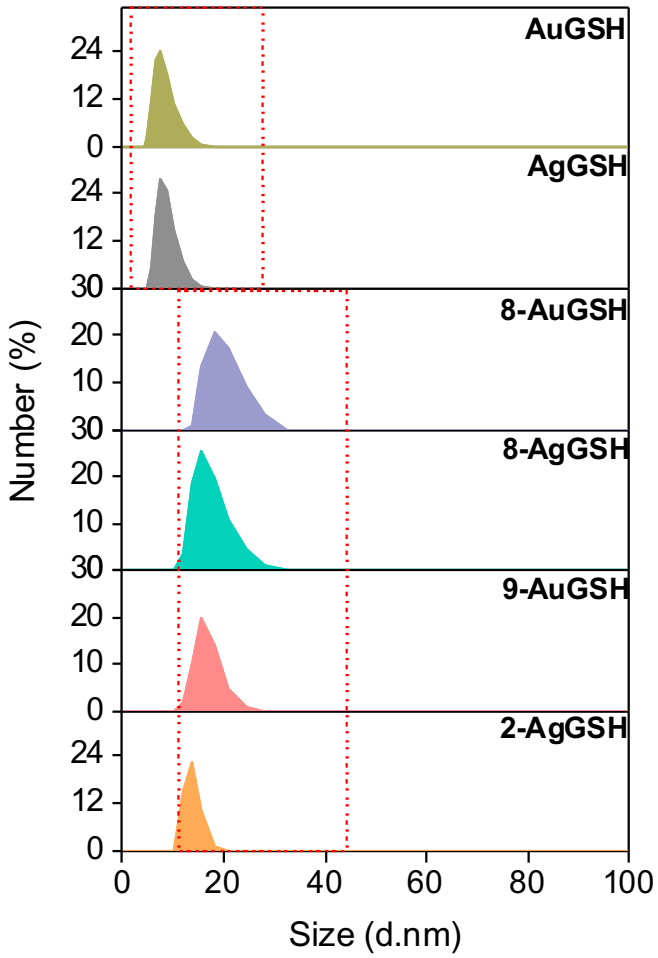

Figure 3.15. The DLS plots for the NPs and the Pc 8-conjugates in water.

The loading values for the Pcs on the AuGSH and AgGSH were calculated using the Beer Lamberts Law as reported before in the literature [**157,159**]. The loading on the AuGSH were found to be 1.45 $mmol_{Pc}$/ mg_{conj} and 1.26 $mmol_{Pc}$/ mg_{conj} for the Pc **8** and Pc **9**, respectively. Where the loading on the AgGSH was 1.25 $mmol_{Pc}$/ mg_{conj} and 1.01 $mmol_{Pc}$/ mg_{conj} for the Pc **8** and Pc **9**, respectively. The loading was lower for Pc **9** compared to Pc **8** on both the AuGSH and AgGSH NPs. This observation may be due to steric hinderance introduced by the relatively bulkier ethyl- groups compared to the methyl- groups in **8**, causing lesser Pc to attach to the surfaces of the NPs. The lower

loading on AgGSH compared to AuGSH may be attributed to the surface area of the NPs, where the AuGSH were relatively larger than the AgGSH as seen in **Table 3.1**.

Although the sizes of the NGQDs and NSGQDs conjugates were larger compared to those of the AuGSH and AgGSH, the Pcs showed generally higher loading on the metallic AuGSH and AgGSH compared to the graphitic NGQDs and NSGQDs **Table 3.1**. The increase in the sizes of the GQDs may be attributed to the formation of GQDs-GQDs multilayers.

3.3. Electronic absorption spectroscopy.

The UV-vis absorption spectra of the Pcs and conjugates were determined to evaluate their absorption and solubility profiles in organic and aqueous solvents. The UV-vis spectra may be used to determine the ease of disassociation of the Pcs in the specific solvent [**143**].

The broadening or splitting of the Q-bands is indicative of aggregation [**160**], with the high energy band (blue-shifted band) due to the formation of H-aggregates formed when the Pcs stack together face-on [**161**]. The lower energy band is due to the monomer. The UV-vis absorption spectra were obtained in DMSO and in water for the new Pc **6** – Pc **11** and the conjugates of the Pc **8** and Pc **9** with the AuGSH, AgGSH and GQDs NPs.

3.3.1. Absorption spectroscopy for phthalocyanines alone.

The UV-vis spectra of the zwitterionic Pc **6** and Pc **7** are shown in the **Fig. 3.16**.

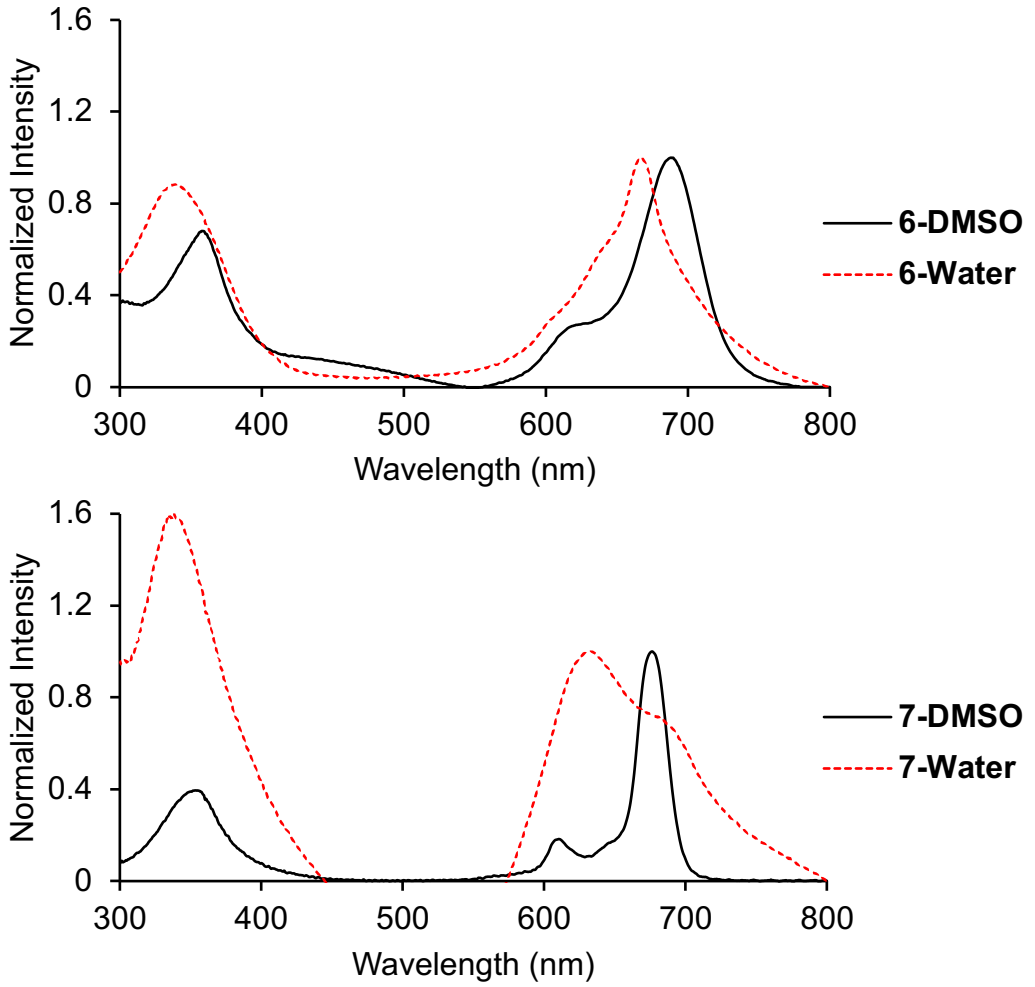

Figure 3.16. The UV-vis spectra of the Pc **6** and Pc **7** in water and in DMSO.

From the **Fig. 3.16**, the characteristic Q-band and B-band are seen for Pc **6** and Pc **7**. For the Pc **6**, the Q-band occurs at 687 nm (**Table 3.2**) with the B-band at 390 nm in DMSO. For the Pc **7**, the Q-band was observed at 680 nm and the B-band at 360 nm in DMSO. Both the Pc **6** and Pc **7** showed a broader Q-band in water. In water, the Pc **6** shows aggregation peak at 669 nm (**Table 3.2**) and the monomer peak at 718 nm. For the Pc **7** in water, the aggregation peak is seen at 642 nm and the monomer peak at 692 nm.

The log ε for the Pc **6** and Pc **7** (687 nm and 680 nm) in DMSO were calculated to be 4.76 and 4.74.

The UV-vis absorption spectra of the thiazole- Pc **8** and Pc **9** are shown in **Fig. 3.17**.

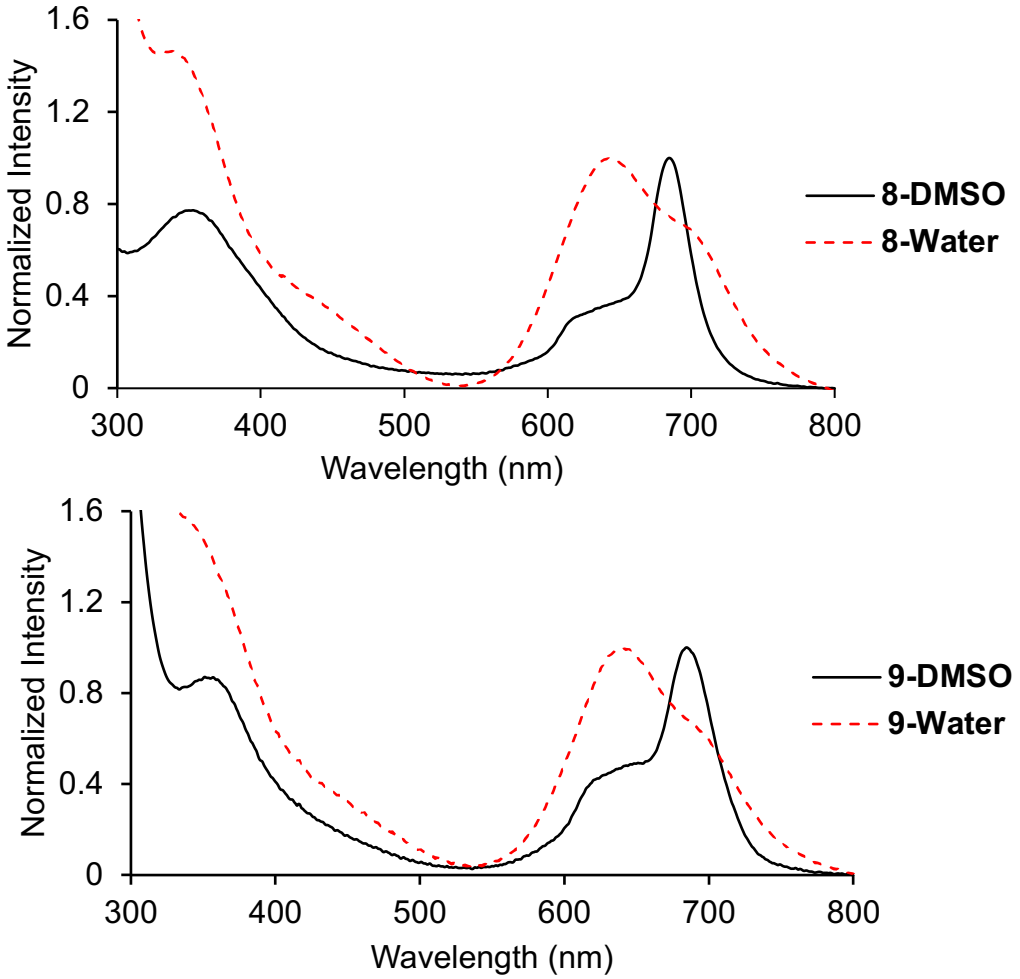

Figure 3.17. UV-vis spectra of the Pc **8** and Pc **9** in water and in DMSO.

From the **Fig. 3.17**, the UV-vis spectra in DMSO, shows the charcteristic Q-band and B-bands at 685 nm and 358 nm for Pc **8** respectively, and at 684 nm and 362 nm for the Pc **9**, respectively (**Table 3.2**). In water, for the Pc **8**, the aggregation peak appears at 644 nm and the monomer peak at 703 nm. For the Pc **9**, the aggregation peak appears at 643 nm and the and the monomer peak at 700 nm, in water (**Table 3.2**).

The log ε for the Pc **8** and Pc **9** (at 685 and 684 nm) were found to be 4.47 and 4.69 in DMSO, respectively.

The UV-vis absorption spectra for the Pc **10** and Pc **11** are shown in the **Fig. 3.18**.

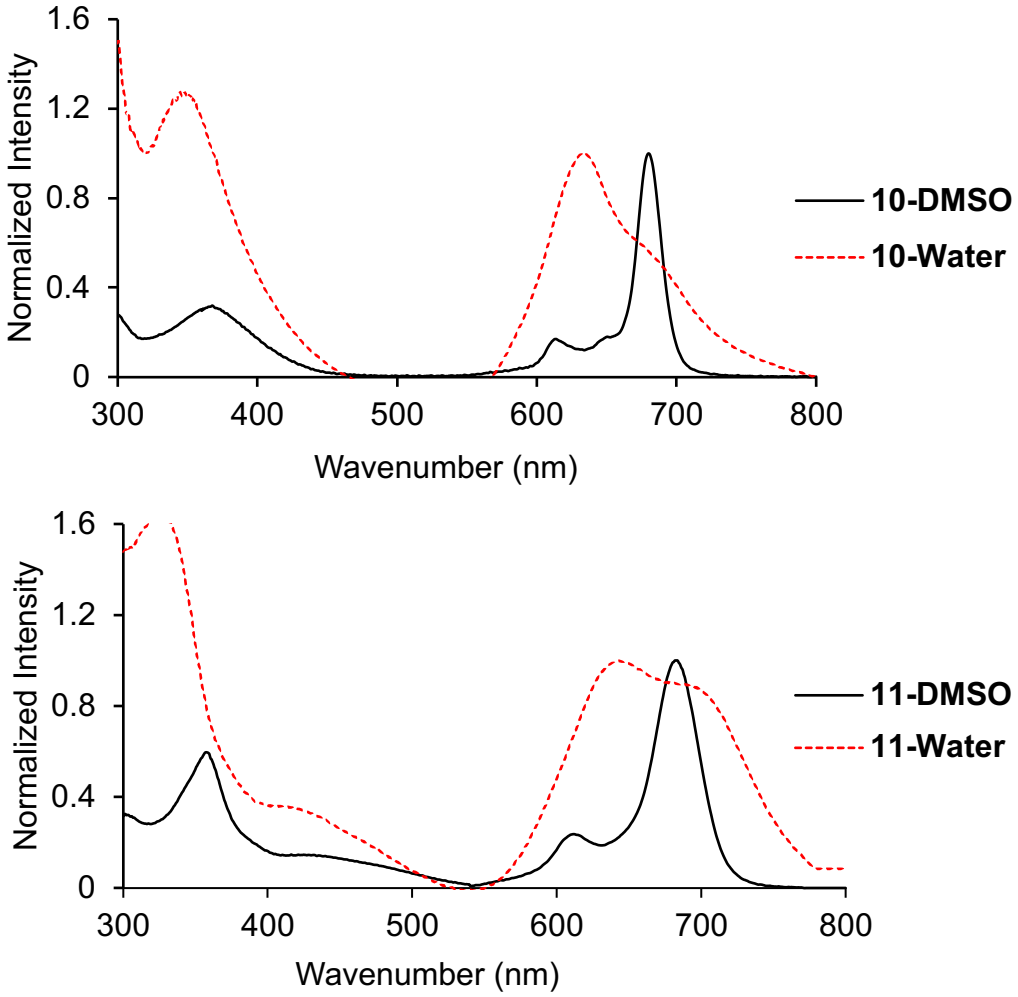

Figure 3.18. UV-vis spectra of the Pc 10 and Pc 11 in water and in DMSO.

From the **Fig. 3.18**, the characteristic Q-band and B-band in DMSO for the Pc **10**, occur at 680 nm and 364 nm, respectively. For the Pc **11**, the Q- and B-bands in DMSO were seen at 682 nm and 360 nm, respectively. In water, the aggregation peak appears at 633 nm and the monomer peak at 680 nm for the Pc **10**, **Table 3.2**. For Pc **11** in water, the aggregation peak appears at 648 nm and the monomer peak at 704 nm, **Table 3.2**. Additionally, a charge-transfer band was observed for the Pc **11** spectra in DMSO and in water at 445 nm and 439 nm, respectively, **Fig. 3.18**. Charge transfer bands have also been reported for the corresponding Pc **4** [**107**].

The log ε for the Pc **10** and Pc **11** (at 680 and 682 nm) in DMSO were calculated to be 4.99 and 4.84, respectively.

All the Pcs show maximum absorption at wavelengths within the therapeutic window of tissue (600 nm – 900 nm) [**162**]. Overall, the Pc **6** showed the most red-shifting, **Table 3.2**, followed by the Pc **8** and Pc **9**. This is due to the presence of the sulfur/ nitrogen groups linking the R-groups to the Pc core which are known to cause the red-shifting of the Q-bands [**163**].

Overall, the absorption of the Pcs in the NIR is important since the ideal sensitizer absorption should be within the NIR as previously mentioned.

3.3.2. Absorption spectroscopy for nanoparticles and conjugates.

The UV-vis absorption spectra for the Pcs-conjugates with the NGQDs and NSGQDs were also obtained. The UV-vis spectra for the Pc **9** conjugates with the NGQDs, NSGQDs are shown in the **Fig. 3.19** as examples.

The UV-vis spectra for the NGQDs and NSGQDs alone show maximum absorbance within the blue region at 345 nm and 340 nm for the NGQDs and NSGQD, respectively, **Fig. 3.19**. Upon conjugation to the Pc **9**, the enhancement of the absorption intensities at this region for the conjugates is observed, indicating the presence of both the Pc and GQDs in the sample. The absorption of the Pcs in the conjugated are also broadened, indicating increased aggregation of the Pcs. A similar trend was observed for the absorption of the **8**-NGQDs and the **8**-NSGQDs in water.

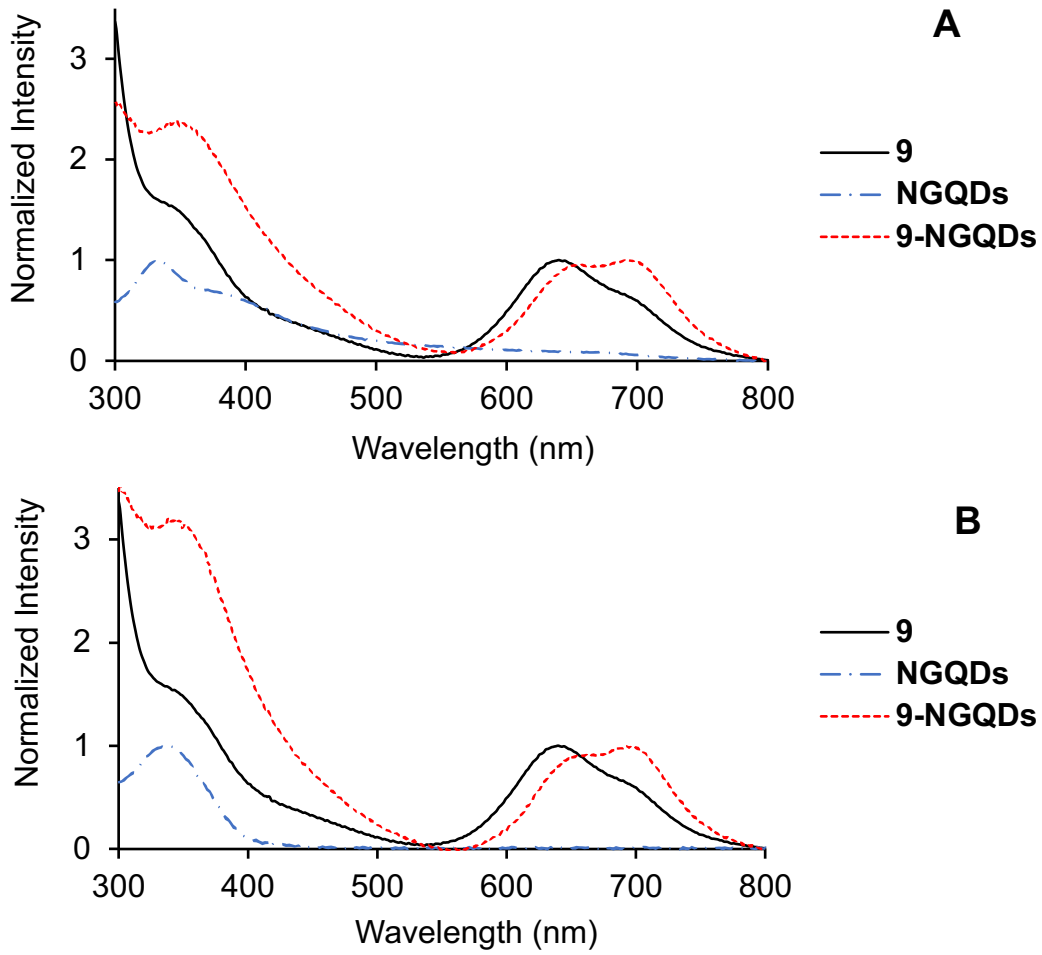

Figure 3.19. The UV-vis spectra of A) Pc **9**, **9**-NGQDs and **9**-NSGQDs and B) Pc **9**, **9**-NGQDs and **9**-NSGQDs in water.

The UV-vis absorption spectra for the Pcs-conjugates with the AuGSH and AgGSH were obtained. The UV-vis absorption spectra for the Pc **8** conjugates with the AuGSH and AgGSH are shown in the **Fig. 3.20** as examples.

From the **Fig. 3.20**, the UV-vis spectra of the NPs alone show the maximum absorbance at 540 nm and 420 nm for the AuGSH and AgGSH, respectively. This UV-vis spectroscopy properties of these NPs is due to a phenomenon known as surface plasmon resonance [**164**]. Upon conjugation of the Pcs to the NPs, the absoprbance intensity in the blue-region at wavelength between 300 nm – 500 nm increases. The

increased absorbance intensities the UV-vis spcetra of the conjugates is indicative of the presence of the AuGSH and AgGSH NPs.

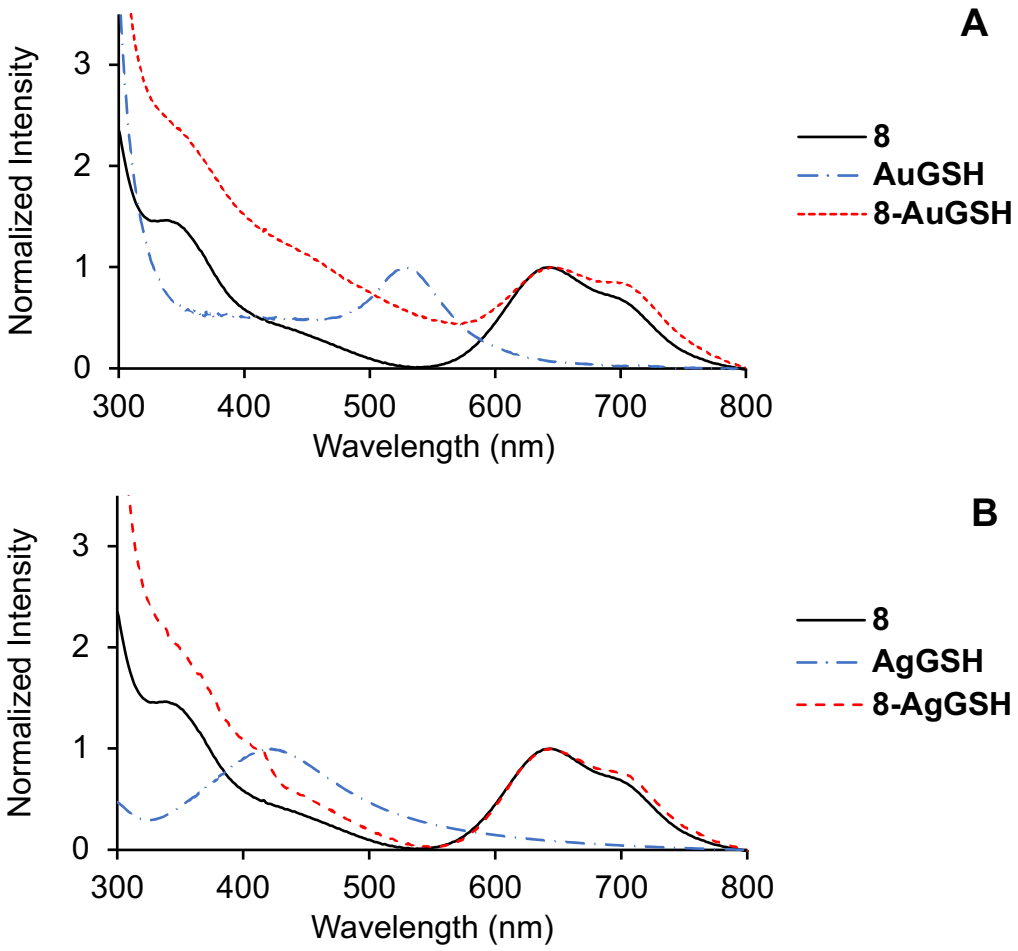

Figure 3.20. UV-vis spectra of Pc **8**, the AuGSH, AgGSH and respective conjugates in water.

Table 3.2 shows that there is a slight blue-shifting (and no shifting in some cases) in the Q-band wavelengths for Pc **8** and Pc **9** linked to NPs, compared to the non-conjugated Pcs as seen with the GQDs and the metallic-NPs conjugates.

Table 3.2. Summary of the UV-vis absorption behavior of the Pcs in DMSO and water.

	λ_{max} (nm)	log ε ($M^{-1}cm^{-1}$)	Ref
1	676 (649)	5.20	[**104**]
2	670 (634)	4.88*	[**105**]
3	683 (630)	4.86*	[**165**]
4	674 (-)	5.33	[**107**]
5	682 (647)	4.87	[**108**]
6	687 (669)	4.76	-
7	680 (642)	4.74	-
8	685 (644)	4.47	-
9	684 (643)	4.69	-
10	680 (633)	4.99	-
11	682 (648)	4.84	-
		With nanoparticles	
NGQDs	(345)	-	-
NSGQDs	(340)	-	-
8-NGQDs	682 (658)	-	-
8-NSGQDs	684 (659)	-	-
9-NGQDs	683 (658)	-	-
9-NSGQDs	683 (658)	-	-
AuGSH	(540)	-	-
AgGSH	(420)	-	-
8-AuGSH	683 (639)	-	-
8-AgGSH	684 (644)	-	-
9-AuGSH	684 (639)	-	-
9-AgGSH	684 (640)	-	-

*Values determined in this thesis not reported in the reference; values in brackets are in water (for Pcs, only the aggregate peaks are given in water).

3.4. Summary of chapter.

New ionic Pcs were prepared and structural characterized using various analytical techniques to confirm their structures. The results from the structural characterizations were satisfactory results and agreed with predicted/ theoretical characterizations.

The thiazole Pc **8** and Pc **9** were conjugated to the NGQDs and NSGQDs through non-covalent π-π interactions to form Pc-GQD nano-systems. The NGQDs showed higher Pc loading compared to the NSGQDs for both Pcs. Pc **8** and Pc **9** were also conjugated to the metallic NPs, AuGSH and AgGSH through covalent amide bonds. The affinity S-metal bonds between the Pcs and NPs were confirmed by XPS. The loading of the Pcs was higher on the AuGSH compared to the AgGSH. The NPs and Pc-NPs conjugates were characterized using various techniques. The TEM and DLS size estimations showed a general increase in the sizes of the NPs upon conjugation to the Pcs.

The electronic absorption studies of the Pcs were obtained. The Q-bands of the Pcs were red-shifted and occurred within the NIR at $\lambda_{max} > 670$ nm. Blue-shifting of the λ_{max} was observed in water for the Pcs to ~630 nm. The UV-vis spectra of the conjugates were slightly different from the Pcs alone. An increase in the absorption intensities in the blue region, indicating the presence of the NPs.

CHAPTER FOUR

4. Sono-Photophysical Properties

This chapter reports on the sono-photophysical characterization of the Pcs. The photophysical parameters including the fluorescence and triplet population of the Pcs and the Pc-NPs conjugates were determined. Furthermore, the stabilities of the Pcs upon sono-irradiations using varying ultrasonic parameters for the Pcs are reported. The effects of the Pcs R-groups and the type of NPs on the photo- and sono-activities of the Pcs are compared.

Outline of phthalocyanine structural differences and comparisons

The following structural features were compared between the Pcs.

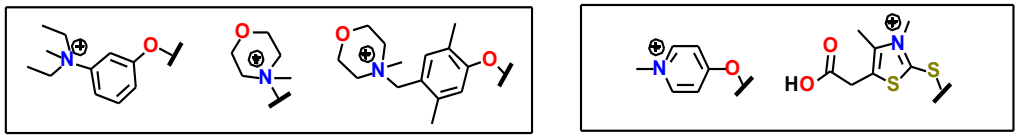

- N-group in aliphatic vs aromatic moiety: Pcs **1, 4, 5** vs Pc **3**, Pc **8**.

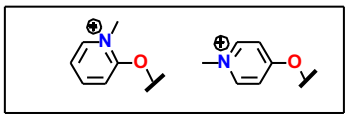

- group on *meta* vs *para* position on pyridine substituted Pcs: Pc **2** vs Pc **3**.

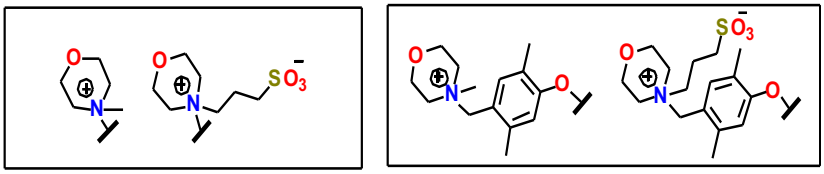

- R-group extension on morpholine Pcs: Pc **4**, Pc **6** vs Pc **5**, Pc **7**.

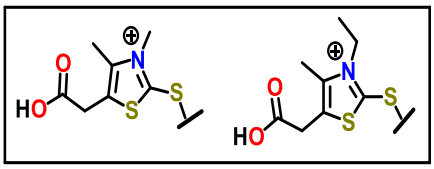

- Methyl- vs ethyl-: Pc **8** vs Pc **9**.

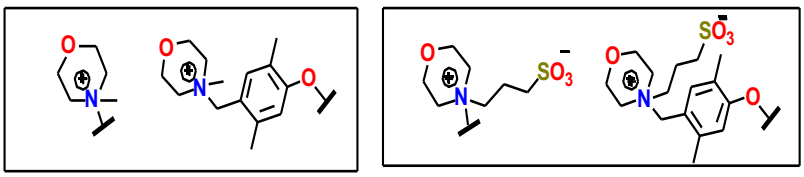

- Methyl- vs propanesultone- (cationic vs zwitterionic): Pc **4**, Pc **5** vs Pc **6**, Pc **7**.

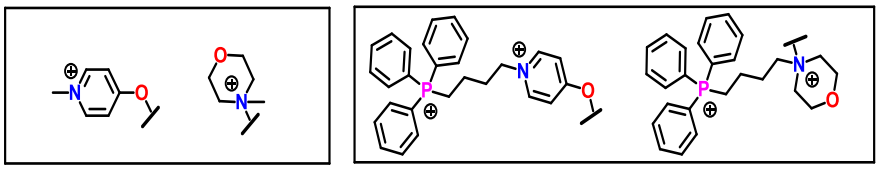

- Methyl- vs TPP (number of cations): Pc **3**, **4** vs Pc **10**, Pc **11**.

4.1. Photophysical characterization.

The photophysical parameters, including the fluorescence (Φ_F and τ_F) and triplet (Φ_T and τ_T) parameters, were calculated for the Pcs and Pc-NPs conjugates using comparative methods as defined previously in section 2.4.1 and 2.4.2.

4.1.1. Fluorescence quantum yields and fluorescence lifetime.

The fluorescence behaviour of the Pcs upon exposure to light where studied. The absorption, emission, and excitation spectra for the Pc **10** in DMSO are shown in the **Fig. 4.1** as examples.

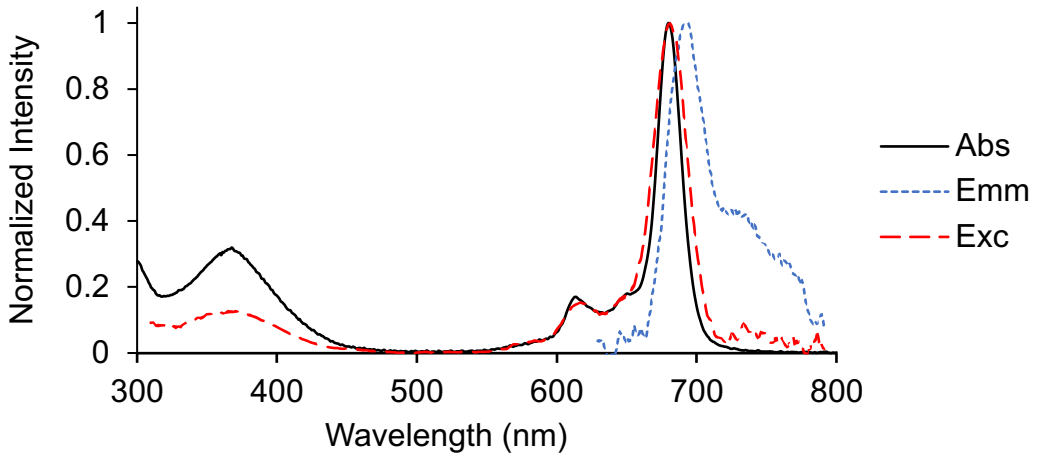

Figure 4.1. The absorption, emission, and excitation spectra for Pc **10**.

The emission spectra of the Pcs were mirror images to their respective excitation spectra. The excitation spectra were similar to the absorption spectra for the Pcs as shown in the **Fig. 4.1** for the Pc **10**. This suggests that the molecules absorbing photon energy from the light to which they are exposed are the same molecules that are emitting during fluorescence [**42**]. This observation also suggests that the nuclear configurations of the Pcs in the ground state are similar as in the excited states upon light exposure [**166,167**].

The TCSPC fluorescence decay curve was used to determine the time the excited Pcs remain at the excited states before returning to the ground state through fluorescence. This time is represented as the τ_F. The τ_F values for the Pc **1** – Pc **11** were determined using TCSPC.

A typical fluorescence decay curve for Pcs **10** is shown in **Fig. 4.2**, as an example.

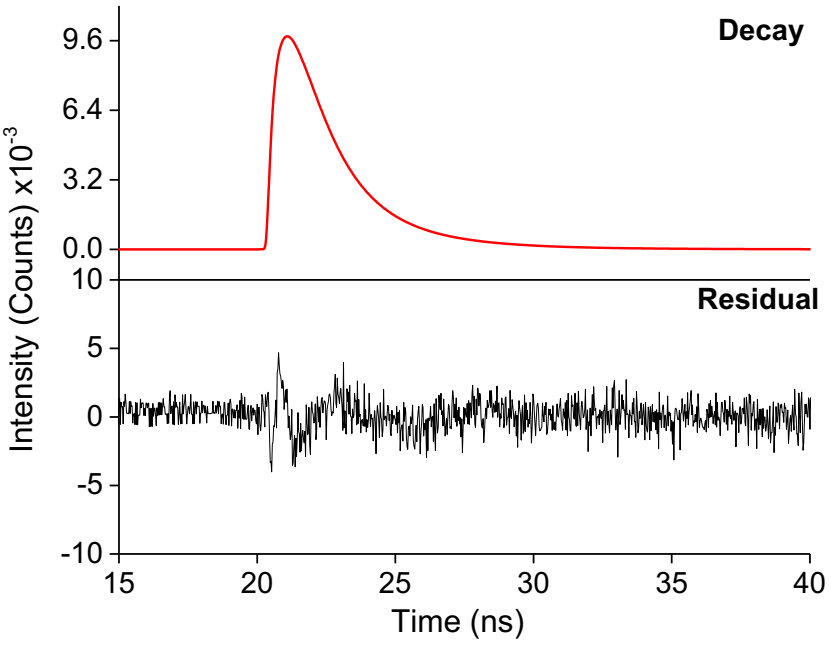

Figure 4.2. The TCSPC fluorescence decay curve for Pc **10** in DMSO.

The fluorescence decay for Pcs is within the ns time range, **Fig. 4.2**. The fluorescence properties of Pcs are affected by the nature of the substituents around the Pcs core. The differently substituted Pcs used in this work showed varying fluorescence profiles. The Φ_F and τ_F values were calculated for the Pcs in DMSO.

A summary of the calculated Φ_F and τ_F values of the Pcs and the Pc-NPs conjugates is given in the **Table 4.1**, together with the reported values [**104,105,107,108,165**]

Table 4.1. Summary of the Φ_F and τ_F values for the Pcs, NPs, and Pc-NPs conjugates in DMSO.

	Φ_F± 0.01	τ_F (ns) ± 0.01	Ref
1	0.12	1.72[b]	[**104**]
2	0.17	2.10[b]	[**105**]
3	0.17	2.70	[**165**]
4	0.24	2.84	[**107**]
5	0.20	2.83	[**108**]
6	0.12	2.68	-
7	0.18	3.03	-
8	0.06	1.06	-
9	0.06	1.01	-
10	0.10	1.58	-
11	0.08	1.21	-
	With Nanoparticles		
NGQDs	(0.70)[a]	(2.70)[a]	-
NSGQDs	(0.80)[a]	(5.40)[a]	-
8-NGQDs	0.04	0.93	-
8-NSGQDs	0.05	1.02	-
9-NGQDs	0.03	0.07	-
9-NSGQDs	0.04	0.08	-
AuGSH	n.d.	n.d.	-
AgGSH	n.d.	n.d.	-
8-AuGSH	n.d.	n.d.	-
8-AgGSH	0.07	1.15	-
9-AuGSH	n.d.	n.d.	-
9-AgGSH	0.09	1.01	-

[a]Values for excitation where GQDs absorb, values in brackets are in water, [b]values determined in this work and not reported in the references. n.d.: not detected.

4.1.1.1. Effect of R-groups.

The Φ_F values differed for the Pcs with differing R-groups, **Table 4.1**. For the Pc **1** – Pc **5** the Φ_F values have been reported in the literature. The Φ_F values for all the Pcs (**Pc 1** – Pc **11**) were <0.25. Lower Φ_F values are ideal for PDT as they may suggest increase intersystem crossing to the T_1 instead. The pyridine Pc **2** and Pc **3** had the same Φ_F values of 0.17. The Φ_F values for the zwitterionic Pc **6** and Pc **7** were calculated to be 0.12 and 0.18 in DMSO, respectively. These values were lower compared to the cationic counterparts, Pc **4** and Pc **5**. The reduction of the Φ_F values for zwitterionic Pcs compared to their neutral or cationic Pcs counterparts has been reported for some Pcs in the literature [**168,169**]. The Φ_F values for the thiazole Pc **8** and Pc **9** were calculated to be 0.06 for both Pcs in DMSO. Low Φ_F values have been reported for Pcs bearing thiazole R-groups [**136,170,171**]. For the Pc **10** and Pc **11**, the Φ_F values were calculated to be 0.10 and 0.08 in DMSO, respectively. The larger TPP-labelled Pcs **10** and **11** had reduced Φ_F values compared to their corresponding methylated Pc **3** and Pc **4** counterparts, respectively. Low Φ_F values (<1) have been reported for TPP-substituted Pcs in the literature [**172**].

The τ_F values varied for the different Pcs, **Table 4.1**. For the Pc **3** – Pc **5**, the τ_F values have been reported in the literature. The τ_F values for the Pcs zwitterionic Pc **6** and Pc **7** were determined to be 2.68 ns and 3.03 ns in DMSO, respectively. For the Pc **6**, the τ_F value was lower compared to the corresponding Pc **4**. For the Pc **7**, instead, the τ_F value was higher compared to the counterpart, Pc **5**. For the Pc **8** and Pc **9**, the τ_F values were calculated to be 1.06 ns and 1.01 ns, respectively. The τ_F values for the thiazole Pc **8** and Pc **9** are lower compared to the other Pcs, corresponding to their

low Φ_F. For Pc **10** and Pc **11**, the τ_F values were calculated to be 1.58 ns and 1.21 ns, respectively. The values were lower than the corresponding Pc **3** and Pc **4**.

4.1.1.2. Effect of nanoparticles.

The Φ_F and τ_F values for the Pcs were obtained using the excitation wavelengths where Pcs absorb. For the Pc **8** and Pc **9** conjugated to the NGQDs and NSGQDs, the Φ_F and τ_F values were relatively lower (or remained the same in some cases) compared to those calculated for the Pcs, **Table 4.1**. The decrease in the Φ_F for the Pcs in the conjugates may be attributed to the photoinduced electron transfer between the excited singlet state of the Pc and the graphitic NPs in the conjugates [**173,174**]. The τ_F values followed similar trends as the Φ_F. The Φ_F and τ_F values for the GQDs alone were obtained at excitation where the GQDs absorb (at 355 nm). For the Pc **8** and Pc **9** conjugated to the AuGSH and AgGSH, the Φ_F and τ_F values were also reduced compared to those calculated for the non-conjugated Pc **8** and Pc **9** alone, **Table 4.1**. No fluorescence was observed for the conjugates of the Pc **8** and Pc **9** with the AuGSH, therefore, the Φ_F values for the conjugates could not be calculated. For the AgGSH conjugates, the calculated Φ_F values were 0.07 and 0.09 for the **8**-AgGSH and **9**-AgGSH, respectively, when exciting where the Pcs absorb. The τ_F values for the **8**-AgGSH and **9**-AgGSH found were 1.15 and 1.01 ns, respectively, when exciting where the Pcs absorb. The reduction in the Φ_F values in the conjugates compared to the Pcs alone was expected for the metallic NPs since they promote intersystem crossing through the heavy atom effect, thus lower Φ_F values, if any, in the conjugates were expected.

4.1.2. Triplet quantum yield and triplet lifetime.

The laser flash photolysis technique involves the introduction of an intense pulse of light to a Pc sample. This results in the generation of time-evolved electronic absorption within the excited triplet states. The Φ_T and τ_T values for the Pc **1** – Pc **11**, and the conjugates of the Pc **8** and Pc **9** with the AuGSH, AgGSH, NGQDs and NSGQDs were determined in DMSO. The triplet decay curves represent the time taken by the Pcs in the excited triple states to relax pack to the ground state. The triplet decay curves for the Pcs were obtained in DMSO. The decay curve for the Pc **7** is shown in the **Fig 4.3**, as an example.

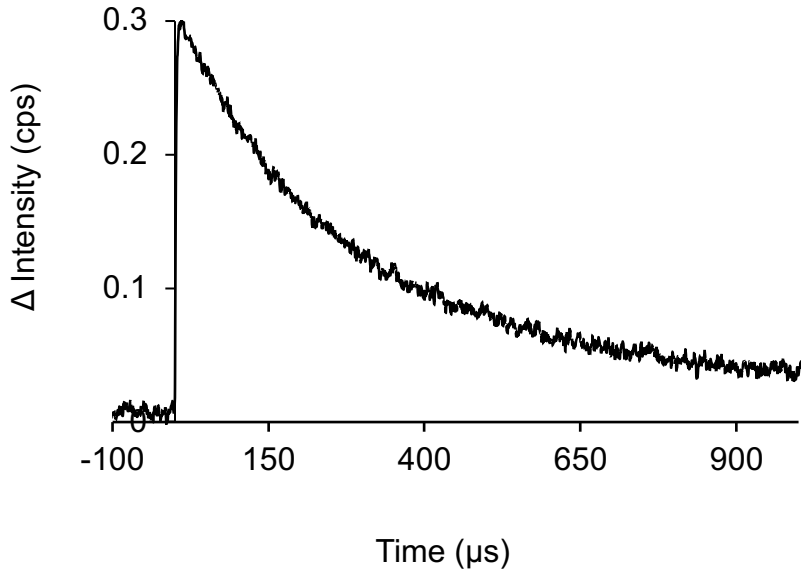

Figure 4.3. The triplet decay curve for the Pc **7** in DMSO.

The decay curve obeyed the second order kinetics, **Fig 4.3**. This type of decay is typical for Pcs and is attributed to the triplet-triplet recombination [**175-177**].

The triplet transient curves were also obtained for the Pcs. The triplet transient curve is shown in **Fig. 4.4** for the Pc **7** as an example.

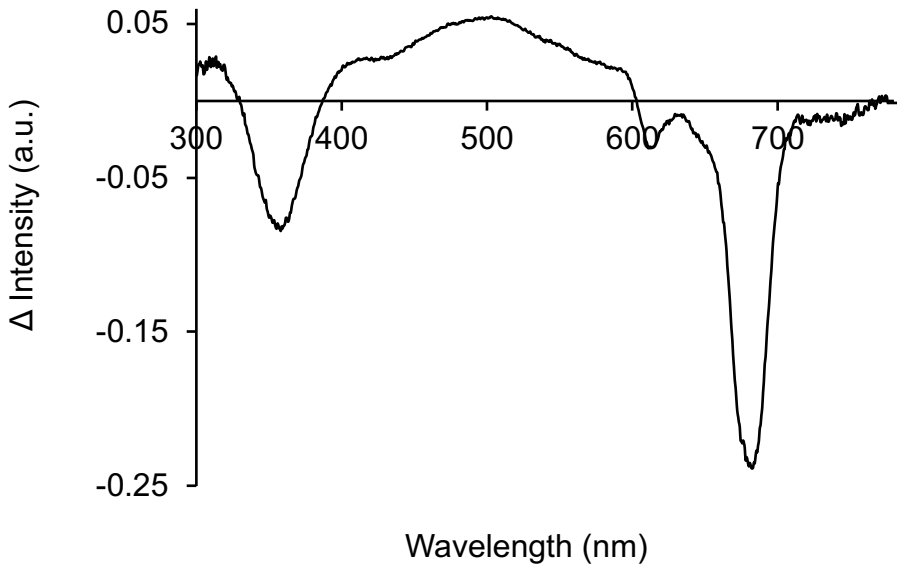

Figure 4.4. The triplet transient curve for the Pc **7** in DMSO.

A typical triplet transient curve for Pcs is shown in the **Fig. 4.4** for the Pc **7** in DMSO, as an example. The transient curve is characterized by a broad band which occurs at the wavelength range between 400 nm – 600 nm, **Fig. 4.4**. This observation is due to the triplet-triplet excited absorption [**50**]. Furthermore, the spectrum is generally similar to an inverted ground state UV-vis absorption spectrum. The negative peaks as seen in the transient curve at wavelengths ~680 nm and 359 nm occur due to the depletion of the ground state population of the Pc molecules upon exposure to light.

A summary of the Φ_T and τ_T values is given in the **Table 4.2**.

Table 4.2. Summary of the Φ_T and τ_T parameters for the Pcs complexes in DMSO.

	Φ_T	τ_T (μs)	Ref
1	0.79	323	-
2	0.78	300	[**105]**
3	0.73	326	[**165**]
4	0.66	292	[**107**]
5	0.64	269	[**108**]
6	0.62	279	-
7	0.58	261	-
8	0.59	257	-
9	0.61	283	-
10	0.69	318	-
11	0.67	297	-
	With Nanoparticles		
NGQDs	-	-	-
NSGQDs	-	-	-
8-NGQDs	0.64	272	-
8-NSGQDs	0.60	291	-
9-NGQDs	0.70	298	-
9-NSGQDs	0.57	239	-
AuGSH	-	-	-
AgGSH	-	-	-
8-AuGSH	0.62	323	-
8-AgGSH	0.62	228	-
9-AuGSH	0.69	309	-
9-AgGSH	0.71	299	-

4.1.2.1. Effect of R-groups.

The Φ_T and τ_T values for the Pc **2** – Pc **5** are reported in the literature. The Φ_T values differed for the differently substituted Pcs. However, the values were ≥ 0.58, **Table 4.2**. The Φ_T values for the zwitterionic Pc **6** and Pc **7** found were 0.62 and 0.58, respectively. These values were relatively lower than their cationic counterparts, the Φ_T values for Pc **4** and Pc **5**, which have been reported to be 0.66 and 0.64 In DMSO, respectively. Although the Φ_F of the zwitterionic Pcs were reduced compared to their cationic counterparts, the Φ_T were not improved for both the Pcs. Similarly, to the Φ_T, the τ_T values for the Pc **6** and Pc **7** were 279 μs and 261 μs, respectively, and were lower compared to their corresponding Pc **4** and Pc **5** with τ_T values of 292 μs and 269 μs, respectively. Substantial Φ_T yield were also observed for the thiazole Pc **8** and Pc **9** which were calculated to be 0.59 and 0.61 in DMSO, for the Pcs respectively. The τ_T values for the Pcs were found to be 257 μs and 283 μs for the Pc **8** and Pc **9**, respectively. The ethylated Pc **9** showed improved triplet state profile compared to the methylated Pc **8**. The TPP-labelled Pc **10** and Pc **11** also showed high Φ_T and τ_T values, with the Pc **1** – Pc **3** showing high Φ_T values. The calculated Φ_T values for the Pc **10** and Pc **11** were 0.69 and 0.67. The τ_T values obtained were 318 μs and 297 μs. An improvement was observed in terms of the Φ_F and τ_T parameters for the TPP-labelled Pc **10** and Pc **11,** compared to their corresponding methylated counterparts, the Pc **3** and Pc **4**, respectively.

The Φ_T values is an important parameter for the activity of the Pcs in PDT, this is because the excited Pcs that populate the triplet state can potentially generate ROS through energy/ electron transfer to nearby $^1O_2$. Low Φ_F may sometimes correspond with high Φ_T values making the two parameters inversely proportional. However, this

is not always the case as the excited Pcs may undergo other pathways in addition to fluorescence and intersystem crossing.

4.1.2.2. Effect of nanoparticles.

The Φ_T values and τ_T values for the Pc **8** and Pc **9** when conjugated to the graphitic NGQDs and NSGQDs and the metallic AuGSH and AgGSH NPs, were determined in DMSO.

An increase in the Φ_T values was observed for the Pc **8** and Pc **9** conjugates with the NGQDs and NSGQDs, except for the **9**-NSGQDs which showed a decrease compared to the Pc **9** alone instead, **Table 4.2**. The decrease may be due the intermolecular π-π interactions between the Pcs and GQDs in the nano-systems which may promote the rate of the non-radiative relaxation through internal conversion and consequently reducing the triplet population [**178**]. Increase in the Φ_T values for Pc-GQDs conjugates have been reported in the literature [**134**]. An increase in the Φ_T values observed for the Pcs in the presence of the AuGSH and AgGSH corresponds to the lower Φ_F values observed for the conjugates compared to the Pcs alone. This observation is a result of the heavy atom effect. The heavy atom effect, as previously stated, improves the efficiency of the intersystem crossing of the excited Pcs to populate the triplet state. An increase in the Φ_T values for Pcs upon conjugation to metallic NPs has been reported in the literature [**179,180**]. Overall, the NPs improve the triplet state properties of the Pcs.

4.2. Stability of phthalocyanine under the sono-irradiations.

The stability of the Pcs under the sono-irradiations at different parameter combinations were studied varying the frequency (MHz) and power ($W.cm^{-2}$) to determine the best

conditions for SPDT. The four parameters studied were: *Par I* (1 MHz: 1 W.cm^{-2}); *Par II* (1 MHz: 2 W.cm^{-2}); *Par III* (3 MHz: 1 W.cm^{-2}) and *Par IV* (3 MHz: 2 W.cm^{-2}). Two methods were used, the UV-vis method, to determine the Pc degradation; and EPR spectroscopy, to measure the generation of Pc-derived •C in water.

4.2.1. Degradation studies (UV-vis spectroscopy).

The effects of the sono-parameters on the stability of the Pcs were monitored using UV-vis spectroscopy. The UV-vis spectra of the Pc **4** before and after sono-irradiations at the *Par I* - *Par IV*, at increasing time intervals are shown in the **Fig. 4.5** as examples.

A decrease in the Q-band intensities was seen for the Pc **4** after the sono-irradiations at the different parameters, **Fig. 4.5**. For the *Par II* and *Par IV*, a relatively more significant decrease was observed in the absorbance intensities of the Pc compared to that observed for the *Par I* and *Par III*. For both the *Par II* and *Par IV*, the power is increased to 2 W.cm^{-2}. This may suggest that the power (W.cm^{-2}) of the US used in the sono-irradiations is more likely to affect the structure of the Pc-based sono-sensitizers compared to the frequency of the ultrasonic mechanical waves. The *Par II* showed the highest decrease of the Q-band intensities compared to all the other three tested parameter combinations. The absorbance intensities at the Q-bands for the Pcs were recorded for each time interval. Plots of the change in the Q-band absorption intensities against time are shown in the inserts for the four sono-parameters, **Fig. 4.5**.

The slopes of the linear equations from the plots of the Q-band intensities against time were recorded and compared for the Pcs for the sono-irradiations at the different parameters in water. The slopes (m-values) from the curves of the Q-band intensities against time Pcs post sono-irradiations at the *Par I – Par IV* are summarized in the **Table 4.3**.

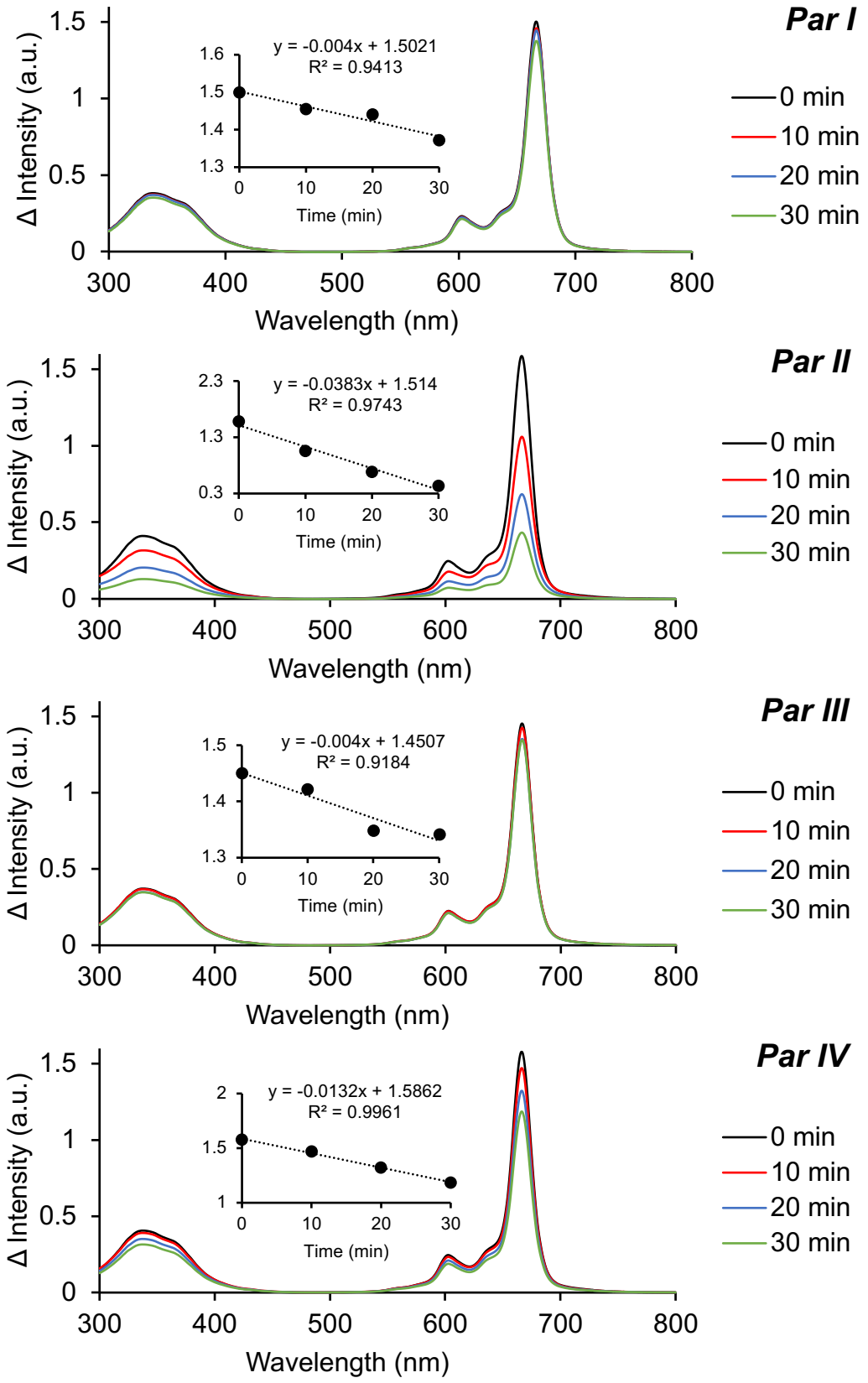

Figure 4.5. UV-vis spectra of Pc **4** (10 μM) after sono-irradiations at *Par I* - *Par IV* for 30 min at 10 min intervals in water. Insert: Absorbance intensities at Q-bands. *Par I* (1 MHz, 1 W. cm^{-2}), *Par II* (1 MHz, 2 W. cm^{-2}), *Par III* (3 MHz, 1 W. cm^{-2}), and *Par IV* (3 MHz, 2 W. cm^{-2}).

Table 4.3. Summary of the m-values and the EPR PBN intensities after sono-irradiations of the Pcs at the different sono-parameters in water.

	UV-vis (*m*) $\times 10^{-3}$				PBN intensity (a.u.) 10^{-3}			
	Par I	*Par II*	*Par III*	*Par IV*	*Par I*	*Par II*	*Par III*	*Par IV*
1	4.1	31.1	5.3	11.1	n.d.	22.0	n.d.	11.0
2	n.d.	4.3	n.d.	2.2	n.d.	n.d.	n.d.	n.d.
3	n.d.	6.5	n.d.	n.d.	n.d.	17.2	n.d.	n.d.
4	4.0	38.3	4.0	13.2	n.d.	28.6	n.d.	10.0
5	3.5	31.8	3.9	3.7	n.d.	25.3	n.d.	n.d.
6	7.2	42.1	13.2	15.7	<8.0	30.0	n.d.	13.1
7	9.1	39.1	11.9	17.1	<8.0	21.4	n.d.	11.5
8	1.4	6.9	3.1	3.6	n.d.	17.5	n.d.	n.d.
9	4.2	7.8	3.7	4.7	n.d.	18.3	n.d.	n.d.
10	10.1	41.5	15.9	19.1	11.1	30.4	8.0	13.6
11	15.2	45.9	18.7	22.2	12.3	31.3	8.0	16.7

(-) no degradation observed. *Par I* (1 MHz, 1 W. cm^{-2}), *Par II* (1 MHz, 2 W. cm^{-2}), *Par III* (3 MHz, 1 W. cm^{-2}), and *Par IV* (3 MHz, 2 W. cm^{-2}). n.d.: not detected.

When comparing the methylated cationic Pc **1** – Pc **5** and Pc **8**, the Pcs with the tertiary-N on the aliphatic moieties (Pc **1**, Pc **4**, and Pc **5**) showed relatively more susceptibility to the US under the sono-irradiations compared to those with the tertiary-N on the aromatic moieties (Pc **2**, Pc **3**, Pc **8**), as seen with the higher slope values from the degradation of the Q-band, **Table 4.3**. When comparing the Pc **2** and Pc **3,** the *para*-pyridine Pc **3** showed higher m values compared to the *ortho*-pyridine Pc **2** for *Par II*. Both Pc **2** and Pc **3** were stable at *Par I* and *Par III*. The zwitterionic Pc **6** and Pc **7** also showed relatively more susceptibility to degradation compared to their cationic counterpart, Pc **4** and Pc **5**, respectively. The propanesultone on the zwitterionic Pcs may be easily fractured compared to the methyl-groups on the cationic

Pcs. For the thiazole substituted Pc **8** and Pc **9** the ethylated Pc **9** was more susceptible to the US compared to the methylated Pc **8** under all the parameters. The triphenyl-phosphine (TPP)-labelled Pc **10** and Pc **11** showed less stability compared to their methylated counterparts, Pc **3** and Pc **4**, respectively. The bigger TPP-moiety compared to the methyl quaternizing agent may be easily affected by the ultrasonic mechanical waves in the aqueous media. The increase in the molecular weight of the quaternizing agent showed a decrease in stability for the Pcs. The order of decreasing stability observed for the different quaternizing agents used was methyl- < ethyl- < propanesultone- < triphenylphosphine.

4.2.2. Generation of carbon radicals.

The decrease in the UV-vis absorption intensities for some of the Pcs under the different sono-parameters, as shown by the m-values in the **Table 4.3**, may suggest the fragmentation of the carbon bonds on the Pcs structure upon exposure to the US in the aqueous media. Thus, there is a possibility of the formation of carbon radicals (•C). This effect has not yet been reported for Pcs. However, the fragmentations of sensitizers though pyrolysis have been reported in the literature [**75,181**]. Bakhshizadeh *et al.* reported on the effect of the order of irradiations in SPDT treatments using liposomal Pc sensitizers, where the activity of the Pcs reduced when sono-irradiations were performed first [**18**]. This observation was speculated to be due to the fragmentation of the Pcs during the sono-irradiations. To evaluate the formation of the •C from the Pcs under sono-irradiations, the EPR spectroscopy was used. The PBN spin trapping reagent was used to detect the •C. The EPR spectra for the Pc **4** and Pc **6** post the sono-irradiations at the *Par I – Par IV* are shown in the **Fig. 4.6** as examples.

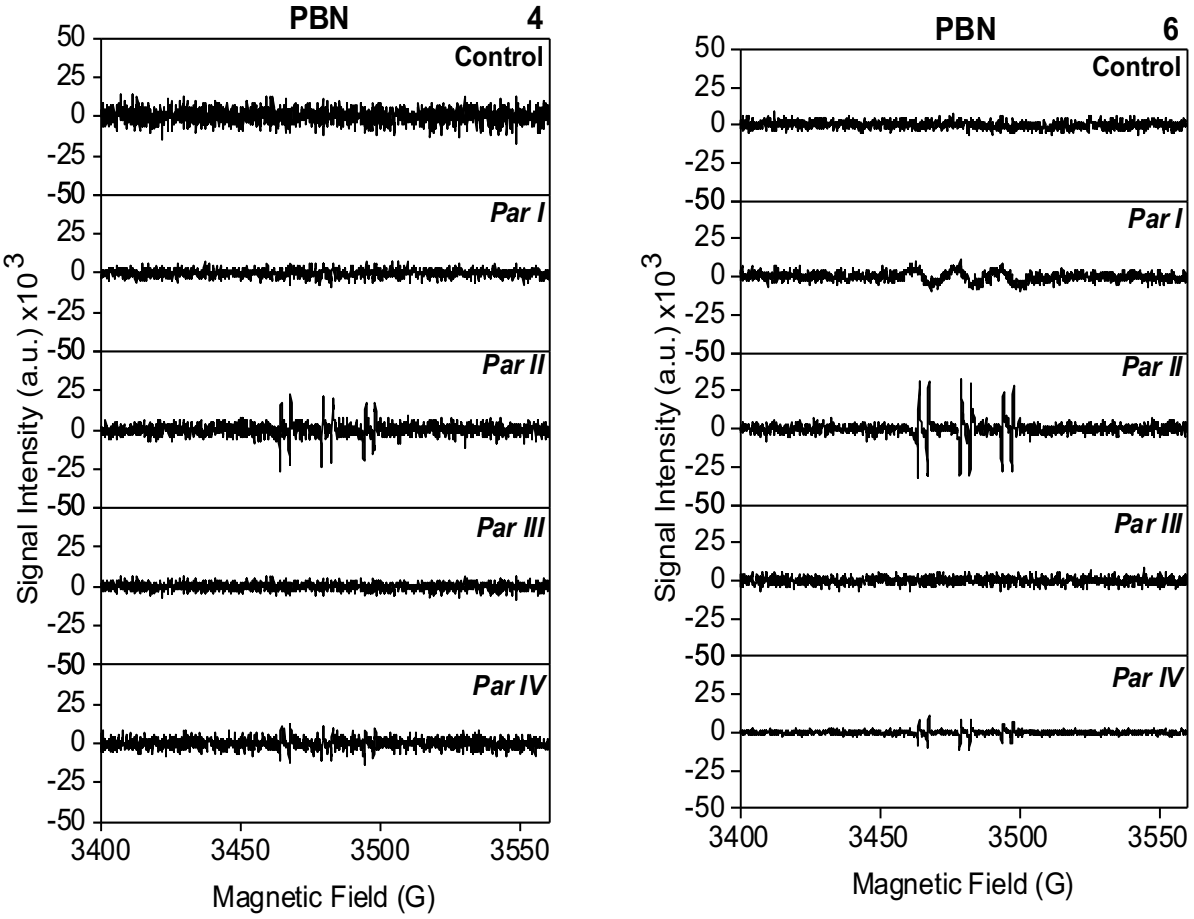

Figure 4.6. The EPR spectra showing the generation of •C using PBN (50 mM) in the presence of the Pc **4** and Pc **6** water after 10 min exposure to the sono-irradiations at *Par I* (1 MHz, 1 W. cm^{-2}), *Par II* (1 MHz, 2 W. cm^{-2}), *Par III* (3 MHz, 1 W. cm^{-2}), and *Par IV* (3 MHz, 2 W. cm^{-2}), at 100% duty cycles.

In the presence of •C, the PBN will form an adduct which will show a three-pair-peak signal at magnetic fields between 3450 G – 3520 G. In this work, the EPR signal intensities for the different sono-irradiations systems were recorded and compared for the Pcs under the different sono-irradiations. The EPR signal peak intensities are directly proportional to the concentration of analyte of study, in this case •C. Thus, an increase in the signal intensity indicates an increase in the quantity of the •C generated. From the **Fig. 4.6**, different intensities of the PBN signals are observed for the four parameters for the Pc **4**. Thus, suggesting that the different parameters affect the Pcs differently. As seen with the Pc degradation in section 4.2.1, previously. The

EPR signal intensities for the PBN signal intensities were recorded for all the Pcs at the under the different sono-parameters and are summarized in the **Table 4.3**. The average intensities for the first peak-pair are recorded for the Pcs **Table 4.3**.

From the **Table 4.3**, the *Par II* and *Par IV* showed relatively higher PBN signal intensities compared to the *Par I* and *Par III*, with the *Par II* showing the highest intensities. These observations are synonymous with those seen for the Pcs degradation studies. Where higher m values obtained for the Pcs corresponded with higher PBN intensities. The R-groups also influence the degree of the effects of the sono-parameters as varying results were seen for the different structures, **Table 4.3**. From the series of the Pcs when comparing only the cationic, Pcs with methyl-quaternizing groups, the *Par II* showed relatively more severe effect on the Pcs bearing aliphatic N-bearing R-groups such as the ethyl- for Pc **1** and morpholino- for Pc **4** and Pc **5**, compared to those with aromatic N-bearing groups such as the Pcs **2**, **3**, and Pc **8**. The zwitterionic Pc **6** and Pc **7** showed higher PBN intensities at the *Par I* and *Par IV* compared their cationic counterparts, Pc **4** and Pc **5**. At the *Par II*, Pc **5** showed higher PBN intensity compared to the corresponding Pc **7.** The zwitterionic Pcs comprise a propyl-chain with a sulphonyl-terminal. The ultrasonic mechanical waves may be affecting the Pcs structures at these non-covalent extension points. Furthermore, the degradation of the Pc **5** and Pc **7** (Pcs with alkyl extensions), is reduced compared to the Pcs from Pc **4** and Pc **6**. This effect is not yet clear. However, the direct linkage of the morpholine group to the Pc core, as seen on the structures of the Pc **4** and Pc **6** may be causing the Pcs to be susceptible to the degradation unlike the linkage of the morpholine linked to an aliphatic chain as in the Pc **6**. Furthermore, when comparing Pcs with the different quaternizing agents, the larger quaternizing agents, ethyl (Pc **1**), 1,3-propanesultone (Pc **6** and Pc **7**) and the TPP (Pc **10** and Pc

11) showed more susceptibility to the US compared to the related Pcs with methyl as the quaternizing agent.

Overall, the observation with the effects of the sono-parameters were interesting. The *Par II* and *Par IV* both have a power of 2 W.cm^{-2}, and therefore, generate bubbles of bigger radii compared to those generated with the lower power of 1 W.cm^{-2} for the *Par I* and *Par III*. The energy released from the jetting of these larger bubbles therefore result in the pyrolysis of the Pcs. Hypothetically, the *Par IV* would be expected to degrade the Pcs more significantly since larger bubble are formed rapidly as a result of increasing both the frequency and power. The increase in both the frequency and power (*Par III*, 3 MHz: 2 W.cm^{-2}), however, showed a lesser extent of Pc degradation compared to the increase in the power only (*Par II*, 1 MHz: 2 W.cm^{-2}). Although this observation is not yet clear, it is however, suspected that the increase in the frequency may cause the bubble to burst rapidly and therefore do not grow to larger radii as it would be expected with the lower frequency. Therefore, the lower frequency in the *Par II* may allow for the formation of larger bubbles which lead to the yield of higher energies during acoustic cavitation. Hence, the degradation of Pcs occurs more significantly at the *Par II* compared to *Par IV.*

4.2.3. Stability of the phthalocyanines in cell culture media under the sono-irradiations.

The stabilities of the Pcs at the *Par I* were relatively better compared to the *Par II – Par IV* as seen with the reduced degradation, **Table 4.3**. Therefore, the *Par I* was selected as the sono-parameters to use for the SPDT treatments. Since the Pcs will be applied in the SPDT treatments of cell lines *in vitro*, the stabilities of the Pcs under sono-irradiations at the *Par I*, including the UV-vis degradation and •C generations

studies, were therefore performed in the cell culture DMEM and compared to those in water. The UV-vis spectra for the Pcs **1**, **3** and **4** are shown in the **Fig. 4.7** as examples.

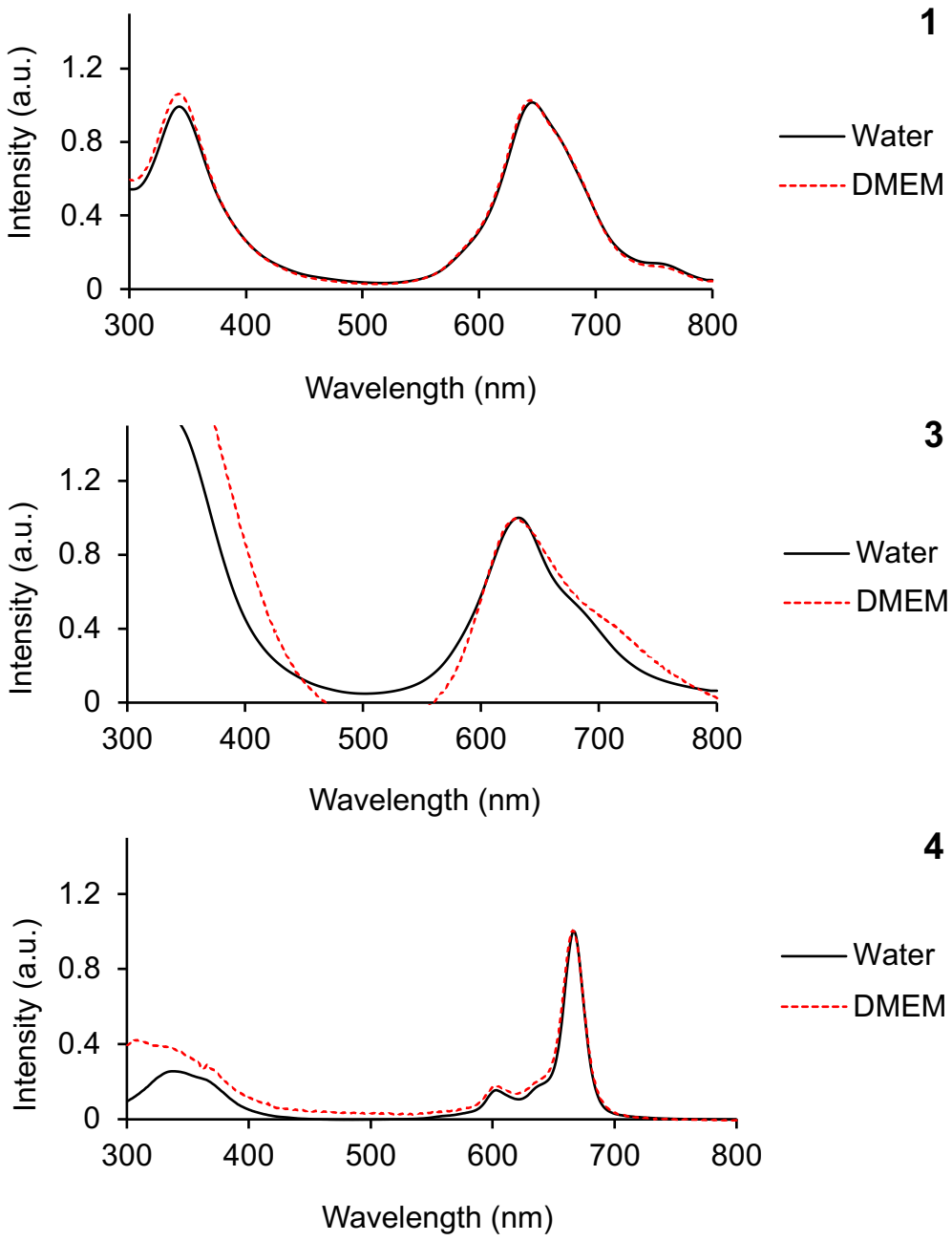

Figure 4.7. UV-vis spectra of the Pc **1**, Pc **3** and Pc **4** (~10 μM) in water and in DMEM.

The UV-vis Q-bands for the Pcs remained relatively unchanged in DMEM compared to water for the Pc **1** and Pc **4**. For the Pcs **3**, the Q-band was slightly broadened, **Fig. 4.7**. The UV-vis λ_{max} in DMEM were recorded for the Pcs and are given in **Table 4.4.**

No significant changes were observed in the λ_{max} in DMEM compared to water for the Pc **1**, Pc **4** – Pc **11**, **Table 4.4**. For the Pc **2** and Pc **3**, the λ_{max} in DMEM were relatively more blue-shifted compared to those obtained in water.

The UV-vis spectra for the Pc **1**, Pc **3** and Pc **4** post sono-irradiations at the *Par I* in DMEM are shown in the **Fig. 4.8** as examples.

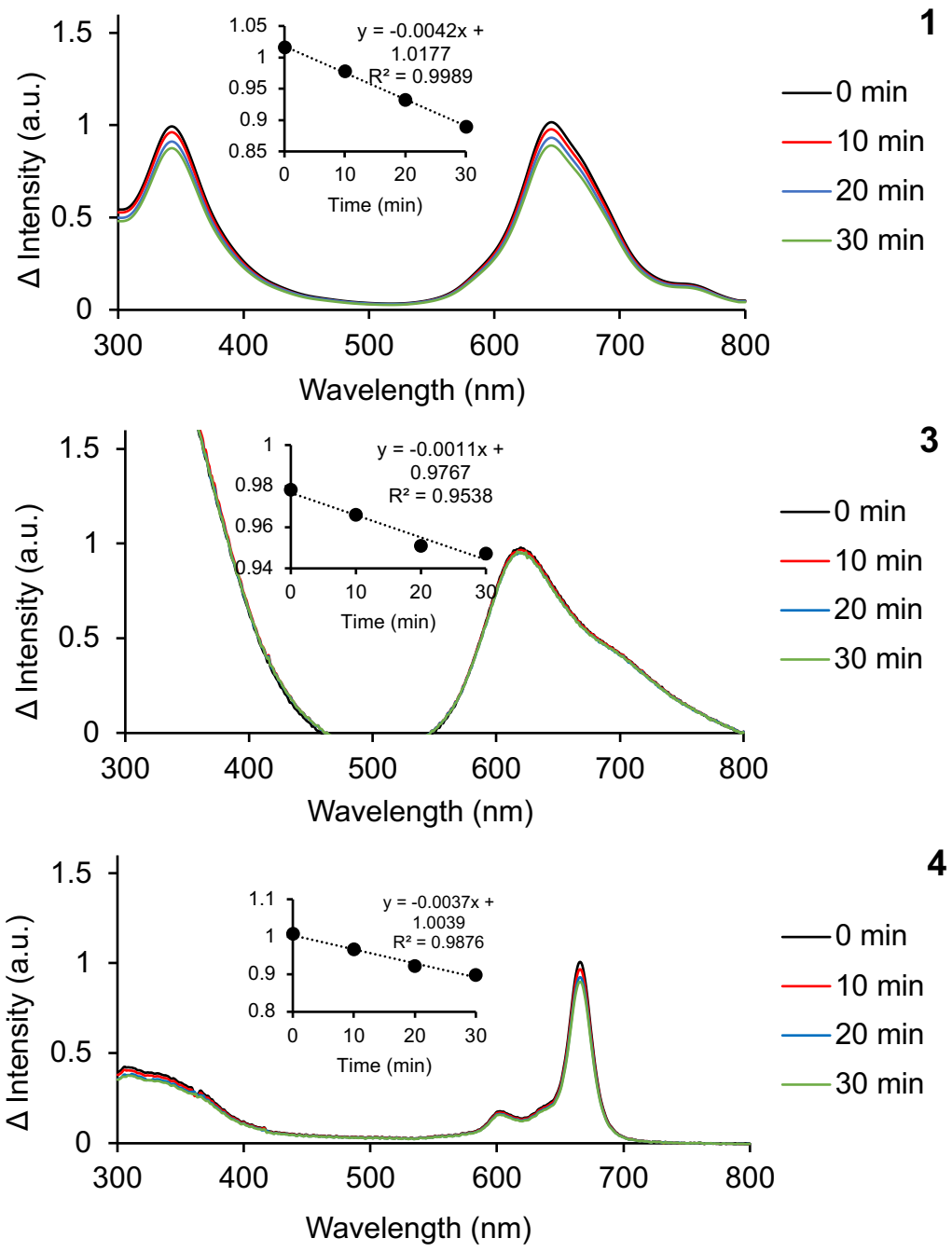

Figure 4.8. Degradation of the Pc **1**, Pc **3** and Pc **4** (10 μM) after the sono-irradiations at *Par I* (1 MHz: 1 W.cm^{-2}, 100% duty cycles) for 30 min in DMEM.

From the **Fig. 4.8**, no significant differences in the stability of the Pc **4** in DMEM was observed compared to those in water for the *Par I* irradiations as judged by the changes in the Q-band intensities. The degradation observed for the Pc **1** Q-band intensities was higher compared to the Pc **3** in DMEM, **Fig. 4.8**. The Pc **3** showed relatively more stability in DMEM.

The UV-vis spectroscopy degradation m-values for all the Pcs in DMEM were calculated and are summarized in the **Table 4.4**.

Table 4.4. Summary of the m-values and the EPR PBN intensities after sono-irradiations of the Pcs at *Par I* in DMEM.

	λ_{max}	UV-vis (*m*) $\times 10^{-3}$	PBN intensity (a.u.) $\times 10^{3}$
1	650 (649)	4.2	8.2
2	642 (634)	1.1	n.d.
3	643 (630)	n.d.	n.d.
4	674 (674)	3.7	8.5
5	647(669)	3.4	n.d.
6	669 (647)	7.9	10.0
7	642 (642)	9.0	9.0
8	645 (644)	1.3	n.d.
9	645 (643)	4.7	n.d.
10	634 (633)	9.8	12.1
11	650 (648)	14.3	13.5

Values in bracket are in water. n.d.: not detected.

The m-values in the DMEM were similar to those obtained in water, with the Pc **6**, Pc **7**, Pc **10** and Pc **11** showing increase m-values relative to the other Pcs, **Table 4.4**.

For the Pc **3**, no degradation was observed in DMEM. This suggests a similar behaviour or the Pcs in DMEM as observed in water.

The EPR PBN specrtra for the Pc **1** – Pc **11** after the sono-irradiations at the *Par I* in DMEM are shown in the **Fig. 4.9**.

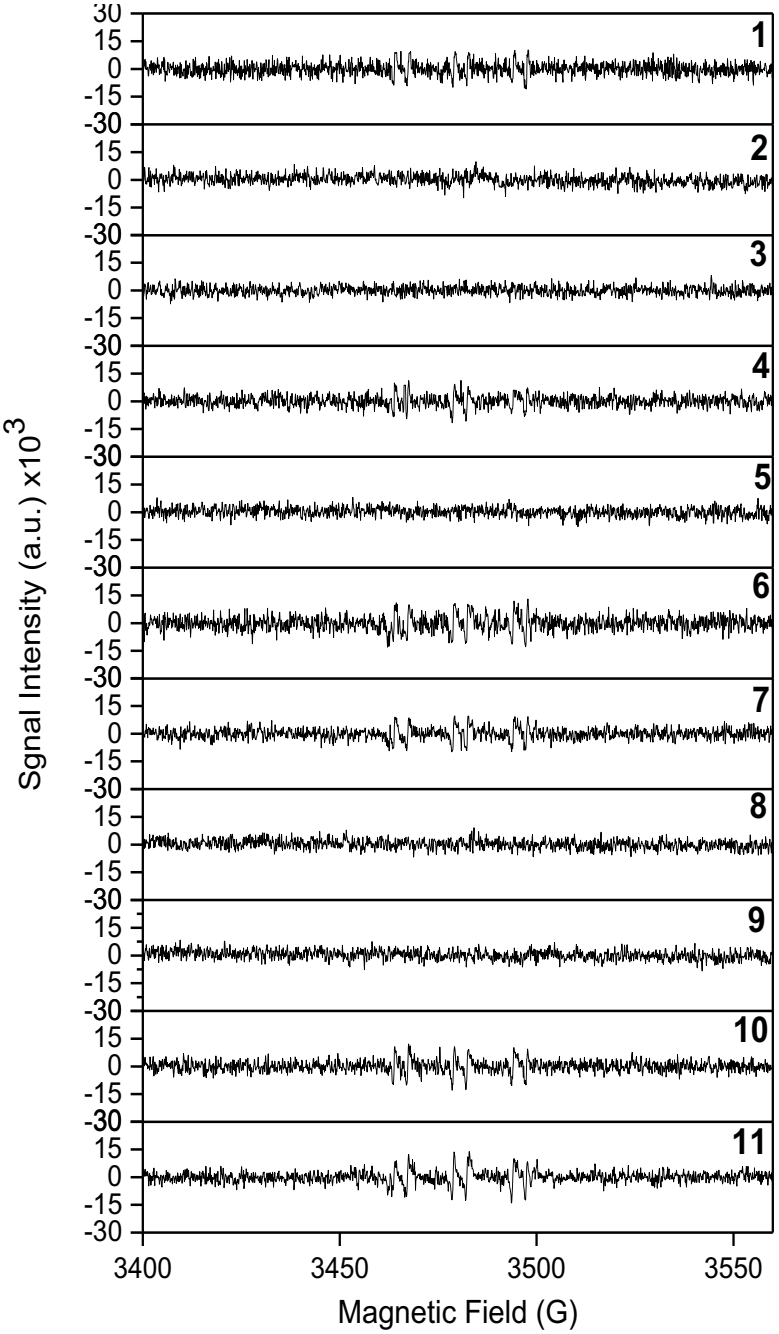

Figure 4.9. The EPR spectra showing the generation of •C using PBN (50 mM) in the presence of the Pc **1** – Pc **11** after 10 min exposure to the sono-irradiations at *Par I* (1 MHz: 1 W.cm^{-2}), at 100% duty cycles in DMEM.

A a summary of the PBN signal intensities in DMEM is also given in the **Table 4.4**.

For the Pc **1** at *Par I,* PBN signals were seen in DMEM, **Table 4.2**, however, no signals were seen for in water, **Table 4.3**. For the Pc **4**, Pc **6**, Pc **7**, Pc **10** and Pc **11**, PBN signals were observed in DMEM at the *Par*, **Table 4.4**, corresponding to the results obtained for the Pcs in water at the *Par I*, **Table 4.3**.

The results obtained from the EPR studies in DMEM were similar to those obtain in water and corresponded to the UV-vis degradation. Therefore, no significant changes in the structures of the Pcs are expected for the sono-irradiations under the *Par I*.

4.3. Summary of chapter.

The photophysical parameters differed for the different Pcs and the Pc-NPs conjugates. The Pcs and conjugates generally showed Φ_F values lower than 0.25 and Φ_T values greater than 0.58. For the NPs conjugates, the Φ_T values increased compared to the Pcs alone. This suggests that the NPs promote intersystem crossing and therefore increase the T_1 populations of the Pcs under the photo-irradiations. This observation is important as it may suggest the improvement of $^1O_2$ yields for the Pcs in the presence of the NPs. The stability studies for the Pcs under the sono-irradiations also showed parameter-dependent results. Generally, lower power (1 $W.cm^{-2}$) maintained the Pcs' stability in water as seen with the UV-vis spectra after irradiations at the *Par I* and *Par III*. The increase in the power (2 $W.cm^{-2}$) showed an increase in the degradation of the Pcs as seen with the *Par II* and *Par IV*. The generation of •C were also seen for some of the Pcs at the some of the studied parameters. The *Par II* showed the highest •C yields for the Pcs.

The Pcs were relatively stable at the *Par I* compared to the other sono-parameters in water. In DMEM, the Pcs after irradiations with the *Par I* maintained similar behaviours

CHAPTER FIVE

5. Sono-Photochemical Properties

This chapter reports on the study of the ROS generation of the ionic Pcs under the photo- and/ or sono-irradiations. Two methods were used to determine ROS generation; using the colorimetric method by UV-vis spectroscopy; and the spin trapping method using electron paramagnetic spectroscopy. The effects of the sono-parameters (frequency and power) on the ROS yields by the Pcs are presented. The ROS yields for the Pcs under photo-, sono- and sono-photo combination irradiations are also presented. For these studies, the effects of the Pcs' R-groups and the conjugation of the graphitic and metallic NPs on the ROS yields of the different Pcs are reported.

5.1. Photoinduced reactive oxygen species generation.

The photoinduced generation of $^1O_2$ by the Pcs and the Pcs-NPs conjugates were determined using DPBF and ADMA as the $^1O_2$ quenchers in DMSO and water, respectively. The calculations for the Φ_Δ were done using methods as defined in the section 2.4.3.1.

The UV-vis spectra showing a decrease in the DPBF absorption intensities under photo- irradiations are shown in **Fig. 5.1** for Pc **9** and Pc **10** in DMSO as examples.

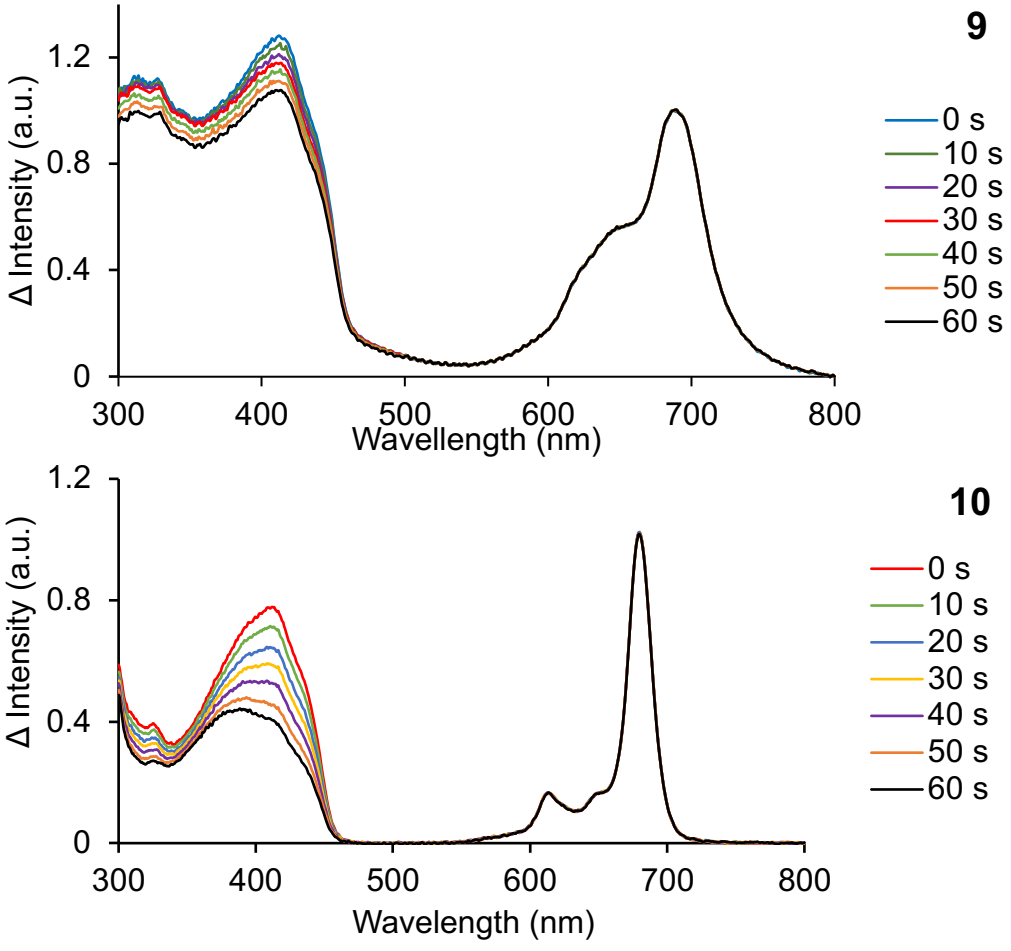

Figure 5.1. The generation of $^1O_2$ by the Pc **9** and Pc **10** under the photo-irradiations (at 670 nm ± 40 nm, 300 W, generating 2.97 × 10^{16} photons^{-1} cm^{-2}) at varied time intervals monitored using DPBF in DMSO.

The UV-vis spectra showing the decrease in ADMA absorption intensities during photo- irradiations are shown in the **Fig. 5.2** for Pc **9** and Pc **10** in water as examples.

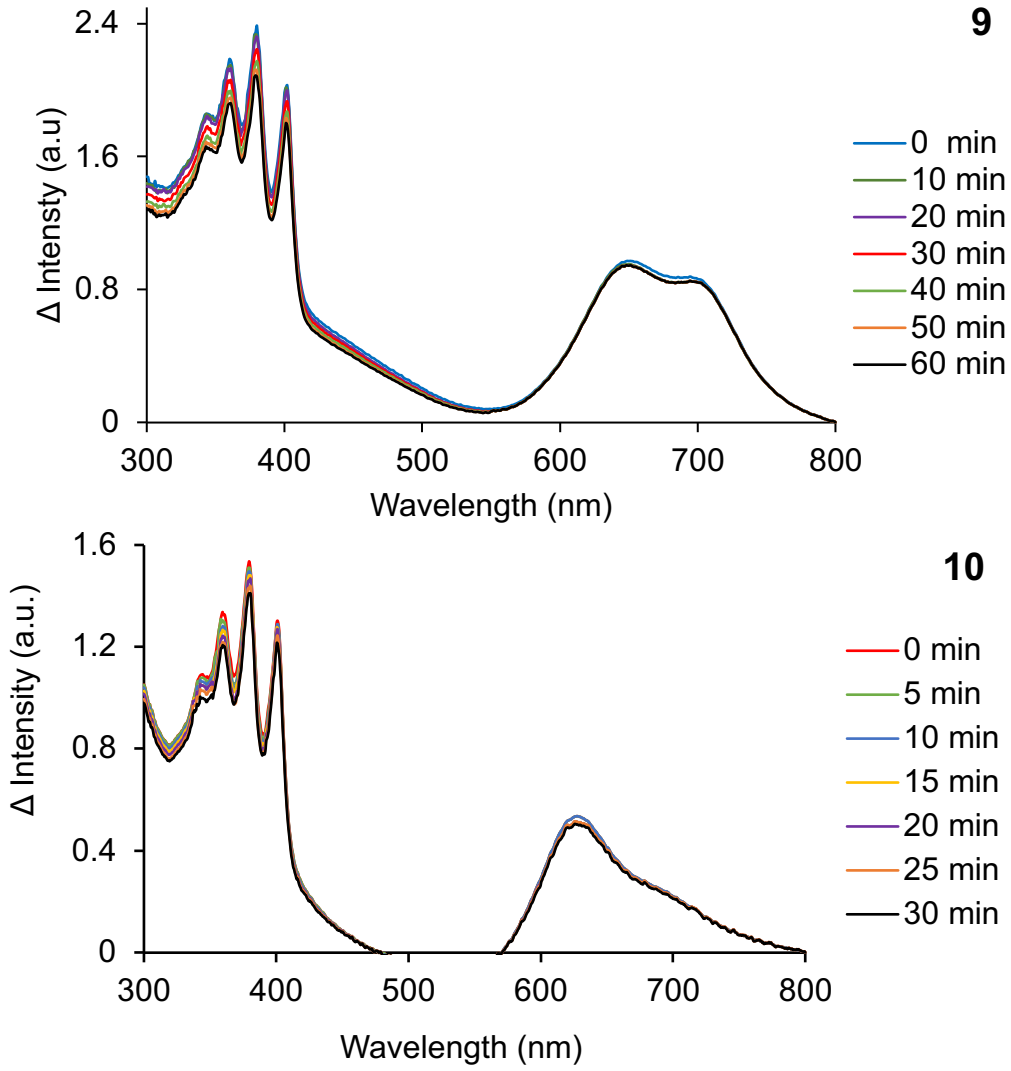

Figure 5.2. The generation of $^1O_2$ by the Pc **9** and Pc **10** under the photo- irradiations (at 670 nm ± 40 nm, 300 W, generating 2.97 × 10^{16} photons^{-1} cm^{-2}) at varied time intervals monitored using ADMA in water.

A decrease in the UV-vis absorption intensities for both the quenchers (between 320 nm – 480 nm) was observed post photo- irradiations of Pc **9** and Pc **10**, **Fig. 5.1** and **Fig. 5.2**. This suggests that there is a photoinduced generation of $^1O_2$ by the Pcs. The Φ_Δ values for the Pcs were thereafter calculated in DMSO and in water. A summary of the Φ_Δ values for the Pcs is given in the **Table 5.1**.

Table 5.1. Summary of the Φ_Δ under photo-irradiations in DMSO and in water.

	Φ_Δ (DMSO)	Φ_Δ (water)	Ref
1	0.58	0.19	-
2	0.60	0.22*	[**105**]
3	0.41	0.13*	[**165**]
4	0.51	0.21	[**107**]
5	0.50	0.14	[**108**]
6	0.50	0.18	-
7	0.43	0.10	-
8	0.31	0.05	-
9	0.35	0.05	-
10	0.56	0.12	-
11	0.53	0.10	-
	With nanoparticles		
NGQDs	n.d.	n.d.	-
NSGQDs	n.d.	n.d.	-
8-NGQDs	0.49	0.09	-
8-NSGQDs	0.43	0.08	-
9-NGQDs	0.51	0.10	-
9-NSGQDs	0.48	0.08	-
AuGSH	n.d.	n.d.	-
AgGSH	n.d.	n.d.	-
8-AuGSH	0.46	0.10	-
8-AgGSH	0.44	0.07	-
9-AuGSH	0.49	0.09	-
9-AgGSH	0.46	0.09	-

n.d.: not detected.

The rates of $^1O_2$ generation differed for the Pcs and therefore, different Φ_Δ values were obtained. A decrease in the Φ_Δ values for the Pcs in water was observed. This is a common observation for Φ_Δ in water compared to the Φ_Δ in organic solvents such as DMSO. Water is known to also quench the $^1O_2$, hence the relatively low Φ_Δ values [**143**]. Reduced Φ_Δ values in water compared to Φ_Δ values in organic solvents have been reported in the literature for Pcs [**182-184**].

5.1.1. Effect of type R-group.

The Pc **1 –** Pc **11** showed evidence of ROS generation under the photo-irradiations. Thus, the Pcs are considerable as sensitizers for PDT. The Pc **1**, Pc **2**, Pc **4** – Pc **6**, Pc **10** and Pc **11** showed Φ_Δ values ≥ 0.50, whereas Pc **7** - Pc **9** had Φ_Δ values <0.50, **Table 5.1**. When comparing the *ortho* pyridyl Pc **2** and the *para* pyridyl Pc **3**, higher Φ_Δ values were obtained for the Pc **2**. The cationic morpholine Pc **5** showed higher Φ_Δ values compared to the zwitterionic Pc **7**. The Φ_Δ values were similar for the Pc **4** and Pc **6**. Increased Φ_Δ values have been reported for some cationic Pcs compared to the zwitterionic Pc counterparts in the literature before [**91,168,182**]. The thiazole Pc **8** and Pc **9** showed the least Φ_Δ values compared to the other Pcs. For the TPP Pcs, the pyridine Pc **10** showed higher Φ_Δ values compared to the morpholine Pc **11**. This observation corresponds to the high Φ_T values obtained for the Pc **10** and Pc **11, Table 4.2**. When comparing the Pc **10** and Pc **11** to the methylated corresponding Pc **3** and Pc **4**, respectively, higher Φ_Δ values were obtained for the TPP-labelled Pcs. The increase in the Φ_Δ values for TPP-Pcs has been reported in the literature [**172**].

5.1.2. Effect of nanoparticles

The Pcs conjugated to the NPs also showed ROS generation under photo- irradiations in DMSO and in water **Table 5.1**. An increase in the Φ_Δ values was observed for all the conjugates compared to the Pc **8** and Pc **9** alone, in both water and DMSO.

The GQDs have generally been shown to improve the photoactivity of Pcs including the increase in their $^1O_2$ generation [**134**]. The conjugates of the Pc **9**, (**9**-NGQD and **9**-NSGQDs) showed relatively higher Φ_Δ values compared to the conjugates of the Pc **8** (**8**-NGQD and **8**-NSGQDs). This observation was expected, since the Φ_Δ value of the non-conjugated Pc **9** was higher compared to Pc **8**. The increase in the Φ_Δ observed for the Pcs upon conjugation with the GQDs has been reported to be due to a phenomenon known as Förster resonance energy transfer (FRET) or the non-radiative dipole–dipole coupling [**185,186**]. FRET involves the quenching of the photoluminescence of the GQDs by nearby Pc molecules, causing an energy transfer from the GQDs to the Pcs. This type of interaction between the Pcs and the GQDs results in the increase in the T_1 population of the Pcs and thus higher Φ_Δ. Moreover, higher Φ_Δ values were seen for the NGQDs conjugates (the **8**-NGQDs and **9**-NGQDs) compared to the NSGQDs conjugates (the **8**-NSGQDs and **9**-NSGQDs), **Table 5.1**. This may be attributed to the higher loading of the Pcs on the NGQDs compared to the NSGQDs.

Metallic NPs are known to improve the intersystem-crossing pathways for Pcs resulting in increased T_1 population through enhance spin-orbital coupling caused by the heavy metal effect as previously stated in the Chapter One [**187,188**]. An increase in the T_1 populations may result in an increase in the of the Φ_Δ Pcs. Improvements in the Φ_Δ values has been reported for the conjugates of the Pcs with Au and Ag NPs in

the literature [**49,127,141**]. Higher Φ_Δ values were generally observed for the Pc conjugated to the AuGSH (the **8**-AuGSH and **9**-AuGSH) compared to those obtained for the conjugates with the AgGSH (the **8**-AgGSH and **9**-AgGSH), **Table 5.1**.

5.2. Reactive oxygen species generation: Effect of ultrasound parameters.

The ROS generation of the Pcs under the sono-irradiations at the varied parameter combinations were determined using the EPR spectroscopy. The parameter combinations for the sono-irradiations were *Par I* (1MHz, 1W.cm^{-2}), *Par II* (1MHz, 2W.cm^{-2}), *Par III* (3MHz, 1W.cm^{-2}) and *Par IV* (3MHz, 2W.cm^{-2}). Two EPR spin trapping reagents were used, including TEMP (for $^1O_2$) and DMPO for (•OH) for ROS detection. The EPR spectra were first collected for the control samples including water alone, Pc solutions alone, the spin trapping reagent solutions alone, all before and after exposure to the sono-irradiations at the different parameters. All the control samples showed no EPR signals. Thus, no ROS generation was observed.

The EPR spectra for the study of the effect of the ultrasonic parameters on the ROS generation are shown in the **Fig. 5.3** for the Pc **5** and Pc **7** as examples.

Both the $^1O_2$ and •OH generation was observed for the Pcs at the different sono-irradiations. This is seen with the EPR TEMP and DMPO signals for the Pc **5** and Pc **7**, used as examples, in **Fig 5.3**.

The different EPR signal intensities suggests that the changes in the frequency and power affects the efficiencies of ROS yields by the Pcs during the sono-irradiations.

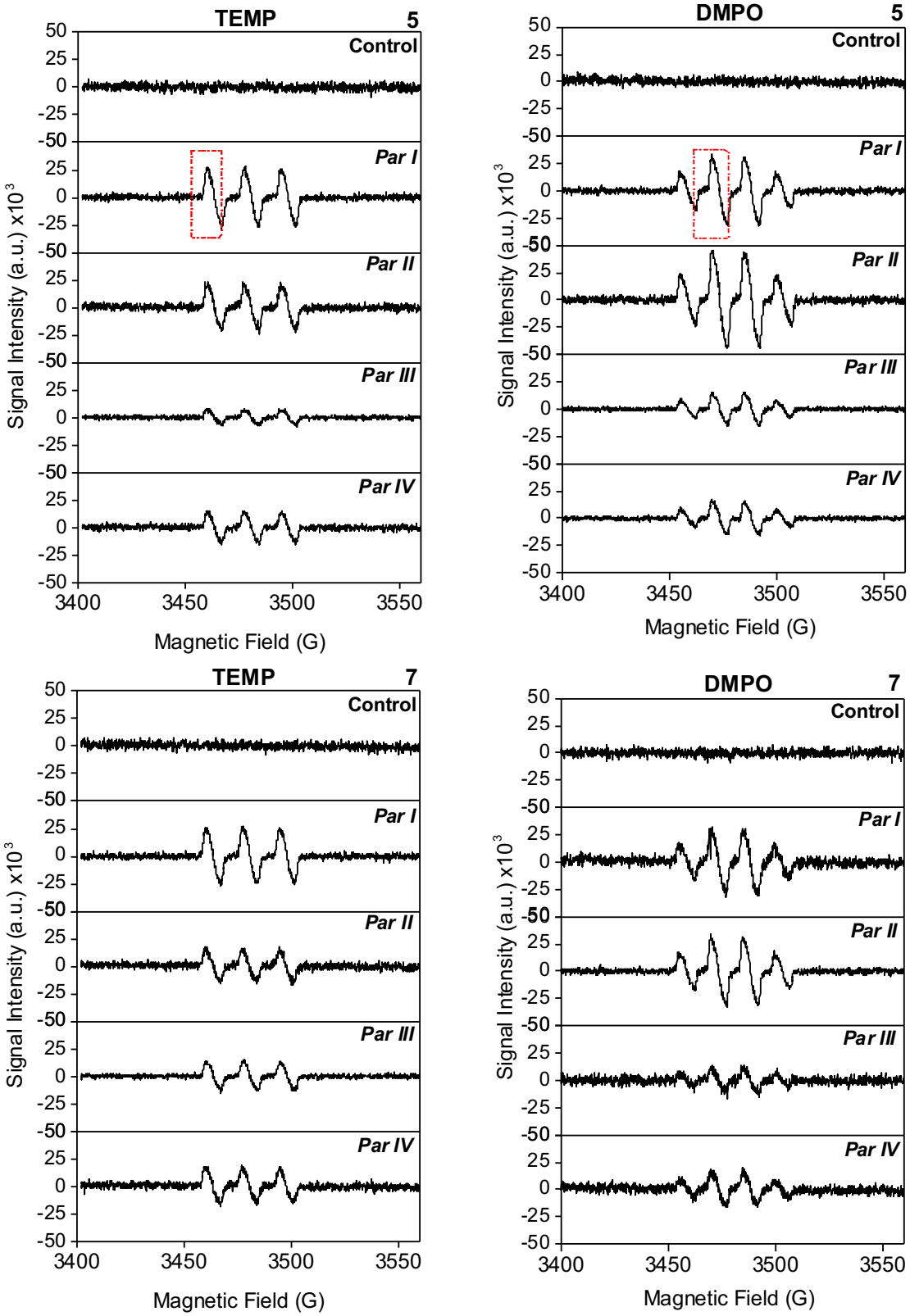

Figure 5.3. The EPR spectra showing the generation of $^1O_2$ using TEMP (50 mM) and •OH using DMPO (50 mM) in the presence of Pc **5** and Pc **7** after sono-irradiations at the *Par I* (1 MHz, 1 W. cm^{-2}), *Par II* (1 MHz, 2 W. cm^{-2}), *Par III* (3 MHz, 1 W. cm^{-2}), and *Par IV* (3 MHz, 2 W. cm^{-2}), at 100% duty cycles, for 10 min in water.

The TEMP and DMPO EPR signal intensities were recorded for the Pcs and compared. The signal intensities of the first peaks from the TEMP, and the signal intensities of the second peaks from the DMPO signals were recorded for the Pcs as shown in **Fig. 5.3**.

The EPR TEMP and DMPO signal intensities for the Pcs under the sono-irradiations were obtained and are summarized in **Table 5.2**.

Table 5.2. Summary of the EPR TEMP and DMPO signal intensities for the sono-irradiations of the Pcs at the different parameters.

	Signal Intensity (a.u.) x10^3							
	TEMP ($^1O_2$)				DMPO ($^{\bullet}$OH)			
	Par I	*Par II*	*Par III*	*Par IV*	*Par I*	*Par II*	*Par III*	*Par IV*
1	8.7	8.9	8.4	14.2	4.0	0.0	0.0	0.0
2	16.9	9.6	12.9	13.8	27.0	29.2	0.0	20.0
3	25.3	19.8	18.5	23.7	13.5	57.0	0.0	31.1
4	24.7	14.7	11.0	20.0	30.5	74.3	17.5	42.5
5	27.0	21.6	18.9	22.1	33.8	57.8	23.5	38.0
6	19.8	10.1	9.9	11.7	15.3	17.2	10.1	17.0
7	20.1	17.2	13.9	17.7	28.8	31.7	13.7	19.8
8	18.3	11.4	9.0	15.8	11.3	14.4	0.0	8.0
9	18.9	12.9	9.7	17.9	13.9	14.7	0.0	8.0
10	43.3	29.9	25.9	33.2	63.0	78.2	32.3	72.2
11	37.0	26.0	18.8	25.3	42.0	65.5	28.9	43.9

Par I (1 MHz, 1 W. cm^{-2}), *Par II* (1 MHz, 2 W. cm^{-2}), *Par III* (3 MHz, 1 W. cm^{-2}), and *Par IV* (3 MHz, 2 W. cm^{-2}).

The *Par I* showed higher $^1O_2$ generation compared to all the parameters for the Pc **2** – Pc **11**, **Table 5.2**. For the Pc **1**, the *Par IV* showed higher $^1O_2$ generation. This observation is not well understood. The *para*-pyridyl Pc **3** generally performed better at the different parameters (for both $^1O_2$ and •OH), compared to the *ortho*-pyridyl Pc **2**. The zwitterionic Pcs **6** and **7** showed lower $^1O_2$ and •OH generations under the different parameters compared to their cationic counterparts, Pc **4** and Pc **5**, respectively. The Pcs with an alkyl extension to their morpholine groups Pc **5** and Pc **7** performed better under all the treatments when compared to the Pc **4** and Pc **6** respectively. The ethylated Pc **9** generally showed slightly higher ROS yields for both $^1O_2$ and •OH compared to those observed for the methylated Pc **8** under the different parameters. The TPP-labelled Pc **10** and Pc **11** showed the highest ROS generation of $^1O_2$ and •OH compared to all Pcs at the respective parameters. For the TPP Pcs, the pyridine Pc **10** had higher ROS yields compared to the morpholine Pc **11**.

Although this effect has not been reported for Pcs, the efficiency of acoustic cavitation is reported in the literature to improve for larger molecules such as NPs [**119,189**]. Therefore, the use of bulkier Pcs (Pc **10** and Pc **11**) may result in increased nucleation sites for bubble formation during acoustic cavitation and therefore improved ROS generation under the sono-irradiations, on condition that the Pcs are sono-active in the specific irradiation conditions.

Overall, the *Par I* showed higher $^1O_2$ generation compared to the other parameters, followed by the *Par IV*, **Table 5.2**. The *Par II* and *Par III* generally showed the lowest $^1O_2$ generation. For the •OH generation, the *Par II* was generally higher compared to the other parameters, followed by the *Par IV*. The increase in the US power to 2 W. cm^{-2} (*Par II* and *Par IV*) generally resulted in an increase in the •OH yields for the ionic

Pcs. This was, however, not observed for the Pc **1**. For the Pc **1**, •OH was only detected at *Par I*. Increasing the frequency without increasing the power of the US, 3 MHz, 1 W.cm^{-2} (*Par III*), did not show improvement in the $^1O_2$ and •OH yields when comparing *Par III* to *Par I*, **Table 5.2**. Increasing the power without increasing the frequency of the US, 1 MHz, 2 W.cm^{-2} (*Par II*), showed improved •OH yields for the Pc **2** – Pc **11**, comparing the *Par II* to *Par I*. Increasing both the frequency and power of the US, 3 MHz, 2 W.cm^{-2} (*Par IV*), generally resulted in reduced $^1O_2$ yields when comparing the *Par IV* to the *Par I*. The trends for •OH yields were not clear for the Pcs at *Par IV* compared to *Par I*.

Overall, the ultrasonic power, which results in the formation of larger bubbles during acoustic cavitation, may cause the pyrolysis of some Pcs to yield fragments with reduced ROS generation. Otherwise, the increase power may be used to potentially improve the •OH yields of Pcs in water instead. The frequency of the US, which results in the rapid formation of bubbles during acoustic cavitation, did not improve the $^1O_2$ yields, and did not show a clear trend in terms of •OH yields. Therefore, the lower frequency maintained higher $^1O_2$ yields for the Pcs.

All the control samples showed no EPR signals. The detected $^1O_2$ and •OH under the treatments are dependent on the synergistic activities of both the Pcs and the sono-irradiations at the different parameters in water. The *Par I* (1 MHz: 1 W.cm^{-2}) was selected as the sono- parameters for the combination irradiations. The *Par I* was selected on the basis of high $^1O_2$ generation, and the low degradation of the Pcs observed from the UV-vis and EPR spectroscopy as seen previously. The high degradation in the Pcs during treatments, as seen in the *Par II*, for example, may not

be ideal for the biological applications since the structural identities and the cytotoxic activities of the fragments from the Pcs are not yet known.

5.3. Photo-sono induced reactive oxygen generation.

The EPR spectra for the $^1O_2$ and •OH generation of the Pcs under the photo-, sono- and sono-photo irradiations were obtained. The TEMP and DMPO EPR spectra for the Pc **10** and Pc **11** under the photo- and/ or sono-irradiations are shown in the **Fig. 5.4** as example.

The $^1O_2$ and •OH generation in the combination irradiations was evident for the Pcs as seen with the TEMP and DMPO signals, **Fig. 5.4**. Generally, the signal intensities for the both the $^1O_2$ and •OH increased for the combination irradiations compared to those observed from the photo- and sono- mono-irradiations, **Fig. 5.4**. This observation was expected as the Pcs are excited using both stimuli in the combination irradiations. An increase in the ROS generation has been reported for Pcs under combination irradiations compared to the mono-irradiations in the literature [**55,190,191**].

The EPR signal intensities of the TEMP and DMPO for the Pcs under the photo-, sono- and sono-photo irradiations in water are summarized in the **Table 5.3**. The results for the Pcs-NPs are also given in the **Table 5.3**.

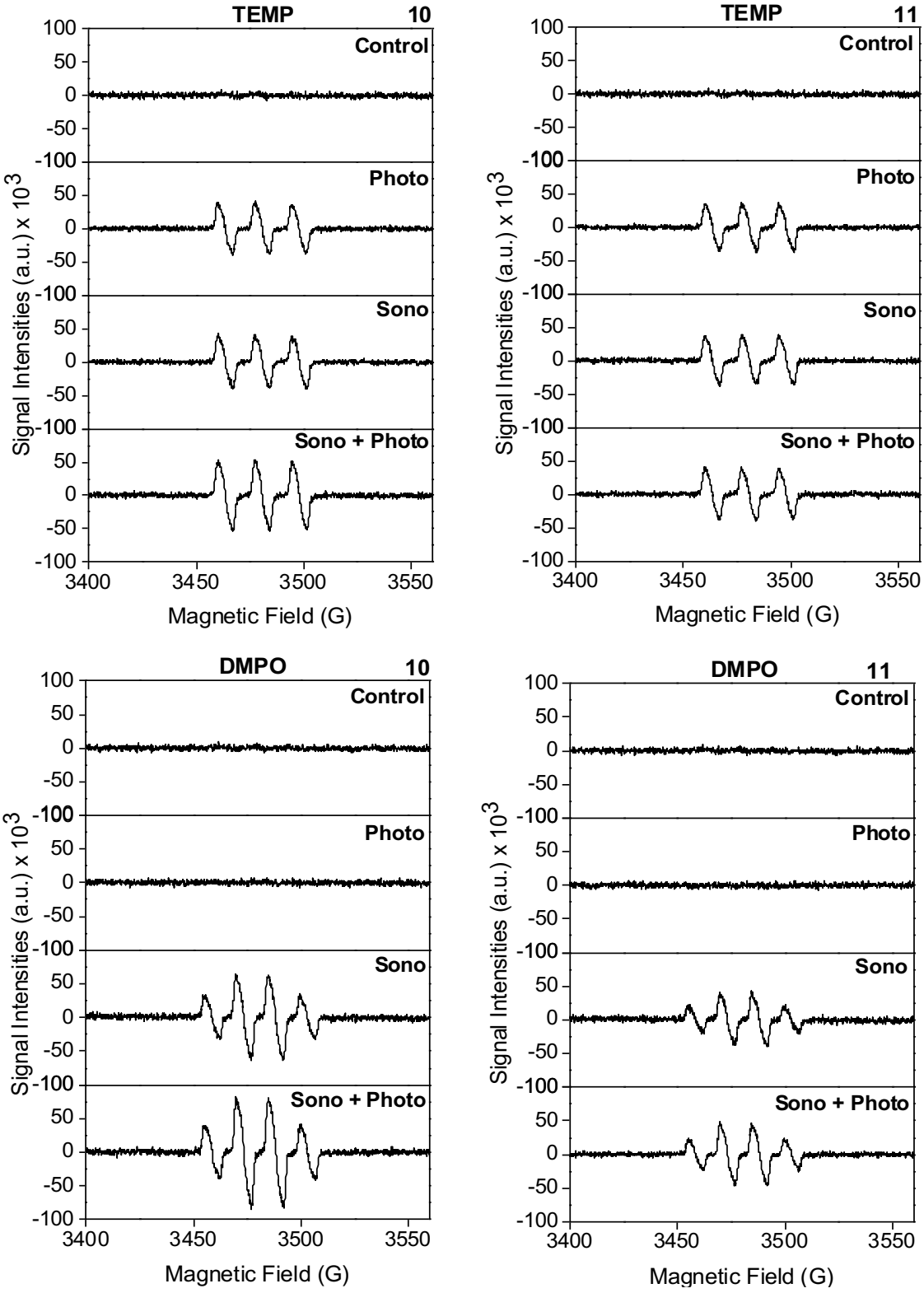

Figure 5.4. The EPR spectra showing the generation of $^1O_2$ using TEMP (50 mM) and •OH using DMPO (50 mM) as the quencher in the presence of the Pc **10** and Pc **11** in water after photo- (at 670 nm ± 40 nm, 300 W, generating 2.97 × 10^{16} photons^{-1} cm^{-2}) or sono- (at 1 MHz, 1 W. cm^{-2}, 100% duty cycles) or the combination of both photo- and sono-irradiations.

Table 5.3. Summary of the EPR TEMP and DMPO signal intensities for photo-, sono- and sono-photo irradiations of the Pcs and Pc-NPs conjugates in water.

	Signal Intensity (a.u.) x10^3					
	TEMP ($^1O_2$)			DMPO ($^{\bullet}OH$)		
	Photo	Sono	Sono-photo	Photo	Sono	Sono-photo
1	26.7	8.7	29.3	n.d.	4.0	6.3
2	29.9	16.9	33.7	n.d.	27.0	33.6
3	33.2	25.3	39.1	n.d.	13.5	30.3
4	36.4	24.4	40.2	n.d.	30.5	35.3
5	26.5	27.0	42.7	n.d.	33.8	49.4
6	34.2	19.8	20.4	n.d.	15.3	33.1
7	14.2	20.1	25.5	n.d.	28.8	44.7
8	16.2	18.3	21.8	n.d.	11.3	12.6
9	17.9	18.9	27.2	n.d.	13.3	13.9
10	37.0	43.3	50.0	n.d.	63.0	83.0
11	35.7	37.0	41.4	n.d.	42.0	51.2
	With nanoparticles					
NGQDs	n.d.	29.2	30.6	n.d.	40.6	63.2
NSGQDs	n.d.	27.2	29.6	n.d.	10.4	19.3
8-NGQDs	36.2	39.5	53.2	n.d.	50.1	67.1
8-NSGQDs	29.9	35.8	50.0	n.d.	25.0	38.5
9-NGQDs	38.2	43.2	58.4	n.d.	55.0	70.0
9-NSGQDs	31.2	37.8	51.3	n.d.	33.0	40.0
AuGSH	n.d.	9.9	16.1	n.d.	<8.0	8.4
AgGSH	n.d.	9.2	14.7	n.d.	<8.0	<8
8-AuGSH	28.6	21.6	33.8	n.d.	16.5	18.6
8-AgGSH	25.5	20.0	32.8	n.d.	20.3	23.4
9-AuGSH	41.4	28.3	50.3	n.d.	26.3	28.7
9-AgGSH	34.6	23.2	48.6	n.d.	21.5	23.8

n.d.: not detected.

5.3.1. Effect of type of R-group.

The Pc **1** – Pc **4** and Pc **6** showed higher $^1O_2$ generation under the photo-irradiations compared to sono-irradiations in water, **Table 5.3**. Whereas the Pc **5**, Pc **7**, Pc **10** and Pc **11** showed higher $^1O_2$ generation under the sono-irradiations compared to the photo-irradiations. The •OH were evident for the sono-irradiations in the mono-irradiations and the combination irradiations. For the photo-irradiations, none of the Pcs were able to generate the •OH. For the Pcs, the $^1O_2$ has been reported to be the predominant ROS generated in PDT [**192**].

The combination treatments showed higher ROS generation compared to the photo and sono- mono-irradiations for all the Pcs except for the Pcs **6**, showing lower $^1O_2$ for the combination irradiations compared to photo-irradiations, **Table 5.3**. This observation was not expected. The *ortho*-pyridine Pc **2** generally showed lower $^1O_2$ compared to the *para*-pyridine Pc **3** for photo-, sono-, and combination irradiations. However, the Pc **2** performed better in the •OH generation compared to the Pc **3** for the photo- and/ sono- irradiations. The cationic Pc **4** and Pc **5** showed higher ROS generation compared to their corresponding zwitterionic counterparts, Pc **6** and Pc **7**, respectively. Where the Pc **5** and **7** with an alkyl extension to the morpholine showed better $^1O_2$ and •OH yields under the sono- and combination irradiations compared to the Pc **4** and Pc **6**, respectively. The ethylated Pc **9** generally showed high $^1O_2$ and •OH yields compared to the methylated Pc **8** for the photo- and/ sono- irradiations. The TPP-labelled Pc **10** and Pc **11** generally showed higher $^1O_2$ and •OH generation compared to the other Pcs, however, the $^1O_2$ for the Pc **11** was slightly lower compared to the Pc **4** under the photo-irradiations and lower than the Pc **5** under the combination irradiations.

5.3.2. Effect of nanoparticles.

The effects of NPs on the ROS yields of the Pc **8** and Pc **9** were evaluated. The TEMP and DMPO EPR spectra for the Pc **9** and the NGQDs and NSGQDs NPs and conjugates under the sono-photo combination irradiations are shown in the **Fig. 5.5.** as examples.

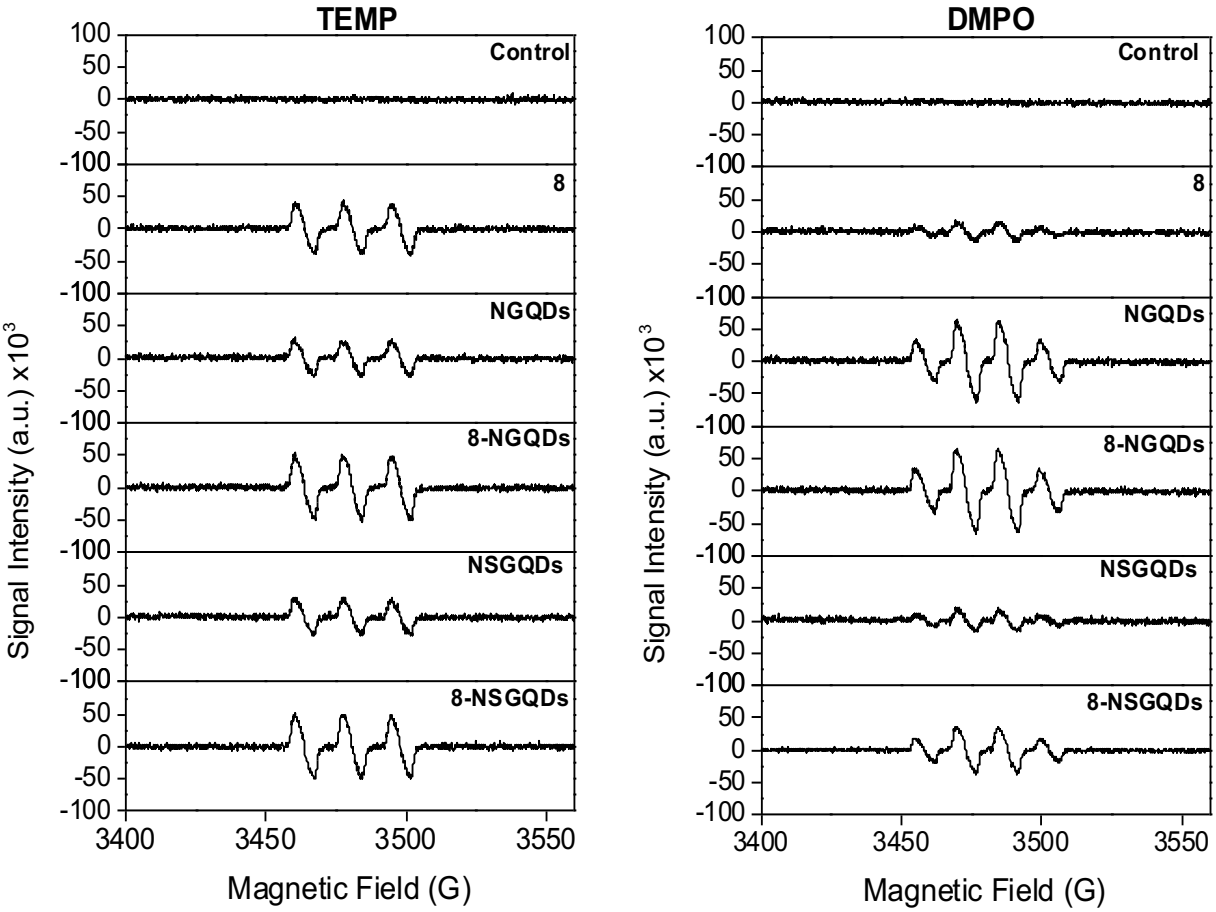

Figure 5.5. The EPR spectra showing the generation of $^1O_2$ using TEMP (50 mM) or $^{\bullet}OH$ using DMPO (50 mM) as the quencher in the presence of 5 μg/mL of Pc **9** and its NGQDs and NSGQDs conjugates after photo- (at 670 nm ± 40 nm, 300 W, generating 2.97 × 10^{16} photons^{-1} cm^{-2}) and sono- (at 1 MHz, 1 W. cm^{-2}, 100% duty cycles) combination irradiations in water.

Evidence of both the $^1O_2$ and •OH at varying intensities under the combination irradiations were seen for the Pcs, NGQDs, NSGQDs and conjugates, **Fig. 5.5** in water. The TEMP and DMPO EPR spectra for the Pc **9** and the AuGSH and AgGSH

NPs and conjugates under the sono-photo combination irradiations are shown in the **Fig. 5.6.** as an example.

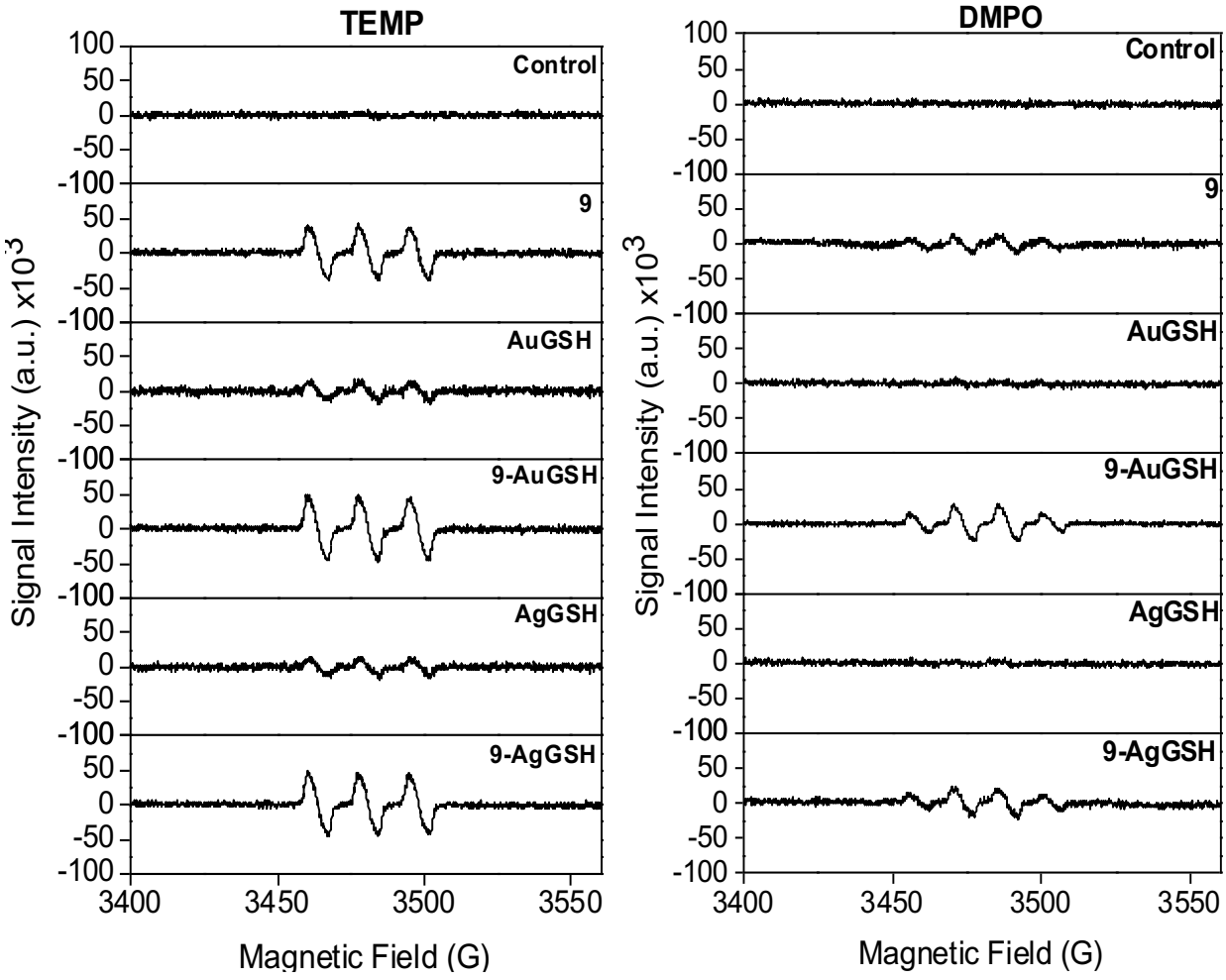

Figure 5.6. The EPR spectra showing the generation of $^1O_2$ using TEMP (50 mM) or $^{\bullet}OH$ using DMPO (50 mM) as the quencher in the presence of 5 µg/mL of Pc **9** and its AuGSH and AgGSH conjugates after the photo- (at 670 nm ± 40 nm, 300 W, generating 2.97 × 10^{16} photons^{-1} cm^{-2}) and sono- (at 1 MHz, 1 W. cm^{-2}, 100% duty cycles) combination irradiations in water.

Evidence of both the $^1O_2$ and •OH under the combination irradiations were seen for the Pcs, AuGSH, AgGSH and conjugates, **Fig. 5.6** in water. Generally, lower •OH yields were observed compared to the $^1O_2$ yields, **Fig. 5.6**.

The TEMP and DMPO EPR signal intensities were recorded for the NGQDs, NSGQDs, AuGSH and AgGSH NPs and Pc-NPs and the conjugates with the Pc **8**, Pc **9** under the photo- and/ or sono-irradiations and are summarized in the **Table 5.3**.

The NGQDs generally showed higher $^1O_2$ and •OH yields compared to the NSGQDs alone and in the conjugates for all the treatment types, **Table 5.3**. For the photo-treatments, these observations are synonymous with those observed for the photoinduced Φ_Δ as shown previously. For the sono-irradiations, the higher ROS generations seen for the NGQDs and NGQDs conjugates may be due to the increased in the NPs size compared to the NSGQDs as shown by the TEM and DLS size estimations earlier.

The ethylated Pc **9** conjugates with the NGQDs and NSGQDs showed better performance compared to the methylated Pc **8** conjugates, **Table 5.3**.

The ROS generation of the AuGSH and AgGSH alone were generally lower compared to those observed for the Pcs alone and the Pc-NPs conjugates under the photo- and/ or sono-irradiations, **Table 5.3**. The $^1O_2$ yields were slightly higher for the AuGSH, AgGSH NPs and the Pc-NPs compared to the •OH yields. The $^1O_2$ and •OH generation was slightly higher for the AuGSH and the Pc-AuGSH conjugates compared to the AgGSH NPs and the Pc-AuGSH conjugates for the photo- and/ or sono-irradiations. These results completement the results observed with the Φ_Δ values previously with the AuGSH conjugates showing higher Φ_Δ values compared to the AgGSH conjugates.

Additionally, for US mediated treatments, larger NPs are reported to increase the surface area for bubble nucleation, therefore improving the efficiency of acoustic

cavitation and ROS generation as stated previously [**117**,**120,193**]. Similar to the results seen for the GQDs conjugates, the ethylated Pc **9** conjugates with the AuGSH and AgGSH showed better $^1O_2$ and •OH yields compared to the conjugates of the methylated Pc **8**. The trends in the $^1O_2$ yields of the Pcs upon conjugation with the NPs was not clear when comparing the yield from the Φ_Δ values (**Table 5.1)** and the photoinduced EPR signals for the $^1O_2$ yields (**Table 5.3**). However, when comparing ROS yields on sono-irradiations for the conjugates, the NGQDs and NSGQDs showed higher yields compared to the AuGSH and AgGSH for $^1O_2$ and •OH.

5.4. Summary of chapter.

The Pcs showed ROS generation under the sono-irradiations at the different ultrasonic parameters varying the frequency and power. Two ROS were detected by EPR spectroscopy included $^1O_2$ and •OH. The *Par I* generally showed higher $^1O_2$ generation compared to the other parameters for all the Pcs, as seen with the high TEMP signals. The *Par II* generally showed a higher increase in the •OH generation for all the Pcs. The photo-, sono- and sono-photo irradiations also showed ROS generation. Where the photo- irradiations showed only the generation of $^1O_2$. The sono- and sono-photo combination irradiations showed the generation of both the $^1O_2$ and •OH. The combination irradiations generally showed higher $^1O_2$ and •OH yields compared to the photo- or sono- mono- irradiations. When comparing the Pcs, the larger TPP-labelled Pcs showed higher $^1O_2$ and •OH yields under the sono-irradiations in both the mono- and combination irradiations. An increase in the $^1O_2$ and •OH generation of the thiazole Pc **8** and Pc **9** was observed upon conjugation to the organic and inorganic NPs. The NPs alone including the NGQDs, NSGQDs, AuGSH and AgGSH showed the ROS generation under the sono-irradiations. For the organic NPs, the Pc conjugates with the NGQDs showed higher $^1O_2$ and •OH yields under photo-, sono- and combination irradiations compared to those with the NSGQDs. And in the case of the inorganic NPs, the Pc conjugates with the AuGSH showed higher $^1O_2$ and •OH yields under the photo- and/ or sono-irradiations compared to those with the AgGSH.

Overall, the NGQDs and NSGQDs NPs showed higher $^1O_2$ and •OH yields compared to the AuGSH and AgGSH NPs under the photo- and/ or sono-irradiations.

CHAPETR SIX

6. Biological Studies

This chapter reports on the *in vitro* anticancer activities of the ionic Pcs on the HeLa and MCF-7 cells under different treatments. The SDT activities of the Pcs under the different sono-parameters varying the frequency and power of the ultrasound are presented. Additionally, the PDT and SDT mono-treatments as well as the SPDT combinatorial treatments are also presented. The cell survival percentages of the cells and IC_{50} concentrations for the Pcs under the treatments are reported. The effects of the treatments on the cellular morphologies for the different treatments are also presented. Additionally, the cellular uptake studies for the Pcs are reported. The effects of the Pcs R-groups as well as the effect of the NPs on these studies are evaluated.

The BSA protein binding studies in water are also reported for the Pcs in this chapter.

6.1. Sonodynamic therapy: Effect of ultrasonic parameters.

The effects of the ultrasonic parameters on the SDT activities of the ionic Zn Pcs were evaluated on the HeLa and MCF-7 cell lines *in vitro*. The US parameters as studied for the ROS generation previously were evaluated on the cells: *Par I* (1 MHz: 1 W.cm^{-2}), *Par II* (1 MHz: 2 W.cm^{-2}), *Par III* (3 MHz: 1 W.cm^{-2}) and *Par IV* (3 MHz: 2W.cm^{-2}).

6.1.1. Cytotoxicity and IC_{50} studies.

The cell survival percentages 24 h post sono-treatments alone at test parameters were determined to evaluate the effects of the US on the cells *in vitro*, **Fig. 6.1**.

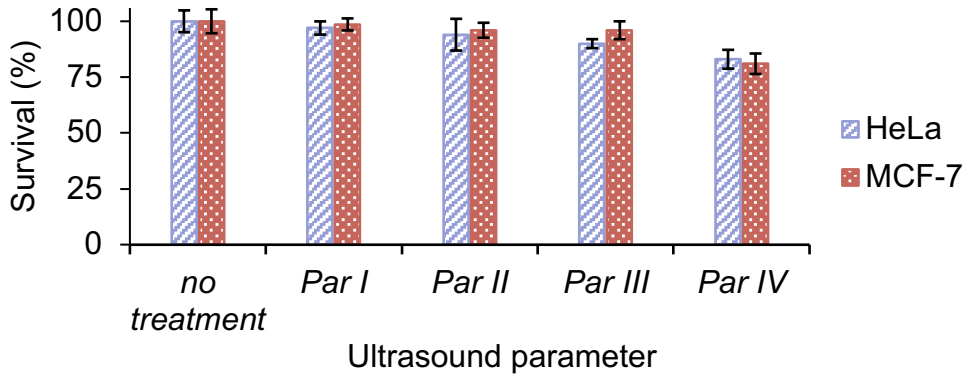

Figure 6.1. Cell survival plots for the HeLa and MCF-7 cells 24 h post sono-treatments with at different parameters: *Par I* (1 MHz, 1 W. cm^{-2}), *Par II* (1 MHz, 2 W. cm^{-2}), *Par III* (3 MHz, 1 W. cm^{-2}), *Par IV* (3 MHz, 2 W. cm^{-2}), at 100% duty cycles *in vitro*. n=3.

There was a slight decrease in the cell survival percentages for the sono treated cells for the *Par I – Par IV* compared to the untreated cells **Fig. 6.1**. This was seen in both cell lines *in vitro*. The cells, however, showed >80% survival under all the sono-treatments at the different parameters. This suggest that the sono-treatments alone are minimally or are not causing cytotoxicity. The cell survival percentages for the SDT treated cells (with the Pcs, 0 μM – 100 μM) were obtained at the different parameters for both cell lines.

The cell survival plots for the Pcs **10** and **11** are shown in **Fig. 6.2** as examples.

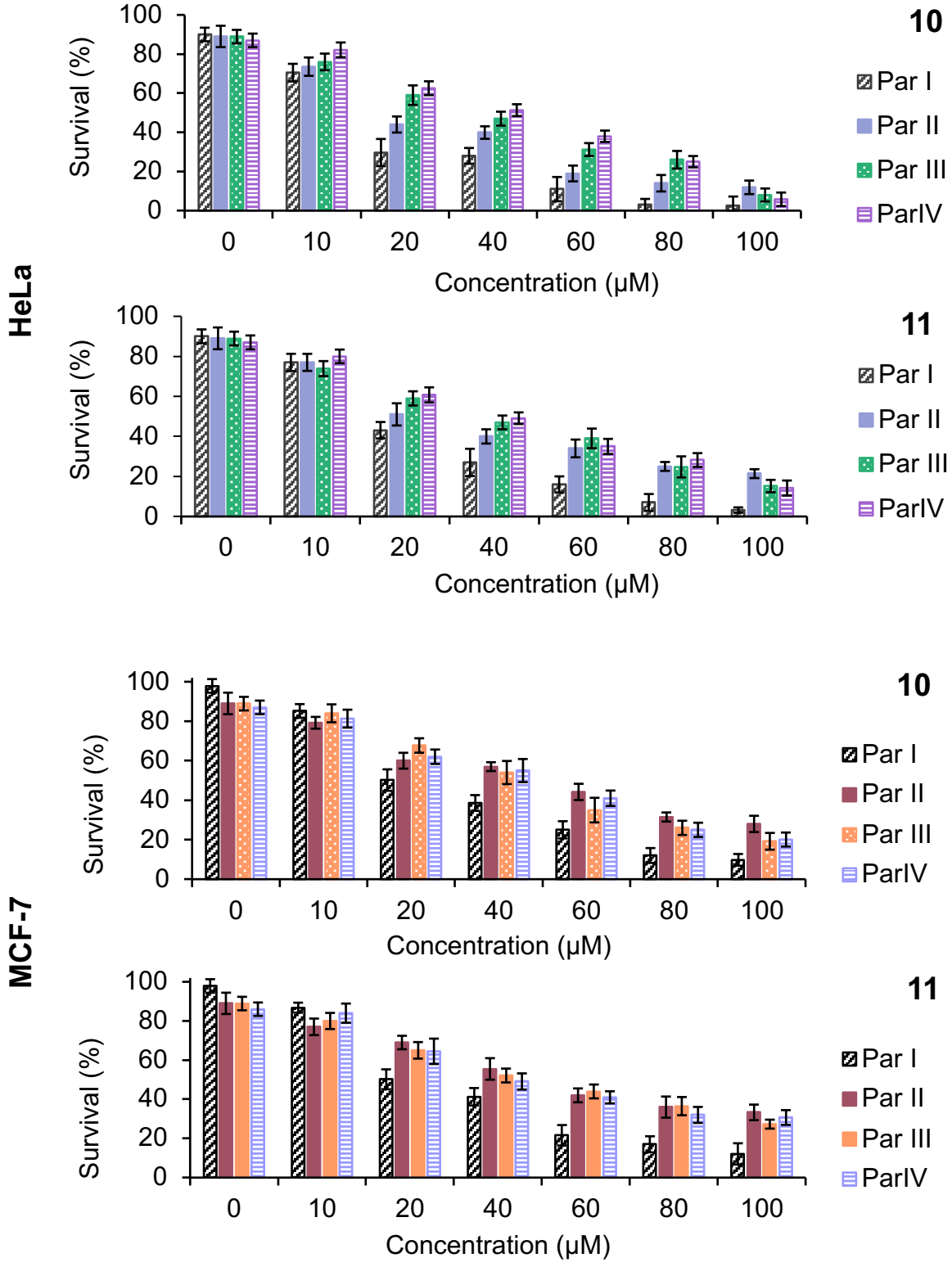

Figure 6.2. Cell survival plots for the HeLa and MCF-7 cells 24 h post SDT treatments at: *Par I* (1 MHz, 1 W. cm^{-2}), *Par II* (1 MHz, 2 W. cm^{-2}), *Par III* (3 MHz, 1 W. cm^{-2}), *Par IV* (3 MHz, 2 W. cm^{-2}), at 100% duty cycles, in the presence of Pc **10** and Pc **11** *in vitro*. n=3.

A decrease in the cell survival percentages was observed with increasing Pc concentrations for both the cell lines for the *Par I – Par IV*, **Fig. 6.2**. The trends for cell eradication *in vitro* under the different parameters differed slightly for the Pcs. The *Par I* generally showed relatively higher *in vitro* therapeutic efficacies as seen with the lower cell survival percentages compared to the *Par II – Par IV*, **Fig. 6.2**. This observation may be attributed to the reduced Pcs degradation observed for the *Par I*, therefore retaining the sono-active Pcs for therapy. The *Par II* and *Par III* showed the least efficacy compared to the other parameters, as seen with a higher cell survival percentage despite the *Par II* showing high •OH yield, seen previously in **Table 5.2**. This may indicate that the $^1O_2$ may be the predominant ROS resulting in the cytotoxic effects observed, compared to the •OH. For the *Par III*, the reduced cellular activity may be due to the reduced ROS production compared to the other parameters. The results are synonymous with the EPR results as seen in the **Table 5.2**, previously.

The effects of the different structural features on the Pcs to determine structural characteristics that may enhance or reduce the SDT activities of Pcs, in addition to the ultrasonic parameters. The survival percentages of the HeLa and MCF-7 cells exposed to the Pcs alone at increasing concentrations were generally >80% (not shown). This suggests reduced toxicity of the Pcs and the dependence of their toxicity on the sono-treatments.

The cell survival percentages for treatments with 100 μM and the IC_{50} concentrations of the Pcs under the SDT treatments at the different parameters are summarized in the **Table 6.1**.

Table 6.1. Summary of the cell percentages and IC_{50} values of HeLa and MCF-7 cells 24 h post SDT treatments at different parameters with the Pc **1** – Pc **11** at 100 μM.

	Cell survival (%)				IC_{50} (μM)			
	Par I	*Par II*	*Par II*	*Par IV*	*Par I*	*Par II*	*Par II*	*Par IV*
	HeLa Cells							
1	56.1	58.45	63.3	51.1	>100	>100	>100	>100
2	16.5	31.1	29.8	33.2	42.0	51.0	73.5	63.5
3	10.4	29.7	13.6	12.3	48.0	52.3	67.0	53.5
4	5.0	31.8	17.9	5.6	22.5	36.5	49.0	41.6
5	0.0	27.2	9.6	0.0	19.5	31.0	22.5	41.3
6	52.8	69.1	62.9	53.8	>100	>100	>100	>100
7	60.4	67.4	60.0	61.2	>100	>100	>100	>100
8	32.2	47.6	50.3	44.0	71.0	78.5	100.0	91.4
9	29.6	38.2	30.7	35.5	63.5	81.0	81.2	88.0
10	2.6	11.9	8.0	5.8	14.3	15.5	35.2	40.2
11	3.2	21.4	15.2	14.2	17.2	22.0	35.8	39.5
	MCF-7 Cells							
1	60.0	60.2	58.9	49.4	>100	>100	>100	98.5
2	18.3	46.2	47.7	35.4	51.3	70.3	72.9	61.2
3	12.1	28.4	19.8	17.2	39.9	50.9	44.4	47.6
4	10.2	17.0	20.0	15.3	33.5	41.8	55.2	39.8
5	10.5	19.1	11.0	11.9	31.2	53.0	41.6	38.3
6	49.4	68.9	52.1	64.2	72.5	>100	>100	>100
7	49.1	63.6	54.6	59.2	62.5	>100	>100	>100
8	41.0	52.6	47.4	41.6	60.1	>100	66.1	59.0
9	37.8	55.3	41.5	38.7	53.5	>100	62.6	55.4
10	9.8	28.0	19.2	20.1	18.2	40.0	43.1	32.1
11	12.1	33.3	27.3	30.7	20.5	43.2	47.7	41.0

The Pc **1** showed the least performance of compared to the cationic Pc **2** – Pc **5** and Pc **8** – Pc **11** for *Par I – Par IV*, on both cell lines. This is seen with higher cell survival percentages post treatments with the Pc **1**. The *para*-pyridyl Pc **3** showed better anticancer activities compared to the *ortho*-pyridine Pc **2** for both the cell types at all four parameters. The cationic Pc **4** and Pc **5** performed better compared to their zwitterionic counterpart Pc **6** and Pc **7**, respectively. Although the Pc **6** and Pc **7** showed evidence of ROS generation under US exposure, zwitterionic Pcs have been reported to show reduced anticancer activity due to reduced cellular uptake since cancer cells take up cationic sensitizers easier through electrostatic interactions with of their anionic membrane [**169,182**]. Kollar *et al.* reported on the improved PDT activities of cationic Pcs compared to their anionic counterparts on HeLa, MF-7 and HCT-116 cell lines *in vitro* [**194**]. Furthermore, Pc **5** with a dimethyl-phenyl extension to the morpholine moiety on the R-group generally showed higher efficacy under the sono-treatments compared to the Pc **4** with the morpholine moiety attached directly to the Pc ring. For the Pc **5**, no HeLa cells were seen post treatments at *Par I* and *Par IV*. These results correspond to the relatively high ROS yields obtained for the Pc **5** at the different sono-parameters compared to the Pc **4** as seen in the **Table 5.2** previously. The thiazole Pc **8** and Pc **9** also showed anticancer activity, with the ethylated Pc **9** generally showing better anticancer activities compared to the methylated Pc **8**. The TPP-labelled Pc **10** and Pc **11** generally showed improved activity at the *Par I – Par IV* for the HeLa cells compared to the corresponding Pc **3** and Pc **4**, respectively, except for the *Par IV* for Pc **11**, where the corresponding Pc **4** showed higher cytotoxicity for the HeLa cells. For the MCF-7 cells, the trends were not clear for the Pc **10** in comparison to the Pc **3**. For the Pc **4**, however, the MCF-7 cell survival percentages were lower under all the treatments compared to the

corresponding Pc **11**. The IC_{50} values for the Pcs at the different parameters were determined.

The IC_{50} plots for the Pcs **10** and Pc **11** are shown in the **Fig. 6.3** as examples.

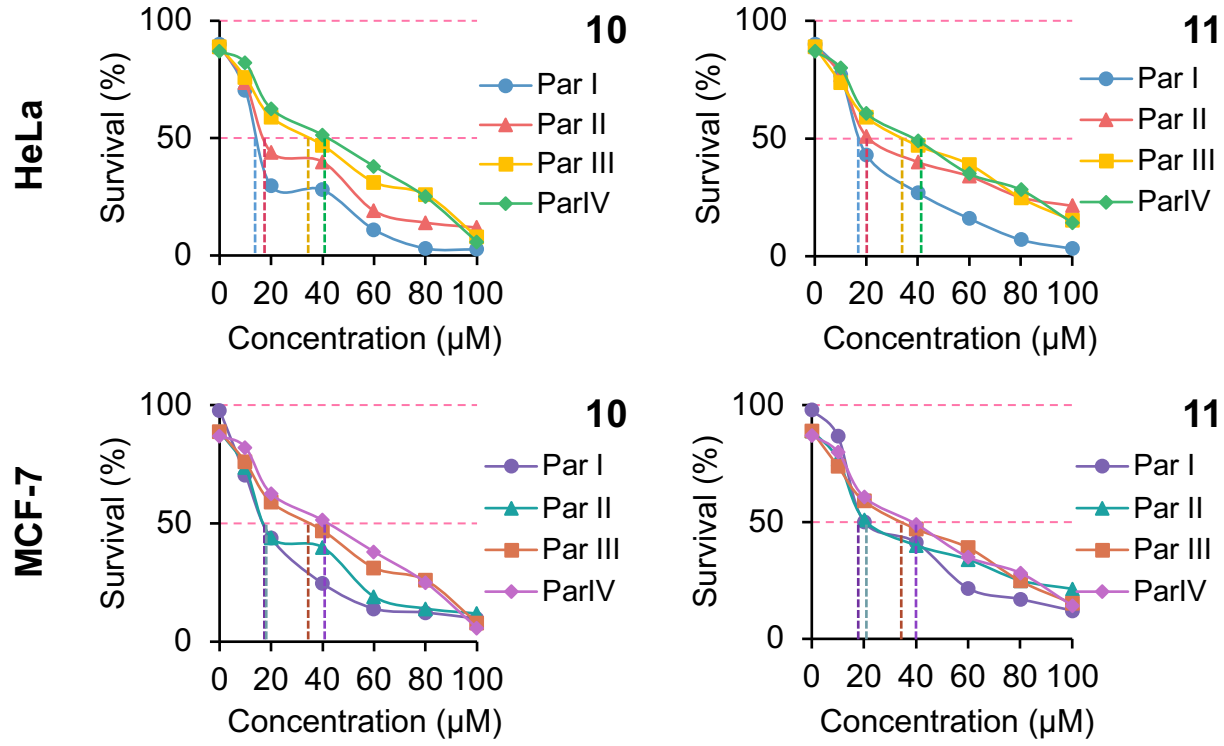

Figure 6.3. Determination of the IC_{50} values for the HeLa and MCF-7 cell 24 h post SDT treatments at different parameters: *Par I* (1 MHz, 1 W. cm^{-2}), *Par II* (1 MHz, 2 W. cm^{-2}), *Par III* (3 MHz, 1 W. cm^{-2}), *Par IV* (3 MHz, 2 W. cm^{-2}), at 100% duty cycles, in the presence of Pc **10** and Pc **11** *in vitro*. n=3.

The IC_{50} values are generally inversely proportional to the therapeutic efficacies of drug molecules. Where an increase in the therapeutic efficacy is usually coupled with a lower IC_{50} value. The IC_{50} values represent the minimum drug concentrations required to eradicate 50% of the cells in the culture. The IC_{50} values extrapolated from the plots in the **Fig. 6.3**, were lower for treatments that showed a higher cell percentage reduction. The *Par I* generally had lower IC_{50} values compared to the other parameters both the cell lines. The *Par III* and *Par IV* showed higher IC_{50} values, corresponding to the higher cell survival.

6.1.2. Effect on cell morphology.

The effects of the SDT treatments at the different sono-parameters on the morphologies of the cells were also studied for the HeLa and MCF-7 cell lines *in vitro*. The cellular morphologies before and post treatments were compared in terms of sizes and shapes.

The images of the control untreated HeLa and MCF-7 cells are shown in **Fig. 6.4**.

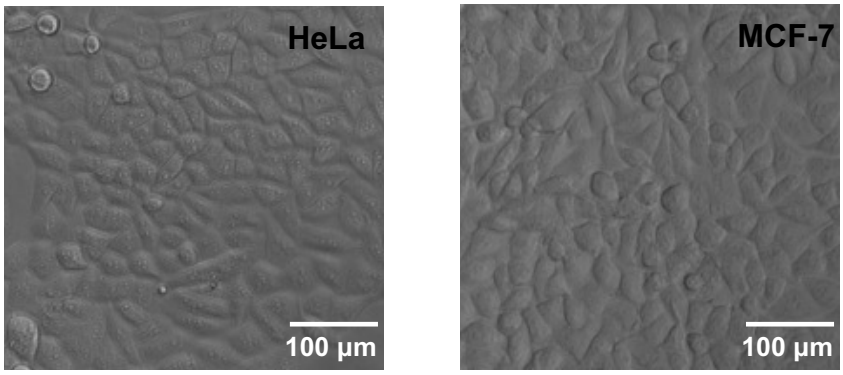

Figure 6.4. The micro-images of the untreated healthy HeLa and MCF-7 cells.

The images of the untreated (control) cells show live cells with a fusiform shape that resemble a cobblestone morphology, for both cell types, **Fig. 6.4**. The cellular images for the HeLa and MCF-7 cells 24 h post SDT treatments at the different parameters and the Pc **3** are shown in the **Fig. 6.5** as examples.

After SDT treatments, the number of the cells decreases as seen for both cell lines. Affected cells shrink and become circular like in shape, appearing rougher in texture compared to live cells, **Fig. 6.5**. From the images, the *Par I* showed a relatively more severe damage on the cells compared to the other parameters. The *Par II* and *Par III* showed more live cells after treatments compared to the *Par I* and *Par IV*, **Fig. 6.5**.

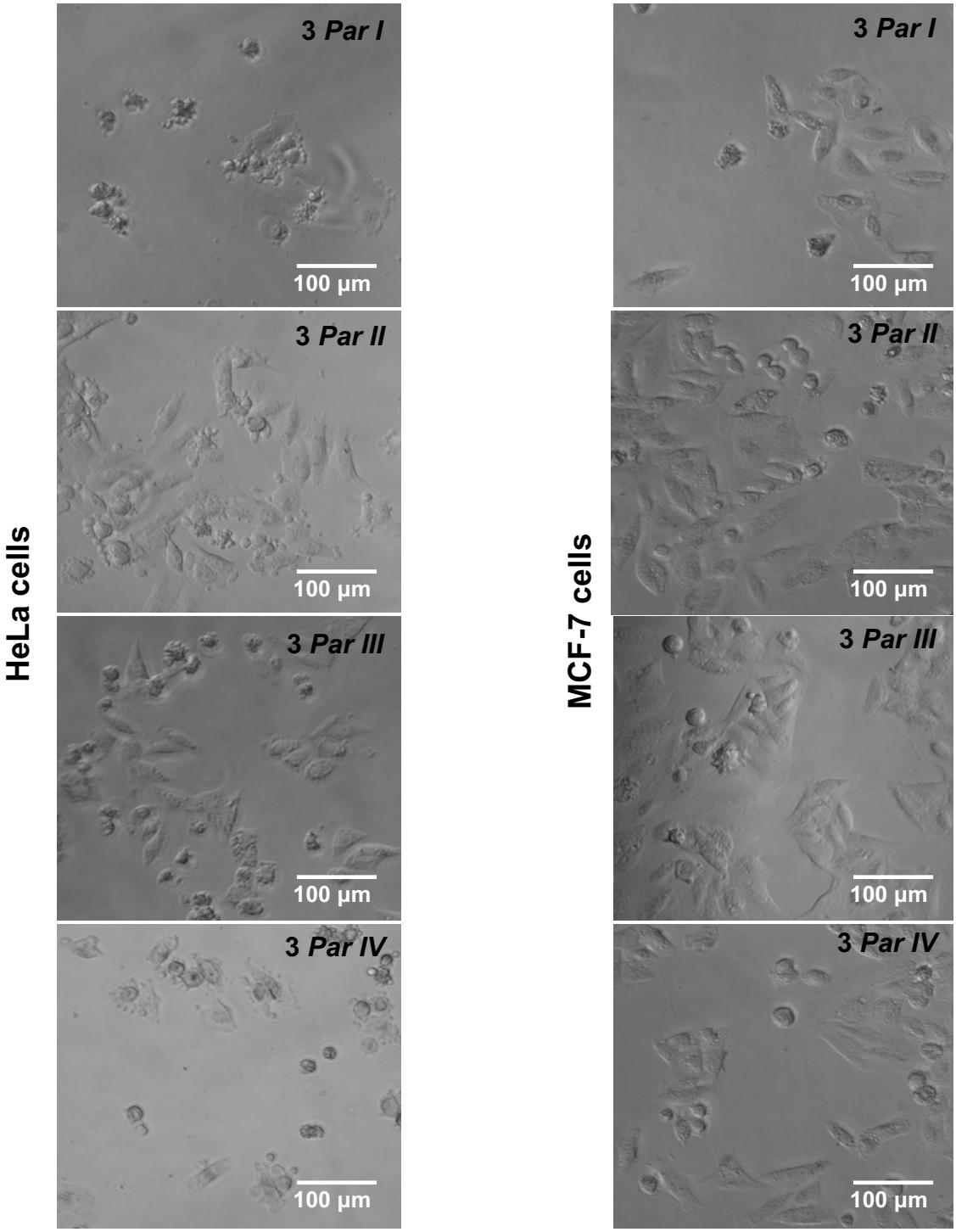

Figure 6.5. The micro-images of the HeLa and MCF-7 cell 24 h post-SDT treatments with the ultrasound *Par I* (1 MHz, 1 W. cm^{-2}), *Par II* (1 MHz, 2 W. cm^{-2}), *Par III* (3 MHz, 1 W. cm^{-2}), *Par IV* (3 MHz, 2 W. cm^{-2}), at 100% duty cycles, in the presence of Pc **3** (80 µM).

The changes in the morphologies of the cells were expected since the treatments induce cell death. The cancer cells are reported to shrink when they undergo

apoptosis. The HeLa and MCF-7 have been reported to undergo apoptosis under SPDT [**195**]. Some of the treated cells showed apoptotic bodies around, **Fig. 6.5**. An image showing an example of cells with apoptotic bodies is shown in the **Fig. S7**.

6.2. Sono-Photodynamic combination therapy.

For the SPDT treatments, the sono *Par I* was used. This is due to the reduced degradation of the Pcs, substantial ROS generation and *in vitro* cancer eradication efficiencies at the *Par I* treatments compared *Par II – Par IV*).

6.2.1. Cytotoxicity and IC_{50} studies.

The effects of the photo-, sono- and combination treatments alone (in the absence of the Pcs) on the HeLa and MCF-7 cells 24 h post exposure, **Fig. 6.6**.

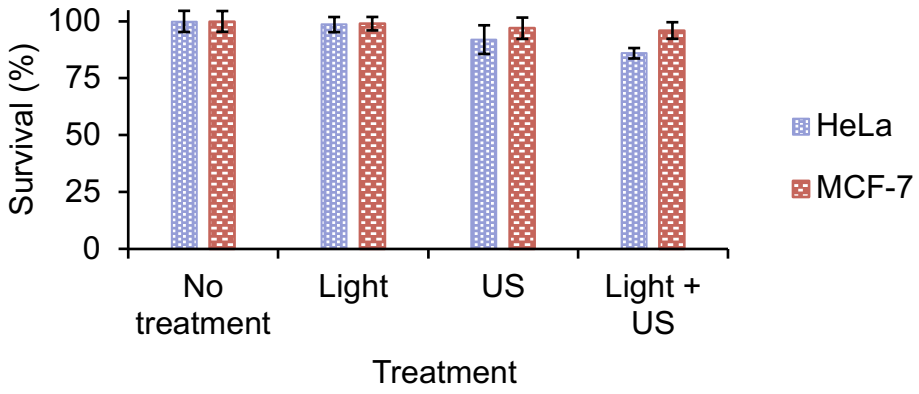

Figure 6.6. The cell survival plots of the HeLa and MCF-7 cells 24 h post photo-(at 680 nm with irradiation doses of 170 $J.cm^{-1}$), sono-(at 1 MHz: 1 W. cm^{-2}, 100% duty cycles), and the combination treatments alone *in vitro*. n=3.

Minimal to no reduction in the cell survival percentages was observed for the cells under photo-, sono- and combination treatments *in vitro*, **Fig. 6.6**. The survival percentages of the HeLa and CF-7 after the PDT, SDT and SPDT treatments for the Pcs at increasing concentrations (0 μM – 100 μM) were calculated.

6.2.1.1. Effects of R-group.

The cell survival plots for the Pc **10** and Pc **11** are shown in the **Fig. 6.7** as examples.

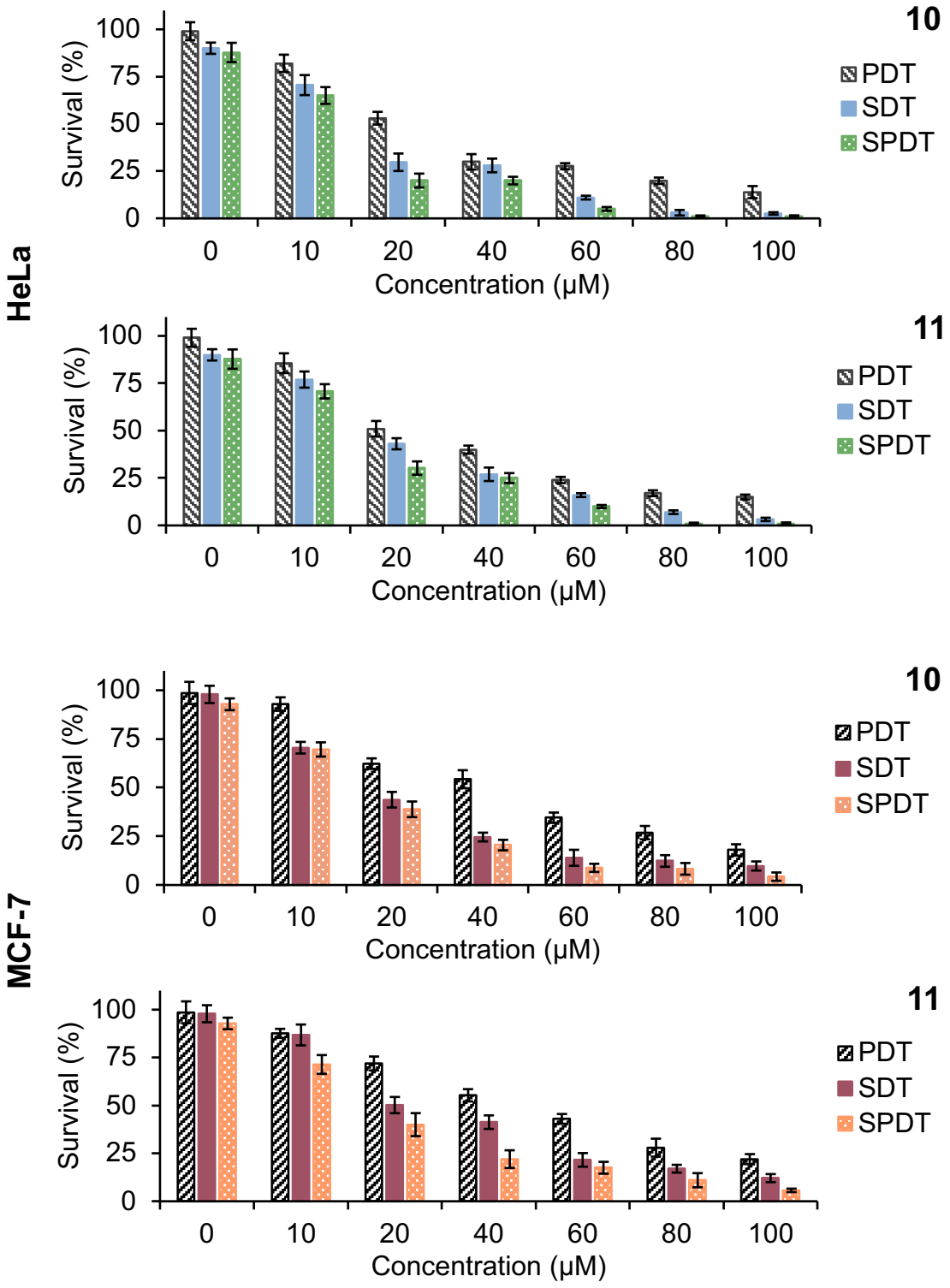

Figure 6.7. The cell survival plots for the HeLa and MCF-7 cells 24 h post PDT (at 680 nm with irradiation doses of 170 J.cm^{-1}), SDT (at 1 MHz: 1 W. cm^{-2}, 100% duty cycles) and SPDT treatments, in the presence of Pc **10** and Pc **11** *in vitro*. n=3.

A decrease in the cell survival percentages was observed with increasing Pc concentrations under the PDT, SDT and SPDT treatment, **Fig. 6.7**. Generally, the SDT treatments showed improved therapeutic efficacies, as seen with the lower cell survival percentages, compared to the PDT monotreatments. The combinatorial treatments, SPDT, showed improved therapeutic efficacies compared to the PDT and SDT monotreatments. The IC_{50} values were obtained for the treatments.

The IC_{50} plots for the Pc **10** and Pc **11** are shown in the **Fig. 6.8** as examples.

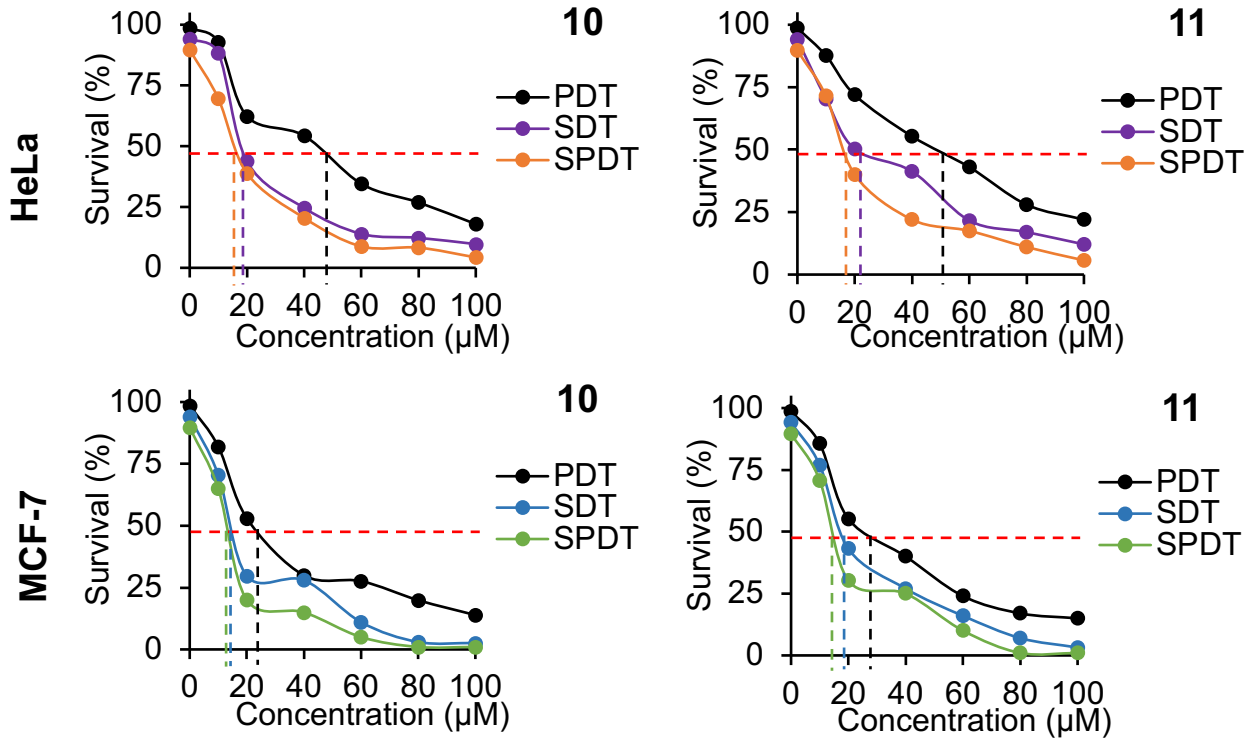

Figure 6.8. Determination of the IC_{50} values for the HeLa and MCF-7 cells 24 h post PDT (at 680 nm with irradiation doses of 170 $J.cm^{-1}$), SDT (at 1 MHz: 1 $W.cm^{-2}$, 100% duty cycles) and SPDT treatments, in the presence of Pc **10** and Pc **11** *in vitro*. n=3.

A summary of the cell survival percentages for cells treated with 100 μM Pcs and the IC_{50} values for the PDT, SDT, and SPDT treatments is given in the **Table 6.2**.

Table 6.2. Summary of cell survival percentages for the HeLa and MCF-7 cells 24 h post PDT, SDT and SPDT treatments with 100 μM Pcs.

	Cell survival (%)			IC_{50} (μM)		
	PDT	SDT	SPDT	PDT	SDT	SPDT
	HeLa Cells					
1	39.4	56.1	29.4	54.3	>100	47.2
2	18.1	16.5	6.1	37.2	26.1	18.2
3	15.6	10.4	3.3	27.0	20.3	16.1
4	8.0	5.0	2.0	45.1	22.5	20.0
5	4.8	0.0	0.0	38.0	19.5	16.0
6	55.9	52.8	46.2	75.5	72.0	48.0
7	63.4	60.4	54.3	75.2	62.5	58.0
8	39.2	32.2	22.4	49.8	49.0	38.1
9	35.5	29.6	17.8	48.2	45.7	34.0
10	13.9	2.6	1.0	21.8	14.3	12.7
11	15.4	3.2	1.0	25.6	17.2	14.4
	MCF-7 Cells					
1	42.3	60.0	37.8	61.2	>100	51.2
2	29.3	18.3	22.6	42.1	32.2	30.5
3	21.6	12.1	12.3	31.5	22.2	20.6
4	20.2	11.2	10.7	38.0	33.5	20.22
5	25.6	10.5	2.0	55.0	31.2	16.2
6	53.0	49.4	41.0	>100	72.5	61.0
7	69.8	49.1	49.9	>100	97.5	62.5
8	41.2	41.0	24.1	55.6	50.0	38.7
9	38.4	37.8	20.9	42.1	47.3	31.2
10	18.1	9.8	4.3	43.3	18.2	13.2
11	22.3	12.1	5.7	45.0	20.5	15.5

The Pc **2** – Pc **11** showed relatively higher anticancer efficacies for the SDT treatments compared to the PDT for both cell lines, **Table 6.2**. This observation may be due to the availability of multiple ROS types in the SDT treatments. For the Pc **1**, however, the PDT treatment showed higher efficacy compared to the SDT monotreatment. Pc **1** shows reduced ROS yield under US treatments as stated above, **Table 5.2**. The *ortho*-pyridine Pc **2** showed relatively lower cytotoxicity seen with the higher cell survival percentages compared to the *para*-pyridine Pc **3**, corresponding to lower singlet oxygen generation in the former. The cationic Pc **4** and Pc **5** had lower cell survival percentages compared to the zwitterionic Pc **6** and Pc **7** for all the treatments, **Table 6.2**. The cationic Pcs are more effective compared to the zwitterionic Pcs as previously mentioned. The ethylated Pc **9** showed relatively higher efficacy compared to the methylated Pc **8**. This observation is consistent with the ROS generation results, as the Pc **9** showed a higher ROS yield compared to the Pc **8**. Furthermore, the extended alkyl-chain with the Pc **9**, allowing for improved lipophilicity, improves the association of the Pcs with the lipid membrane bilayer, thus improving the bioavailability of the compound for treatment. The TPP Pc **10** and Pc **11** generally showed higher SPDT activities for both cell lines compared to their corresponding Pc **3** and Pc **4**, respectively. The trend for the monotreatments were not clear for the Pc **10** and Pc **11** compared to the Pc **3** and Pc **4**.

Overall, the SPDT treatments activities of the Pcs generally showed higher therapeutic efficacies compared to the PDT and SDT monotherapies on both the HeLa and MCF-7 cells *in vitro*, **Table 6.2**. This observation is also evident with the IC_{50} values obtained for the treatments. Where lower IC_{50} values were generally obtained for the combination treatments, SPDT, compared to the corresponding PDT and SDT treatments for the Pcs, **Table 6.2**. When comparing the monotreatments alone, lower

IC_{50} values were obtained for the SDT compared to the PDT treatments. These observations correspond to the cell survival percentages as seen previously for the different treatments on both cell lines.

6.2.1.2. Effects of nanoparticles.

The cytotoxicity studies for the Pc-NPs conjugates were performed to evaluate the effects of the NPs on the PDT, SDT and SPDT activities of the Pcs **8** and Pc **9** against the HeLa and MCF-7 cells *in vitro*. The activities of the Pc **8** and Pc **9** and their conjugates to the NGQDs, NSGQDs, AuGSH and AgGSH were compared. For the study of the effect of NPs on the cytotoxicity therapeutic efficacies of Pcs, concentrations of the Pcs, and conjugates in mg/mL were used (0 mg/mL – 50 mg/mL).

Minimal toxicity was observed for the cells exposed to the NPs and conjugates alone at increasing concentrations without the photo- and sono-irradiations *in vitro*. Where the cell survival percentages obtained for the cells were generally >85%. This suggests that the Pcs, NPs, and the conjugates alone are not toxic to the cells. The cell survival percentages for the HeLa and MCF-7 cells after the PDT, SDT and SPDT treatments using the Pc **8**, Pc **9**, and the respective conjugates with the AuGSH, AgGSH, NGQDs and NSGQDs were determined *in vitro*.

The cell survival plots for the HeLa and MCF-7 cells 24 h after PDT, SDT and SPDT treatments *in vitro* are shown in the **Fig. 6.9** for the Pc **8** and the **8**-NGQDs conjugates, as examples.

A summary of the cell survival percentages for the Pc **8** and Pc **9** conjugates with the NGQDs, NSGQDs, AuGSH and AgGSH at 50 mg/ mL is given in **Table 6.3**.

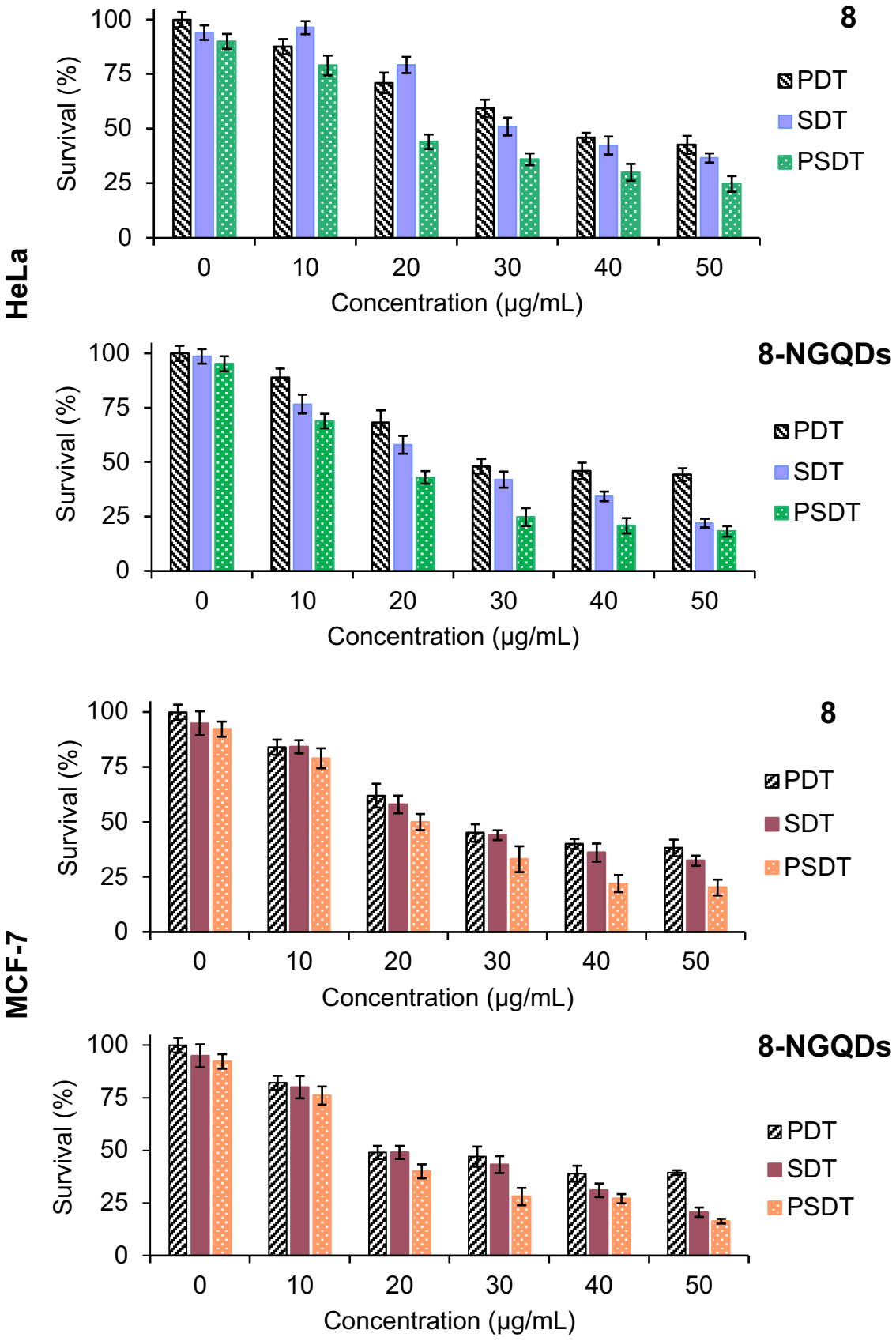

Figure 6.9. The cell survival plots for the HeLa and MCF-7 cells 24 h post PDT (at 680 nm with irradiation doses of 170 J.cm^{-1}), SDT (at 1 MHz: 1 W. cm^{-2}, 100% duty cycles) and SPDT treatments in the presence of Pc **8** and **8**-NGQDs *in vitro*. n=3.

Table 6.3. Summary of cellular survival of the HeLa and MCF-7 cells 24h post treatments with the Pc **8** and Pc **9** and the NPs conjugates at 50 μg/ mL.

	Cell survival (%)			IC_{50} (μg/ mL)		
	PDT	SDT	SPDT	PDT	SDT	SPDT
	HeLa Cells					
8	37.2	32.4	20.2	26.0	25.0	20.0
9	25.0	22.6	16.7	20.0	18.0	15.0
NGQDs	74.2	71.8	62.0	>50.0	>50.0	>50.0
NSGQDs	79.6	77.6	64.1	>50.0	>50.0	>50.0
8- NGQDs	44.3	22.0	18.2	28.0	25.0	17.0
8- NSGQDs	47.2	38.4	31.3	39.0	30.0	20.0
9- NGQDs	32.3	20.1	14.6	24.0	22.0	15.0
9- NSGQDs	41.1	34.5	26.3	32.0	28.0	25.0
AuGSH	80.6	52.2	44.3	>50	>50.0	47.5
AgGSH	72.2	42.3	44.1	>50	49.9	46.5
8-AuGSH	10.1	3.5	0.0	19.0	16.5	11.2
8-AgGSH	27.2	17.2	5.2	25.2	22.3	18.0
9-AuGSH	10.0	0.0	0.0	16.4	12.2	10.0
9-AgGSH	17.9	10.9	0.0	23.1	19.9	11.5
	MCF-7 Cells					
8	42.6	36.6	24.7	40	36.0	30.0
9	28.7	30.1	18.1	38.0	31.0	22.5
NGQDs	78.9	70.9	65.9	>50.0	>50.0	>50.0
NSGQDs	89.9	82.4	66.0	>50.0	>50.0	>50.0
8- NGQDs	44.3	22.0	18.2	28.0	25.0	17.0
8- NSGQDs	47.2	38.4	31.3	39.0	30.0	20.0
9- NGQDs	32.3	20.1	14.6	24.0	22.0	15.0
9- NSGQDs	41.1	34.5	26.3	32.0	28.0	25.0
AuGSH	83.0	54.9	49.3	>50	>50	47.5
AgGSH	76.0	49.9	42.1	>50	49.9	46.5
8-AuGSH	12.8	5.0	2.0	19.5	16.5	13.5
8-AgGSH	29.9	20.0	8.0	25.0	22.3	18.0
9-AuGSH	10.2	2.2	2.0	18.0	16.2	14.0
9-AgGSH	20.1	18.0	4.4	21.3	19.9	15.0

The cell survival percentages also decrease with increasing concentrations of the NPs and Pc-NPs conjugates for both the cell lines *in vitro* as seen in the **Fig. 6.9**, for the NGQDs conjugates.

The NGQDs and NSGQDs alone, a decrease in the cell survival was observed as seen with reduced survival percentages (less than 100%) under the different treatments **Table 6.3**. This observation was expected since the GQDs showed ROS generation under the sono- and combination irradiations, **Table 5.3**. The reduction in the cell survival percentages was, however, higher for the Pcs and the Pc-GQDs conjugates compared to the GQDs alone under the different treatments, **Table 6.3**. Despite higher ROS generation observed for the conjugates under photo-irradiations, lower cell survival was observed for the Pcs compared to the GQDs conjugates. This observation may be explained by the internalization trends of the complexes by the cells. Where facile and rapid cellular uptake may be facilitated for the relatively smaller Pcs compared to the GQDs conjugates. In the case of the sono-treatments, the uptake of the complexes may be improved by the ultrasonic mechanical waves, which may assist in enhancing the permeability of the cell membranes and therefore lead to the improvement in the cellular uptake of therapeutics by the US
[**196,197**], hence, the increased activity of the Pc-GQDs conjugates in SDT compared to PDT. Moreover, the NGQDs alone and in the conjugates showed better therapeutic efficacies compared to the NSGQDs and NSGQDs conjugates for all the treatment types, **Table 6.3**. The IC_{50} values for the NGQDs, NSGQDs and their respective conjugates are also given in the **Table 6.3**. For the NPs alone, the IC_{50} values could not be calculated as the cells did not decrease past 50% after treatments. For the Pcs and conjugates, the IC_{50} values decreased for the combination treatments compared to the monotreatments.

The AuGSH and AgGSH alone also showed a reduction in the cell survival for both cell types, **Table 6.3**. The NPs also improved the therapeutic efficacies of the Pcs for all the treatment types, where the AuGSH generally performed better compared to the AgGSH, for the respective Pc **8** and Pc **9**, as seen with the lower cell survival percentages. Although the GQDs showed higher ROS compared to the metallic NPs, higher therapeutic efficacies were observed for the inorganic metallic NPs. This observation may be attributed to the efficiency of cellular uptake of the NPs and conjugates. Furthermore, various other biochemical process that are independent of ROS generation occur such as photo-/ sono- thermal processes may occur where the metallic NPs may have improved activities compared to the GQDs. Photo and sono-thermal mediated therapies have been reported for metallic NPs on cancer cells in the literature [**198-200**]. The IC_{50} values for the Pc **8** and Pc **9** conjugates with the AuGSH and AgGSH reduced for the combination treatments compared to the mono-treatments for both the cell lines.

6.2.2. Effect on cell morphologies.

The effects of the PDT, SDT and SPDT treatments mediated by the Pcs, and the Pcs conjugated to the NPs on the cell morphologies were determined *in vitro*. The cells exposed to the photo- and/ or sono-treatments alone without the NPs and conjugates showed minimal to no changes in the morphologies 24 h after the treatments, **Fig. S8**, similar to the control cells shown in the **Fig. 6.4**.

6.2.2.1. Effects of R-group.

The cellular images for the HeLa and MCF-7 cells 24 h after PDT, SDT and SPDT treatments using the Pc **5** are shown in the **Fig. 6.10** as examples.

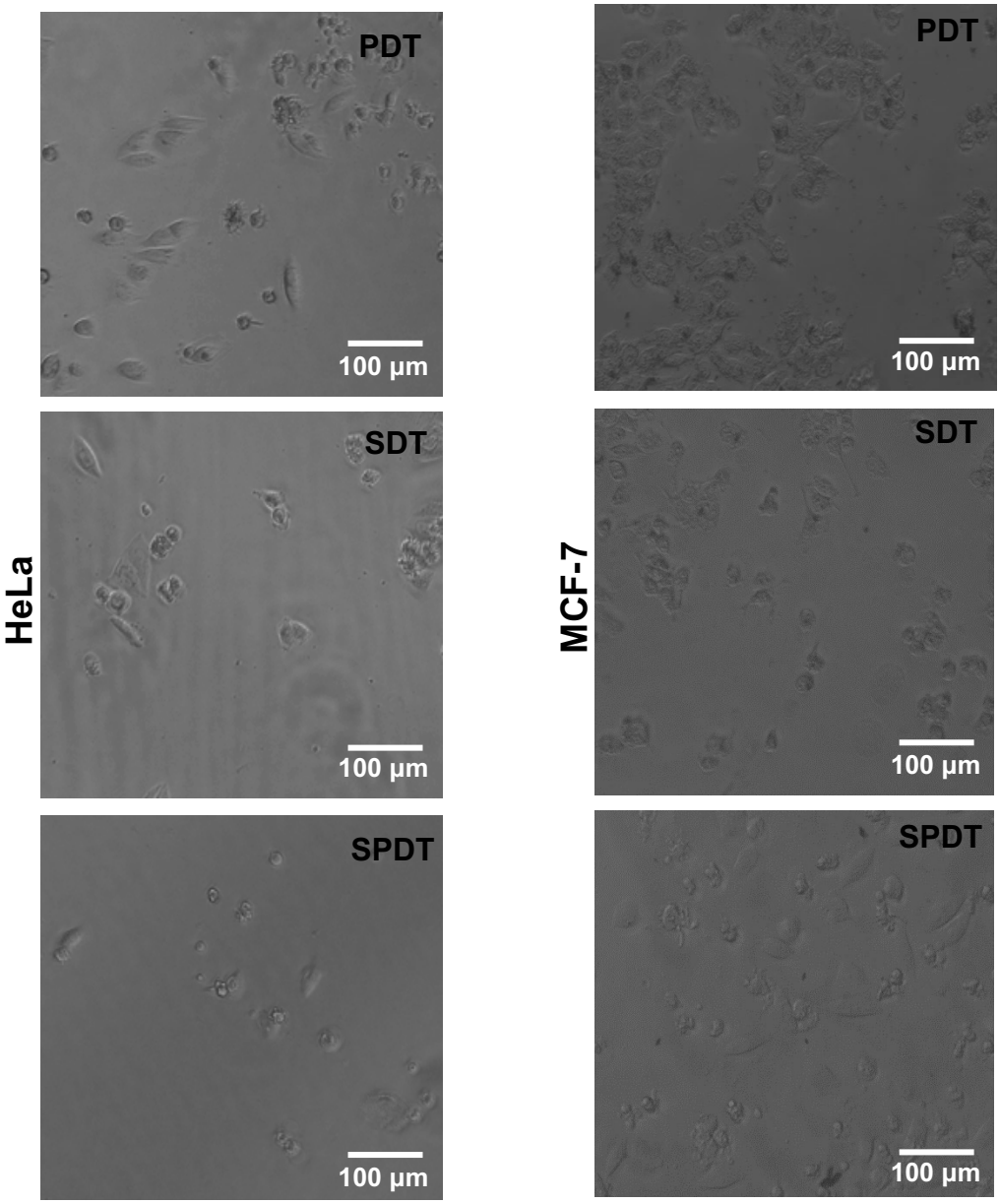

Figure 6.10. The micro-images of the HeLa and MCF-7 cells 24 h post PDT (at 670 nm ± 40 nm, 300 W, generating 2.97 × 10^{16} photons^{-1} cm^{-2}), SDT (at 1 MHz, 1 W. cm^{-2}, 100% duty cycles) and SPDT treatments in the presence of the Pc **5** (at 100 µM).

Changes in the morphologies of the cells were observed after treatments with the Pc **5** for the PDT, SDT and SPDT, **Fig. 6.10**, compared to the control cells as shown in the **Fig. 6.4** previously. The changes observed indicated the cytotoxic effects of the different treatments on the cells. The cell densities reduced for the cells. Shrunk and circular cells were also evident under all treatments for both cell types, **Fig. 6.10**.

6.2.2.2. Effects of nanoparticles.

The cellular images for the HeLa and MCF-7 cells 24 h after SPDT treatments using the Pc **9**, the NGQDs and NSGQDs conjugates are shown in the **Fig. 6.11** as examples.

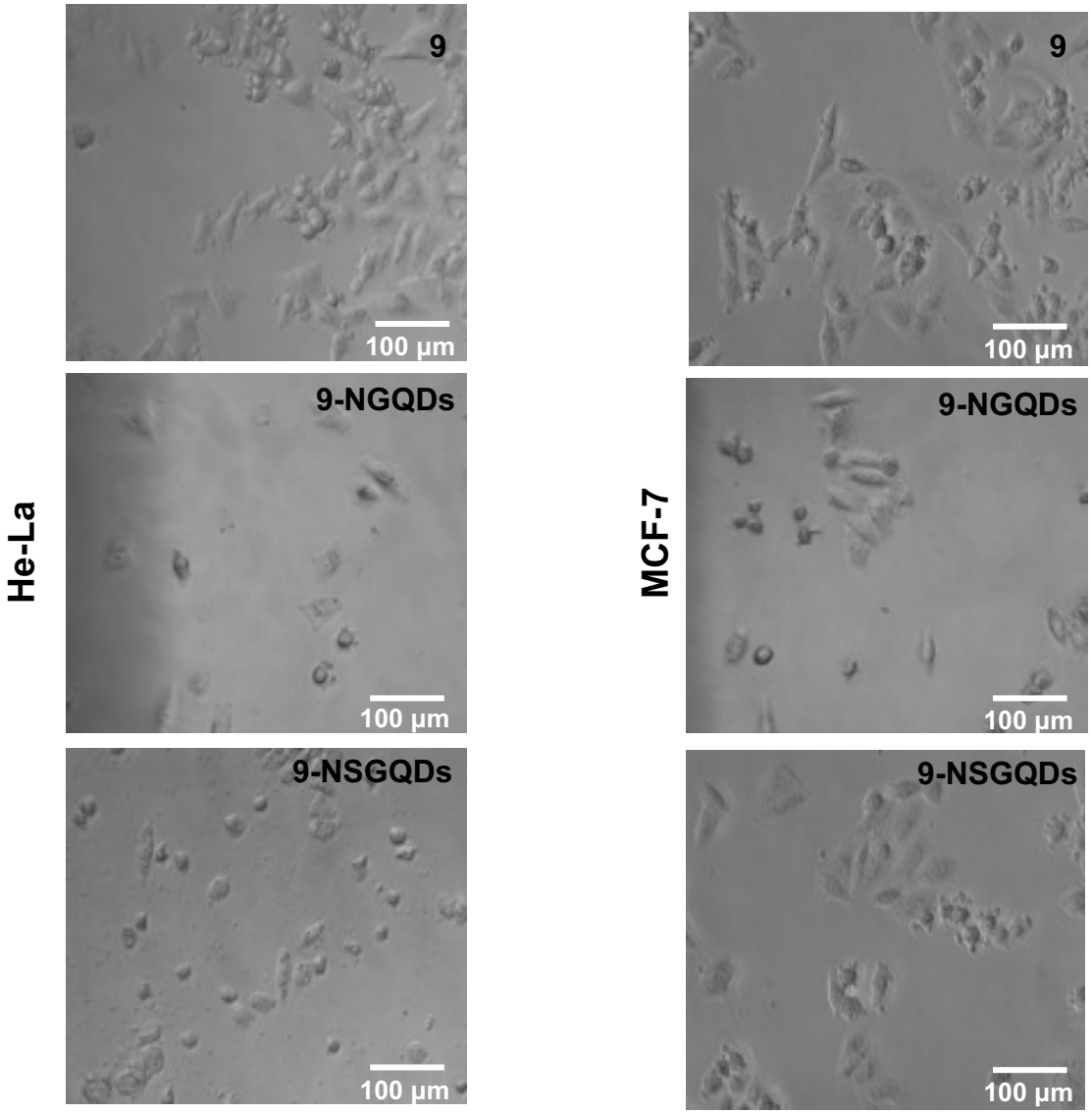

Figure 6.11. The micro-images of the HeLa and MCF-7 cells 24 h post SPDT treatments (light: 670 nm ± 40 nm, 300 W, generating 2.97 × 10^{16} photons^{-1} cm^{-2}, and ultrasound: 1 MHz, 1 W. cm^{-2}, 100% duty cycles) in the presence of the Pc **9**, **9**-NGQDs and **9**-NSGQDs (at 40 µg/ mL).

The cell morphologies were also affected for the HeLa and MCF-7 cell treated with the Pcs conjugates as seen with the Pc **9** and the GQDs conjugates in the **Fig. 6.11**. The conjugates generally showed more severe effects on the cells compared to the Pcs alone as seen with reduced cell quantity indicating cell death. The NGQDs conjugates showed increased cell damage compared to the NSGQDs. This observation corresponds to the ROS generation results and the cell survival percentages of the cells treated with the NGQDs compared to the NSGQDs conjugates as seen previously.

6.3. Cellular uptake studies.

The uptake of the Pcs alone (0 μM – 100 μM) and Pc-NPs conjugates (0 μg/ mL – 50 μg/ mL) by the HeLa and MCF-7 cells were determined 24 h post inoculation *in vitro*.

6.3.1. Effects of R-group.

The plots of the Pc intensities in the cells exposed to Pcs at increasing concentrations *in vitro* are shown for the Pc **4** – Pc **6** plots are shown in the **Fig. 6.12** as examples.

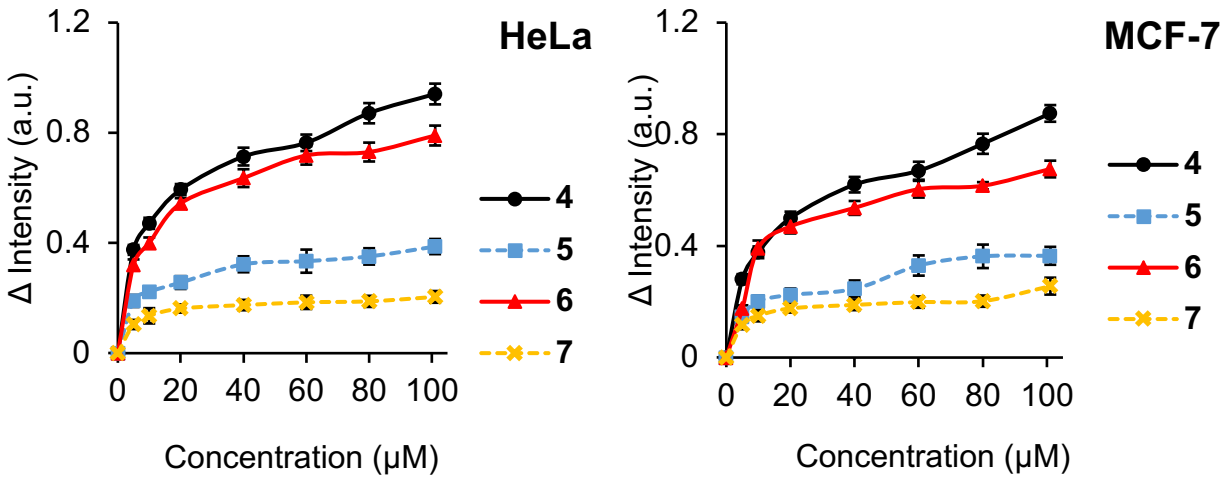

Figure 6.12. The uptake of the Pc **4** – Pc **7** in HeLa and MCF-7 cells 24 h after inoculation.

An increase in the Pc intensities with increasing concentrations was observed for Pcs in both cell lines as shown in the **Fig. 6.12**. The cationic Pc **4** and **5** showed higher uptake compared to the zwitterionic Pc **6** and Pc **7.** Cationic Pcs show improved cellular retention on cancer cells [**65,150**], this is because of the negatively charged membrane of the cells due to the high expression of anionic lipids and lactic acids [**201,202**].

A summary of the Pc intensities for cells exposed to 100 μM of the Pcs after 24 h is given in the **Table 6.4**.

Table 6.4. A summary of Pc intensities (a.u.) in the HeLa and MCF-7 cells exposed to Pcs at 100 μM after 24 h.

	HeLa	MCF-7
1	1.51	1.40
2	1.38	1.33
3	1.34	1.33
4	1.01	1.00
5	0.80	0.80
6	0.44	0.40
7	0.20	0.20
8	0.77	0.71
9	0.79	0.83
10	1.10	1.24
11	0.99	1.09

When comparing the intensities of the Pcs at the highest test concentration (100 μM), the cationic Pc **1** – Pc **5** and Pc **8** – Pc **11** showed relatively higher intensities

compared to the zwitterionic Pc **6** and Pc **7**, **Table 6.4**. This observation corresponds to the cytotoxicity studies showing reduced anticancer activities of the zwitterionic Pc **6** and Pc **7** compared to the cationic counterparts, Pc **4** and Pc **5** under the different treatments. The increased cellular internalization of cationic Pcs in cancer cells compared to zwitterionic Pcs is beneficial as it avails more Pc sensitizer molecules for treatment. As a result, higher intracellular ROS may be generated and therefore increasing the efficacies of the treatments for cell eradication.

6.3.2. Effects of nanoparticles.

The plots of the Pc intensities in the cells that have been exposed to the Pc **8** and its conjugates with the NGQDs and AuGSH conjugates at increasing concentrations *in vitro* are shown for the **Fig. 6.13** as examples.

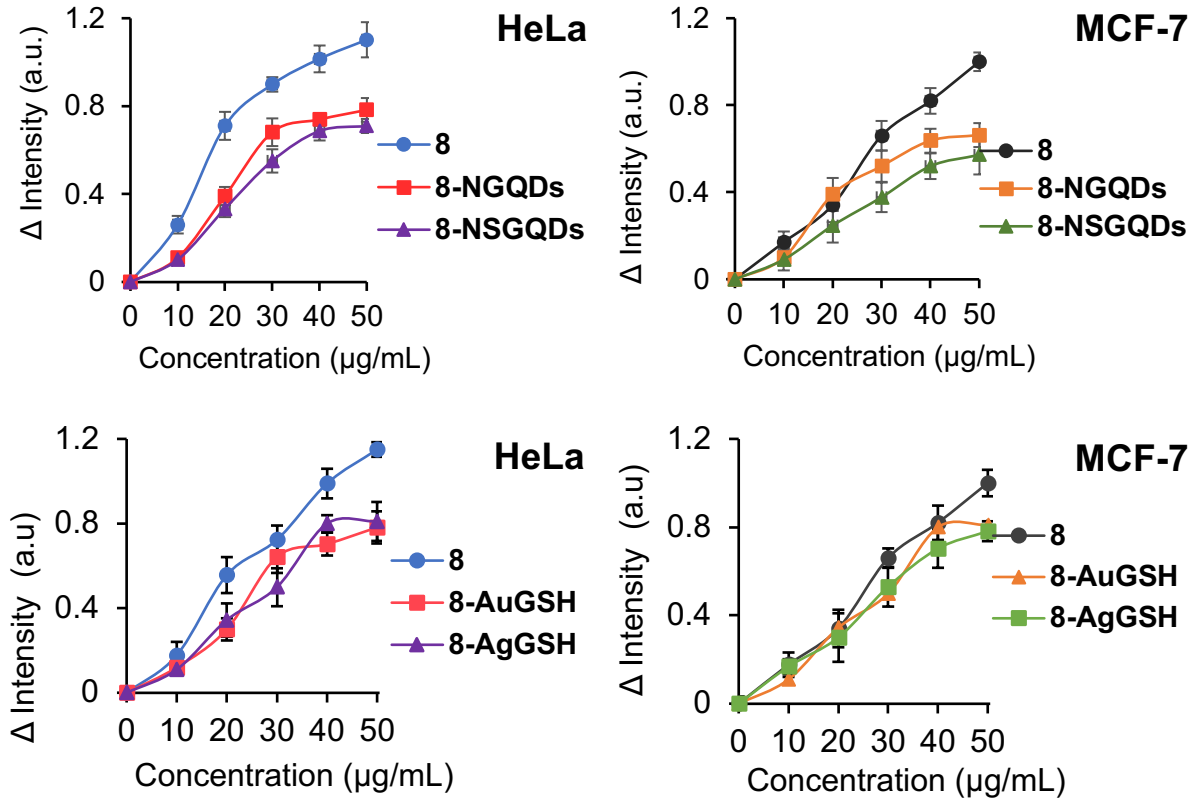

Figure 6.13. The uptake of the Pc **4** and its NPs conjugates by the HeLa and MCF7-cells 24 h after inoculation.

Both the cells showed increasing uptake of the Pcs and Pc-NPs conjugates at increasing concentrations after 24 h *in vitro*, **Fig. 6.13**. The NPs are also known to passively enter cancerous cells as the cell membranes are more porous compared to the stringent healthy cells, thus allowing larger molecules to enter and accumulate in the cells. This phenomenon of passive cellular transport in cancer drug delivery is known as enhanced permeation and retention [**203,204**] and has been reported for AuNPs and AgNPs for cancer in the literature [**205-207**].

The intensities of the Pcs in the cells after 24 h are summarized in the **Table 6.5**.

Table 6.5. A summary of Pc intensities (a.u.) in the HeLa and MCF-7 cells exposed to Pcs and Pc-NPs conjugates at 50 µg/ mL.

	HeLa	MCF-7
8	1.10	1.00
9	1.16	1.12
8- NGQDs	0.76	0.65
8- NSGQDs	0.70	0.57
9- NGQDs	0.68	0.65
9- NSGQDs	0.65	0.64
8-AuGSH	0.87	0.81
8-AgGSH	0.85	0.78
9-AuGSH	0.84	0.80
9-AgGSH	0.84	0.75

Overall, both the cell lines showed relatively higher intensities of the Pcs alone compared to the Pcs in the conjugates, **Table 6.5**. This observation may be due to the

increase molar units of the Pcs in the non-conjugated Pcs samples, since the mass concentrations were used for these studies. In the case of the conjugates, the mass is a sum of the mass of the Pc and the mass of the NPs, therefore, the molar units of the Pcs are reduced in the conjugates. Moreover, the relatively smaller Pcs may be facilitated more easily and faster into the cells compared to the relatively larger conjugates. Hence, the higher Pc intensities for the non-conjugated Pc **8** and Pc **9** are obtained for both cell lines *in vitro*.

For the GQDs, the intensities of the Pc **8** and Pc **9** were generally higher in the NGQDs conjugates compared to the NSGQDs conjugates, **Table 6.5**. This corresponds to the relatively higher loading of the Pcs on the NGQDs compared to the NSGQDs as seen previously in the **Table 3.1**. The conjugates of the Pc **8** and Pc **9** with the AuGSH generally showed relatively higher Pc intensities compared to the conjugates of the Pc with the AgGSH. For the HeLa cells, the Pc intensities were similar for the **9**-AuGSH and **9**-AgGSH, **Table 6.5**. This is also believed to be due to the relatively higher loading of the Pcs on the surfaces of the AuGSH compared to the AgGSH as seen previously in the **Table 3.1**.

Overall, the uptake of the Pc conjugates with the metallic AuGSH and AgGSH for both the cell lines *in vitro* was increased compared to the conjugates with the NGQDs and NSGQDs, **Table 6.5**. This observation is not yet clear. It may, however, be related to the sizes of the NPs. Where the larger NGQDs and NSGQDs NPs conjugates with the Pcs possibly become saturated in the cells faster than the relatively smaller AuGSH and AgGSH conjugates. Meng *et al* reported on the effects of NPs sizes on the internalization where the size reduction and surface functionalization of SiNPs showed improved uptake by a Murine tumour model [**208**].

6.4. BSA Protein Binding.

The Pcs binding behaviors to the BSA protein in water were determined by fluorescence spectroscopy using methods described in the literature [**152**]. The fluorescence spectra of the BSA in the presence of the Pcs at increasing concentration are shown in **Fig. 6.14** for the Pc **4** – Pc **7** as examples.

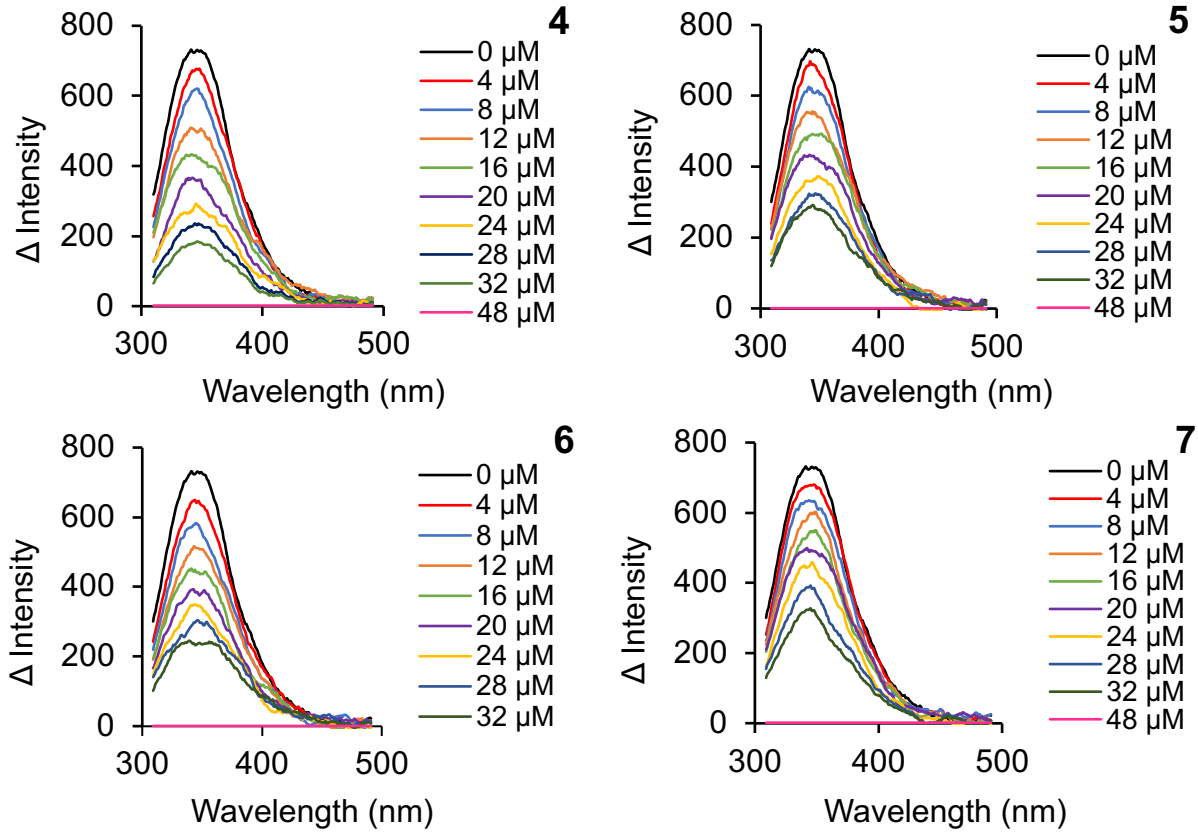

Figure 6.14. Fluorescence emission spectra of BSA (30 μM) upon excitation at 280 nm in the presence of Pcs at increasing concentrations from 0 μM – 48 μM in water.

The Stern-Volmer plots for the determination of the Stern-Volmer constants, and the plots for the determination of the binding constants and number of binding sites for the Pc **4** – Pc **7** are shown in the **Fig. 6.15** and **Fig. 6.16**, respectively, as examples.

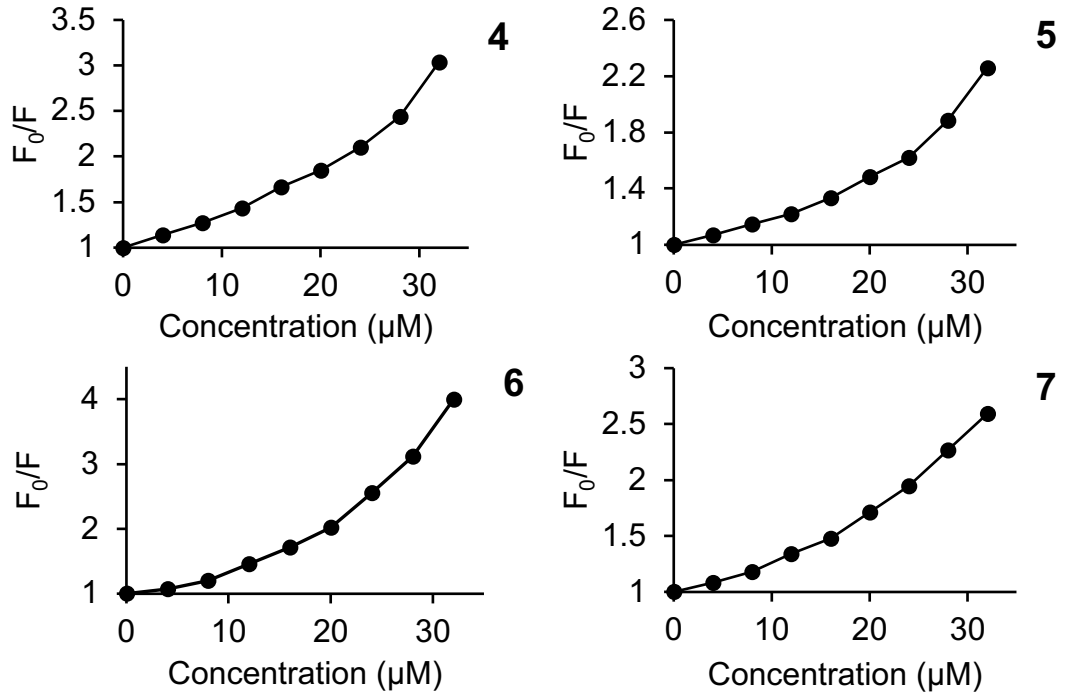

Figure 6.15. The Stern-Volmer Plots for the determination of the binding constants of the Pcs at varied concentrations on the BSA-protein in water.

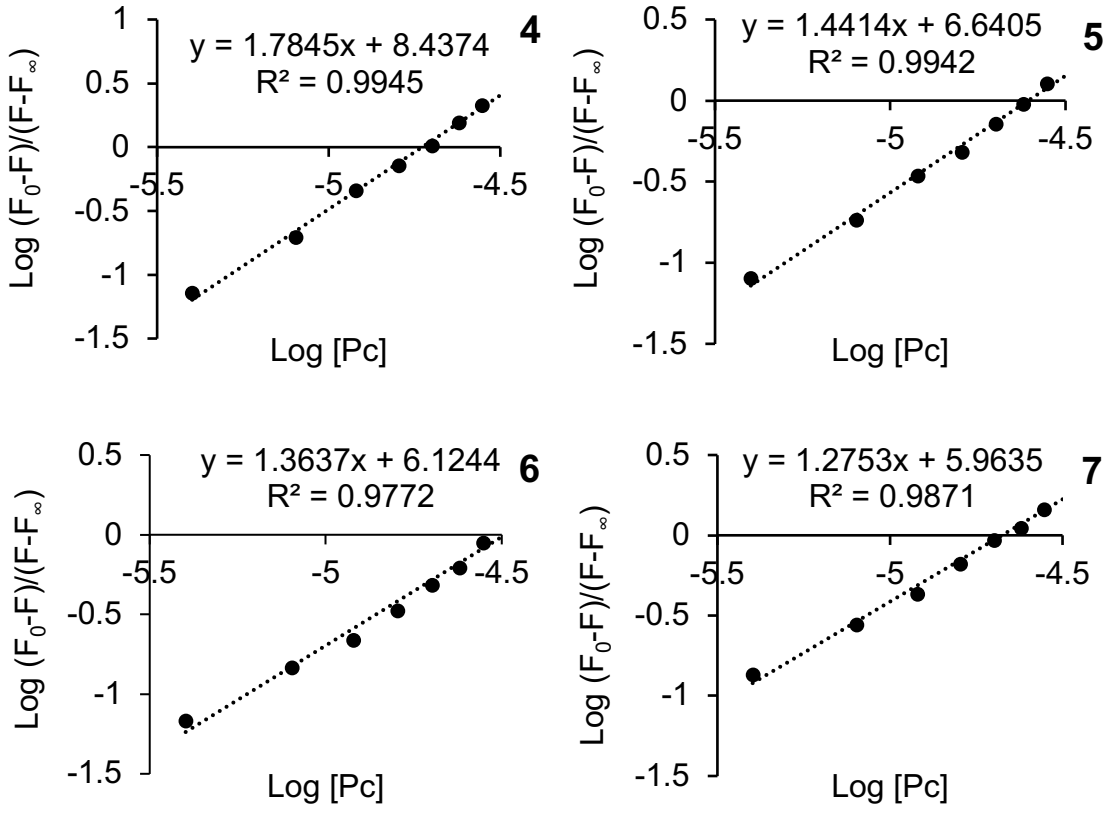

Figure 6.16. Plots for the determination of the number of Pcs-binding sites on BSA and the binding constants of Pcs on BSA at varied concentrations in water.

A decrease in the fluorescence emissions of the BSA protein in the presence of the Pcs with increasing concentrations is observed, **Fig. 6.14**. The quenching of the fluorescence of BSA indicates the binding of the Pcs to the protein [**209,210**]. The binding constants (K_b), number of binding sites (n) on the BSA, the Stern-Volmer quenching constants (K_{SV}) including the association constant (K_a), and the bimolecular quenching constants (k_q) were calculated from the quenching rates of the BSA fluorescence (300 nm – 500 nm) by the Pcs at increasing concentrations. The equations employed for the calculations of the BSA binding constants are given in the in the experimental section 2.6.

A summary of the BSA binding constants including the calculated number of binding sites for the Pcs is given in the Table **6.6**.

Table 6.6. Summary of the binding parameters of the Pcs to the BSA protein in water.

	$K_{SV}/10^6$ (M^{-1})	$K_a/10^6$ (M^{-1})	$k_q/10^{13}$ (M^{-1} s^{-1})	K_b (M^{-1})	n
1	0.74	3.1	0.74	2.0×10^{10}	2.2
2	0.87	2.0	0.87	1.2×10^{8}	1.6
3	0.83	2.4	0.83	1.8×10^{8}	1.7
4	0.88	2.0	0.88	2.8×10^{8}	1.8
5	0.97	1. 8	0.97	4.4×10^{6}	1.4
6	0.99	1. 7	0.99	1.3×10^{6}	1.4
7	0.97	1.4	0.97	0.9×10^{6}	1.3
8	0.96	1.1	0.96	2.0×10^{6}	1.4
9	0.94	2.0	0.94	1.7×10^{7}	1.6
10	0.96	2.3	0.96	0.7×10^{6}	1.3
11	0.92	1.9	0.92	3.2×10^{6}	1.5

A modified Stern-Volmer equation was used to determine the K_{SV} and K_a values for the Pcs as defined previously in the literature [**211-213**]. The Stern-Volmer plots are shown in the **Fig. 6.15** for the Pc **4** – Pc **7**. The K_{SV} values represent dynamic quenching where the K_a values represent the static quenching of the Pcs on the BSA proteins. The K_{SV} values observed for the Pcs were found to be in the order of 10^6 which is typical for Pcs-BSA adducts as reported in the literature [**152,214**], **Table 6.6**. The K_a values, representing static quenching, suggests that there is a stacking interaction between the Pcs and the protein [**53,209**]. The k_q values are in the order of 10^{13}, indicating static type quenching according to the Einstein-Smoluchowski approximation [**215,216**]. The K_b and n values were obtained from plots as shown in the **Fig. 6.16**. The K_b values for the cationic Pcs (Pc **1** – Pc **5** and Pc **8** – Pc **11**) were generally higher compared to their zwitterionic Pcs (Pc **6** and Pc **7**). This suggests stronger association of the cationic Pcs compared to the zwitterionic Pcs. Moreover, the BSA protein has an overall negative charge [**217,218**]. Cationic Pcs have been reported to bind more efficiently to the BSA protein compared to the zwitterionic counterparts [**213**].

The number of binding sites, n, for the Pc **1** – Pc **4,** Pc **9** and Pc **11** is ~2, suggesting that the Pc-BSA adduct formation ration is 2:1. For the Pc **5** – Pc **8**, and Pc **10**, the n values are reduced and are ~1, **Table 6.6**. The Pc-BSA adduct formation ratio for these Pcs is 1:1. The most reported interaction of BSA and phthalocyanines is 1:1 [**219**], the interaction of two phthalocyanines with BSA molecule has been reported for lipophilic phthalocyanines [**219**]. The Pc **11** is expected to be more lipophilic than the Pc **10**, hence the former is 2:1 as examples.

6.5. Summary of chapter.

The differently substituted ionic Pcs demonstrated cytotoxic effects on the cell lines under SDT treatments at the varied sono-parameters. The *Par I* (1 MHz: 1 W.cm^{-2}) generally showed higher cell eradication efficacies compared to the other parameters. The *Par I* was therefore selected at the sono-parameter for the SPDT treatments. Moreover, there was no cell damage was observed for the sono treated cells (at the different parameters) in the absence of the Pcs. This suggests the potential of non-invasiveness with SDT treatments generally. When comparing the PDT, SDT and SPDT treatments from the studies, the SDT monotreatments generally showed higher therapeutic efficacies, shown by lower cell survival percentages post treatments, compared to the PDT monotreatments, for both the cell lines. And the SPDT combination treatments showed higher therapeutic efficacies compared to both the SDT and PDT monotreatments for both the cell lines, *in vitro*. When comparing the Pcs, the larger TPP-labelled Pc **10** and Pc **11** demonstrated higher anticancer activities under the SDT and SPDT treatments. The zwitterionic Pcs showed the least anticancer efficacies compared to the cationic Pcs.

An improvement was seen on the therapeutic efficacies for the Pcs conjugated to the graphitic and metallic NPs compared to the Pcs prior conjugation or the NPs alone.
Cellular morphology changes were observed for the HeLa and MCF-7 cells after the PDT, SDT and SPDT treatments
The Pcs all showed the ability to associate with the BSA proteins.

CHAPETR SEVEN

7. **Conclusion and Proposed Future Work**

7.1. Conclusion.

The new cationic Pc **8** – Pc **11** and zwitterionic Pc **6** and Pc **7** were prepared by the quaternization of Pcs bearing tertiary N-groups. Different quaternizing agents, including methane, ethane, propanesultone and triphenylphosphine, were used to prepare the ionic Pcs. Two Pcs were also conjugated to organic NPs: NGQDs, NSGQDs, and inorganic NPs: AuGSH and AgGSH. The structural characterization confirmed the formation of the Pcs. The Pcs demonstrated different photophysical parameters, however, were all absorbing light of wavelength in the NR and showed substantial T_1 population.

The ultrasonic power and frequency affected the stabilities of the Pcs. Where an increase in the power of the US to 2 $W.cm^{-2}$ resulted in an increased rate of degradation for the Pcs. Increasing the frequency to 3 MHz, however, did not show significant degradations of the Pcs. Therefore, it is important to carefully select the conditions for sono-treatments mediated by Pcs. When comparing the Pcs, those bearing the TPP as the quaternizing agent showed more susceptibility to sono-mediated degradation. And those quaternized using a methyl- group showed the least susceptibility to the degradation under the sono-treatments. The ability of the Pcs to generate $^1O_2$ and •OH was observed under the sono-treatments at the varied parameters. The *Par I* showed substantial $^1O_2$ and •OH yields and was therefore applied for the sono-photo combination treatments. The ROS generation studies for the photo-, sono- and the sono-photo combination treatments for the Pcs are reported. The combination treatments showed an improvement in both the $^1O_2$ and •OH yields compared to the photo- and sono- monotreatments for all the Pcs.

For the cell studies, the *Par I* also maintained high therapeutic efficacies judged by the improved cell eradications (low cell survival after treatments) *in vitro* compared to the

other parameters. In the case of the SPDT combination treatments, higher therapeutic efficacies were obtained compared to the SDT and PDT monotherapies. Therefore, SPDT is a promising modality for cancer eradication compared to the monotherapies. The NPs generally improve the sono-photochemical properties of the Pcs, seen with the increase in the $^1O_2$ and •OH yields compared to the Pcs. Furthermore, improvements anticancer activities of the Pcs were observed in the presence of AuGSH and AgGSH for in the PDT, SDT and SPDT treatments on both the HeLa and MCF-7 cell *in vitro*. These NPs may be potentially effective nano-systems offering a cancer targeting complexes with SPDT therapeutic activities. The Pcs also showed ability to bind to the BSA proteins. This is beneficial as the BSA proteins are usually targeted in the development of cancer therapeutics to assist with the delivery and biodistribution in the biological systems.

Overall, the SPDT mediated anticancer technique can potentially address the limitation of the conventional cancer treatments as it offers a controllable and non-invasive technique, and further allowing for the eradication of deep tissue tumours. The mechanism of inducing cytotoxicity in sono-photodynamic therapy using Pc-based sensitizers is shown in **Fig. 7.1**.

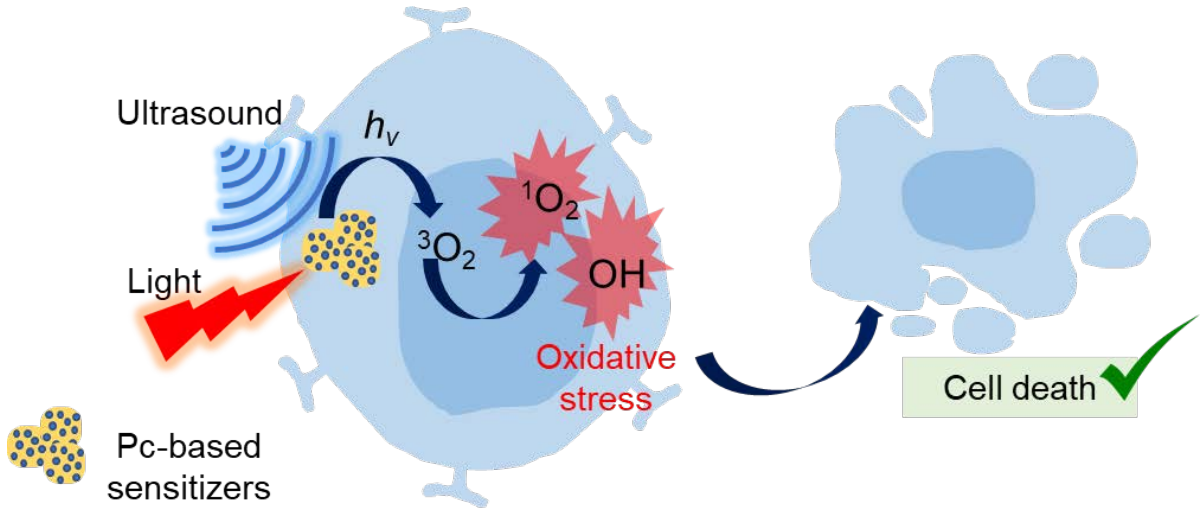

Figure 7.1. A generalized mechanism of cancer cell eradication mediated by Pc-based sensitizers in Sono-photodynamic combination therapy.

7.2. Proposed future work.

7.2.1. Selection of Pcs

The Pcs can be prepared with varying R-groups (R and Ri). This affects the symmetry of the tetra-unit macrocycle as shown in the figure below. The reduction in the symmetry of Pcs has been shown to improve the photophysical properties of Pcs and therefore improve their anticancer activities [**220,221**]. It would be interesting to investigate the effects of the structural symmetries of different Pcs and how they may influence their general SDT and SPDT activities. Moreover, the number of substituents on the Pcs ring may be varied.

An example of the synthetic methods for the preparation of asymmetric Pcs is shown in **Fig. 7.2**.

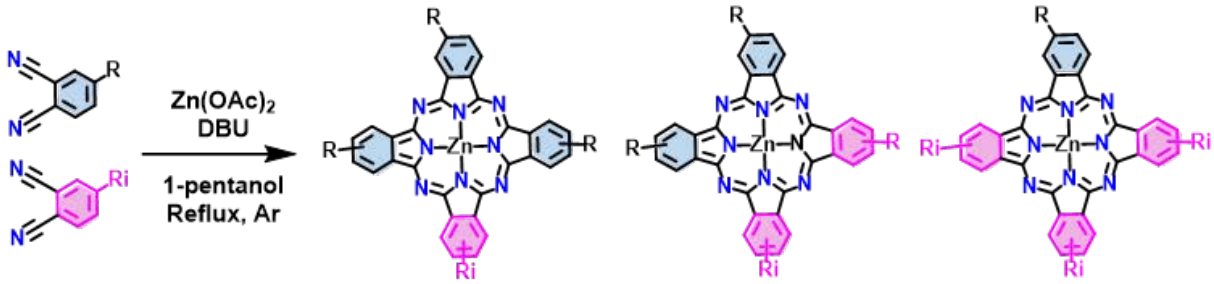

Figure 7.2. Example of the preparation of asymmetrical Pcs using two differently substituted Pn precursors.

7.2.2. Conjugation of therapeutic agents.

Pcs are easily modifiable and may be functionalized with various biomolecules and therapeutic agents to improve their activities. These may include:

- The conjugation of cancer imaging probes on the Pcs to prepare theranostics for SPDT.

- The conjugation of targeting/ delivery agents such as folic acid, biotin and glucose to the Pcs.
- Or the conjugation of the Pcs to other different NPs.

7.2.3. Stability and ROS studies.

In this work, the stability of the Pcs was shown to reduce under sono-treatments at some parameters, and for some the C were detected. The study of the mechanism of Pcs degradation and identification of the structures of the resulting fragments may be interesting to explore in detail.

7.2.4. Biological studies.

The Pcs and Pcs-NPs conjugates reported in this work showed substantial anticancer activities. Some of the studies that may be explored further may include cell localization studies, to determine the organelle uptake of the intracellular sensitizers.

Supplementary Information

Figure S1. Image of the Modulight® system.

Figure S2. Image of the ultrasound sonicator set-up.

Figure S3. Image of the EPR spectrometer.

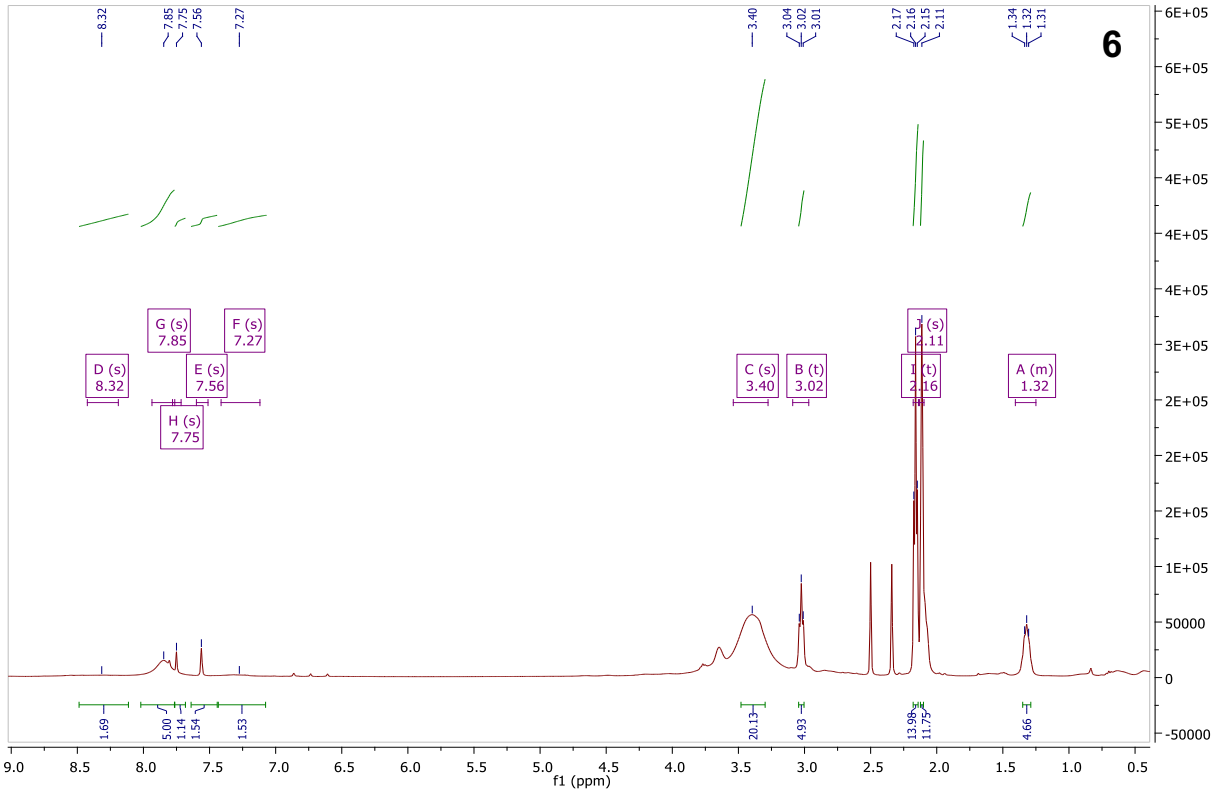

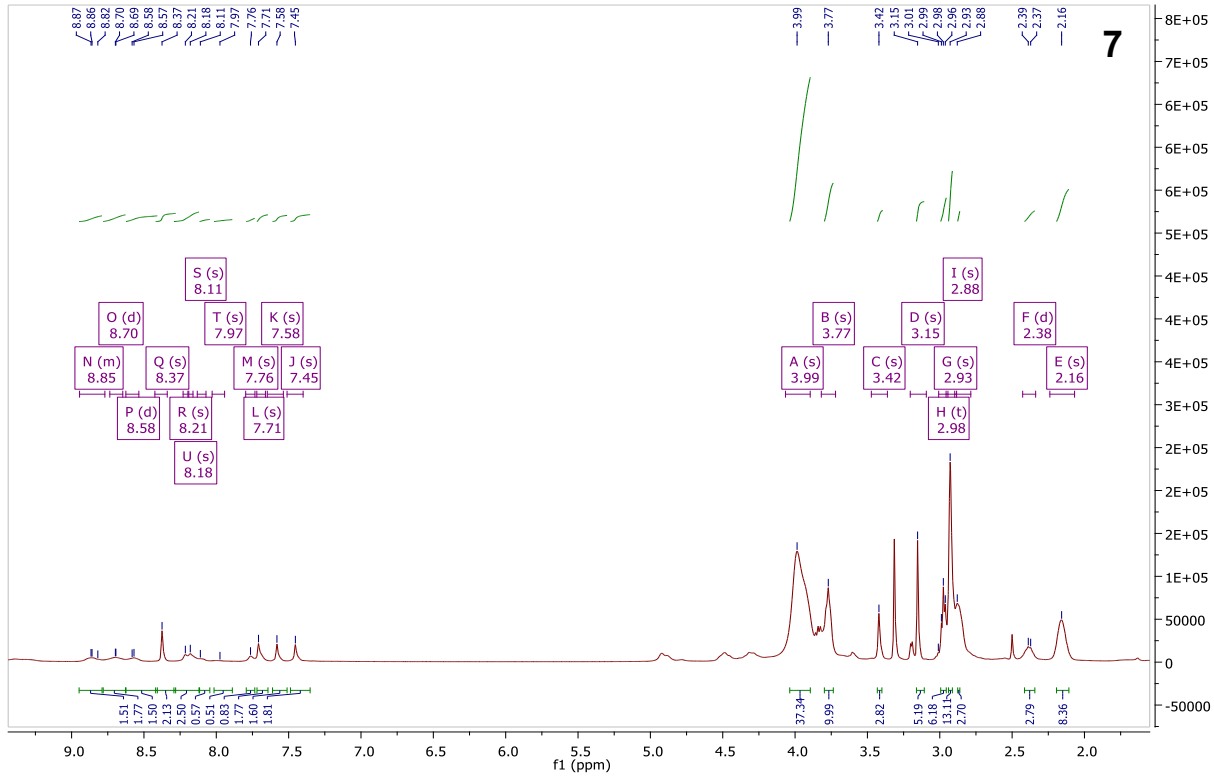

Figure S4. The NMR spectra for Pc **6** and Pc **7**.

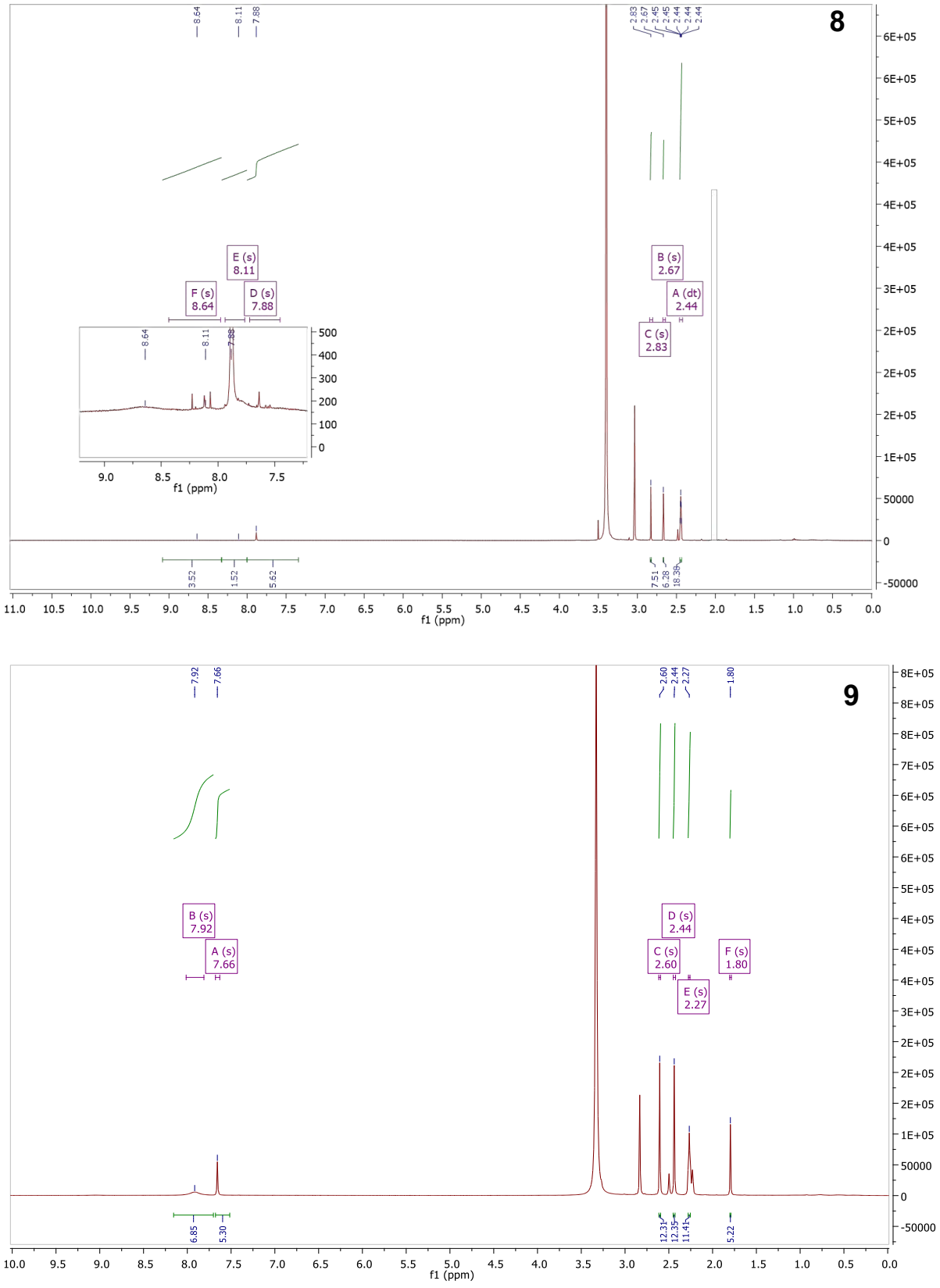

Figure S5. The NMR spectra for Pc **8** and Pc **9**.

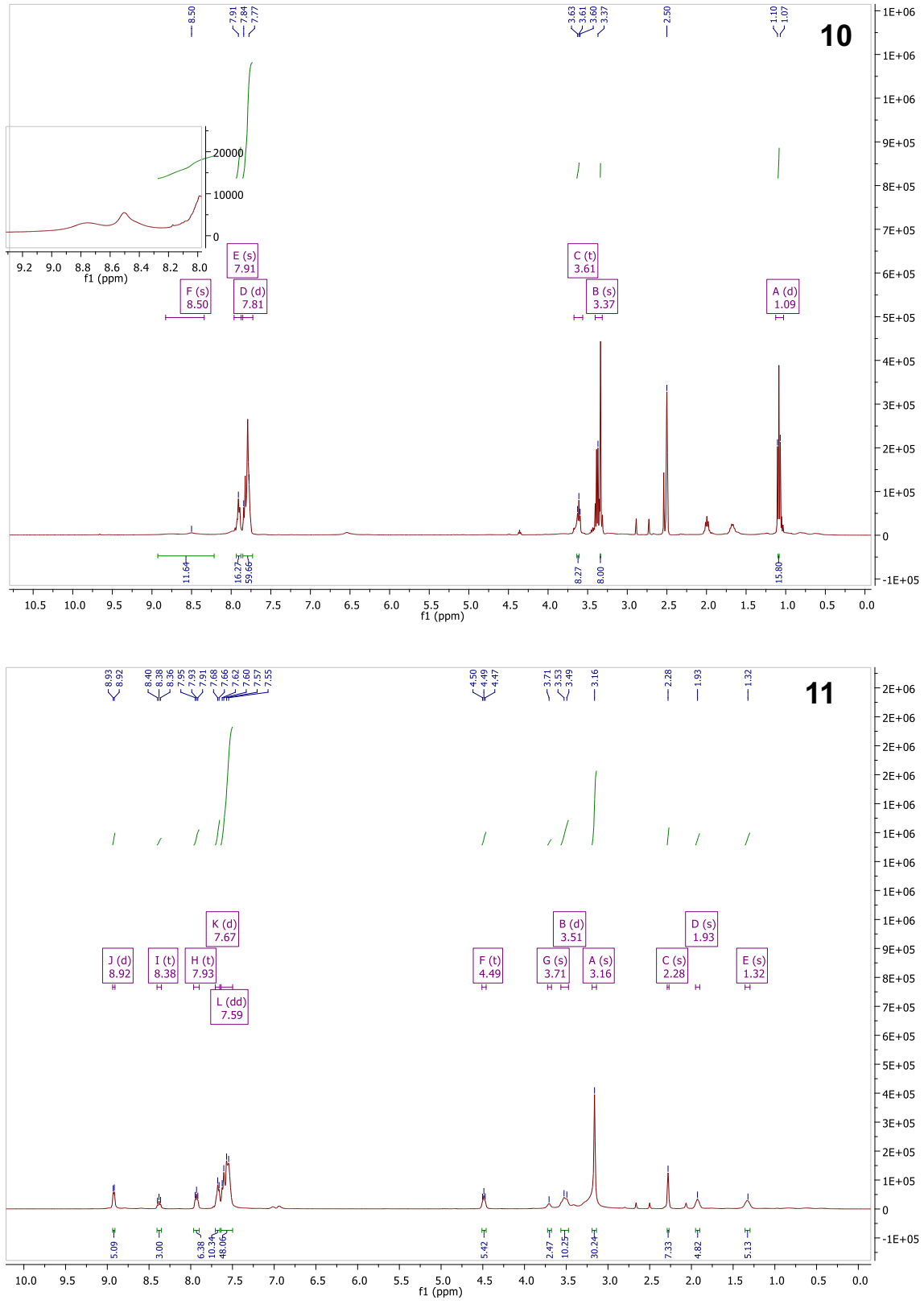

Figure S6. The NMR spectra for Pc **10** and Pc **11**.

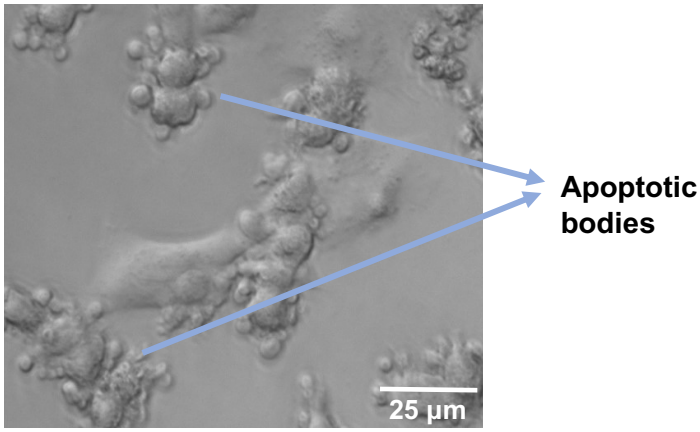

Figure S7. A micro-image of apoptotic cells showing apoptotic bodies: Showing HeLa cells treated with Pc 10 under SPDT as an example.

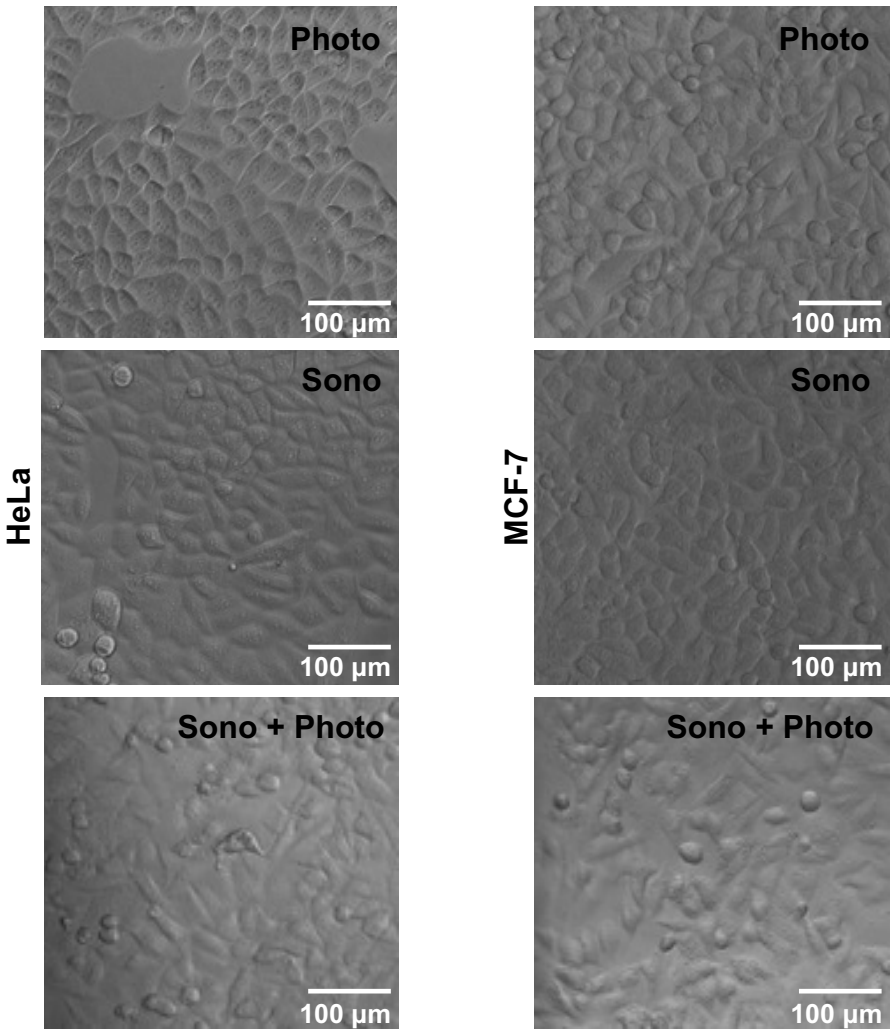

Figure S8. The micro images of the HeLa and MCF-7 cells 24 h after exposure to the photo-, sono- and the sono-photo treatments in the absence of Pcs.

References

[1] The Cancer Association of South Africa, “Cancer Statistics: Global Cancer Statistics”, *CANSA*, https://cansa.org.za/south-african-cancer-statistics/, accessed on 11/10/2022.

[2] X. Jin and P. Mu, “Targeting breast cancer metastasis,” *Breast Cancer Basic Clin. Res.*, 9, 23, 2015.

[3] S. Zhou and F. Peng, “Patterns of metastases in cervical cancer: a population-based study.,” *Int. J. Clin. Exp. Pathol.*, 13, 1615, 2020 .

[4] I. F. Tannock, “Conventional cancer therapy: Promise broken or promise delayed?,” *Lancet*, 351, SII9, 1998.

[5] C. Moorthi, R. Manavalan, and K. Kathiresan, “Nanotherapeutics to overcome conventional cancer chemotherapy limitations,” *J. Pharm. Pharm. Sci.*, 14, 67, 2011.

[6] D. T. Debela, S. G. Mazuzu, K. D. Heraro, M. T. Ndalama, B. W. Mesele, D. C. Haile, S. K. Kitui and T. Manyazewal, “New approaches and procedures for cancer treatment: Current perspectives,” *SAGE Open Med.*, 9, 205031212110343, 2021.

[7] P. Agostinis, K. Berg, K. A. Cengel, T. H. Foster, A. W. Girotti, S. O. Gollnick, S. M. Hahn, M. R. Hamblin, A. Juzeniene and D. Kessel, “Photodynamic therapy of cancer: An update,” *CA. Cancer J. Clin.*, 61, 250, 2011.

[8] C.-N. Lee, R. Hsu, H. Chen, and T.-W. Wong, “Daylight Photodynamic Therapy: An Update,” *Molecules*, 25, 5195, 2020.

[9] Y. Zheng, J. Ye, Z. Li, H. Chen, and Y. Gao, “Recent progress in sono-photodynamic cancer therapy: From developed new sensitizers to nanotechnology-based efficacy-enhancing strategies,” *Acta Pharm. Sin. B*, 11, 2197, 2021.

[10] M. M. Kim and A. Darafsheh, “Light Sources and Dosimetry Techniques for Photodynamic Therapy,” *Photochem. Photobiol.*, 96, 280, 2020.

[11] A. P. McHale, J. F. Callan, N. Nomikou, C. Fowley, and B. Callan, “Sonodynamic therapy: Concept, mechanism and application to cancer treatment,” *Adv. Exp. Med. Biol.*, 880, 429, 2016.

[12] G. Y. Wan, Y. Y. Y. Liu, B. W. Chen, Y. Y. Y. Liu, Y. S. Wang, and N. Zhang, “Recent advances of sonodynamic therapy in cancer treatment,” *Cancer Biol. Med.*, 13, 325, 2016.

[13] S. Sun and M. Wu, “Sonodynamic therapy: Another ‘light’ in tumour treatment by exogenous stimulus,” *Smart Mater. Med.*, 2, 145, 2021.

[14] N. Yumita and S. Umemura, “Sonodynamic therapy with photofrin II on AH130 solid tumour: Pharmacokinetics, tissue distribution and sonodynamic

antitumoural efficacy of photofrin II," *Cancer Chemother. Pharmacol.*, 51, 174, 2003.

[15] Q. Li, X. Wang, P. Wang, K. Zhang, H. Wang, X. Feng and Q. Liu, "Efficacy of chlorin e6-mediated sono-photodynamic therapy on 4T1 cells," *Cancer Biother. Radiopharm.*, 29, 42, 2014.

[16] X. Li and D. Xing, "Sonodynamic diagnosis of cancer with sonosensitization of ATX-70 mediated by chemiluminescence probe," *SPIE*, 5630, 52, 2005.

[17] B. Zhu, Q. Liu, Y. Wang, X. Wang, P. Wang, L. Zhang and S. Su, "Comparison of accumulation, subcellular location, and sonodynamic cytotoxicity between hematoporphyrin and protoporphyrin IX in L1210 cells," *Chemotherapy*, 56, 403, 2010.

[18] M. Bakhshizadeh, T. Moshirian, H. Esmaily, O. Rajabi, H. Nassirli, and A. Sazgarnia, "Sonophotodynamic therapy mediated by liposomal zinc phthalocyanine in a colon carcinoma tumour model: Role of irradiating arrangement," *Iran. J. Basic Med. Sci.*, 20, 1088, 2017.

[19] T. Osaki, I. Yokoe, Y. Uto, M. Ishizuka, T. Tanaka, N. Yamanaka, T. Kurahashi, K. Azuma, Y. Murahata, T. Tsuka, N. Ito, T. Imagawa and Y. Okamoto, "Bleomycin enhances the efficacy of sonodynamic therapy using aluminum phthalocyanine disulfonate," *Ultrason. Sonochem.*, 28, 161, 2016.

[20] H. N. Xu, H. J. Chen, B. Y. Zheng, Y. Q. Zheng, M. R. Ke, and J. D. Huang, "Preparation and sonodynamic activities of water-soluble tetra-α-(3-carboxyphenoxyl) zinc(II) phthalocyanine and its bovine serum albumin conjugate," *Ultrason. Sonochem.*, 22, 125, 2015.

[21] F. Giuntini, F. Foglietta, A. M. Marucco, A. Troia, N. V. Dezhkunov, A. Pozzoli, G. Durando, I. Fenoglio, L. Serpe and R. Canaparo, "Insight into ultrasound-mediated reactive oxygen species generation by various metal-porphyrin complexes," *Free Radic. Biol. Med.*, 121, 190, 2018.

[22] X. Wang, W. Zhang, Z. Xu, Y. Luo, D. Mitchell, and R. W. Moss, "Sonodynamic and Photodynamic Therapy in Advanced Breast Carcinoma: A Report of 3 Cases," *Integr. Cancer Ther.*, 8, 283, 2009.

[23] V. K. Sharma, A. Mahammed, M. Soll, B. Tumanskii, and Z. Gross, "Corroles and corrole/transferrin nanoconjugates as candidates for sonodynamic therapy," *Chem. Commun.*, 55, 12789, 2019.

[24] N. Yumita and S. Umemura, "Sonodynamic antitumour effect of chloroaluminum phthalocyanine tetrasulfonate on murine solid tumour," *J. Pharm. Pharmacol.*, 56, 85, 201.

[25] M. Aksel, O. Bozkurt-Girit, and M. D. Bilgin, "Pheophorbide a-mediated sonodynamic, photodynamic and sonophotodynamic therapies against prostate cancer," *Photodiagnosis Photodyn. Ther.*, 31, 101909, 2020.

[26] Y. W. An, H. Q. Liu, Z. Q. Zhou, J. C. Wang, G. Y. Jiang, Z. W. Li, F. Wang and

H. T. Jin, “Sinoporphyrin sodium is a promising sensitizer for photodynamic and sonodynamic therapy in glioma,” *Oncol. Rep.*, 44, 1596, 2020.

[27] R. Hou, X. Liang, X. Li, X. Zhang, X. Ma, and F. Wang, “In situ conversion of rose bengal microbubbles into nanoparticles for ultrasound imaging guided sonodynamic therapy with enhanced antitumour efficacy,” *Biomater. Sci.*, 8, 2526, 2020.

[28] T. Osaki, M. Ono, Y. Uyo, M. Ishizuka, T. Tanaka, N. Yamanaka, T. Kurohashi, K. Azuma, Y. Marahata, T. Tsuka, N. Ito, T. Imagawa and Y. Okamoto, “Sonodynamic therapy using 5-aminolevulinic acid enhances the efficacy of bleomycin,” *Ultrasonics*, 67, 76, 2016.

[29] N. Nomikou, C. Sterrett, C. Arthur, B. Mccaughan, J. F. Callan, and A. P. Mchale, “The Effects of Ultrasound and Light on Indocyanine-Green-Treated Tumour Cells and Tissues,” *Chem. Med. Chem.*, 7, 1465, 2012.

[30] M. D. Bilgin, M. Aksel, E. H. Degirmenci, O. Bozkurt Girit, and A. Ozmen, “Efficacy of Methylene Blue and Aluminium Phthalocyanine Mediated Sonophotodynamic Therapy on Prostate Cancer Cell Lines,” *Biophys. J.*, 112, 282a, 2017.

[31] Y. Li, Q. Zhou, Z. Deng, M. Pan, X. Liu, J. Wu, F. Yan and H. Zheng, “IR-780 Dye as a Sonosensitizer for Sonodynamic Therapy of Breast Tumour,” *Sci. Rep.*, 6, 25968, 2016.

[32] V. N. Nemykin and E. A. Lukyanets, “Synthesis of substituted phthalocyanines,” *Arkivoc*, 2010, 136, 2010.

[33] J. Alzeer, P. J. C. Roth, and N. W. Luedtke, “An efficient two-step synthesis of metal-free phthalocyanines using a Zn(ii) template,” *Chem. Commun.*, 15, 1970, 2009.

[34] P. Gregory, “Industrial applications of phthalocyanines,” *J. Porphyr. Phthalocyanines*, 04, 432, 2000.

[35] Y. Zhang and J. F. Lovell, “Recent applications of phthalocyanines and naphthalocyanines for imaging and therapy,” *Wiley Interdiscip. Rev. Nanomed.*, 9, e1420, 2017.

[36] J. Andzelm, A. M. Rawlett, J. A. Orlicki, J. F. Snyder, and K. K. Baldridge, “Optical properties of phthalocyanine and naphthalocyanine compounds,” *J. Chem. Theory Comput.*, 3, 870, 2007.

[37] L. Edwards and M. Gouterman, “Porphyrins. XV. Vapor absorption spectra and stability: Phthalocyanines,” *J. Mol. Spectrosc.*, 33, 292, 1970.

[38] M. Gouterman, G. H. Wagnière, and L. C. Snyder, “Spectra of porphyrins. Part II. Four orbital model,” *J. Mol. Spectrosc.*, 11, 108, 1963.

[39] P. C. Lo, M. S. Rodríguez-Morgade, R. K. Pandey, D. K. P. Ng, T. Torres, and F. Dumoulin, “The unique features and promises of phthalocyanines as advanced photosensitisers for photodynamic therapy of cancer,” *Chem. Soc.*

Rev., 49, 1041, 2020.

[40] S. i. Ogura, K. Tabata, K. Fukushima, T. Kamachi and I. Okura, “Development of phthalocyanines for photodynamic therapy,” *J. Porphyr. Phthalocyanines*, 10, 1116, 2006 .

[41] T. Nyokong, “Desired properties of new phthalocyanines for photodynamic therapy,” *Pure Appl. Chem.*, 83, 1763, 2011.

[42] Z. Diwu and J. William Lown, “Phototherapeutic potential of alternative photosensitizers to porphyrins,” *Pharmacol. Ther.*, 63, 1, 1994.

[43] C. Morville, J. Chaud, F. Bolze, and A. Specht, “Photolytical reactions for light induced biological effectors release: on the road to the phototherapeutic window,” *J. Incl. Phenom. Macrocycl. Chem.*, 101, 291, 2021.

[44] X. Li, k. Jeong, Y. Lee, T. Guo, D. Lee, J. Park, N. Kwon, J. H. Na, S. K. Hong, S. S. Cha, J. D. Huang, S. Choi, S. Kim and J. Yoon, “Water-soluble phthalocyanines selectively bind to albumin dimers: A green approach toward enhancing tumour-targeted photodynamic therapy,” *Theranostics*, 9, 6412, 2019.

[45] Y. Chin, S. H. Lim, Y. Zorlu, V. Ahsen, L. V. Kiew, L. Y. Chung, F. Dumoulin and H. B. Lee, “Improved Photodynamic Efficacy of Zn(II) Phthalocyanines via Glycerol Substitution,” *PLoS One*, 9, e97894, 2014.

[46] A. L. Lin, P. P. Fan, S. F. Liu, J. H. Chen, Y. Y. Zhao, B. Y. Zheng, M. R. Ke and J. D. Huang, “A phthalocyanine-based liposomal nanophotosensitizer with highly efficient tumour-targeting and photodynamic activity,” *Dye. Pigment.*, 180, 108455, 2020.

[47] A. Ormond and H. Freeman, “Dye Sensitizers for Photodynamic Therapy,” *Materials (Basel).*, 6, 817, 2013.

[48] H. Abrahamse and M. R. Hamblin, “New photosensitizers for photodynamic therapy,” *Biochem.*, 473, 347, 2016.

[49] T. P. Mthethwa, S. Tuncel, M. Durmuş, and T. Nyokong, “Photophysical and photochemical properties of a novel thiol terminated low symmetry zinc phthalocyanine complex and its gold nanoparticles conjugate,” *Dalt. Trans.*, 42, 4922, 2013.

[50] M. Van Leeuwen, A. Beeby, I. Fernandes, and S. H. Ashworth, “The photochemistry and photophysics of a series of alpha octa(alkyl-substituted) silicon, zinc and palladium phthalocyanines,” *Photochem. Photobiol. Sci.*, 13, 62, 2014.

[51] L. Huang, Y. Xuan, Y. Koide, T. Zhiyentayev, M. Tanaka, and M. R. Hamblin, “Type i and Type II mechanisms of antimicrobial photodynamic therapy: An in vitro study on gram-negative and gram-positive bacteria,” *Lasers Surg. Med.*, 44, 490, 2012.

[52] M. S. Baptista, J. Cadet, P. D. Mascio, A. A. Ghogare, A. Greer, M. R. Hamblin,

C. Lorente, S. C. Nunez, M. S. Ribeiro, A. H. Thomas, M. Vignoni and T. M. Yoshimura, “Type I and Type II Photosensitized Oxidation Reactions: Guidelines and Mechanistic Pathways,” *Photochem. Photobiol.*, 93, 912, 2017.

[53] C. M. Quinzii, L. López, R. W. Gilkerson, B. Dorado, J. Coku, A. B. Naini, C. Lagier-Tourenne, M. Schuelke, L. Salviati, R. Carrozzo, F. Santorelli, S. Rahman, M. Tazir, M. Koenig, S. DiMauro and M. Hirano “Reactive oxygen species, oxidative stress, and cell death correlate with level of CoQ10 deficiency,” 24, 3733, 2010.

[54] A. Allegra, G. Pioggia, A. Tonacci, C. Musolino, and S. Gangemi, “Oxidative stress and photodynamic therapy of skin cancers: Mechanisms, challenges and promising developments,” *Antioxidants*, 9, 448, 2020.

[55] H. Kolarova, K. Tomankova, R. Bajgar, P. Kolar, and R. Kubinek, “Photodynamic and Sonodynamic Treatment by Phthalocyanine on Cancer Cell Lines,” *Ultrasound Med. Biol.*, 35, 1397, 2009.

[56] G. Y. Atmaca, “Synthesis of Palladium Phthalocyanine and Investigation of Sono-Photodynamic Therapy Properties,” *Celal Bayar Üniversitesi Fen Bilim. Derg.*, 16, 367, 2020.

[57] Y. Iwase, N. Yumita, K. Nishi, H. Kuwahara, T. Fukai, T. Ikeda, F. S. Chen, Y. Momose and S. I. Umemura, “Apoptosis induction by aluminum phthalocyanine tetrasulfonate-based sonodynamic therapy in HL-60 cells,” *Jpn. J. Appl. Phys.*, 54, 07HD05, 2015.

[58] Y. A. Martins, M. J. Fonseca, T. Z. Pavan, and R. F. Lopez, “Bifunctional Therapeutic Application of Low-Frequency Ultrasound Associated with Zinc Phthalocyanine-Loaded Micelles” *Int. J. Nanomedicine*, 15, 8075, 2020.

[59] Y. Gong, X. Wang, F. Gong, G. Li, Y. Yang, L. Hou, Q. Zhang, Z. Liu and L. Chneg, “Phthalocyanine iron nanodots for combined chemodynamic-sonodynamic cancer therapy,” *Sci. China Mater.*, 65, 2600, 2022.

[60] E. Güzel, G. Y. Atmaca, A. E. Kuznetsov, A.Turkkol, M. D. Bilgin and A. Erdoğmuş, “Ultrasound versus light: exploring photophysicochemical and sonochemical properties of phthalocyanine-based therapeutics, theoretical study, and In Vitro evaluations”, *ACS Appl. Bio Mater.*, 5, 1139, 2022.

[61] K. Tomankova, H. Kolarova, P. Kolar, K. Kejlova, and D. Jirova, “Study of cytotoxic effect of photodynamically and sonodynamically activated sensitizers in vitro,” *Toxicol. Vitr.*, 23, 1465, 2009.

[62] H. Kolářová, R. Bajgar, K. Tománková, E. Krestýn, L. Doležal, and J. Hálek, “In vitro study of reactive oxygen species production during photodynamic therapy in ultrasound-pretreated cancer cells,” *Physiol. Res.*, 56, S27, 2007.

[63] G. Y. Atmaca, M. Aksel, B. Keskin, M. D. Bilgin, and A. Erdoğmuş, “The photo-physicochemical properties and in vitro sonophotodynamic therapy activity of Di-axially substituted silicon phthalocyanines on PC3 prostate cancer cell line,”

Dye. Pigment., 184, 108760, 2021.

[64] P. Zhao, Y. L. Wu, X. Y. Li, L. L. Feng, L. Zhang, B. Y. Zheng, M. R. Ke, and J. D. Huang, "Aggregation-Enhanced Sonodynamic Activity of Phthalocyanine–Artesunate Conjugates," *Angew. Chemie Int. Ed.*, 61, e202113506, 2022.

[65] M. Halaskova, A. Rahali, V. Almeida-Marrero, M. Machacek, R. Kucera, B. Jamoussi, T. Torres, V. Novakova, A. de la Escosura and P. Zimcik, "Peripherally Crowded Cationic Phthalocyanines as Efficient Photosensitizers for Photodynamic Therapy," *ACS Med. Chem. Lett.*, 12, 502, 2021.

[66] S. Gavas, S. Quazi, and T. M. Karpiński, "Nanoparticles for Cancer Therapy: Current Progress and Challenges," *Nanoscale Research Letters*, 16, 173, 2021.

[67] I. Rosenthal, J. Z. Sostaric, and P. Riesz, "Sonodynamic therapya review of the synergistic effects of drugs and ultrasound," *Ultrason. Sonochem.*, 11, 349, 2004.

[68] A. K. W. Wood and C. M. Sehgal, "A review of low-intensity ultrasound for cancer therapy," *Ultrasound. Med. Biol.*, 41, 905, 2015.

[69] M. Trendowski, "Using the Promise of Sonodynamic Therapy in the Clinical Setting against Disseminated Cancers," *Chemother. Res. Pract.*, 2015, 316015, 2015.

[70] T. Yamaguchi, S. Kitahara, K. Kusuda, J. Okamoto, Y. Horise, K. Masamune and Y. Muragaki, "Current landscape of sonodynamic therapy for treating cancer," *Cancers*, 13, 6184, 2021.

[71] E. Beguin, S. Shrivastava, N. V. Dezhkunov, A. P. Mchale, J. F. Callan, and E. Stride, "Direct Evidence of Multibubble Sonoluminescence Using Therapeutic Ultrasound and Microbubbles," *ACS Appl. Mater. Interfaces*, 11, 19913, 2019.

[72] A. Sazgarnia, A. Shanei, H. Eshghi, M. Hassanzadeh-Khayyat, H. Esmaily, and M. M. Shanei, "Detection of sonoluminescence signals in a gel phantom in the presence of Protoporphyrin IX conjugated to gold nanoparticles," *Ultrasonics*, 53, 29, 2013.

[73] D. Costley C. Mc Ewan, C. Fowley, A.P. McHale, J.Atchison, N. Nomikou and J.F. Callan, "Treating cancer with sonodynamic therapy: A review," *Int. J. Hyperth.*, 31, 107, 2015.

[74] Q. Lacerda, M. Tantawi, D. B. Leeper, M. A. Wheatley, and J. R. Eisenbrey, "Emerging Applications of Ultrasound-Contrast Agents in Radiation Therapy," *Ultrasound. Med. Biol.*, 47, 1465, 2021.

[75] V. Mišík and P. Riesz, "Free radical intermediates in sonodynamic therapy," *Ann. N.Y. Acad. Sci.*, 899, 335, 2000.

[76] D. Kessel, J. Lo, R. Jeffers, J. Brian Fowlkes, and C. Cain, "Modes of photodynamic vs. sonodynamic cytotoxicity," *J. Photochem. Photobiol. B Biol.*,

28, 219, 1995.

[77] S. Merouani, O. Hamdaoui, Y. Rezgui, and M. Guemini, “Effects of ultrasound frequency and acoustic amplitude on the size of sonochemically active bubbles-Theoretical study,” *Ultrason. Sonochem.*, 20, 815, 2013.

[78] A. Brotchie, F. Grieser, and M. Ashokkumar, “Effect of power and frequency on bubble-size distributions in acoustic cavitation,” *Phys. Rev. Lett.*, 102, 2009.

[79] S. M. Z. Uddin, D. E. Komatsu, T. Motyka, and S. Petterson, “Low-Intensity Continuous Ultrasound Therapies—A Systematic Review of Current State-of-the-Art and Future Perspectives,” *J. Clin. Med.*, 10, 2698, 2021.

[80] P. Sen, M. Managa, and T. Nyokong, “New type of metal-free and Zinc(II), In(III), Ga(III) phthalocyanines carrying biologically active substituents: Synthesis and photophysicochemical properties and photodynamic therapy activity,” *Inorganica Chim. Acta*, 491, 1, 2019.

[81] A. Tuhl, S. Makhseed, P. Zimcik, N. Al-Awadi, V. Novakova, and J. Samuel, “Heavy metal effects on physicochemical properties of non-aggregated azaphthalocyanine derivatives,” *J. Porphyr. Phthalocyanines*, 16, 817, 2012.

[82] E. Güzel, G. Y. Atmaca, A. E. Kuznetsov, A. Turkkol, M. D. Bilgin, and A. Erdoğmuş, “Ultrasound versus Light: Exploring Photophysicochemical and Sonochemical Properties of Phthalocyanine-Based Therapeutics, Theoretical Study, and in Vitro Evaluations,” *ACS Appl. Bio. Mater.*, 5, 1139, 2022.

[83] T. de Souza, F. Antonio, M. Zanotto, P. Homem-de-Mello, and A. Ribeiro, “Photophysical and Photochemical Properties and Aggregation Behavior of Phthalocyanine and Naphthalocyanine Derivatives,” *J. Braz. Chem. Soc.*, 29, 1199, 2017.

[84] R. R. Millard and B. I. Greene, “Direct determination of nonradiative relaxation rates in nonfluorescent metallophthalocyanines,” *J. Phys. Chem.*, 89, 2976, 1985.

[85] P. Zimcik, A. Malkova, L. Hruba, M. Miletin, and V. Novakova, “Bulky 2,6-diphenylphenylsulfanyl substituents efficiently inhibit aggregation in phthalocyanines and tetrapyrazinoporphyrazines and control their photophysical and electrochemical properties,” *Dye. Pigment.*, 136, 715, 2017.

[86] T. Ikeuchi, J. Mack, T. Nyokong, N. Kobayashi, and M. Kimura, “Aggregation Control of Robust Water-Soluble Zinc(II) Phthalocyanine-Based Photosensitizers,” *Langmuir*, 32, 11980, 2016.

[87] C. P. S. Ribeiro and L. M. O. Lourenço, “Overview of cationic phthalocyanines for effective photoinactivation of pathogenic microorganisms,” *J. Photochem. Photobiol. C: Photochem. Rev.*, 48, 100422, 2021.

[88] G. Ongarora, X. Hu, S. D. Verberne-Sutton, J. C. Garno, and M. G. H. Vicente, “Syntheses and photodynamic activity of pegylated cationic Zn(II)-phthalocyanines in HEp2 cells,” *Theranostics*, 2, 9850, 2012.

[89] B. Chen, W. Le, Y. Wang, Z. Li, D Wang, L. Ren, L. Lin, S. Cui, J.J. Hu, Y. Hu, P. Yang, R.C. Ewing, D. Shi and Z. Cui, “Targeting negative surface charges of cancer cells by multifunctional nanoprobes,” *Theranostics*, 6, 1887, 2016.

[90] C. Young, A. Vedadghavami, and A. G. Bajpayee, “Bioelectricity for Drug Delivery: The Promise of Cationic Therapeutics,” *Bioelectricity*, 2, 68, 2020.

[91] L. Gui, Q. Zhang, Y. Wang, K. Fang, A. Wang, Z. You, L. Zhou, J. Zhou and S. Wei, “Zwitterionic phthalocyanine zinc (II) synthesis, and photodynamic activity comparison with nonionic and cationic phthalocyanine,” *Inorg. Chem. Commun.*, 75, 1, 2017,

[92] G. G. Matlou, D. O. Oluwole, E. Prinsloo, and T. Nyokong, “Photodynamic therapy activity of zinc phthalocyanine linked to folic acid and magnetic nanoparticles,” *J. Photochem. Photobiol. B Biol.*, 186, 216, 2018 .

[93] Y. Uruma, L. Sivasamy, P. M. Y. Yoong, K. Onuma, Y. Omura, M. Doe, M. Osaki and F. Okada, “Synthesis and biological evaluation of glucose conjugated phthalocyanine as a second-generation photosensitizer,” *Bioorganic Med. Chem.*, 27, 3279, 2019.

[94] A. Okoth, Z. Zhou, B. Ongarora, A. Stutes, J. M. Mathis, and M. G. H. Vicente, “Synthesis and investigation of phthalocyanine-biotin conjugates,” *J. Porphyr. Phthalocyanines*, 23, 125, 2019.

[95] L. H. Reddy, “Drug delivery to tumours: recent strategies,” *J. Pharm. Pharmacol.*, 57, 1231, 2010 .

[96] S. Chen, X. Zhao, J. Chen, L. Kuznetsova, S. S. Wong and I, Ojima, “Mechanism-based tumour-targeting drug delivery system. Validation of efficient vitamin receptor-mediated endocytosis and drug release,” *Bioconjug. Chem.*, 21, 979, 2010.

[97] Y. Ge, X. Weng, T. Tian, F. Ding, R. Huang, L. Yuan, J. Wu, T. Wang, P. Guo and X. Zhou, “A mitochondria-targeted zinc(ii) phthalocyanine for photodynamic therapy,” *RSC Adv.*, 3, 12839, 2013.

[98] J. Marino, M. C. García Vior, V. A. Furmento, V. C. Blank, J. Awruch, and L. P. Roguin, “Lysosomal and mitochondrial permeabilization mediates zinc(II) cationic phthalocyanine phototoxicity,” *Int. J. Biochem. Cell Biol.*, 45, 2553, 2013.

[99] R. Wang, X. Li, and J. Yoon, “Organelle-Targeted Photosensitizers for Precision Photodynamic Therapy,” *ACS Appl. Mater. Interfaces*, 13, 19543, 2021.

[100] Y. Nakamura, A. Mochida, P. L. Choyke, and H. Kobayashi, “Nanodrug Delivery: Is the Enhanced Permeability and Retention Effect Sufficient for Curing Cancer?,” *Bioconjug. Chem.*, 27, 2225, 2016.

[101] R. Prabhu, V. Patravale, and M. D. Joshi, “Polymeric nanoparticles for targeted treatment in oncology: current insights,” *Int. J. Nanomedicine*, 10, 1001, 2015.

[102] Y. Yao, Y. Zhou, L. Liu, Y. Xu, Q. Chen, Y. Wang, S. Wu, Y. Deng, J. Zhang and A. Shao, “Nanoparticle-Based Drug Delivery in Cancer Therapy and Its Role in Overcoming Drug Resistance,” *Front. Mol. Biosci.*, 7, 193, 2020.

[103] M. Camerin, m. Magaraggia, M. Soncin, G. Jori, M. Moreno, I. Chambrier, M. J. Cook and D. A. Russell, “The in vivo efficacy of phthalocyanine-nanoparticle conjugates for the photodynamic therapy of amelanotic melanoma,” *Eur. J. Cancer*, 46, 1910, 2010.

[104] D. Dei, G. Chiti, M. P. De Filippis, L. Fantetti, F. Giuliani, F. Giuntini, M. Soncin, G. Jori and G. Roncucci, “Phthalocyanines as photodynamic agents for the inactivation of microbial pathogens,” *J. Porphyr. Phthalocyanines*, 10, 147, 2006.

[105] S. Moeno, T. Nyokong, “Opposing responses elicited by positively charged phthalocyanines in the presence of CdTe quantum dots,” *Photochem. Photobiol. A Chem.*, 201, 228, 2009.

[106] I. Scalise and E. N. Durantini, “Synthesis, properties, and photodynamic inactivation of Escherichia coli using a cationic and a noncharged Zn(II) pyridyloxyphthalocyanine derivatives,” *Bioorg. Med. Chem.*, 13, 3037, 2005.

[107] A. Sindelo, N. Kobayashi, M. Kimura, and T. Nyokong, “Physicochemical and photodynamic antimicrobial chemotherapy activity of morpholine-substituted phthalocyanines: Effect of point of substitution and central metal,” *J. Photochem. Photobiol. A Chem.*, 374, 58, 2019

[108] L. C. Nene, M. Managa, and T. Nyokong, “Photo-physicochemical properties and in vitro photodynamic therapy activity of morpholine-substituted Zinc(II)-Phthalocyanines π-π stacked on biotinylated graphene quantum dots,” *Dye. Pigment.*, 165, 488, 2019,

[109] X. Lin, Y. Qiu, L. Song, S. Chen, X. Chen, G. Huang, J. Song, X. Chen and H. Yang, “Ultrasound activation of liposomes for enhanced ultrasound imaging and synergistic gas and sonodynamic cancer therapy,” *Nanoscale Horiz.*, 4, 747, 2019.

[110] Y. Horise, M. Maeda, Y. Konishi, J. Okamoto, S. Ikuta, Y. Okamoto, H. Ishi, S. Yoshizawa, S. Umemura, T. Ueyama, S. Tamano, A. Sofuni, K. Takemae, K. Masamune, H. Iseki, N. Nishiyama, K. Kataoka and Y. Muragaki, “Sonodynamic therapy with anticancer micelles and high-intensity focused ultrasound in treatment of canine cancer,” *Front. Pharmacol.*, 10, 545, 2019.

[111] J. Wang, Y. Jiao, and Y. Shao, “Mesoporous silica nanoparticles for dual-mode chemo-sonodynamic therapy by low-energy ultrasound,” *Materials (Basel).*, 11, 2041, 2018.

[112] A. Shanei, A. Sazgarnia, N. T. Meibodi, H. Eshghi, M. Hassanzadeh-Khayyat, H. Esmaily and N. A. Kakhki, “Sonodynamic therapy using protoporphyrin IX conjugated to gold nanoparticles: An in vivo study on a colon tumour model,”

Iran. J. Basic Med. Sci., 15, 759, 2012.

[113] I. Kumari, R. Singla, A. Guliani, and S. K. Yadav, “Nanoencapsulation for drug delivery,” *EXCLI Journal*, 13. 265, 2014.

[114] L. A. Osminkina, A. L. Nikolaev, A. P. Sviridov, N. V. Andronova, K. P. Tamarov, M. B. Gongalsky, A. A. Kudryavtsev, H. M. Treshalina and V. Y. Timoshenko, “Porous silicon nanoparticles as efficient sensitizers for sonodynamic therapy of cancer,” *Microporous Mesoporous Mater.*, 210, 169, 2015.

[115] L. Li, H. Lin, D. Li, Y. Zeng, and G. Liu, “Ultrasound activated nanosensitizers for sonodynamic therapy and theranostics,” *Biomed. Mater.*, 16, 022008, 2021.

[116] P. Zhao, Y. Deng, G. Xiang, and Y. Liu, “Nanoparticle-assisted sonosensitizers and their biomedical applications,” *Int. J. Nanomedicine.*, 16. 4615, 2021.

[117] H. Xu, X. Zhang, R. Han, P. Yang, H. Ma, Y. Song, Z. Lu, W. Yin, X. Wu and H. Wang, “Nanoparticles in sonodynamic therapy: State of the art review,” *RSC Advances*, 6, 50697, 2016.

[118] G. Canavese, A. Ancona, L. Racca, M. Canta, B. Dumontel, F. Barbaresco, T. Limongi and V. Cauda, “Nanoparticle-assisted ultrasound: A special focus on sonodynamic therapy against cancer,” *Chem. Eng. J.*, 340, 155, 2018.

[119] A. Shanei and M. M. Shanei, “Effect of gold nanoparticle size on acoustic cavitation using chemical dosimetry method,” *Ultrason. Sonochem.*, 34, 45, 2017.

[120] A. Sazgarnia and A. Shanei, “Evaluation of acoustic cavitation in terephthalic acid solutions containing gold nanoparticles by the spectrofluorometry method,” *Int. J. Photoenergy*, 2012, 376047, 2012.

[121] D. G. You, V. G. Deepagan, W. Um, S. Jeon, S. Son, H. Chang, H. I. Yoon, Y. W. Cho, M. Swierczewska, S. Lee, M. G. Pomper, I. C. Kwon, K. Kim and J. H. Park, “ROS-generating TiO2 nanoparticles for non-invasive sonodynamic therapy of cancer,” *Sci. Rep.*, 6, 23200, 2016.

[122] M. Aksel, Ö. Kesmez, A. Yavaş, and M. D. Bilgin, “Titaniumdioxide mediated sonophotodynamic therapy against prostate cancer,” *J. Photochem. Photobiol. B Biol.*, 225, 112333, 2021.

[123] A. Sazgarnia, A. Shanei, N. T. Meibodi, H. Eshghi, and H. Nassirli, “A Novel Nanosonosensitizer for Sonodynamic Therapy,” *J. Ultrasound Med.*, 30, 1321, 2011.

[124] J. J. Liu, X. L. Zhang, Z. X. Cong, Z. T. Chen, H. H. Yang, and G. N. Chen, “Glutathione-functionalized graphene quantum dots as selective fluorescent probes for phosphate-containing metabolites,” *Nanoscale*, 5, 1810, 201.

[125] O. J. Achadu and T. Nyokong, “Interaction of Graphene Quantum Dots with 4-Acetamido-2,2,6,6-Tetramethylpiperidine-Oxyl Free Radicals: A Spectroscopic and Fluorimetric Study,” *J. Fluoresc.*, 26, 283, 2016.

[126] R. H. Wu, T. P. Nguyen, G. W. Marquart, T. J. Miesen, T. Mau, and M. R. Mackiewicz, “A facile route to tailoring peptide-stabilized gold nanoparticles using glutathione as a synthon,” *Molecules*, 19, 6754, 2014.

[127] N. Rapulenyane, E. Antunes, and T. Nyokong, “A study of the photophysicochemical and antimicrobial properties of two zinc phthalocyanine-silver nanoparticle conjugates,” *New J. Chem.*, 37, 1216, 2013.

[128] I. Khan, K. Saeed, and I. Khan, “Nanoparticles: Properties, applications and toxicities,” *Arab. J.Chem.*, 12, 908, 2019.

[129] A. C. Burdușel, O. Gherasim, A. M. Grumezescu, L. Mogoantă, A. Ficai, and E. Andronescu, “Biomedical applications of silver nanoparticles: An up-to-date overview,” *Nanomaterials*, 8, 681, 2018.

[130] Shanei and H. Akbari-Zadeh, “Investigating the sonodynamic-radiosensitivity effect of gold nanoparticles on HeLa cervical cancer cells,” *J. Korean Med. Sci.*, 34, e243, 2019.

[131] Shanei, H. Akbari-Zadeh, H. Fakhimikabir, and N. Attaran, “The role of gold nanoparticles in sonosensitization of human cervical carcinoma cell line under ultrasound irradiation: An in vitro study,” *J. Nano Res.*, 59, 1, 2019 .

[132] L. Qi, T. Pan, L. Ou, Z. Ye, C. Yu, B. Bao, Z. Wu, D. Cao and L. Dai, “Biocompatible nucleus-targeted graphene quantum dots for selective killing of cancer cells via DNA damage,” *Commun. Biol.*, 4, 214, 2021.

[133] D. Iannazzo, C. Celesti, and C. Espro, “Recent Advances on Graphene Quantum Dots as Multifunctional Nanoplatforms for Cancer Treatment,” *Biotechnol. J.*, 16, 1900422, 2021.

[134] N. Nwahara, J. Britton, and T. Nyokong, “Improving singlet oxygen generating abilities of phthalocyanines: aluminum tetrasulfonated phthalocyanine in the presence of graphene quantum dots and folic acid,” *J. Coord. Chem.*, 70, 1601, 2017.

[135] Y. N. Antonenko, S. S. Denisov, D. N. Silachev, L. S. Khailova, S. S. Jankauskas, T. I. Rokitskaya, T. I. Danilina, E. A. Kotova, G. A. Korshunova, E. Y. Plotnikov and D. B. Zorov, “A long-linker conjugate of fluorescein and triphenylphosphonium as mitochondria-targeted uncoupler and fluorescent neuro- and nephroprotector,” *Biochim. Biophys. Acta - Gen. Subj.*, 1860, 2463, 2016.

[136] M. Ambroz, A. Beeby, A. J. MacRobert, M. S. C. Simpson, R. K. Svensen, and D. Phillips, “Preparative, analytical and fluorescence spectroscopic studies of sulphonated aluminium phthalocyanine photosensitizers,” *J. Photochem. Photobiol. B Biol.*, 9, 87, 1991.

[137] S. Moeno, E. Antunes, S. Khene, C. Litwinski, and T. Nyokong, “The effect of substituents on the photoinduced energy transfer between CdTe quantum dots and mercapto substituted zinc phthalocyanine derivatives,” *Dalt. Trans.*, 39,

3460, 2010.

[138] Y. I. Openda, P. Sen, M. Managa, and T. Nyokong, “Acetophenone substituted phthalocyanines and their graphene quantum dots conjugates as photosensitizers for photodynamic antimicrobial chemotherapy against Staphylococcus aureus,” *Photodiagnosis Photodyn. Ther.*, 29, 101607, 2020.

[139] D. AlMarzouq, S. A. Majeed, Ö. Budak, and A. Koca, “Manganese phthalocyanine and its graphene quantum dot conjugate: Synthesis, characterization electrochemistry, spectroelectrochemistry, electropolymerization, and electrochromism,” *Inorganica Chim. Acta*, 527, 120558, 2021.

[140] D. O. Oluwole, S. L. Manoto, R. Malabi, C. Maphanga, S. Ombinda-Lemboumba, P. Mthunzi-Kufa and T. Nyokong, “Evaluation of the photophysicochemical properties and photodynamic therapy activity of nanoconjugates of zinc phthalocyanine linked to glutathione capped Au and Au3Ag1 nanoparticles,” *Dye. Pigment.*, 150,139, 2018.

[141] E. Dube, D. O. Oluwole, N. Nwaji, and T. Nyokong, “Glycosylated zinc phthalocyanine-gold nanoparticle conjugates for photodynamic therapy: Effect of nanoparticle shape,” *Spectrochim. Acta - Part A Mol. Biomol. Spectrosc.*, 203, 85, 2018.

[142] S. Fery-Forgues and D. Lavabre, “Are fluorescence quantum yields so tricky to measure? A demonstration using familiar stationery products,” *J. Chem. Educ.*, 76, 1260, 1999.

[143] A. Ogunsipe, J. Y. Chen, and T. Nyokong, “Photophysical and photochemical studies of zinc(II) phthalocyanine derivatives - Effects of substituents and solvents,” *New J. Chem.*, 28, 822, 2004.

[144] M. P. Sk and A. Chattopadhyay, “Induction coil heater prepared highly fluorescent carbon dots as invisible ink and explosive sensor,” *RSC Adv.*, 4, 31994, 2014.

[145] T. H. Tran-Thi, C. Desforge, C. Thiec, and S. Gaspard, “Singlet-singlet and triplet-triplet intramolecular transfer processes in a covalently linked porphyrin-phthalocyanine heterodimer,” *J. Phys. Chem.*, 93, 1226, 1989.

[146] A. Ogunsipe, D. Maree, and T. Nyokong, “Solvent effects on the photochemical and fluorescence properties of zinc phthalocyanine derivatives,” *J. Mol. Struct.*, 650, 131, 2003.

[147] F. Wilkinson, W. P. Helman, and A. B. Ross, “Quantum Yields for the Photosensitized Formation of the Lowest Electronically Excited Singlet State of Molecular Oxygen in Solution,” *J. Phys. Chem. Ref. Data*, 22, 113, 1993.

[148] W. Strober, “Trypan Blue Exclusion Test of Cell Viability,” *Curr. Protoc. Immunol.*, 111, A3.B.1, 2015.

[149] Z. B. Cincin, M. Unlu, B. Kiran, E. S. Bireller, Y. Baran, and B. Cakmakoglu,

"Apoptotic Effects of Quercitrin on DLD-1 Colon Cancer Cell Line," *Pathol. Oncol. Res.*, 21, 333, 2015.

[150] S. Çolak, M. Durmuş, and S. Z. Yildiz, "The water-soluble zwitterionic and cationic tetra-substituted zinc(II) phthalocyanines: Synthesis, photophysical, photochemical and protein binding properties," *Polyhedron*, 113, 115, 2016.

[151] D. Çakir, V. Çakir, Z. Biyiklioğlu, M. Durmuş, and H. Kantekin, "New water soluble cationic zinc phthalocyanines as potential for photodynamic therapy of cancer," *J. Organomet. Chem.*, 745–746, 423, 2013.

[152] M. Idowu, E. Lamprecht, and T. Nyokong, "Interaction of water-soluble thiol capped CdTe quantum dots and bovine serum albumin," *J. Photochem. Photobiol. A Chem.*, 198, 7, 2008.

[153] R. Matshitse, M. Managa and T. Nyokong, "The modulation of the photophysical and photodynamic therapy activities of a phthalocyanine by detonation nanodiamonds: Comparison with graphene quantum dots and carbon nanodots", *Diam. Relat. Mater.*, 101, 107617, 2020.

[154] D. M. Mafukidze and T. Nyokong, "Graphene quantum dot-phthalocyanine polystyrene conjugate embedded in asymmetric polymer membranes for photocatalytic oxidation of 4-chlorophenol," J. Coord. Chem., 70, 3598, 2017.

[155] Z. Ni, Y. Wang, T. Yu and Z. Shen, "Raman spectroscopy and imaging of graphene", *Nano Res.*, 1, 273, 2008.

[156] T. G. F. Souza, V. S. T. Ciminelli, and N. D. S. Mohallem, "A comparison of TEM and DLS methods to characterize size distribution of ceramic nanoparticles," *J. Phys.*, 733, 012039, 2016.

[157] L. Li, J-F. Zhao, N. Won, H. Jin, S. Kim and J-Y. Chen, "Quantum dot-aluminum phthalocyanine conjugates perform photodynamic reactions to kill cancer cells via fluorescence resonance energy transfer (FRET)", *Nanoscale Res. Lett.*, 7, 386, 2012.

[158] S. Nath, S. K. Ghosh, S. Kundu, S. Praharaj, S. Panigrahi, and T. Pal, "Is Gold Really Softer than Silver? HSAB Principle Revisited," *J. Nanoparticle Res.*, 8, 111, 2006.

[159] T. B. Ogunbayo, I. A. Akinbulu, G. Mbambisa, M. A. Olusegun, and J. O. Olafimihan, "Sythesis, characterization and Pd(II) ions coordination equilibrium studies of a-octasubstituted octylthio- and dodecylthio-derivatsed phthalocyanines," *Ife J. Sci.*, 18775, 2017.

[160] A. Eisfield and J.S. Briggs, "The J- and H-Bands of organic dye aggregates", *Chem. Phys*. 324, 376, 2006.

[161] S. Doria, A. Lapini, M. Di Donato, R. Righini, N. Azzaroli, A. Oagatti, J. R. Caram, T. S. Sinclair, L. Cupellini, S. Jurinovich, B. Mennucci, G. Zanotti, A. M. Paoletti, G. Pennesi and P. Foggi, "Understanding the influence of disorder on the exciton dynamics and energy transfer in Zn-phthalocyanine H-aggregates,"

Phys. Chem. Chem. Phys., 20, 2022331, 2018.

[162] J. M. Dąbrowski and L. G. Arnaut, "Photodynamic therapy (PDT) of cancer: From local to systemic treatment," *Photochem. Photobiol. Sci.*, 14, 1765, 2015.

[163] Y-Y. Zhao, J-Y. Chen, J-Q. Hu, L. Zhang, A-L. Lin, R. Wang, B-Y. Zheng, M.R. Ke, X. Li and J-D. Huang, "The substituted zinc(II) phthalocyanines using "sulfur bridge" as the linkages. Synthesis, red-shifted spectroscopic properties and structure-inherent targeted photodynamic activities", *Dyes. Pigm.*, 189, 109270, 2021.

[164] S. W. Verbruggen, M. Keulemans, J. A. Martens and S. Lenaerts, "" Predicting the surface plasmon resonance wavelength of gold-silver alloy nanoparticles, *J. Phys. Chem. C*, 11719142, 2013

[165] S. Peteni, K. E. Sekhosana, J. Britton, and T. Nyokong, "Effects of charge on the photophysicochemical properties of zinc phthalocyanine derivatives doped onto silica nanoparticles," *Polyhedron*, 138, 37, 2017.

[166] A. Erdoğmuş, A. Ogunsipe, and T. Nyokong, "Synthesis, photophysics and photochemistry of novel tetra(quinoxalinyl)phthalocyaninato zinc(II) complexes," *J. Photochem. Photobiol. A Chem.*, 205, 12, 2009.

[167] B. Keskin, O. Okuyucu, A. Altindal, and A. Erdoğmuş, "Novel indium(iii) phthalocyanines; Synthesis, photophysical and humidity sensing properties," *New J. Chem.*, 40, 5537, 2016.

[168] S. Çolak, M. Durmuş, and S. S. Yıldız, "Investigation of the photophysical and photochemical properties of peripherally tetra-substituted water-soluble zwitterionic and cationic zinc(II) phthalocyanines," *Dalt. Trans.*, 45, 10402, 2016.

[169] M. Çamur, V. Ahsen, and M. Durmuş, "The first comparison of photophysical and photochemical properties of non-ionic, ionic and zwitterionic gallium (III) and indium (III) phthalocyanines," *J. Photochem. Photobiol. A Chem.*, 219, 217, 2011.

[170] R. Matshitse, N. Nwaji, M. Mananga, E. Prinsloo, and T. Nyokong, "Effect of number of positive charges on the photophysical and photodynamic therapy activities of quarternary benzothiazole substituted zinc phthalocyanine," *J. Photochem. Photobiol. A Chem.*, 367, 253, 2018.

[171] S. Mgidlana, D. O. Oluwole, and T. Nyokong, "Fabrication of efficient nonlinear optical absorber using Zn phthalocyanine-semiconductor quantum dots conjugates," *Polyhedron*, 159, 102, 2019.

[172] A. Magadla, B. Babu, J. Mack, and T. Nyokong, "Positively charged styryl pyridine substituted Zn(ii) phthalocyanines for photodynamic therapy and photoantimicrobial chemotherapy: Effect of the number of charges," *Dalt. Trans.*, 50, 9129, 2021.

[173] D. Masih, S. M. Aly, A. Usman, E. Alarousu, and O. F. Mohammed, "Real-time

observation of ultrafast electron injection at graphene-Zn porphyrin interfaces," *Phys. Chem. Chem. Phys.*, 17, 9015, 2015.

[174] T. Nojiri, M. M. Alam, H. Konami, A. Watanabe, and O. Ito, "Photoinduced electron transfer from phthalocyanines to fullerenes (C60 and C70)," *J. Phys. Chem. A*, 101, 7943, 1997.

[175] M. G. Debacker, O. Deleplanque, B. Van Vlierberge, and F. X. Sauvage, "A Laser Photolysis Study of Triplet Lifetimes and of Triplet–Triplet Annihilation Reactions of Phthalocyanins in DMSO Solutions," *Laser Chem.*, 8, 497437, 1988.

[176] M. Canlica and T. Nyokong, "Synthesis, characterization, and photophysical properties of novel ball-type dinuclear and mononuclear containing four 1,1′-binaphthyl-8, 8′-diol bridged metallophthalocyanines with long triplet state lifetimes," *Dalt. Trans.*, 40, 5285, 2011.

[177] T. N. Singh-Rachford and F. N. Castellano, "Pd(II) phthalocyanine-sensitized triplet - Triplet annihilation from rubrene," *J. Phys. Chem. A*, 112, 3550, 2008. Old 178.

[178] K. Virkki, H. Hakola, M. Urbani, L. Tejerina, M. Ince, M. V. Martines-Diaz, T. Torres, V. Golovanova, V. Golovanov and N. V. Tkachenko, "Photoinduced Electron Injection from Zinc Phthalocyanines into Zinc Oxide Nanorods: Aggregation Effects," *J. Phys. Chem. C*, 121, 9594, 2017.

[179] D. C. Hone, P. I. Walker, R. E. Evans-Gowing, S. FitzGerald, A. Beepy, I. Chambrier, M. J. Cook and D. A. Russell, "Generation of cytotoxic singlet oxygen via phthalocyaninel-stabilized gold nanoparticles: A potential delivery vehicle for photodynamic therapy," *Langmuir*, 18, 2985, 2002.

[180] S. N. Nyamu, L. Ombaka, E. Masika, and M. Ng'ang'a, "Antimicrobial Photodynamic Activity of Phthalocyanine Derivatives," *Adv. Chem.*, 2018, 2598062, 2018.

[181] F. Nakonechny, M. Nisnevitch, Y. Nitzan, and M. Nisnevitch, "Sonodynamic excitation of rose bengal for eradication of gram-positive and gram-negative bacteria," *Biomed Res. Int.*, 2013, 684930, 2013.

[182] G. Dilber, M. Durmuş, and H. Kantekin, "Non-aggregated zwitterionic Zinc(II) phthalocyanine complexes in water with high singlet oxygen quantum yield," *Dye. Pigment.*, vol. 160, 267, 2019.

[183] E. Güzel, G. Yaşa Atmaca, A. Erdoğmuş, and M. B. Koçak, "Novel sulfonated hydrophilic indium(III) and gallium(III) phthalocyanine photosensitizers: preparation and investigation of photophysicochemical properties," *J. Coord. Chem.*, 70, 2659, 2017.

[184] M. Çamur, M. Durmuş, and M. Bulut, "Highly singlet oxygen generative water-soluble coumarin substituted zinc(II) phthalocyanine photosensitizers for photodynamic therapy," *Polyhedron*, 41, 92, 2012.

[185] A. M. Santiago, C. I. M. Santos, L. M. O. Lourenço, I. F. A. Mariz, J. P. C. Tomé, and E. Maçôas, “Graphene quantum dots and phthalocyanines turn-off-on photoluminescence nanosensor for ds-DNA,” *Nanomaterials*, 12, 1892, 2022.

[186] D. Yakovlev, E. Kolesova, S. Sizova, K. Annas, M. Tretyak, V. Loschenov, A. Orlova and V. Oleinikov, “New bonjugates based on AIS/ZnS quantum dots and aluminum phthalocyanine photosensitizer: synthesis, properties and some perspectives,” *Nanomaterials*, 12, 3874, 2022.

[187] S. A. Majeed, K. E. Sekhosana, and A. Tuhl, “Progress on phthalocyanine-conjugated Ag and Au nanoparticles: Synthesis, characterization, and photo-physicochemical properties,” *Arab. J. Chem.*, 13, 8848, 2020.

[188] X. Chen, Q. Ye, D. Ma, J. Chen, Y. Wang, H. Yang, S. Xie, R. Yu and Y. Peng, “Gold nanoparticles-pyrrolidinonyl metal phthalocyanine nanoconjugates: Synthesis and photophysical properties,” *J. Lumin.*, 195, 348, 2018.

[189] P. Tharkar, R. Varanasi, W. S. F. Wong, C. T. Jin, and W. Chrzanowski, “Nano-Enhanced Drug Delivery and Therapeutic Ultrasound for Cancer Treatment and Beyond,” *Frontiers in Bioengineering and Biotechnology*, 7, 324, 2019.

[190] C. C. Karanlık, G. Y. Atmaca, and A. Erdoğmuş, “Improved singlet oxygen yields of new palladium phthalocyanines using sonochemistry and comparisons with photochemistry,” *Polyhedron*, 206, 115351, 2021.

[191] N. Farajzadeh, G. Y. Atmaca, A. Erdoğmuş, and M. B. Koçak, “Comparatively singlet oxygen efficiency by sono-photochemical and photochemical studies of new lutetium (III) phthalocyanines,” *Dye. Pigment.*, 190, 109325, 2021.

[192] B. Ghazal, A. Husain, A. Ganesan, M. Durmuş, X. F. Zhang, and S. Makhseed, “Exceptionally effective generation of singlet oxygen in aqueous media via iodinated zinc-phthalocyanine,” *Dye. Pigment.*, 164, 296, 2019.

[193] L. Serpe, F. Foglietta, and R. Canaparo, “Nanosonotechnology: The next challenge in cancer sonodynamic therapy,” *Nanotechnol. Rev.*, 1, 173, 2012.

[194] J. Kollar, M. Machacek, M. Halaskova, J. Lenco, R. Kucera, J. Demuth, M. Rohlickova, K. Hasonova, M. Miletin, V. Novakova and P. Zimcik, “Cationic versus anionic phthalocyanines for photodynamic therapy: what a difference the charge makes,” *J. Med. Chem.*, 63, 7616, 2020.

[195] P. Wang, C. Li, X. Wang, W. Xiong, X. Feng, Q. Liu, A. W. Leung, C. Xu, “Anti-metastatic and pro-apoptotic effects elicited by combination photodynamic therapy with sonodynamic therapy on breast cancer both in vitro and in vivo,” *Ultrason. Sonochem.*, 23, 116, 2015.

[196] A. Ahmadi, S. Hosseini-Nami, Z. Abed, J. Beik, L. Aranda-Lara, H. Samadian, E. Morales-Avila, M. Jaymand and A. Shakeri-Zadeh, “Recent advances in ultrasound-triggered drug delivery through lipid-based nanomaterials,” *Drug Discov.*, 25, 2182, 2020.

[197] S. Ciancia, A. Cafarelli, A. Zahoranova, A. Menciassi, and L. Ricotti, “Pulsatile

Drug Delivery System Triggered by Acoustic Radiation Force," *Front. Bioeng. Biotechnol.*, 8, 317, 2020.

[198] X. Huang, P. K. Jain, I. H. El-Sayed, and M. A. El-Sayed, "Plasmonic photothermal therapy (PPTT) using gold nanoparticles," *Lasers Med. Sci.*, 23, 217, 2008.

[199] Y. Hu, S. Xue, T. Long, P. Lyu, X. Zhang, J. Chen, S. Chen, C. Liu and X. Chen, "Opto-acoustic synergistic irradiation for vaporization of natural melanin-cored nanodroplets at safe energy levels and efficient sono-chemo-photothermal cancer therapy," *Theranostics*, 10, 10448, 2020.

[200] J. Y. An, W. Um, D. G. You, Y. Song, J. Lee, N. V. Quy, H. Joo, J. Jeon and J. H. Park, "Gold-installed hyaluronic acid hydrogel for ultrasound-triggered thermal elevation and on-demand cargo release," *Int. J. Biol. Macromol.*, 193, 553, 2021.

[201] M. L. Jobin, P. Bonnafous, H. Temsamani, F. Dole, A. Grélard, E. J. Dufourc and I. D. Alves, "The enhanced membrane interaction and perturbation of a cell penetrating peptide in the presence of anionic lipids: Toward an understanding of its selectivity for cancer cells," *Biochim. Biophys. Acta - Biomembr.*, 1828, 1457, 2013.

[202] Y. Chang, J-Y. Chen, Y. Yang, T. Lin, L. Zeng, J-F. Xu, J-L. Hou, X. Zhang, "Targeting the cell membrane by charge-reversal amphiphilic pillar[5]arene for the selective killing of cancer cells," *ACS Appl. Mater. Interfaces*, 11, 38497, 2019.

[203] K. Cho, X. Wang, S. Nie, Z. Chen, and D. M. Shin, "Therapeutic nanoparticles for drug delivery in cancer," *Clinical Cancer Research*, 14, 1310, 2008.

[204] A. Dadwal, A. Baldi, and R. Kumar Narang, "Nanoparticles as carriers for drug delivery in cancer," *Artif. Cells, Nanomedicine, Biotechnol.*, 46, 295, 2018.

[205] M. R. Papasani, G. Wang, and R. A. Hill, "Gold nanoparticles: The importance of physiological principles to devise strategies for targeted drug delivery," *Nanomed. Nanotechnol.*, 8, 804, 2012.

[206] L. A. Austin, M. A. MacKey, E. C. Dreaden, and M. A. El-Sayed, "The optical, photothermal, and facile surface chemical properties of gold and silver nanoparticles in biodiagnostics, therapy, and drug delivery," *Arch. Toxicol.*, 88, 1391, 2014.

[207] N. Desai, M. Momin, T. Khan, S. Gharat, R. S. Ningthoujam, and A. Omri, "Metallic nanoparticles as drug delivery system for the treatment of cancer," *Opin. Drug Deliv.*, 18, 1261, 2021.

[208] H. Meng, M. Xue, T. Xia, Z. Ji, D. Y. Tarn, J. I. Zink and A. E. Nel, "Use of size and a copolymer design feature to improve the biodistribution and the enhanced permeability and retention effect of doxorubicin-loaded mesoporous silica nanoparticles in a murine xenograft tumour model," *ACS Nano*, 5, 4131, 2011.

[209] Y. Li, Y. Wang, A. Wang, S. Lu, L. Zhou, J. Zhou, Y. Lin and S. Wei, “Spectroscopic study on the interaction of bovine serum albumin with zinc(II) phthalocyanine,” *Luminescence*, 30, 1367, 2015.

[210] K. Khezami, K. Harmandar, E. Bağda, E. Bağda, G. Şahin, N. Karakodak and M. Durmuş, “BSA/DNA binding behavior and the photophysicochemical properties of novel water soluble zinc(II)phthalocyanines directly substituted with piperazine groups,” *J. Biol. Inorg. Chem.*, 26, 455, 2021.

[211] S. M. T. Nunes, F. S. Sguilla, and A. C. Tedesco, “Photophysical studies of zinc phthalocyanine and chloroaluminum phthalocyanine incorporated into liposomes in the presence of additives,” *Brazilian J. Med. Biol. Res.*, 37, 273, 2004.

[212] A. Ogunsipe and T. Nyokong, “Photophysicochemical consequences of bovine serum albumin binding to non-transition metal phthalocyanine sulfonates,” *Photochem. Photobiol. Sci.*, 4, 510, 2005.

[213] A. A. Esenpinar, M. Durmu, and M. Bulut, “Photophysical, photochemical and BSA binding/BQ quenching properties of quaternizable coumarin containing water soluble zinc phthalocyanine complexes,” *Spectrochim. Acta - Part A Mol. Biomol. Spectrosc.*, 79, 608, 2011.

[214] L. Zheng, Y. He, P. Lin, L. Liu, H. Yang, Y. Peng and S. Xie, “Spectroscopic analysis of the interaction between tetra-(p-sulfoazophenyl-4-aminosulfonyl)-substituted aluminum (III) phthalocyanines and serum albumins,” *J. Innov. Opt. Health Sci.*, 10, 1650043, 2017.

[215] S.L. Murov, I. Carmichael, G.L. Hug, Handbook of Photochemistry, 2nd edition (M. Decker, New York), 1993.

[216] G. Peskir, “On the Diffusion Coefficient: The Einstein Relation and Beyond,” *Stoch. Model.*, 19, 383, 2003.

[217] D. Fologea, B. Ledden, D. S. McNabb, and J. Li, “Electrical characterization of protein molecules by a solid-state nanopore,” *Appl. Phys. Lett.*, 91, 539011, 2007.

[218] X. Wang, G. Herting, I. O. Wallinder and E. Blomberg, “Adsorption of bovine serum albumin on silver surfaces enhances the release of silver at pH neutral conditions”, *Phys. Chem. Chem. Phys.*, 17, 18524, 2015.

[219] J. Kollar, M. Machacek, A. Jancarova, P. Kubat, R. Kucera, M. Miletin, V. Novakova and P. Zimcik “Effect of bovine serum albumin on the photodynamic activity of sulfonated tetrapyrazinoporphyrazine,” *Dye. Pigment.*, 162, 358, 2019.

[220] J. T. F. Lau, P-C. Lo, X-J. Jiang, Q. Wang and D. K. P. Ng, “A dual activatable photosensitizer toward targeted photodynamic therapy”, *J. Med. Chem*., 57, 4088, 2014.

[221] E. Dube, N. Nwaji, J. Mack and T. Nyokong, “The photophysicochemical

behavior of symmetric and asymmetric zinc phthalocyanines, surface assembled onto gold nanotriangles", *New J. Chem.*, 42, 14290, 2018.